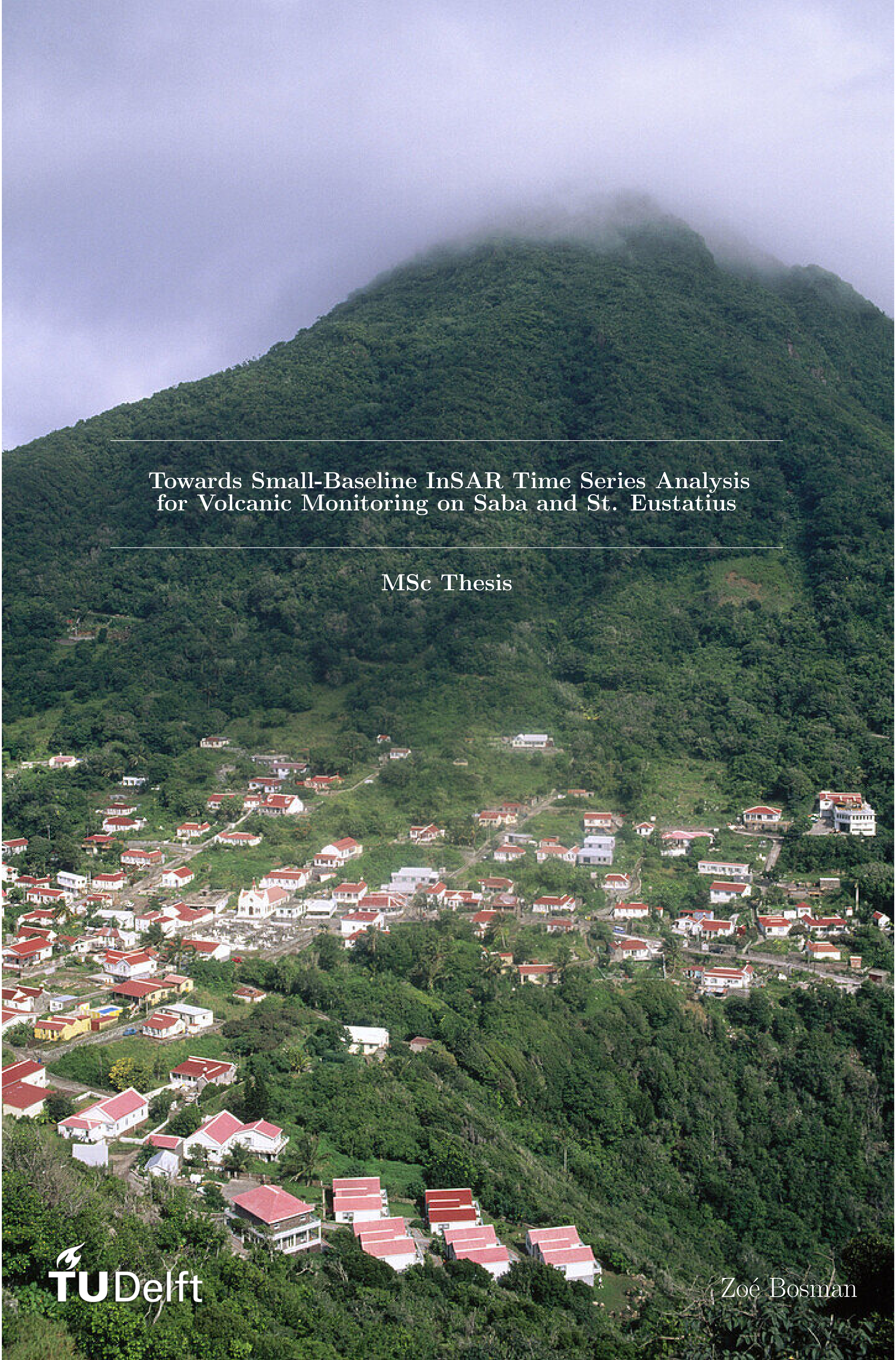

Towards Small-Baseline InSAR Time Series Analysis for Volcanic Monitoring on Saba and St. Eustatius

MSc Thesis

Zoé Bosman

Towards Small-Baseline InSAR Time Series Analysis for Volcanic Monitoring on Saba and St. Eustatius

MSc Thesis

by

Zoé Bosman

to obtain the degree of Master of Science
at the Delft University of Technology,
to be defended publicly on November 24, 2023 at 13:00.

Student number:	4693329	
Project duration:	Feb 13, 2023 – Nov 24, 2023	
Thesis committee:	Dr. E. de Zeeuw-van Dalfsen,	TU Delft/KNMI, daily supervisor
	Dr. ir. F. J. van Leijen,	TU Delft, daily supervisor
	Prof. dr. ir. R. F. Hanssen,	TU Delft
	Dr. J. E. A. Storms,	TU Delft

This thesis is confidential and cannot be made public until November 24, 2023.

Preface

This thesis is the product of roughly nine months of research in InSAR time series analysis for volcanic monitoring on Saba and St. Eustatius and marks the end of my master's studies in Applied Earth Sciences/Civil Engineering. Throughout my journey at the TU Delft I have had the chance to grow and, although at times challenging, make great memories. I am grateful for the countless experiences and the people I have met along the way.

First and foremost I would like to thank my main supervisors, Elske de Zeeuw-van Dalfsen and Freek van Leijen, who have guided me all the way through this project. Thank you for always being available, even outside of the weekly meetings, and for sharing your valuable knowledge, enthusiasm and ideas. I would also like to thank my other supervisors, Ramon Hanssen and Joep Storms, for their constructive and helpful feedback.

To my friends and family, thank you for your support and for the much-needed distractions. To my bachelor friends, thank you for making the countless late-night study sessions enjoyable, and my master friends, for inspiring me to start studying earlier and much more. To my 'thesis buddies', Sofia and Felix, thank you for making me look forward to working on the thesis and for the CC&C lunch dates. Last but not least, thank you to my parents, Wim and Nadine, my sister Kim, and Ismet for always being there.

Zoé Bosman
Delft, November 2023

Abstract

Over the years, InSAR has become an indispensable tool in the study of ground deformation, including volcanic deformation, and this continues to be the case in times of improved technology. Since the volcanoes on the Caribbean islands of Saba and St. Eustatius are active, the implementation of an InSAR-based monitoring system is crucial to enhance the spatial resolution of volcano monitoring beyond the capabilities of the ground-based monitoring network, for instance in the case of localized deformations such as dike intrusions. However, technical challenges arise in these tropical settings, caused by dense rainforest, atmospheric artifacts and terrain variability, posing serious challenges to the use of InSAR. Time series InSAR, including SBAS and PSI, can be used to overcome these limitations. A previous study has explored the use of PSI for monitoring, using the already available DePSI software. In this research, an SBAS approach within the Delft InSAR software framework is developed using state-of-the-art Python packages, including (SAR)XARRAY, DASK and ZARR, and is used to assess whether there is capability to develop SBAS into a volcanic monitoring tool for Saba and St. Eustatius. In addition, a preliminary comparison between the SBAS and PSI methodologies is performed based on a theoretical and (semi-)quantifiable approach. This study combines data from two satellites operating at different wavelengths: Sentinel-1 (C-band) and ALOS-2 (L-band).

Assuming no ongoing deformation, based on GNSS results, the variability of the results around zero can be used as an indicator of precision. The results obtained through SBAS are promising, in particular for L-band, on account of e.g., extensive spatial coverage, efficiency and relatively low variability even with the presence of atmospheric and DEM components. Overall, the results reveal mm order deviations. In the event of volcanic activity, the expected deformation signals are in the range of cm-dm's and can therefore be detected, i.e., with an estimated minimal detectable deformation of 1.5 cm/year in the worst-case scenario. The implementation of three different coherence-based masking approaches—water, single and individual—give an indication of the level of robustness and reliability of the results. Generally, a relatively high level of consistency can be observed among the different masking results of ALOS-2 for both islands, for St. Eustatius following the correction of the unwrapping errors using two testing approaches: an interferogram removal approach and an adaptive approach based on the DIA procedure. The latter procedure allows for retaining all observations and their residuals and is therefore preferred. In contrast, the Sentinel-1 results reveal a lower level of consistency. It is suspected that this inconsistency mainly arises on account of the numerous unwrapping errors within the single masking approach. The individual masking approach appears to be less susceptible to unwrapping errors, however is more prone to outliers than the single masking approach. Further research, following the correction of the atmospheric component and DEM errors, may offer insights into the preferred masking approach. Overall, the use of L-band imagery shows potential, offering spatial coverage where C-band does not, even with limited ALOS-2 data availability and large temporal baselines. The preliminary comparative analysis with the PSI approach, based on the respective strengths and limitations from literature, spatial coverage, processing steps, precision and computational requirements, suggests that a hybrid method could prove to be advantageous to minimize (potential) signal loss, e.g. either from limited spatial coverage or spatial resolution, and enhance volcanic risk assessment. SBAS excels in the extensive spatial coverage, especially using L-band, providing nearly homogeneous coverage of St. Eustatius, even on the flanks of the Quill, and on the outer flanks Mt. Scenery on Saba. However, regardless of the mask, wavelength or method, acquiring coverage around the summit of Mt. Scenery on Saba remains challenging.

The study contributes to advancing InSAR time series analysis for the volcanic monitoring on Saba and St. Eustatius through the successful implementation of an SBAS approach within the Delft InSAR software framework based on state-of-the-art packages, the implementation and evaluation of new approaches to enhance the method in terms of the efficiency and robustness and a comparison with existing software. In addition, the software can be applied in a generic sense for various applications and can be extended for further improvements.

Acronyms

ALOS Advanced Land Observing Satellite. iii, 4, 6, 25, 27, 29, 32–34, 37, 38, 49, 51, 55, 56, 58, 60, 62, 66–73, 75, 76, 82–90, 92, 96–107

B.P. Before Present; dating system relative to the origin of radiocarbon dating in $\sim$ 1950. 23, 96

CONAE Comisión Nacional de Actividades Espaciales. 29

DEM Digital Elevation Model. iii, 10, 13, 14, 18, 31, 37, 38, 48, 56, 61, 67, 75, 80, 81, 86, 100–104

DePSI Delft Persistent Scatterer Interferometry. iii, 2, 3, 16, 18, 31, 48, 86, 87, 92

DIA (Delft) Detection, Identification and Adaptation. iii, 44, 102, 103

DORIS Delft object-oriented radar interferometric software. 16, 31–33, 35, 39, 47, 61, 80, 81, 86, 101, 104

EC European Commission. 25

ESA European Space Agency. 25

GIS Geographic Information System. 32, 48

GNSS Global Navigation Satellite System. iii, 6, 25, 30, 41, 49, 50, 56, 90, 91, 101, 102, 104

HPC High performance computing. 32, 48, 52

InSAR Interferometric Synthetic Aperture Radar. i–iii, 1–6, 8, 10, 13, 14, 30, 31, 38, 41, 49, 55, 86, 90, 96, 104

ISRO Indian Space Research Organisation. 29

JAXA Japan Aerospace Exploration Agency. 27

LOS Line of Sight. 6, 10, 14–16, 38, 40, 56

MDD Minimal Detectable Deformation. 85, 101

NASA National Aeronautics and Space Administration. 29

NGL Nevada Geodetic Laboratory. 30, 49

NISAR NASA-ISRO SAR. 2, 3, 25, 29, 34, 85, 103, 104

OMT Overall Model Test. 18, 44, 45, 62, 64

PALSAR-2 Phased-Array type L-band Synthetic Aperture Radar-2. 27

PSI Persistent Scatterer Interferometry. iii, 1–5, 8, 13, 16–19, 31, 35, 36, 49, 86, 91, 92, 94–100, 102, 103

SAOCOM SAtélite Argentino de Observación COn Microondas. 2, 6, 29, 30, 34, 104

SAR Synthetic Aperture Radar. 1, 3, 5, 8, 11–14, 16, 21, 25, 28–30, 40, 42, 91, 101

SBAS Small BAseline Subset. iii, 1–6, 8, 13–16, 31–36, 42, 43, 49, 51, 54, 56, 58, 86, 87, 90–92, 94, 96–104

SLC Single-Look Complex. 9, 10, 18, 25, 31, 34–36, 42, 43, 51, 52, 71

SNAPHU Statistical-Cost, Network-Flow Algorithm for Phase Unwrapping. 39, 40

SNR Signal to noise ratio. 4, 13

SVD Singular Value Decomposition. 15, 34, 41, 56, 71, 91

Contents

1 Introduction

Volcanic eruptions are one of the most powerful agents of change, causing the destruction of life and civilization. During an eruption, a great deal of lava, pyroclastic material, ash and dangerous gases are released into the atmosphere with disastrous consequences that are not limited to the surrounding area. The local landscape is altered and lives and ecosystems are threatened. The volcanic gases pose a serious threat to the local communities and, in the long run, can even affect the climate on a global scale (Slawinska and Robock, 2018; Robock, 2000; USGS, 2023). With over 1500 potentially active volcanoes shaping the surface of the Earth (Bai et al., 2022), many of which are located in tropical regions (Ebmeier, Biggs, et al., 2013), the monitoring of this hazard is crucial for disaster risk reduction. However, merely 35 % of these volcanoes are monitored adequately (De Zeeuw - van Dalfsen and Sleeman, 2018).

In the last decade, satellite imagery has served as an indispensable tool in understanding volcanic eruptions and continues to be in times of improved technology (Pultarova, 2022). An interesting mapping and monitoring technique regarding volcanism, in part owing to its all-weather and all-time capabilities allowing for (semi-) continuous monitoring (Aswathi et al., 2022), is Interferometric Synthetic Aperture Radar (InSAR). Over the years, InSAR has become a key tool in the study of ground deformations, including volcanic deformations. The ever-increasing data availability and resolution has enabled the possibility of using InSAR as a volcanic monitoring tool. In contrast to other techniques, the unique combination of high spatial resolution, wide-scale coverage, and medium temporal sampling, allows for measuring volcanic phenomena without subjection to hazardous conditions (Van Leijen, 2014). However, the accuracy of InSAR measurements is highly dependent on the environmental conditions (Albino et al., 2020). In comparison to higher latitudes, studies involving InSAR as a tool for volcanic monitoring in tropical settings are limited (Ebmeier, Biggs, et al., 2013). Technical challenges arise in tropical settings, as a result of atmospheric artifacts as well as the dense tropical rainforest cover, resulting in the loss of radar coherence. Furthermore, when the terrain is particularly steep, the radar image may be distorted due to layover and shadowing effects. In addition, the resolution and sensitivity of InSAR may not be detailed enough to detect small, yet possibly important, deformation signals. In contrast, considering the fact that InSAR is a relative technique, if the spatial size of the deformation signal exceeds the size of the island, part of the signal is not captured. Given that a significant amount of the active volcanoes are located in tropical regions, it is of utmost importance to optimize the InSAR methodology for these challenging conditions.

Time series interferometry can be used to tackle the limitations of conventional InSAR: decorrelation phenomena and atmospheric signal delay (Van Leijen, 2014). Previous work has shown promise in time series InSAR, particularly for detection of slow and time-variable deformation in smaller areas (Morishita et al., 2020) as a result of high deformation measurement accuracy. Different time series methodologies exist, among these, one may be more suitable than others for tropical island volcanoes and would therefore be useful for monitoring purposes. The two main approaches, which can be combined to form a hybrid method, are Persistent Scatterer Interferometry (PSI) and Small BAseline Subset (SBAS). The primary distinction lies in their respective approach to processing InSAR data to obtain deformation estimates as well as the use of point or distributed scatterers (Fárová et al., 2019). PSI relies on a subset of points which show stable scattering behaviour in time, whereas SBAS relies on subsets of interferograms with small spatio-temporal baselines. Furthermore, the correct estimation of phase ambiguities (phase unwrapping) is related to the reliability of the time series and therefore an important step to consider. Considering PSI, individual pixels are first unwrapped in time, followed by a spatial unwrapping step. In contrast, for SBAS, the unwrapping procedure is done spatially, followed by an integration in time (Van Leijen, 2014). As both techniques have their respective strengths and limitations, it is difficult to state which technique will perform better for volcanic monitoring purposes in tropical settings. Also considering the increasing number of SAR satellite missions, with reducing revisit time and varying wavelength. SBAS allows for a relatively large spatial coverage compared to PSI, especially over non-urban areas (Guzzetti, 2021). PSI can be more effective in correcting for atmospheric and orbital errors (Li et al., 2022), but can have problems in non-urban areas because of the limited stable scattering behaviour in natural environments (Guzzetti, 2021). Therefore careful consideration of the specific limitations of each method is of great importance.

The tropical islands of Saba and St. Eustatius, which are part of the Lesser Antilles volcanic island arc, host the active stratovolcanoes of Mt. Scenery and The Quill, respectively (De Zeeuw - van Dalfsen and Sleeman, 2018). These volcanoes are considered to be active, but quiet, and pose a significant threat to the ∼ 5000 people living on the islands (De Zeeuw - van Dalfsen and Sleeman, 2018). Figure 1.1a and Figure 1.1b illustrate the general (physical) geography of the islands. In addition to sharing similar climates and wind and sea state regimes (Allen, 2017), both islands lack information regarding their eruption histories, which complicates hazard assessment (De Zeeuw - van Dalfsen and Sleeman, 2018). Therefore, InSAR measurements are crucial in the detection of signals over larger areas that may be overlooked by sparsely distributed ground monitoring systems. Furthermore, both offer interesting research opportunities, with regards to InSAR monitoring, considering the challenges posed by their landscape characterized by tropical rainforests and steep slopes. Previous research has considered the application of PSI to radar imagery of different frequency bands, using the Delft Persistent Scatterer Interferometry (DePSI) software, as an extension of the ground monitoring network of Saba and St. Eustatius as described by Korevaar (2020). However, the PSI time series were affected by decorrelation at the summit and the flanks of both Mt. Scenery and The Quill which is the area expected to show the strongest deformations in the case of volcanic unrest. Therefore, an SBAS approach is developed to investigate its potential for the volcanic monitoring of Saba and St. Eustatius. Moreover, a comparative analysis is conducted to assess the performance of the PSI and SBAS InSAR time-series techniques for monitoring volcanic activity in these tropical regions, such that an automated multi-technique InSAR-based volcanic monitoring system can be realized in the future.

In addition, L-band has shown potential as a volcanic monitoring tool in densely vegetated areas due to the longer wavelength able to penetrate the dense vegetation (Konings et al., 2017). Yet, most radar satellites currently in operation operate at C-band wavelengths, which are known to be have a limited penetration depth through vegetation cover compared to L-band (Ebmeier, Biggs, et al., 2013). The NISAR mission, planned to launch in 2024, could potentially overcome the limited availability of L-band wavelength data. By considering L-band data from current satellite missions, such as SAOCOM, the value of L-band in the monitoring of volcanic activity can be evaluated.

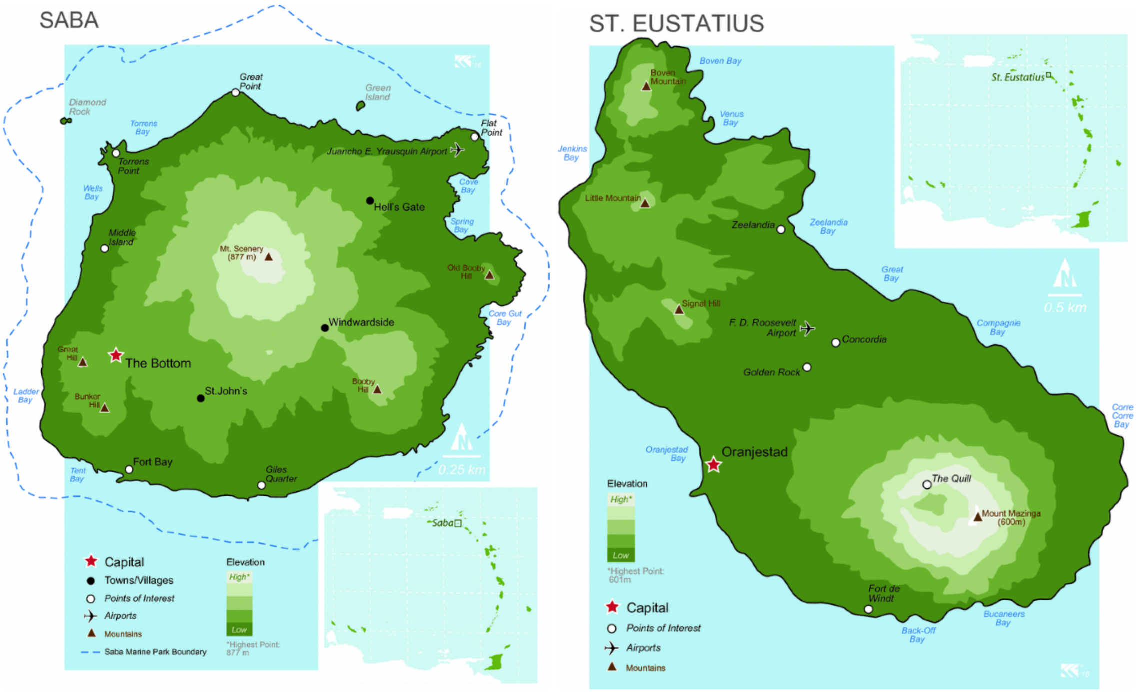

(a) Saba (b) St. Eustatius

Figure 1.1: Physiographic Maps of Saba and St. Eustatius. Source: (Allen, 2017).

1.1 Research Objectives

1.1.1 Problem Statement

Previous research concerning the use of InSAR as a tool for volcanic monitoring in tropical regions, in particular the Lesser Antilles, is limited (Garthwaite et al., 2019). Considering the tropical conditions on the Caribbean islands, technical challenges arise as a result of the loss of radar coherence. In addition, layover and shadowing effects result from the steep terrain causing distortion to the radar image. Given that the majority of volcanoes worldwide are located in tropical regions, it is crucial to investigate which InSAR methodology is best suited for an InSAR-based volcanic monitoring system in these regions. InSAR time-series analyses are considered to overcome the degrading factors of conventional InSAR i.e., atmospheric disturbances and the occurrence of decorrelation phenomena (Van Leijen, 2014). PSI and SBAS have shown promise in the monitoring of volcanic activity (Li et al., 2022; Hooper et al., 2004; Joseph et al., 2022), both having different strengths and limitations that need to be explored. In a previous study, the use of PSI for monitoring purposes on Saba and St. Eustatius was explored, using the available DePSI software. The PSI time-series revealed decorrelation at the summit and the flanks of volcanoes, as a result of the dense vegetation (Korevaar, 2020). In addition, the dependence on persistent scatterers constrains PSI in capturing abrupt changes. To address these challenges, it is crucial to exploit the spatial information inherent in the SBAS approach, particularly in light of the upcoming L-band missions providing higher spatial coherence.

1.1.2 Research Questions

In this project, a case study will be conducted at the small volcanic islands of Saba and St. Eustatius to determine if SBAS InSAR time series can be used to develop a multi-technique volcanic monitoring system for these and potentially other tropical islands. Moreover, a comparison of the PSI and SBAS methods could provide insights into how to improve the accuracy and efficiency of a volcanic monitoring system in tropical settings. In addition, a promising monitoring technique in the tropics, in part owing to its large penetration depth, involves L-band SAR imaging. In light of the NISAR satellite mission, planned to launch in 2024, the additional value of L-band imaging can be explored.

The research question is formulated accordingly:

**Is the SBAS approach a viable technique
for an InSAR-based volcanic monitoring system
on the tropical islands of Saba and St. Eustatius?**

Additional sub-questions related to the main research question are explored:

- **What is the procedure involved in the implementation of the SBAS time series software and which steps can be improved to enhance the efficiency and robustness of SBAS with respect to the standard approach?**

  To successfully implement and enhance the SBAS approach, a detailed understanding of the step-by-step procedure is crucial. As technology advances, it is essential to improve the standard method. Data processing can be time expensive. Efficient data processing, in particular in time-sensitive applications such as volcano monitoring, is crucial to provide data within a reasonable time frame. In addition, the robustness of the software, specifically its ability to handle varying parameters, is another important component. Hence, new approaches are explored to enhance the efficiency and the robustness of the SBAS approach.

  An extensive description of the (semi-) automatized processing flow of the SBAS method is provided, including the theoretical foundation as well as technical considerations such as the (pre-)processing steps and packages used. Additionally, the key technical challenges encountered in the implementation process are addressed, such as data management.

- **How can the obtained results from the SBAS and PSI method be compared?**

  The distinct processing approaches and the use of point (PSI) or distributed scatterers (SBAS) complicate the comparison. A combination of both a theoretical as well as a quantifiable approach is considered. Some general ideas are explored in the report.

- **What are the advantages, limitations and sources of error associated with the SBAS method in relation to the PSI approach in the area of interest?**

  Due to the limited comparative analyses between SBAS and PSI, a comprehensive overview of the advantages and limitations is lacking. Therefore, an assessment is made of the suitability of the respective methods, in terms of the specific requirements and limitations, based on theory.

- **How do PSI and SBAS compare in their ability to detect potential volcanic deformation signals on the islands of Saba and St. Eustatius?**

  One technique may be more suitable than the other for the volcanic monitoring of these specific islands. Therefore, the performance of both methods is assessed such that a volcanic monitoring system can be realized in the future. The assessment is based on both theoretical and quantifiable factors, such as spatial coverage and precision.

- **What is the added value of the SAR L-band imaging in the volcanic monitoring system?**

  L-band imagery has shown to provide higher coherence than C-band. To realize a volcanic monitoring system, the added value of using L-band data should also be considered. In reference to the launch of the NISAR mission, the quality of the L-band results is assessed using current satellite missions such as SAOCOM and ALOS-2 compared to Sentinel-1 (C-band).

1.2 Previous Research

Previous research regarding InSAR monitoring in tropical settings is limited. Multiple factors contribute to this, as described by Ebmeier, Biggs, et al. (2013) following a survey conducted in Central America. The project involves the use of ALOS L-band data to study the applicability of InSAR on the scale of a whole volcanic arc, the Central American Volcanic Arc. The application of InSAR in tropical settings is hindered by dense vegetation, water vapor variations and steep terrain. Features that are also all characteristic of the Lesser Antilles arc. Possible solutions have been explored for these limitations. First of all, integration of longer wavelengths (e.g. L-band) have shown to improve the coherence on account of the radar penetration, which has been the primary limiting factor of InSAR in tropical settings. ALOS data, following the launch in 2006, reflected this finding. However, an additional obstacle towards the application of L-band InSAR as a real-time monitoring technique is caused by the long satellite revisit times. The majority of radar satellites have operated at C-band, providing data since 1993. However, C-band wavelengths are known to be affected by vegetation cover. Due to the dynamic vegetation, the scattering properties change with time leading to temporal decorrelation. Furthermore, the extent to which the vegetation affects the measurements is not only dependent on the density of the vegetation, but also on the vegetation type. Secondly, it is crucial to correct for atmospheric artifacts caused by the great variability in water vapor concentrations in the tropics, as it can be difficult to distinguish the atmospheric signal from the true deformation signal. One of the methods proposed to reduce the atmospheric effects involves considering a stack of interferograms, such that the SNR increases. Another approach involves direct measurements of water vapor, e.g. using GPS, which require high spatial and temporal density. It has been shown, through the development of correction methods, that measurement thresholds have been lowered from cm's to mm's (Ebmeier, Andrews, et al., 2018). The third and final factor involve layover and shadowing effects which arise in high relief terrain, resulting in radar image distortion or even no data at all. The extent of the geometric distortions is dependent on the radar look angle as well as the terrain slope angle. By considering both ascending and descending paths, data from both sides of the volcano can be acquired. In spite of these difficulties, the findings of the study by Ebmeier, Biggs, et al. (2013) hold promise. i.e., based on a coherence threshold equal to 0.15, from the 26 considered volcanoes in the arc merely three could not be used to produce deformation maps. In another study, Wadge et al. (2000), following the 1995-1999 eruption of the Soufrière Hills volcano in Montserrat, it is shown that the quality of InSAR measurements and hence the monitoring ability is highly dependent on the type of volcano. Specifically, broadly two types of volcanoes are distinguished. First the basaltic shield volcano, characterized by low relief and known for their frequent effusive eruptions, resulting in limited vegetation cover, and relatively shallow magma reservoirs. This combination allows for high coherence. These volcanoes often accommodate large magnitude ground deformations, which enhances the ability to measure the surface deformation. Second the more silicic volcanoes, characterized by high relief, and thus susceptible to layover and shadowing effects, with great vegetation cover. Generally, the eruptions are infrequent yet explosive and the magma reservoirs are deeper. The monitoring ability is challenged by the generally low coherence and the small magnitude deformation signals. The volcanoes in the study area are typical of the more silicic type of volcano.

Although the use of conventional InSAR has proven its effectiveness in measuring deformation in areas characterized by good coherence, decorrelation phenomena are observable across significant portions of nearly all volcano interferograms (Hooper et al., 2004). As described by Hooper et al. (2004), aside from the temporal decorrelation and atmospheric disturbances, another main degrading factor includes spatial decorrelation. This refers to the perpendicular baseline, which is the distance between satellite tracks at two acquisition times, leading to a difference in incidence angle which in turn affects the scattering phases. These limitations can be avoided by analyzing time-series InSAR, i.e., PSI and SBAS methods. Both PSI and SBAS have shown promise in volcanic monitoring (Li et al., 2022; Hooper et al., 2004).

However, as highlighted by Shanker et al. (2011), comparative analyses between the methods applied to the same region is limited. Particularly in the context of volcanic regions, little research has been conducted in this regard. Related research conducted in different fields and study areas can offer insights into the primary differences observed between the methods. In the study by Xue Chen et al. (2020), a comparative analysis of landslides is conducted in the mountainous Rovegliana region in northeast Italy. Ascending and descending Sentinel-1 data has been processed according to the PSI and SBAS techniques. A coherence threshold of 0.3 is considered, however the analysis is extended to resolution cells with some coherence values below 0.3. Overall, both techniques yield useful and consistent results. However, differences arise as a result of the different strengths and limitations of both techniques. In the case of linear deformation trends, similar results are obtained. Conversely, the short stack of SAR images limits the capability of PSI to detect a non-linear trend. Secondly, PSI identifies stable scatterers typically found in urban areas. SBAS also provides deformation rates of non-urban regions, where deformation rates could vary. However, PSI focuses on individual pixels rather than spatially correlated pixels like SBAS. This allows for preserving the maximum spatial resolution and avoids signal loss. Yao et al. (2022) performed a landslide study in Tibet in China, highlighting the strength of SBAS in terms of the density and spatial coverage of the pixels. However, due to the multilooking step in the SBAS, pixel resolution is sacrificed and high-quality scatterer signals may be lost. In contrast, PSI enables the identification of relatively stable scattering points without the use of multilook processing. Hence, the success of the techniques is dependent on the specific characteristics of the study area and the application.

The 2020-2021 eruption of the neighboring island of St.Vincent offers insights into the expected deformation in times of volcanic unrest as well as the usage of InSAR as a complementary monitoring tool. On 27 December 2020, La Soufrière volcano erupted after approximately 41 years of quiescence. An initial state of minimal detected volcanic unrest, characterized by seismic activity which was not uncommon for the region, paved the way for three months of effusive (dome-forming) activity, followed by a series of explosions (Joseph et al., 2022). In the midst of the challenges posed by the COVID-19 pandemic and limited resources, the monitoring capacity was reduced when the unrest began in November. i.e., as described by Joseph et al. (2022), the monitoring network included merely one operating seismic station located 9 km from the volcano and a single continuous

GPS station. In response to the activity of the volcano the monitoring network was upgraded, including the installation of eight broadband seismic stations and four additional continuous GPS stations. In addition, InSAR was introduced as a complementary monitoring technique to augment ground deformation monitoring using ALOS-2 and Sentinel-1 images. The ALOS-2 and Sentinel-1 radar detected a LOS deformation signal of a magnitude of less than 10 cm around the crater, between 19 and 31 December 2020, associated with a dike intrusion at less than 500 m of depth. A signal that went unnoticed by the ground-based monitoring network in place (Joseph et al., 2022). In Camejo-Harry et al. (2023), a detailed description of the expansion of the monitoring network of St.Vincent is provided and the available GNSS and InSAR time-series data, which includes data from ALOS-2, Sentinel-1 and SAOCOM-1 are analysed. This paper gives insights into the expected deformation in times of volcanic unrest. Different processing techniques have been applied for the different InSAR data-sets, but all have undergone processing using a SBAS technique. For SAOCOM-1 dedicated software is used and for ALOS-2 a PS-SBAS interferogram is formed using StaMPS on account of the large baselines. Sentinel-1 provided useful results within the crater region but not outside, due to poor coherence as a result of dense vegetation. ALOS-2 and SAOCOM-1 provided valuable results regarding deformation processes taking place at greater depth, beyond the crater region. The resulting time-series for GPS and the unwrapped interferograms for ALOS-2 as well as SAOCOM-1 are visualized in Figure 1.3 and Figure 1.2, respectively. Continuous GPS (cGPS) shows the expected values for the pre-eruptive (effusive), syn-eruptive (explosive) and post-eruptive states. Similarly, for ALOS-2 and SAOCOM-1 the pre-eruptive state is visualized, showing mm up to cm order LOS displacement. From the cGPS results it can be observed that in the event of an eruption, cm-order displacement and eventually even displacement up to the order of dm's occurs. Nonetheless, as described by Roobol and Smith (2004), on account of the last deposits of the Quill on St. Eustatius and the open crater, the eruptive style is expected to be similar to that of the Soufrière volcano, known as a "St.Vincent-style" eruption. Regarding Saba, Pelean-style activity is expected, named after the 1902-05 eruption of Mt. Pelée on Martinique. This eruption style is characterized by dense andesite deposits and a series of phreatic explosions, followed by intermittent dome growth (Roobol and Smith, 2004).

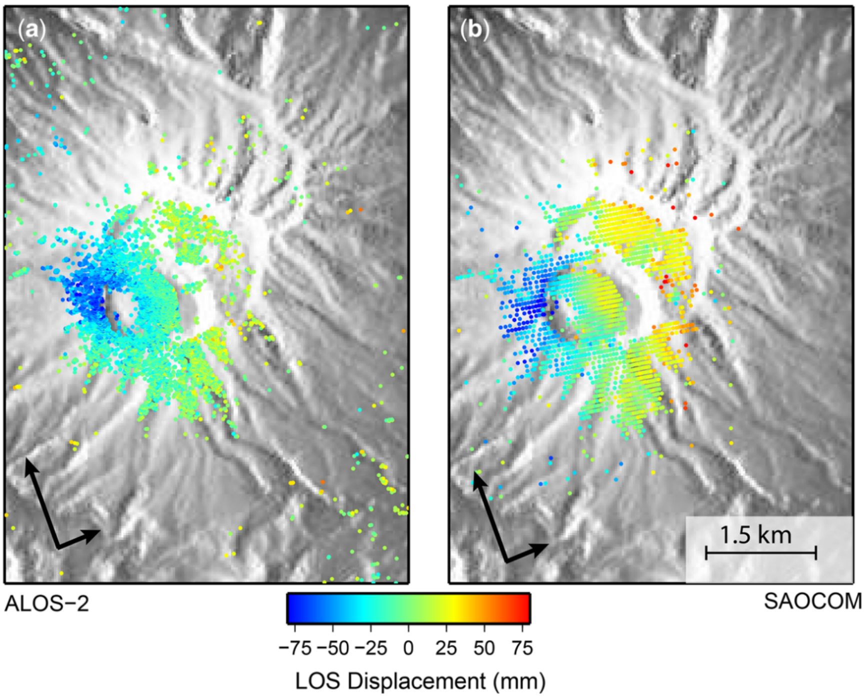

Figure 1.2: Unwrapped interferograms over St. Vincent in pre-eruptive state of ascending tracks from a) ALOS-2 path 36 (Jan 2020–Jan 2021) and b) SAOCOM-1 path 29 (Oct 2020–Feb 2021). Negative LOS represents motion towards the satellite. It is apparent that the spatial coverage is limited for both satellites and that differences in magnitude occur. These differences can possibly be attributed to the distinct time frames or incidence angles. Source: Camejo-Harry et al. (2023).

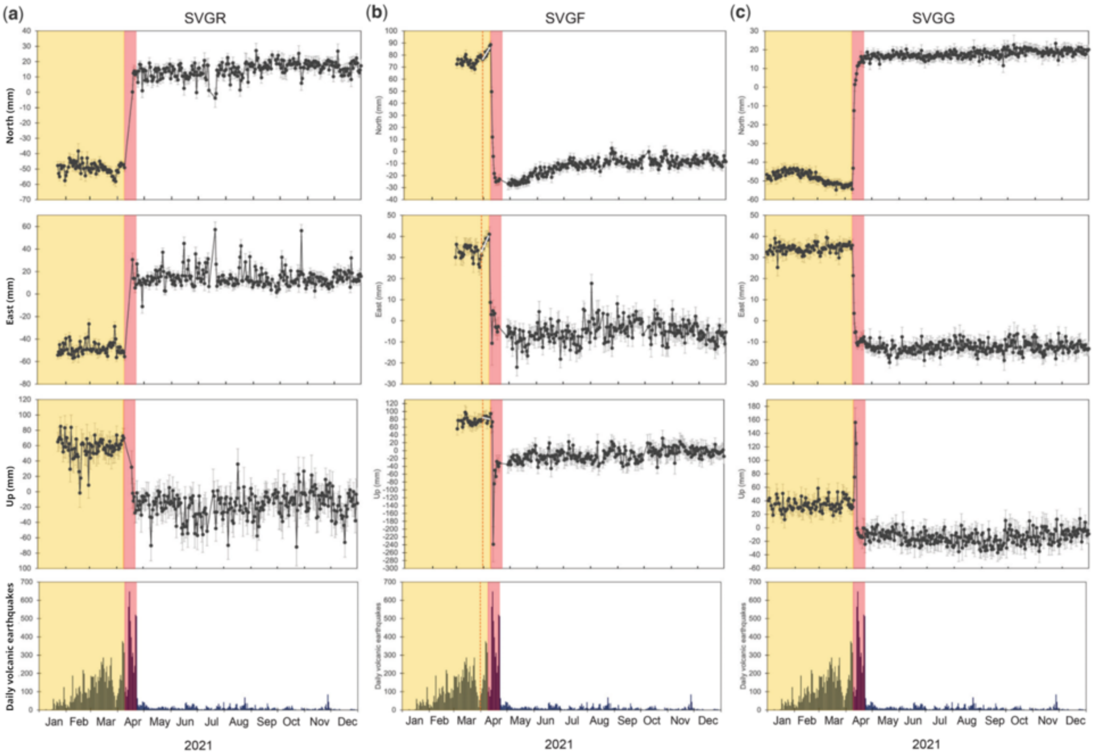

Figure 1.3: Raw cGPS time-series of three different stations located in St. Vincent for the year 2021, showing the different components as well as the daily volcanic earthquake counts. Yellow bars = effusive phase; red bars = explosive eruptive phase. Source: Camejo-Harry et al. (2023).

1.3 Terminology

Throughout the report numerous terms are used to describe the produced results. These terms are defined as:

- **Capability**: the ability to detect deformation signals. In other words, the question is whether the expected deformation signals surpass the detection limit. This can essentially be split up into three key components. First of all, a specific spatial sampling is required, which is dependent on the type of deformation. Extensive coverage is required for local deformations, whereas less coverage may be necessary for large-scale deformations. Secondly, a high temporal sampling is essential for timely detection of a deformation signal. Finally, a certain precision is needed, i.e., the precision determines the value of the minimal detectable deformation.
- **Consistency**: the agreement between the produced results following from different data sets as well as the masking approaches, in terms of trends, patterns, sign and magnitudes.
- **Robustness**: the resilience to varying parameters. To what extent do different settings/parameters produce similar results, e.g., in terms of the level of consistency.

The reliability in this context is then formulated accordingly:

- **Reliability**: the ability of the method to produce consistent results between data sets of different tracks, that are overall resilient to varying parameters. In other words, the robustness and the consistency can be indicative of the overall reliability of the produced results.

  In addition, to complement the assessment of the reliability, an understanding of the limitations and potential sources of error of the method and data sets is crucial.

2 Background

In this chapter, an overview of relevant theory, important to gain understanding on the main principles of both conventional (Section 2.1) and time series InSAR (Section 2.2), is provided. In terms of time series InSAR, the two main approaches are considered, i.e., SBAS in Section 2.2.1 and PSI in Section 2.2.2. The key features and limitations of conventional InSAR as well as both time series approaches are explored.

2.1 InSAR

Interferometric Synthetic Aperture Radar (InSAR), as the name suggests, is a (ground deformation) mapping technique based on Synthetic Aperture Radar (SAR) imagery. InSAR is a Lagrangian method, meaning that it tracks particles on the Earth's surface over time. This sets it apart from the Eulerian technique, which evaluates elevation changes over time at fixed horizontal coordinates, rather than considering the actual path taken by particles. In the InSAR technique, two radar images are interfered to extract information, by means of exploiting phase differences, about the Earth's surface and atmosphere (Van Leijen, 2014). SAR is a notable observation technique, partially owing to its all-weather and all-time capabilities (Shinozuka and Mansouri, 2009). In other words, the fact that SAR produces quality data under most weather conditions, including rain and clouds, as well as the ability to operate at night, allows for (semi-)continuous monitoring. SAR can be defined as an active microwave remote sensing instrument, either terrestrial, airborne or space-borne, comprising of a sensor which serves both as an energy source and a receiver for the reflected radar signal (Pepe and Calò, 2017). As the sensor moves along the flight path, the azimuth direction, the transmitter releases successive pulses focused into a narrow beam by the aligned antenna, directed downwards, under a certain angle to the side, onto the Earth's surface. The specific geometry of SAR is visualized in Figure 2.1a. The principles of SAR rely on the simulation of a long antenna, called the aperture, synthesised using the movement of the radar antenna. The azimuth resolution is closely related to the dimensions of the radar antenna. That is, the azimuth resolution is determined by the beam width, which is inversely proportional to the length of the antenna. A smaller antenna, and thus a broad beam width, will result in a wider bandwidth and, accordingly, a finer resolution (Hanssen, 2001).

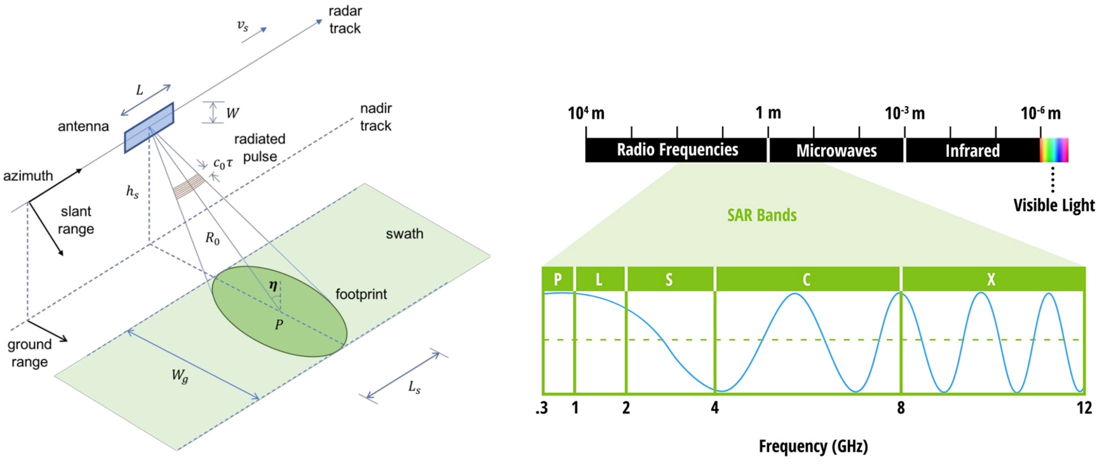

(a) Configuration of a radar in motion. Source: Dell'Amore et al. (2019).

(b) SAR frequency bands. Source: NASA (2020).

Figure 2.1: SAR principles.

The radar measures radar reflectivity of features as a function of distance. More specifically, the SAR signal, also called radar backscatter, contains intensity and phase information (Van Leijen, 2014). The phase (ψ) of the SAR image is determined by the distance between the satellite antenna and the reflecting surface based on the two-way travel time, and represents the fraction of one complete sine wave cycle. The intensity (I) is often represented by the amplitude (A), which is defined as the strength of the radar response (Online, 2023) and related to I as $A = \sqrt{I}$. Both the time delay and the strength of the return signal depend on the physical and electrical surface properties, primarily on the surface cover and roughness as well as the dielectric properties (Van Leijen, 2014; Hanssen, 2001). The total radar measurement per pixel is the summation of all reflections. The phase and amplitude can collectively be represented using a complex phasor (P), defined as

$$P = Ae^{i\psi}. \tag{2.1.1}$$

The phasor corresponds to a complex value of a resolution cell within a radar image. Specifically, the real ($\mathrm{Re}(P) = A\cos(\psi)$) and imaginary ($\mathrm{Im}(P) = A\sin(\psi)$) part of P are saved using a regular grid to produce a two-dimensional radar image (Van Leijen, 2014). A and ψ can accordingly be derived as

$$\begin{aligned} A &= \sqrt{(\mathrm{Re}(P))^2 + (\mathrm{Im}(P))^2}, \\ \psi &= \mathrm{arctan2}\left(\frac{\mathrm{Im}(P)}{\mathrm{Re}(P)}\right). \end{aligned} \tag{2.1.2}$$

The reflections result from interactions between the radar waves and the target surface or object. The reflection mechanisms can be broadly divided into two extreme scattering types, respectively: point scattering and distributed scattering. Point scattering occurs when the radar measurement is predominantly from a single strong reflecting object, referred to as a point scatterer. In the case of distributed scattering, in contrast, the total radar measurement is formed by various scattering objects. These scattering mechanisms can either be coherent or incoherent over time (Van Leijen, 2014).

Considering data in SLC format, as done in this research, the SLC phase for a pixel can be defined as the sum of a variety of phase components:

$$\psi = -2\pi a + \psi_{\mathrm{range}} + \psi_{\mathrm{atmo}} + \psi_{\mathrm{scat}} + \psi_{\mathrm{noise}}, \tag{2.1.3}$$

in which the components include the range dependent phase ψ_{range}, the atmospheric signal delay ψ_{atmo}, the scattering phase ψ_{scat} and the noise ψ_{noise}. In addition the (wrapped) phase is ambiguous and thus the phase ambiguity is included, as represented by a. Specifically, the ambiguity is the number of full (2π) phase cycles.

2.1.1 Interferometric Phase

A complex interferogram can be obtained by performing multiplication of one SLC image by the complex conjugate of the other image

$$P^{md} = P^m P^{d*} = A^m A^d \exp\left(i\left(\psi^m - \psi^d\right)\right), \tag{2.1.4}$$

where the * represents the complex conjugate, m is the mother and d is the daughter (Van Leijen, 2014; Hanssen, 2001).

The interferometric phase, also denoted φ^{md}, for a single pixel is composed of various phase contributions as expressed here

$$\varphi^{md} = \psi^m - \psi^d = -2\pi a + \varphi_{\mathrm{range}} + \varphi_{\mathrm{atmo}} + \varphi_{\mathrm{orb}} + \varphi_{\mathrm{scat}} + \varphi_{\mathrm{noise}}. \tag{2.1.5}$$

Aside from the noise terms (φ_{noise}, φ_{scat}, φ_{orb}), the phase contributions include an atmospheric (φ_{atmo}) and a range part (φ_{range}). The range contribution can be expressed in terms of a flat Earth (φ_{flat}), topographic (φ_{topo}) and deformation component (φ_{defo}), respectively.

More specifically, the different positions of the antennas from the mother and daughter are the source for two phase contributions. First of all, the flat Earth phase denotes a reference surface, such as an ellipsoid in the case of the Earth. Secondly, the topographic phase results from the topography above this reference surface. Assuming that the travel paths to the mother and daughter antenna's are parallel, it can be shown that as the perpendicular baseline increases, so does the sensitivity for height (Hanssen, 2001). Both the flat Earth phase and the topographic phase can, to a large extent, be modeled by a DEM. The deformation phase holds information regarding the displacement of the surface and needs to be estimated to obtain deformation estimates (Van Leijen, 2014). The differential phase term resulting from the change in the signal travel path is defined as

$$\varphi_{\text{defo}} = \frac{-4\pi}{\lambda} D_{\text{LOS}}, \tag{2.1.6}$$

in which D_{LOS} is the deformation in the radar LOS direction, which is in the direction of the incidence angle. Therefore, both horizontal as well as vertical displacement are contained within the measurement. Furthermore, the atmospheric phase results from the different atmospheric states between two acquisitions. An ionospheric and tropospheric term can be distinguished. The dispersive nature of the ionosphere introduces a wavelength dependent delay, that is, longer wavelengths have larger delays. Overall the tropospheric delay is largely constant, however the differential delay is strongly variable. This delay stems from the so-called wet delay, due to the water vapor distribution, and from vertical stratification, introduced in mountainous areas, affecting the radar path length (Van Leijen, 2014; Hanssen, 2001). Finally, the noise terms include the errors in the orbit parameters of the acquisitions (φ_{orb}), the scattering phase, due to changing scatter characteristics and, lastly, the remaining noise term containing e.g. thermal and processing noise (Van Leijen, 2014). The noise and change in scatter characteristics leads to decorrelation. Different sources of decorrelation exist.

In the context of InSAR application, the coherence serves as a measure of the quality of the interferometric phase (Hanssen, 2001). A high coherence suggest minimal contribution from the scattering phase and thus limited decorrelation, thereby increasing the potential for accurately estimating the remaining phase contributions (Van Leijen, 2014). The coherence is a measure of similarity between two radar images (Hanssen, 2001), mathematically defined as

$$\gamma = \frac{E[y_1 \cdot y_2^*]}{\sqrt{E[|y_1|^2] \cdot E[|y_2|^2]}}. \tag{2.1.7}$$

In practice, the expectation is unknown considering that only a single realization per pixel is available (Hanssen, 2001). Therefore, some kind of averaging of pixels is required to be able to obtain an estimation

$$|\hat{\gamma}| = \frac{\left|\sum_{n=1}^{N} y_1^{(n)} y_2^{*(n)}\right|}{\sqrt{\sum_{n=1}^{N} \left|y_1^{(n)}\right|^2 \sum_{n=1}^{N} \left|y_2^{(n)}\right|^2}}, \tag{2.1.8}$$

where $|\hat{\gamma}|$ is the coherence magnitude over a window of N pixels and $y_1^{(n)}$ and $y_2^{(n)}$ are the complex-valued signals at time n, which in this specific context represent the SLC phasors.

2.1.2 Limitations

As any technique, InSAR has its limitations. These limitations stem from the underlying principle of repeat-pass measurement as well as the side-looking configuration (Figure 2.1a) and, in the context of tropical island settings, include decorrelation phenomena, geometric distortion effects and atmospheric signal delay. Each of these will be discussed more thoroughly here.

In addition to system (thermal) and processing noise, a change in the scatter characteristics as described by the interferometric scattering phase φ_{scat}, results in signal decorrelation. There are various sources of decorrelation, the main sources relating to the research are described here. i.e., temporal decorrelation, due to changes in surface scattering over time, volume decorrelation, arises from a radar signal penetrating a scattering medium, and geometric decorrelation, as a result of different imaging geometries during the two acquisitions. The total coherence can be defined as the multiplication of the correlation terms (Hanssen, 2001)

$$\gamma_{\text{tot}} = \gamma_{\text{temporal}} \times \gamma_{\text{geom}} \times \gamma_{\text{vol}} \times \gamma_{\text{thermal}} \times \gamma_{\text{processing}}. \tag{2.1.9}$$

More specifically, geometric decorrelation (γ_{geom}) is the result of different incidence angles during the two acquisitions, which causes a spectral shift between the data frequency spectra. The geometric decorrelation can be defined as a function of the critical baseline $B_{\perp,\text{crit}}$, representing the baseline causing a spectral shift equal to the (range) bandwidth B_r. As a consequence, the range spectrum consists of non-overlapping parts which, in turn, results in noise. The value of $B_{\perp,\text{crit}}$ is a function of the wavelength, incidence angle, (range) bandwidth and topographic slope. Assuming a rectangular spectrum (Van Leijen, 2014; Hanssen, 2001), the following expression can be derived for the geometric decorrelation

$$\gamma_{\text{geom}} = \max\left(\frac{B_{\perp,\text{crit}} - |B_{\perp}|}{B_{\perp,\text{crit}}}, 0\right). \tag{2.1.10}$$

Temporal decorrelation (γ_{temp}) is commonly caused by vegetation, hence arid and polar areas are usually characterized by high (temporal) coherence. In this case, the effect of temporal decorrelation can be reduced by employing longer radar wavelengths. Another common source of temporal decorrelation includes the presence of water bodies, causing complete decorrelation regardless of the wavelength. The volume scattering is highly dependent on the scattering medium in question and the radar wavelength. In addition, thermal decorrelation is dependent on the system characteristics and arises from thermal noise in the instrument and processing decorrelation results from errors in the processing steps, such as the generation of interferograms or the coregistration process (Van Leijen, 2014; Hanssen, 2001).

Considering the atmospheric delay, its spatial correlation makes it challenging to distinguish the atmospheric signal from the deformation signal as well as from topography and orbital errors. The impact can span a range from mm up to cm's in magnitude (Van Leijen, 2014). Especially in mountainous areas, both the amount and spatial distribution of water vapor is highly variable. Nonetheless, apart from turbulent mixing, the vertical stratification effect occurs when dealing with elevated terrain. Specifically, vertical stratification arises due to different vertical refraction profiles of the troposphere between two SAR image acquisitions (Webley et al., 2002). Therefore, the correction of atmospheric phase contributions would be desirable.

Geometric distortion effects, comprising of foreshortening, layover and shadowing effects, are introduced in high relief areas. The viewing geometry of SAR is in the slant range, as depicted in Figure 2.1a. Consequently, depending on the satellite incidence angle and the slope angle, these distortions occur. Given a slope facing the SAR sensor, with a slope angle which is smaller than the satellite incidence angle (θ), the slope will appear smaller in the radar image, as visualized in scenario (b) in Figure 2.2. This effect is referred to as foreshortening and is maximized when the slope angle equals the incidence angle, i.e. the radar beam is perpendicular to the slope. Given scenario (b) in Figure 2.2, the effective length indicated by A'B' would be reduced to zero, resulting in an undetectable slope. Layover is an extreme case of foreshortening and occurs when the slope angle exceeds the incidence angle. As visualized in Figure 2.3 on the left, the top of the mountain (B) reaches the satellite before the backscatter of the foot of the mountain (A). That is, the expected order of backscatter arrival is reversed, which leads to geometrical inversion in the slant range causing the lower part of the slope to be masked by the top. In other words, the slope will appear as though inverted in the radar image. Given a slope facing away from the sensor with a slope angle exceeding $90 - \theta$, the SAR pulses are blocked by the mountain and no measurement can be acquired. This phenomenon is referred to as radar shadow and is illustrated in the right image of Figure 2.3. In contrast, when the opposite occurs, the range resolution of the slope is enhanced (Xiaohong Chen et al., 2018). Hence, using data from both the ascending and descending track is useful such that both sides of the slopes, for instance of a volcano, can be measured.

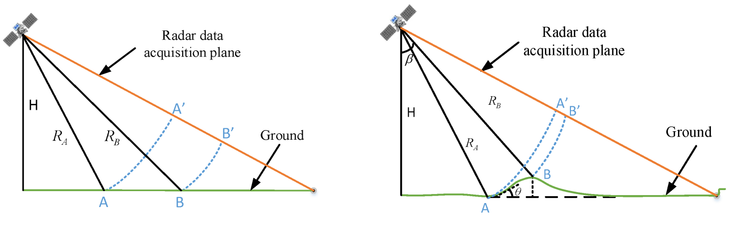

(a) **(b)** **(c)**

Figure 2.2: SAR imaging example for three scenarios, in which R_A/R_B are the slant range distances of targets A/B and A'/B' represent their projections on the acquisition plane. In a) a flat area is visible in which $R_B > R_A$ and no distortion occurs. In b) foreshortening occurs because $R_B < R_A$ due to the elevation, causing the slope (AB) to appear compressed (A'B'). In c) layover occurs as the slope angle increased $R_B >> R_A$, causing geometric inversion in the slant range (B' reaches acquisition plane before A'). Source: Wu et al. (2021).

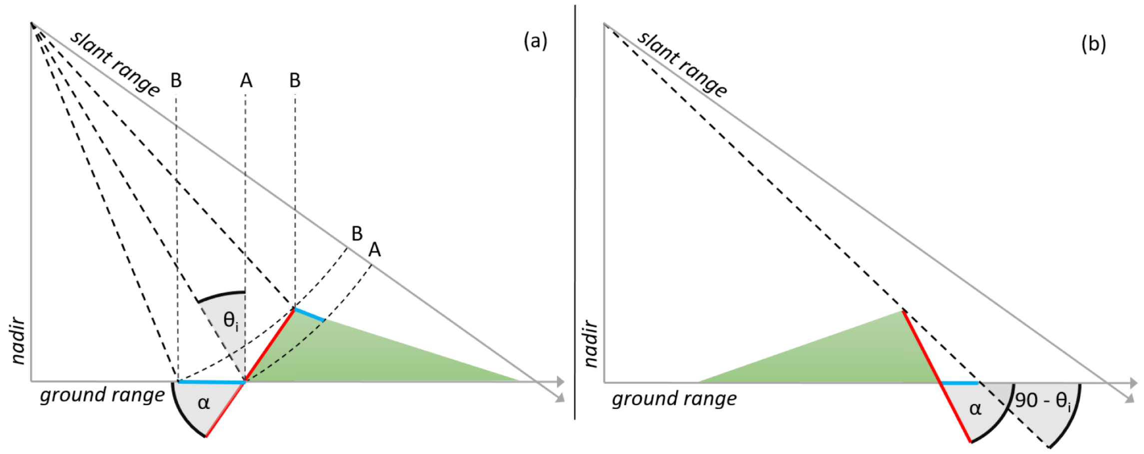

Figure 2.3: This SAR geometry example demonstrates two scenarios. In case a) layover occurs as the slope angle (slope facing the sensor) exceeds the incidence angle (θ), causing geometrical inversion in the slant range. Case b) illustrates radar shadow, in which the slope angle exceeds $90 - \theta$, resulting in no data regions. Source: Vollrath et al. (2020).

2.2 Time Series InSAR

Time series interferometry can be used to tackle the limitations of conventional InSAR, that is atmospheric signal delay, temporal and geometric decorrelation. Time series InSAR is an extension of conventional InSAR. A stack of multiple interferograms is analyzed in a single framework, which overcomes the lack of redundancy as is the case in a single interferogram. i.e., the SNR increases and a deformation time-series can be estimated. The ultimate goal is the detection of pixels for which the deformation time series can be estimated with sufficient reliability (Van Leijen, 2014). There are two main approaches, differing in the way the interferograms are selected and processed to obtain deformation estimates as well as the usage of point scatterers or distributed scatterers: Persistent Scatterer Interferometry (PSI) and Small Baseline Subset Algorithm (SBAS). The main principles and limitations of both techniques are described in this section.

2.2.1 SBAS

The Small Baseline Subset Algorithm (SBAS) procedure was proposed in 2002 by Berardino et al. (2002). Different extensions and variations of the basic principle of the technique have been developed since. In this section a description of the basic processing steps is provided. A detailed outline of the SBAS approach can be found in Berardino et al. (2002).

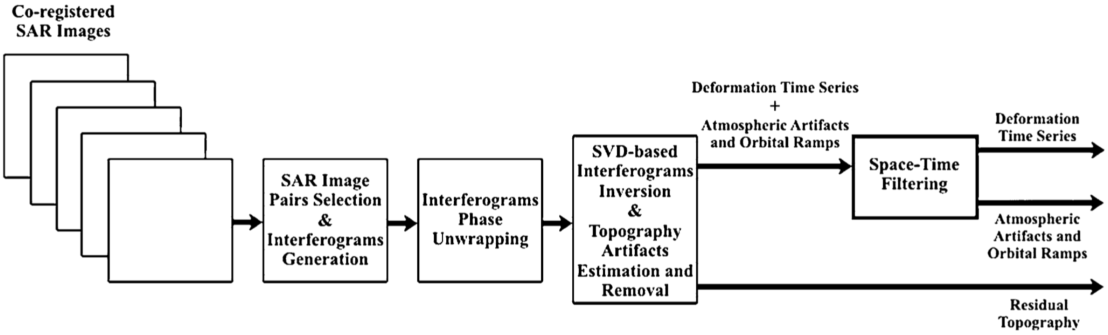

Figure 2.4: Block diagram of the SBAS algorithm. Source: Lanari et al. (2007).

The main principle relies on the selection of combinations of data pairs characterized by small temporal and spatial baselines. The former refers to difference in acquisition time, while the latter refers to the orbital separation. By doing this the decorrelation phenomena are minimized (Yao et al., 2022). In addition, conversely to PSI, distributed scatterers are used (Fárová et al., 2019). Key features of the algorithm include the significant number of SAR images, enabling to maximize the temporal sampling rate of the retrieved signals, and the high spatial coverage provided over the area of investigation, as is characteristic for conventional InSAR, on account of the distribution of the images in small baseline subsets (Berardino et al., 2002).

The approach consists of a number of basic processing steps, a schematic of the general workflow of the SBAS algorithm is visualized in Figure 2.4. Some analytical details of the main basic processing steps are described. It is assumed that the SAR images are coregistered in a common reference grid with respect to one mother image.

SAR Image Pairs Selection & Interferograms Generation

A set of $N + 1$ SAR images, acquired at different times $(t_0, ..., t_N)$ and covering the same area of interest, are considered. From this set of images M differential interferograms are generated, following a short-baseline configuration and based on a selection process, where only image pairs characterized by small spatial and temporal baselines are selected, as well as a small frequency shift between the Doppler centroids. This could yield several independent small baseline subsets. Following the topographic phase removal, using an external DEM, the j^{th} generic interferogram for one pixel (x, r), in range and azimuth coordinates, at times t_A and t_B can be defined as (Berardino et al., 2002; Lanari et al., 2007):

$$\begin{aligned}\delta\phi_j(x,r) =& \phi\left(t_B,x,r\right) - \phi\left(t_A,x,r\right) \\ \approx& \frac{4\pi}{\lambda}\left[d\left(t_B,x,r\right) - d\left(t_A,x,r\right)\right] + \frac{4\pi}{\lambda}\frac{B_{\perp j}\Delta z}{r\sin\vartheta} + \frac{4\pi}{\lambda}\left[d_{atmo}\left(t_B,x,r\right) - d_{atmo}\left(t_A,x,r\right)\right] \\ &+ \Delta n_j, \forall j = 1,\ldots,M.\end{aligned} \tag{2.2.1}$$

In this equation $\phi(t_B, x, r)$ and $\phi(t_B, x, r)$ are the phases of the image pair acquired at times t_A and t_B, $d(t_A, x, r)$ and $d(t_B, x, r)$ represent the radar LOS projections of the cumulative deformation at the respective times with respect to the time reference t_0: $\phi(t_0, x, r) = 0, \forall(x, r)$. λ represents the central wavelength of the transmitted signal. Furthermore, the terms $\frac{4\pi}{\lambda}\frac{B_{\perp j}\Delta z}{r\sin\vartheta}$ and $d_{\text{atm}}(t_A, x, r)$ and $d_{\text{atm}}(t_B, x, r)$ account for the DEM error (Δz) and the atmospheric signal delay. The r, ϑ and $B_{\perp j}$ represent the sensor-target distance, the look angle and the spatial baseline respectively. In addition, the term Δn_j accounts for decorrelation effects (Lanari et al., 2007).

Multilooking

A potential drawback of distributed scatterers, depending on the conditions of the study area, is on account of their inherent phase noise, which results from signal decorrelation (Ansari et al., 2021). Multilooking is commonly used in distributed scatterers inteferometry, including the SBAS technique, to reduce stochastic noise and improve phase estimation in InSAR observations. The multilook operation, also referred to as spatial averaging, involves averaging the complex returns of adjacent pixels (Zheng et al., 2022), see Equation 2.1.8.

However, it was found by Ansari et al. (2021) that multilooking may introduce a noise term correlated with the temporal baseline. Specifically, the discrepancy increases with a decreasing imposed temporal baseline in the image pair selection process. Therefore, considering the key principles of the SBAS method, it is crucial to assess the origin and impact of the noise term. The residual phase signal, resulting from the multilooking-induced inconsistency among a network of three interferometric phases, is referred to as the closure phase. The closure phase is defined as the angle of the triple product of the network of three interferograms: P^{ij}, P^{jk}, P^{ki}, which can also be written as the sum of the interferometric phases $\varphi^{ij}, \varphi^{jk}, \varphi^{ki}$:

$$\Delta\varphi^{ijk} = \angle P^{ij}P^{jk}P^{ki} = \Delta\varphi^{ij} + \Delta\varphi^{jk} + \Delta\varphi^{ki}. \tag{2.2.2}$$

For single-look interferograms, related according to $\Delta\varphi^{\mathrm{ij}} = \varphi^{\mathrm{i}} - \varphi^{\mathrm{j}}$, the closure phase yields $\Delta\varphi^{\mathrm{ijk}} = 0$. On the contrary, for multilooked observations these closure phases are typically nonzero, leading to 'inconsistent phase measurements'. The sign, magnitude and temporal behavior of the closure phase varies with different regions and land covers (Ansari et al., 2021).

The magnitude of the closure phase in multilooked interferograms is deemed to be relatively small, especially compared to atmospheric artifacts. However, the propagation of the phase bias within long time-series can affect the accuracy of displacement velocity maps, potentially introducing errors ranging from sub-millimeter to even centimeter order per year (Ansari et al., 2021). It is therefore crucial to take this effect into account when interpreting displacement estimates.

Finally, it should be noted that the use of multilook imagery in the SBAS method makes it less suitable for detecting local deformations (Crosetto et al., 2016). Depending on the application, this aspect requires careful consideration.

Interferograms Phase Unwrapping

A limitation of the SAR system in signal transmitting and receiving models is that the extracted interferometric phase information represents the absolute phase modulo 2π, due to the cyclic nature of the phase. To recover the absolute phase information (unwrapped phase), an operation known as phase unwrapping is performed (Yu et al., 2019). To illustrate, a simplified representation of

Equation 2.1.5 for the wrapped phase is considered for a pixel s

$$\psi(s) = \delta\phi(s) - 2a(s)\pi, \tag{2.2.3}$$

where $\psi(s) \in (-\pi, \pi]$, $\delta\phi(s)$ represents the unwrapped phase and $a(s)$ is the phase ambiguity, in other words the number of full phase cycles (Van Leijen, 2014), and takes on integer values. Difficulties arise due to the fact that both $\delta\phi(s)$ and $a(s)$ are unknown and thus phase unwrapping is an ill-posed inverse problem. Namely, for one $\psi(s)$ and different $a(s)$ multiple solutions can be obtained for the unwrapped phase. This means that certain assumptions and additional information are required for the correct estimation of phase ambiguities, such that the unique solution for $\delta\phi(s)$ can be obtained (Yu et al., 2019). The characteristics of both the measurements and the signal of interest are determining factors in the ability to correctly estimate the ambiguities. Particularly, the noise levels in the measurements, related to the amount of decorrelation, the spatial gradient in the atmospheric signal and the spatio-temporal smoothness of the deformation signal. As the reliability of the deformation time series can be directly linked to the phase unwrapping process (Van Leijen, 2014), this is a crucial step to consider.

For SBAS a 2D+1D unwrapping approach is typical. That is, the two dimensions in space are unwrapped first, followed by an integration in time. The former is the most important part and strongly depends on the smoothness of the signal. An assumption is made regarding the spatial smoothness of the deformation signal, which allows for improved assessment of the variations in deformation patterns in time (Van Leijen, 2014).

Interferograms Inversion

The unwrapped phase values are then used to obtain the unknown mother and daughter image phases. Using Equation 2.2.1, a system of M equations: $[\delta\phi_0(x,r), ..., \delta\phi_{M-1}(x,r)]$ in N unknowns $[\phi\left(t_1,x,r\right), ..., \phi\left(t_N,x,r\right)]$ $(\phi(t_0,x,r) = 0, \forall(x,r))$ can be set up (Berardino et al., 2002; Lanari et al., 2007) and solved using a Least-Squares operation. This can be reorganized by using matrix formalism

$$\delta\phi = A\phi, \tag{2.2.4}$$

implying pixel-by-pixel (temporal) analysis, in which A is the design matrix relating the set of interferograms following from the pair selection procedure.

In addition, considering that SBAS commonly yields independent subsets as a result of the selection process, rank deficiency of the design matrix occurs. The SVD method can be implemented in case of multiple subsets to effectively combine all available interferograms. Specifically, SVD allows for evaluating the pseudo-inverse of the design matrix, providing the minimum norm Least-Squares solution. Consequently, in accordance with Equation 2.2.4, the method forces the method as close to zero as possible. This could however introduce large discontinuities. To obtain realistic geological processes rather than large discontinuities in the deformation estimates (Berardino et al., 2002), the magnitude and velocity in the LOS direction during each imaging period can be estimated. Using an averaged representation of the deformation pattern, smoothens the large discontinuities. This can be done by replacing the unknowns with the mean phase velocity between adjacent acquisitions in time

$$v = \left[v_1 = \frac{\phi\left(t_1,x,r\right)}{t_1 - t_0}, \ldots, v_N = \frac{\phi\left(t_N,x,r\right) - \phi\left(t_{N-1},x,r\right)}{t_N - t_{N-1}}\right], \tag{2.2.5}$$

resulting in the new system of equations

$$Bv = \delta\phi, \tag{2.2.6}$$

where the new design matrix B relates each imaging period.

Artifacts estimation & Filtering

Finally, the phase contributions from the atmospheric and topographic artifacts are still present in each of the pixels. To improve the estimate of the deformation signal, it is desired to perform a decoupling of these patterns, which can be achieved by considering the respective characteristics of the patterns. For the topographic component, its correlation with perpendicular baselines with respect to the LOS is exploited (Lanari et al., 2007). To estimate the topography, it is crucial to consider the variations in orbits (orbital tube) (Van Leijen, 2014). Concerning the atmospheric phase signal, the signal is known to be highly correlated in space, yet poorly in time (Lanari et al., 2007). Different approaches exist to account for the atmospheric effect, either based on the available data itself or on external data (Ebmeier, Biggs, et al., 2013).

Concluding remarks

The main error sources of the SBAS technique, in detecting deformation signals, include phase unwrapping errors as well as unfiltered atmospheric phase artifacts (Lanari et al., 2007). In addition, the phase closures due to multilooking require careful consideration. SBAS is most suitable for spatially correlated deformation signals. In contrast, the PSI method enables the detection of small-scale displacement, such as that of a single building, using a 1D+2D unwrapping approach.

2.2.2 PSI

Ferretti et al. (2000) introduced the first PSI technique in 2000, followed by an extension in 2001, more specifically referred to as the Permanent Scatterers approach. This work provided a foundation for further development and different extensions followed, differing in e.g. the pixel selection criterion and the deformation model used. Notably, among these developments is the DePSI algorithm proposed by Van Leijen (2014), which is considered in this research.

The main principle exploits the presence of point (persistent) scatterers (PS), that show stable scattering behaviour over several years, to mitigate the impact of temporal decorrelation. Hence it relies on the temporal coherence of the radar signals. In addition, on account of the typically smaller dimensions of the scattering objects compared to the radar resolution, the scattering behavior of the objects is effectively averaged within a single resolution cell. The reflection dominance of a PS within the resolution cell strongly reduces the geometric decorrelation effect. A key feature of the algorithm includes the exploitation of all available SAR images, that is to say not restricted by the baseline, enabled by the selection of single coherent pixels (Ferretti et al., 2000). Consequently, the resulting deformation time series is extensive and rich in useful phase information. In addition, the estimation of the sources of error (e.g. atmospheric signal delay) is improved (Van Leijen, 2014). In general, the location of these PS is unknown beforehand and depending on the study area, the radar wavelength and the spatial extent of objects, the PS density can differ significantly.

Some analytical details of the processing steps followed in DePSI are provided, since the generated outcomes by this algorithm will be considered for the comparative analysis with the SBAS method. The main goal of the DePSI algorithm involves the detection and estimated deformation time-series of the PS by considering a SAR data stack. Other key outputs include different quality indicators, such as the temporal coherence. The approach is based on a hierarchical PS structure and has a so-called modular setup allowing for specific steps to be re-executed or disabled as desired by the user and depending on the application. The approach composes a total of nine modules, some of which are optional to improve the PS detection. The different modules are summarized here, a detailed description is however provided by Van Leijen (2014). The optional steps are discussed in a global context only. It should be noted that DORIS (B. Kampes et al., 2003) is used for the interferometric processing of the data.

Initialization

DePSI starts with the available interferometric data stack after processing with DORIS. A single mother baseline configuration is considered to generate the interferograms. Given $N + 1$ SAR images, a total of N interferograms can be generated with respect to the same mother image. The mother image is selected following minimal overall decorrelation criteria. The metadata specifying the interferometric data set, including the data source and mother image, is used to read the data. Furthermore, the process parameters can be set to define the desired processing flow, selection thresholds and deformation models depending on the specific application.

Persistent Scatterer Candidates selection

Given the fact that the interferometric phase is wrapped and composes a variety of phase contributions (Equation 2.1.5), the phase is not a favorable criterion for the selection of the so-called persistent scatterer candidates (PSC). Instead, amplitude information can be used to detect points with stable phase behavior. This is possible following the assumption that a strong point scatterer is characterized by a notably large amplitude, thereby dominating the resolution cell and limiting other interference on the resulting phase. Specifically, the Normalized Amplitude Dispersion, denoted D_A, is considered and can be related to the phase stability or phase standard deviation (σ_ψ) through the mean (μ_A) and standard deviation (σ_A) of the amplitude

$$\sigma_\psi \approx \tan(\sigma_\psi) = \frac{\sigma_A}{\mu_A} \doteq D_A. \tag{2.2.7}$$

In other words, pixels with a constant amplitude in time and thus characterized by a low D_A and σ_ψ, are selected as candidates. This relation is valid in case of low σ_ψ values, thus limited noise levels, and its reliability is improved with an increasing number of acquisitions.

First and higher-order PSC can be distinguished and require different selection criteria. The first-order PSC make up the reference network, therefore a homogeneous distribution over the image is crucial in establishing a network that provides adequate coverage of the area of interest. To achieve a homogeneous distribution, a uniform grid with a specific resolution (generally 200-500 m) is considered. For each grid cell the candidate is selected based on the set amplitude dispersion threshold (0.2-0.3), which is dependent on the number of images in the interferometric stack. To avoid the PSC being in close proximity a grid adjustment is implemented, where the grid is shifted by half its size in both azimuth and range directions. In doing so, the final selection of first-order PSC is obtained. The higher-order PSC are then selected based on an increased threshold (0.4-0.45) compared to before, such that more PSC are selected, including the first-order points, and a densified network is obtained. Finally side lobe pixels, arising from the spatial signature of a point scatterer, are identified and discarded. Following the selected PSC, the data is reduced significantly.

Network construction

As mentioned in the previous step, the reference network is formed using the selected first-order PSC. The reference network is constructed following an iterative approach in which four steps are repeated after each atmospheric and, possibly, orbital phase screen estimation and removal. The four steps include the estimation of the data precision based on variance component estimation (VCE), the formation of a spatial network between the PSC, the temporal ambiguity resolution for each arc in the network and the spatial ambiguity resolution.

To understand the need for the first two steps, the unwrapping procedure is considered. In the case of PSI, typically a 1D+2D unwrapping approach is followed. That is, the temporal ambiguities are first resolved, followed by the spatial ambiguities. The temporal ambiguity resolution can be expressed mathematically in terms of a functional model $E\{\underline{y}\}$, relating the phase observations to the unknown parameters, and a stochastic model $D\{\underline{y}\}$, accounting for the statistical properties of these observations

$$E\{\underline{y}\} = Ax \quad ; \quad D\{\underline{y}\} = Q_y, \tag{2.2.8}$$

in which $\underline{y}$ is the observation vector, A the design matrix, x the vector of unknowns and Q_y the covariance matrix. In addition, $E\{.\}$ and $D\{.\}$ represent the expectation and dispersion operator, respectively. By estimating the stochastic model of the double-difference (i.e. differences in time and space) phase observations for each arc between the PSC, as described by Q_φ, the ambiguities can be resolved. The latter is done in the first step. Q_φ can be obtained through error propagation on the stochastic model of the original SLC data. To simplify, one single Q_φ is considered for each arc between the candidates, following the assumption that the correlation between different daughter acquisitions is negligible. The (co-)variance components can be estimated by least-squares variance component estimation (VCE), based on the double-difference phase observations of arcs between the first-order PS. The first estimation is however performed before the detection of the first-order points and is therefore based on the PSC observations.

In addition, since PSI relies on individual point scatterers, arcs are required to connect the scatterers such that the spatial relationship between the persistent scatterers can be captured. This is achieved in the second step, in which the spatial network between PSC is constructed. After the selection of the first-order PSC, a spatial network is formed. To do so, a Delaunay triangulation can be used, resulting in a limited number of connecting arc. In addition, arcs that are too long are removed. Another method, proposed by B. M. Kampes (2006), can be employed to maintain a minimal number of connections. Specifically, the redundancy in the network is increased, which is essential for resolving the spatial ambiguities. Extensive network coverage across the area of investigation is essential to ensure accurate deformation estimates, i.e. a more redundant network increases the reliability of the estimates and improves the detection of unwrapping errors. However, this may be challenging to achieve depending on the study area.

Then, the temporal ambiguities can be resolved based on a parameterization within the model given by Equation 2.2.8, in which the functional model incorporates the topographic height error, a deformation model and the mother atmosphere. Different options for a deformation model are available, from a linear deformation rate to a higher-order polynomial. The model can either be assigned based on the deformation history of the area of interest, if known, or based on the data itself using a testing scheme. The stochastic model follows from an iterative procedure and describes the precision of the data. In DePSI three techniques are considered to solve for the mathematical problem, i.e., integer least squares (ILS), integer bootstrapping (IB) and, finally, the ambiguity function (AF). Another common approach involves a Bayesian estimation. The performance of the techniques depend on factors such as the number of available interferograms, expected deformation rates, the number of model parameters being considered and corresponding computational demands.

To relate the unwrapped phase with respect to a single spatial reference, the spatial ambiguity resolution step needs to be considered. The most straightforward approach involves a basic spatial integration and is valid under the assumption that no ambiguity errors result from the temporal ambiguity resolution. However, this assumption cannot be made and possible ambiguity errors should be accounted for. Therefore, the spatial ambiguity resolution commonly involves a two step procedure, as described by Ferretti et al. (2000). In DePSI, a six step procedure is considered. In the first two steps arcs with low quality, in terms of a low temporal coherence or high variance factor, are removed. Accordingly, the resulting PSC with less than three arcs, which is the minimum requirement to identify errors, are also removed. A drawback is that the e.g. low coherence may be on account of the (expected) deformation model, rather than the noise. The third step involves the spatial reference selection. A reference PSC with minimal noise is selected. Depending on the technique used, ILS, IB, AF, this is either based on a PSC connected to an arc with the highest temporal coherence or the lowest variance factor. In the fourth step an iterative statistical testing procedure is implemented, based on the principle that without errors the ambiguities of the arcs should form a closing network and thus the residuals are zero. Hence, ideally, the errors in the full data stack are removed until a closing network is obtained. However, to prevent weakening the network by discarding even relatively small errors, this step is used to remove the largest unwrapping errors and all incoherent points based on alternative stop criteria. The remaining errors are corrected, once again using an iterative approach, in the fifth step. The correction is applied per interferogram and the overall model test (OMT) is used to stop the procedure when a closing network is acquired. The correction is applied to the ambiguity with the maximum residue by means of subtracting the closest integer value of this residue or, when the closest integer of the maximum residue becomes 0, by subtracting or adding 1. After obtaining the final network the last step can be performed, in which the unwrapped interferometric phases with respect to a spatial reference are computed. The parameters of interest (atmosphere, deformation and DEM) can be re-estimated based on the unwrapped data and this process is repeated until the desired results are acquired.

Trend estimation

This step is optional and can be implemented to estimate and correct for the orbital phase screen (OPS). To do so, a linear trend is estimated per interferogram, based on a least-squares estimation and outlier detection. The unknown OPS is described by the slopes, in azimuth and range direction, and an offset. The observation vector consists of the obtained unwrapped phase of the first-order network per interferogram and are related to the unknowns by the line and pixel coordinates and, following a constant offset, a column of ones. After the respective estimation is obtained for each interferogram and corrected, the first-order network construction is repeated. However, it should be noted that by estimation and removal of these trends, potential trends in the surface displacement are removed as well. Therefore, this step requires careful consideration.

Atmosphere estimation

Another error signal is on account of the atmospheric signal delay. The atmospheric signal for each interferogram is referred to here as the atmospheric phase screen (APS). Assuming that the atmospheric signal is uncorrelated in time and by considering a full stack of interferograms, the atmospheric signal can be distinguished from the deformation signal. More specifically, two steps are considered to estimate the APS. The first step entails a low-pass filter, in the time domain, to separate the atmospheric signal and noise from the unmodeled deformation using the different correlations in time. The second step involves a Best Linear Unbiased Prediction (BLUP) to obtain the APS, which effectively forms a low-pass filter in the space domain for noise removal.

Interferogram selection

This step is also optional and involves the selection of a subset of the available interferograms for the deformation analysis. Specifically, while the total stack is considered for accurately estimating the error signals, this option can be useful when the deformation only occurs within a specific time span or when a consistent reflection is obtained only after a certain time frame, e.g. after the construction of a civil structure.

Densification

The first-order network is upgraded by means of densification with higher-order PS, as selected following the procedure described in the PSC selection step. These higher-order PSC are connected to at least three neighboring first-order PS, after which the phase unwrapping is performed similarly as before. The resulting ambiguity solution for each PSC is tested and either sustained or rejected, depending on which of the three available strategies is considered. After the PS are detected, the parameters of interest can be obtained.

Deformation modeling

Another optional step involves the estimation of a deformation model per interferogram, referred to as the deformation phase screen (DPS). In case the deformation history is known for the study area, the estimated deformation model can be removed from the phase. This could potentially enhance the number of detected PS. After doing so, the network is reconstructed and the densification step is once again applied.

Output generation

The output includes the georeferenced end-product. Aside from the quality of the parameters of interest, e.g., estimated deformation time series, the quality of PSI can be defined by the georeferencing of the final PS selection. The georeferencing accuracy is dependent on that of the orbit and image parameters, including the estimated heights of the PS. In addition, high relief areas subjected to layover effects can cause high absolute phase gradients. That is, the phase gradients can yield artificial slopes in an elevation model, formed through interpolation, and with that affect the georeferencing accuracy (Rossi and Eineder, 2015). In addition, several quality indicators are calculated. Even after application of the testing schemes, some falsely detected PS may remain. As described in detail by Van Leijen (2014), the quality of the estimated parameters of interest can be assessed in terms of the ensemble coherence, variance factor, covariance matrix, standard deviation of the displacement estimates, the ambiguity dispersion of precision and, finally, the spatio-temporal consistency (STC).

The deformation estimates are commonly described in terms of the ensemble coherence, also known as the temporal coherence, and is a measure of the difference between the deformation estimates and the estimated deformation model, mathematically defined as

$$\begin{aligned}\hat{\gamma} &= \left| \frac{1}{S} \sum_{s=1}^{S} \exp\left(j \left(\underline{\varphi}_{0i}^{0s} - \varphi_{0i,\text{model}}^{0s} \right) \right) \right| \\ &= \left| \frac{1}{S} \sum_{s=1}^{S} \exp\left(j \left(\underline{e}_{0i}^{0s} \right) \right) \right|,\end{aligned} \tag{2.2.9}$$

in which S is the number of daughter images, $\underline{\varphi}_{0i}^{0s}$ represents the double-difference phase observations between each PS i and the reference PS and, lastly, $\varphi_{0i,\text{model}}^{0s}$ is the model phase. Often a linear model is assumed. The difference $\underline{\varphi}_{0i}^{0s} - \varphi_{0i,\text{model}}$ gives the least-squares residuals $\underline{e}_{0i}^{0s}$. The value of the resulting $\hat{\gamma}$ ranges between $0 - 1$. By doing so, an indication of the scattering noise level of the PS, atmospheric signal delay and the unmodeled deformation is given. A so-called local ensemble coherence can also be determined with respect to the closest point in the network, rather than the reference point. This is done to assess the local quality and to minimize the relative errors in the atmospheric signal delay, which increase with increasing distance from the reference PS. In addition, trends in the data as well as the atmospheric delay have an effect on the distance dependency of the ensemble coherence, with respect to the reference PS. The drawback of this parameter is that it is not susceptible to unwrapping errors, as can be observed in Figure 2.5. The standard deviation and the STC are however.

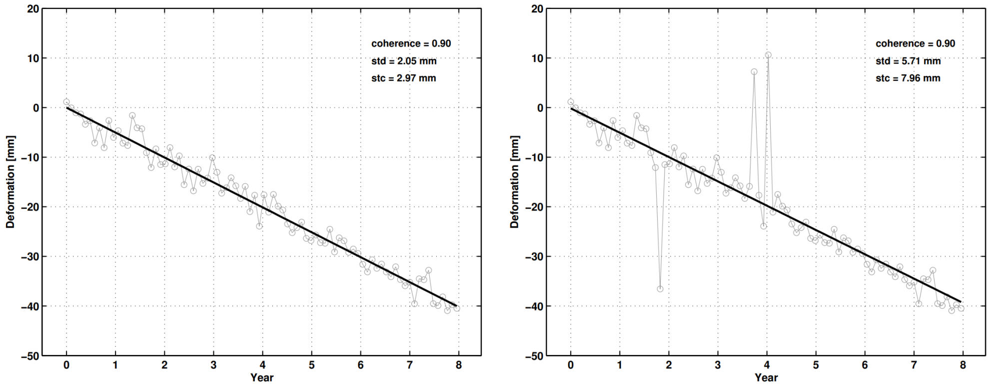

Figure 2.5: Deformation time series with (right figure) and without unwrapping error (left figure) with corresponding values for quality measures. Source: Van Leijen (2014).

3 Data & Study Area

Given the susceptibility of SAR to surface characteristics, in the Subsection 3.1, a detailed description of the study area is given focusing on these characteristics. In addition, the available data over the study area is described and illustrated in the Subsection 3.2.

3.1 Area of investigation

A case study is performed on the Dutch Caribbean volcanic islands of Saba and St. Eustatius, located at the northernmost part of the Lesser Antilles active volcanic arc and spanning an area of 13 and 21 km^2 respectively (De Zeeuw - van Dalfsen and Sleeman, 2018). Both islands are home to an active stratovolcano, Mt.Scenery on Saba and The Quill on St. Eustatius, have similar climates and are characterized by tropical rainforests and terrain variability. Therefore, in line with the research theme, they are suitable study areas. In this section an overview of the geomorphology, geology and other relevant features is provided. In Figure 3.1 the geology of both islands is visualized, as obtained from the 'Geologische Dienst van Nederland', an initiative of TNO. Roobol and Smith (2004) provides an extensive summary regarding the geology of both Saba and St. Eustatius.

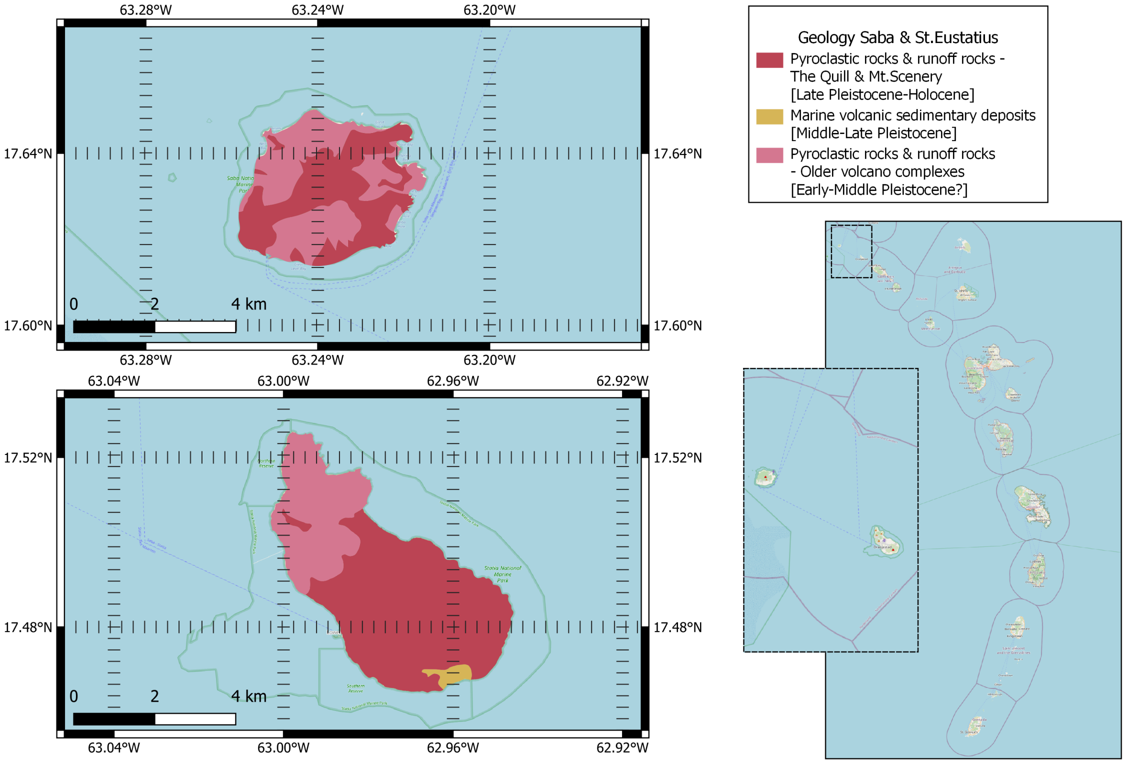

Figure 3.1: Geological map Saba (top map) and St. Eustatius (bottom map). Data source: TNO.

3.1.1 Saba

Saba is the northernmost island along the Lesser-Antilles active volcanic island arc and is the surface manifestation of volcanic activity as a result of subduction. The island consists of one main volcanic structure, known as Mount Scenery, as well as multiple Pelean domes and associated pyroclastic deposits (Roobol and Smith, 2004). Its geological and morphological features are shaped by its volcanic history. The population of the island of Saba has reached over 2000 people (De Zeeuw - van Dalfsen and Sleeman, 2018). As visualized in Figure 1.1a, a total of four main towns exist to accommodate the residents: Zion's Hill (also called Hell's Gate), Windwardside, St. Johns and, finally, the capital The Bottom (Allen, 2017). The towns are located on the more gentle slopes that lie between the peaks of the domes.

Saba is characterized by its rugged terrain, its diverse and densely vegetated rainforests covering the better part of Mount Scenery, and its steep slopes rising to a single peak. With 877 meters Mount Scenery reaches not only the highest point on the island, but also in the Dutch Kingdom. The slopes abruptly descend into the surrounding deep sea leading to a sharp land-water boundary (Allen, 2017). The dating of the last eruption is challenged by poorly preserved pyroclastic deposits, lacking the presence of carbonized wood. This scarcity of wood fragments can be attributed to pyroclastic flows transporting these materials downslope, to ultimately be contained in submarine deposits. However, hand dug pits in the Bottom uncovered the youngest pyroclastic deposit on Saba, dating back to roughly 1640 A.D. and thereby indicating the occurrence of the last recorded eruption (Roobol and Smith, 2004). In addition to the dominating structure of Mount Scenery shaping the island, several hills constructed by old volcanic domes contribute to its diverse and irregular topography, including: Old Booby Hill, Bunker Hill and Great Hill (A.L. Smith, n.d.[a]). The slopes of these domes are steep, reaching angles exceeding 60°. Along these slopes steep-sided features occur (J.A. de Freitas, 2016). Other characteristic features include the islands conical shape which is elongated in the northeast-southwest orientation, hot springs and a volcanic lateral sector collapse scar which has an elongated horseshoe shape that opens to the southwest and is therefore referred to as the horseshoe-shaped structure. The location of the scar is depicted in Figure 3.2b using a dashed red line. This structure is estimated to have formed roughly 100,000 years ago under the influence of rock weakening, following the formation of hydrothermal alteration zones, and slope instability due to inflation of the flanks of Mt. Scenery. While most of the structure has been predominantly filled by the Pelean dome growth and associated pyroclastic deposits, its outer rim is preserved. The capital The Bottom (Figure 1.1a) is located at the lowest elevation in the collapse scar (Roobol and Smith, 2004).

The occurrence of seismic activity, the distribution of hot springs and the orientation of the lateral collapse structure all indicate the possibility of the existence of a potential fault zone, running in a northeast-southwest direction perpendicular to the volcanic arc. This could explain the elongated shape of the island orientated along the fault line. The island is primarily composed of a collection of andesitic Pelean domes, as described before, surrounded by pyroclastic material (Roobol and Smith, 2004). Based on the timing of the sector collapse scar, roughly two major geological units can be distinguished both composing of volcanic debris, as visualized in Figure 3.1. First of all, an older unit consisting of lithified rocks of mainly andesitic composition, pre-dating the lateral collapse event. Secondly, a younger unit of unlithified to weakly lithified rocks of similar composition, which post-date the event (A.L. Smith, n.d.[a]). The walls of the structure form boundaries to the capital of the Bottom. Northeast of the structure older pyroclastic units exist, the domes and lava flows are predominantly concentrated southwest of the structure (Defant et al., 2001). In Figure 3.2a, an example of remnants of the well-preserved 1.8 km long basaltic andesitic lava flow is visualized, located between Upper Hell's Gate and the airport at Flat Point (Figure 1.1a). The slopes of Mount Scenery, which range between 15° − 45°, are covered with weathered basaltic andesitic rocks. The basal unit is dominated by agglomerates and tuffs, while the higher units primarily consist of andesites. Steep-sided valleys, also referred to as 'guts', run down the slopes. Two distinct types exist, i.e., V- and U-shaped guts. The V-shaped guts are concentrated on the southern slopes and occur in the lower units. While the U-shaped guts can be found in the western and northern regions and are not limited to the lower units (J.A. de Freitas, 2016).

(a) Remnants of the basaltic andesitic lava flow.

(b) Aerial Photograph with the horseshoe-shaped structure indicated by the red dotted line.

Figure 3.2: Characteristic Landforms of Saba. Source Allen (2017).

3.1.2 St. Eustatius

St. Eustatius, also referred to as Statia, is a slightly larger island located 35 km south of Saba. Statia and Saba have a similar geologic history. Both are young Pleistocene island arc volcanoes and hence have similar volcanic features. Nonetheless, notable differences exist. Statia is older and is characterized by a gentler topography, more erosional features, sedimentary structures and uplift. The island is home to more than 3000 people. Contrary to Saba, as can be observed from Figure 1.1b, Statia is dominated by two volcanic centers and only has one settlement: Oranjestad, which also serves as the capital (Allen, 2017).

The Quill volcano is an active, but quiescent, stratovolcano located in the southern part of the island, and marks the highest point of the island, reaching a height of about 600 meters. The last recorded volcanic eruption likely occurred between 1755-1625 years B.P. and was the last eruption in a sequence of five successive eruptions, as indicated by the well preserved products composing of distinct layers (Roobol and Smith, 2004). The volcano features steep slopes covered with rain forest (Figure 3.3a) and has a large crater at the summit, spanning 800 m in diameter (Roobol and Smith, 2004). The northwestern slope descends to a flat central plain, referred to as the Kultuurvlakte ('Culture Plain'), known for its fertile volcanic soil and urban areas. The southeastern flank drops abruptly into the sea at the so-called Sugar Loaf-White Wall formations, running east to west and spanning 1 km in length. Other characteristic features include the low-lying volcanic hills located in the northern region, referred to as the Northern volcanic Centers (A.L. Smith, n.d.[b]). Similarly to Saba, Statia is characterized by dense tropical rainforests covering the island (Allen, 2017).

Statia is situated at the north end of a shallow submarine bank, spanning a length of 80 km (Allen, 2017). A total of three distinct geological units can be distinguished on the island of St. Eustatius, as visualized in Figure 3.1. Two geological units composing of volcanic debris from the Quill volcano as well as from older volcano complexes. This has resulted in the formation of two main volcanic centers on the island: the Quill and the North-western volcanic hills. The latter is the oldest geological unit on the island and is built up of remnants of the older volcanic complex with varying degrees of erosion (Allen, 2017). The composition of these structures range from ejactamenta to agglomerates, tuffs and solidified lava flows (J.A. de Freitas, 2014). The entirety of the Quill volcano, with the exception of lava dome remnants, is composed of loose pyroclastic material, predominently (basaltic) pyroxene-andesites. The deposits on the western flank of the volcano are finer in texture than those on the northern, eastern and southern flanks as a result of the north-eastern trade winds. The Kultuurvlakte is characterized by tuff layers. The Quill is characterized by two irregularities marking its geologically diverse slope: the Round Hill and the White Wall complex (J.A. de Freitas, 2014). The latter constitutes the third geological unit found on the southern side of the island and consists of shallow marine volcanic sedimentary deposits, also referred to as the White Wall formation and Sugar loaf ridge (Figure 3.3b). The strata also compose of fragments of volcanic rock, hinting at initial submarine volcanism. These formations were subsequently uplifted and tilted, possibly as a result of volcanic dome growth (Allen, 2017).

The Round Hill is a semi-spherical cone which is composed of tuffs and volcanic debris, concealing the rocks beneath (J.A. de Freitas, 2014). Aside from the distinct rock types, these different units also differ in soil and vegetation type.

(a) The Quill volcano and White wall formation.

(b) Sugar Loaf.

Figure 3.3: Characteristic Landforms of St. Eustatius. Source: Allen (2017).

3.2 Data description

Data from a variety of satellite missions are available providing multi-frequency SAR data, i.e., from PAZ (X-band), Sentinel-1 (C-band) and ALOS-2 (L-band). Given the limited temporal resolution of the ALOS-2 L-band accommodating satellite, Argentina's polarimetric L-band SAR SAOCOM satellite series is also considered. In addition, the NISAR mission is planned to launch in 2024, providing more frequent L-band data. Moreover, for validation purposes and to have an idea of the current deformation that can be expected, GNSS data is used. Some useful parameters for the different missions are included in Table 3.1.

Satellite Mission	Band	Launch date	Revisit time [days]	Incidence angle [degrees]	Swath Width [km]	Spatial Resolution [m]
Sentinel-1	C	1A 2014 1B 2016	6	20-45	250	5 x 20
ALOS-2	L	2014	14	8-70	70/40	10
SAOCOM	L	1A 2018 1B 2020	16	21-50	49.1	L1A: 10 x 5
NISAR	L	2024	12	34-48	> 240	3-10

Table 3.1: Overview of different SAR satellite missions.

3.2.1 Sentinel-1

The Sentinel-1 mission is a collaborative effort between ESA and EC as part of the Copernicus program (ESA, n.d.[a]). It comprises a constellation of two satellites orbiting 180 degrees apart, Sentinel-1A and Sentinel-1B, enabling a shorter revisit time (Table 3.1) upon the launch of the second satellite in April 2016. The main objective of the mission is continuous radar mapping, e.g. land monitoring. The short repeat cycle allows for improved disaster monitoring and is also the main advantage of the Sentinel-1 data in comparison to the other data considered. It facilitates C-band imaging and, in addition to the short repeat cycle, provides wide area monitoring covering distances of up to 400 km, with resolutions as fine as 5 m depending on the four imaging modes available. The imaging modes include: Interferometric Wide swath (IW), Extra Wide swath (EW), Wave Mode (WM) (ESA, n.d.[b]). The acquired data-set over the area of investigation is in the IW acquisition mode, which is the default mode over land and coastal areas. However, as a result of an anomaly related to the electronics power supply, the mission Sentinel-1B has been discontinued in December 2021. Sentinel-1C and Sentinel-1D were to replace the satellites once their operational lifespan has come to an end. Following the anomaly, efforts are being made to launch Sentinel-1C as soon as possible. Specifically, the launch is expected to occur by the end of 2023 (ESA, n.d.[c]).

Data is available from both ascending and descending tracks. Both are considered on account of the terrain variability of the islands, introducing layover and shadowing effects. This results in inaccurate representation or even data gaps in certain parts of the islands. The ascending track is denoted by track 164, while the descending track is referred to as track 127. A more detailed description for both tracks is provided.

Descending track: t127

For the descending track a total of 120 SLC co-registered images are available for Saba for a timespan from October 26 2014 to May 3 2020, while there are merely 116 images for St. Eustatius. This difference in images can be explained due to data gaps of over three months between July 25 2018 and November 10 2018, a bit less than a month between July 20 2019 and August 13 2019 and almost two months between April 27 2019 and June 26 2019 in the St. Eustatius dataset. These gaps stem from variations in swath coverage (Korevaar, 2020), consequently four images covering St. Eustatius were too close to the edge of the swath and therefore discarded. The available interferograms had already been combined into a single-mother configuration, with respect to one single mother image: April 3 2019. The distribution of the data in time (temporal baseline) with respect to the corresponding perpendicular baseline is visualized for St. Eustatius and Saba in

Figure 3.4b and Figure 3.4d respectively.

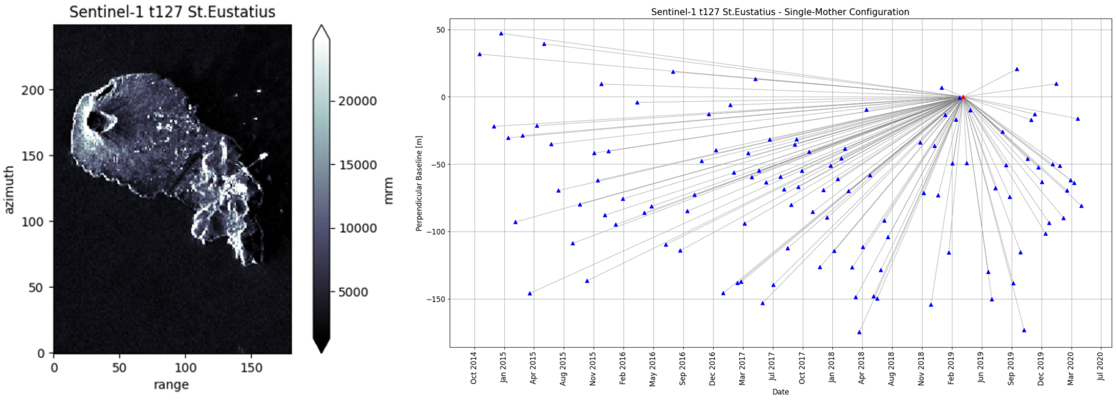

(a) Mean reflection map St. Eustatius.

(b) Baseline plot St. Eustatius.

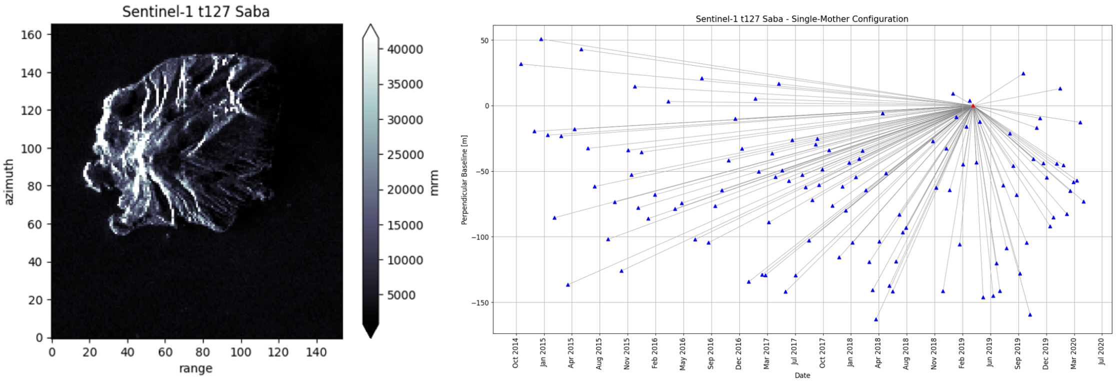

(c) Mean reflection map Saba.

(d) Baseline plot Saba.

Figure 3.4: The mean reflection map of the (multilooked) Sentinel-1 track 127 data sets (left) and the single-mother baseline plot (right) to show the data distribution in time with respect to the perpendicular baseline.

Ascending track: t164

The ascending track composes of a total of 123 coregistered images for both Saba and St. Eustatius, for a timespan from December 3 2014 to May 17 2020. The data has been exclusively collected by Sentinel-1A, as Sentinel-1B did not capture data for the area of investigation. As a result the images have a temporal baseline of twelve days, rather than six days. Saba and St. Eustatius are located in different swaths and bursts and have different incidence angles. In Figure 3.5a and Figure 3.5c, the mean reflection maps of both islands are visualized. Figure 3.5b and Figure 3.5d show baseline plots to give an indication about the distribution of the data.

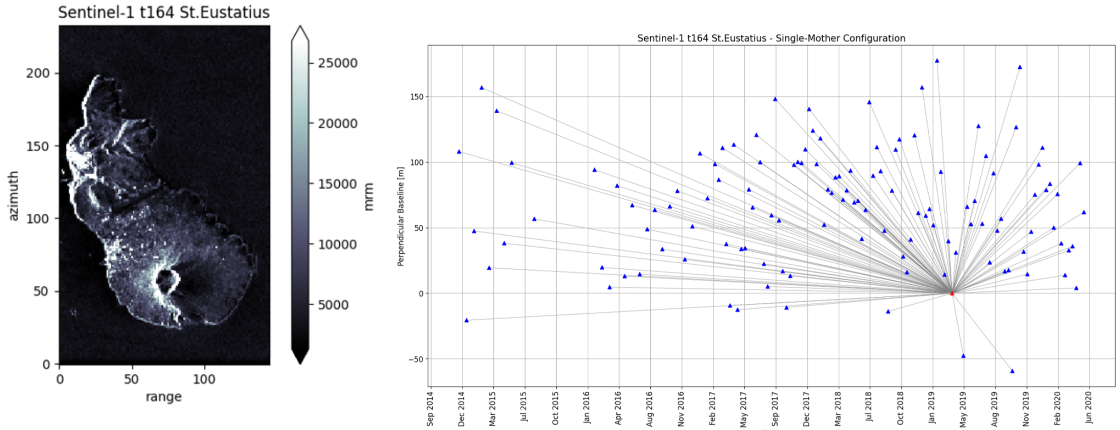

(a) Mean reflection map St. Eustatius.

(b) Baseline plot St. Eustatius.

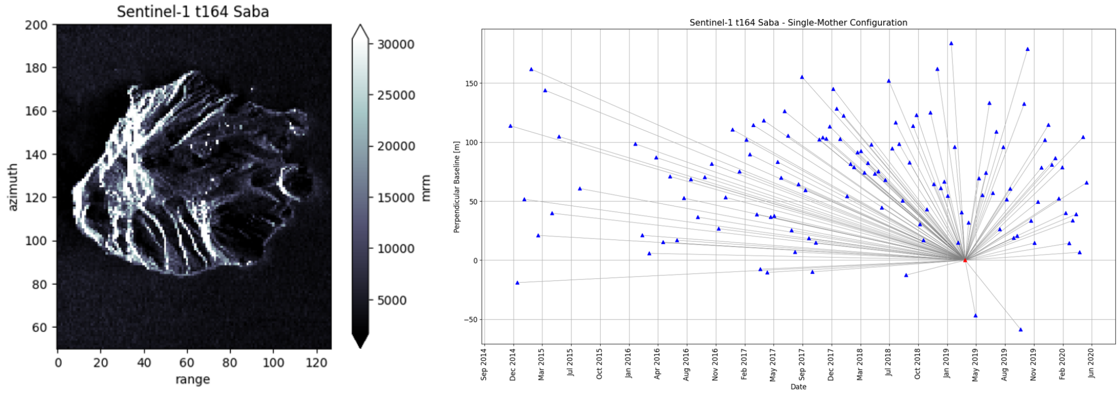

(c) Mean reflection map Saba.

(d) Baseline plot Saba.

Figure 3.5: The mean reflection map of the (multilooked) Sentinel-1 track 164 data sets (left) and the single-mother baseline plot (right) to show the data distribution in time with respect to the perpendicular baseline.

3.2.2 ALOS-2

Launched in 2014, ALOS-2 is a Japanese satellite developed by JAXA and a continuation of the ALOS (or 'Daichi') mission. The mission has numerous goals similar to those of ALOS, including: disaster monitoring, global monitoring of environmental changes and resource surveying (ESA, 2012). The satellite observes with L-band SAR imaging (PALSAR-2). The observations obtained with L-band can be especially effective for monitoring in highly vegetated areas on account of the wavelength penetration, which limits the decorrelation phenomena. There are three distinct imaging modes with different swath widths and resolutions, namely: Stripmap, ScanSAR and Spotlight. Stripmap and ScanSAR are each comprised of several submodes, Stripmap having three and ScanSAR having two submodes. The different modes and the corresponding swaths and resolutions are visualized in Table 3.2 (Motohka et al., 2017).

In this case, data is available from two ascending tracks. The first track is denoted by path 37 and contains data for both island, while the other track is denoted by path 36 and is only available for St. Eustatius. A resolution of 100 m is too coarse, considering that the area of the islands span only a few kilometres, which limits the available data that could be used. For both tracks a more detailed description is provided.

	Mode	Swath width [km]	Resolution [m]	Incidence angle [degree]
Spotlight	SB	25	3	8-70
Stripmap	UB	50	3	8-70
	HB	50 / 40	6	8-70 / 20-40
	FB	70 / 30	10	8-70 / 23
ScanSAR	WB	350	100	8-70
	VB	490	60	8-70

Table 3.2: ALOS-2 Imaging Modes.

Ascending track: p37

The ascending track consists of 10 images for a timespan from January 26 2015 to December 23 2019. Both islands are covered in the image. In contrast to Sentinel-1, the acquisition dates are at irregular time instances, as can be observed from the distribution of SAR images in the baseline plot in Figure 3.6b and Figure 3.6d. In addition, the mean reflection maps are visualized in Figure 3.6a and Figure 3.6c. The incidence angle differ slightly for the islands, i.e., 42° for St. Eustatius and 40.5° for Saba. The observation mode for the available data is Stripmap FB, with a resolution of 10 m.

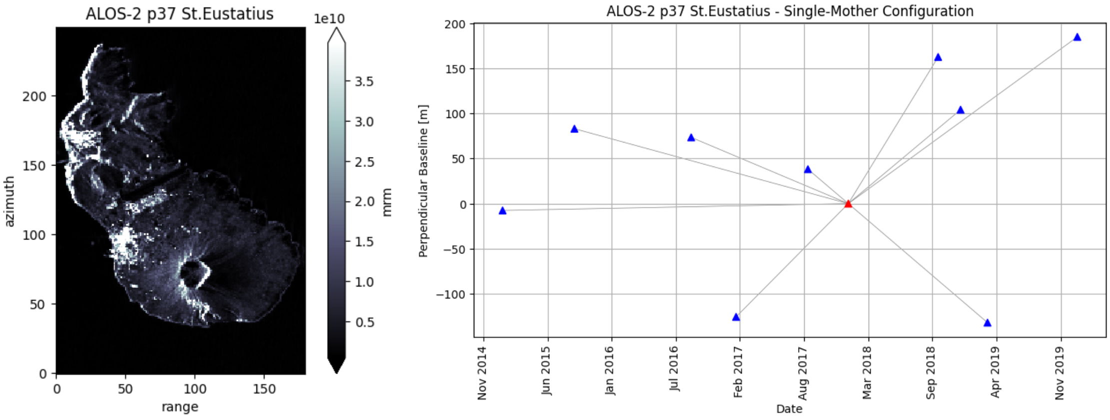

(a) Mean reflection map St. Eustatius.

(b) Baseline plot St. Eustatius.

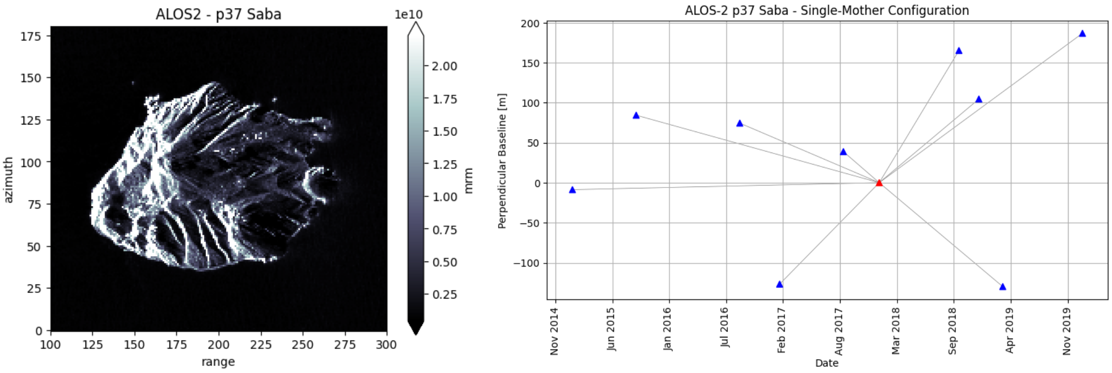

(c) Mean reflection map Saba.

(d) Baseline plot Saba.

Figure 3.6: The mean reflection map of the (multilooked) ALOS-2 path 37 data sets (left) and the single-mother baseline plot (right) to show the data distribution in time with respect to the perpendicular baseline.

Ascending track: p36

This track consists of 11 images, for a timespan from September 17 2014 to January 1 2020.

However, the images do not cover the complete area of investigation, namely only St. Eustatius. Similarly to before, the acquisition times are irregular as shown in Figure 3.7b. The mean reflection map for this path is presented in Figure 3.7a. The observation mode for this track is also Stripmap FB, with a resolution of 10 m and an incidence angle of 29.5°.

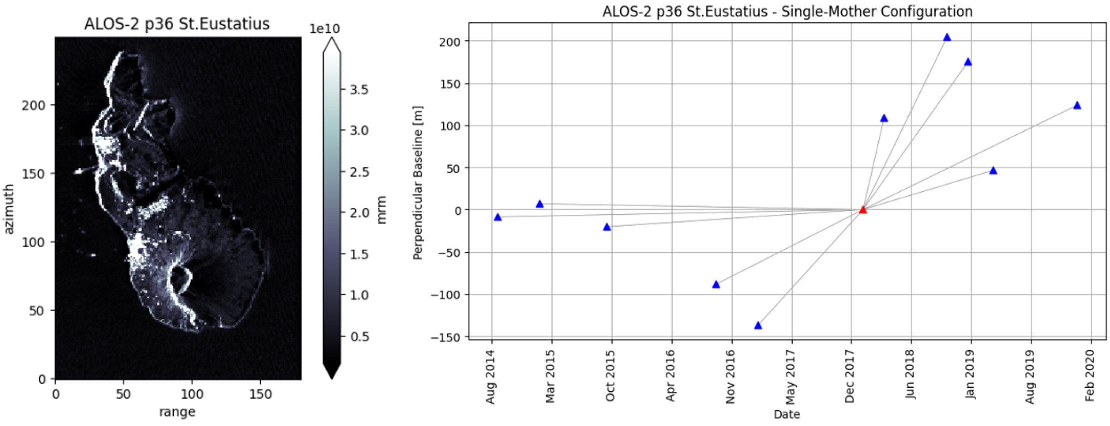

(a) Mean reflection map.

(b) Baseline plot of single-mother configuration.

Figure 3.7: The mean reflection map of the (multilooked) ALOS-2 St. Eustatius path 36 data set (left) and the single-mother baseline plot (right) to show the data distribution in time with respect to the perpendicular baseline.

3.2.3 NISAR

The upcoming NISAR mission, expected to launch in 2024 (NASA, 2022), is a joint initiative between NASA and ISRO comprising the first Earth observation satellite with dual-frequency SAR. Specifically, it carries both the S-band and L-band microwave bandwidth regions (Kellogg et al., 2020). The satellite follows exact repeating orbits every twelve days, providing continuous L-band data for an estimated mission duration of at least three years (NASA, 2022). The revisit time allows for minimizing the temporal decorrelation. In addition, (simultaneous) wide-swath data acquisition with an imaging swath of over 240 km is enabled allowing for global coverage. The mission objectives are plenty, providing measurements in fields including the solid Earth, ecosystems and cryospheric sciences. Regarding the solid Earth, NISAR will enable deformation measurement over the Earth's volcanoes with a fine resolution of 3-10 m, depending on the acquisition mode (Kellogg et al., 2020). The enabled global coverage and short time frames will allow for improved disaster monitoring and damage assessment.

3.2.4 SAOCOM

The SAOCOM mission composes a series of two satellites from Argentina, SAOCOM-1A and SAOCOM-1B, managed by CONAE. It accommodates L-band SAR imaging with a revisit time of twelve days with one satellite, or even eight with the constellation of the two satellites. The main objective is hazard monitoring and effective Earth observation for different fields of study (ESA, n.d.[d]). There are three imaging modes, i.e., Stripmap, Topsar Narrow and Topsar Wide, each with distinct polarization capabilities including two single, two dual, one full and one compact polarization (SAOCOM project, 2020). The available data comprises nine images acquired over a timespan encompassing both 2021 and 2022. Compared to ALOS-2, the images are significantly closer in time, which is expected to limit the temporal decorrelation. The data is obtained using acquisition mode S6, which is the Stripmap imaging mode with dual polarization mode (SAOCOM project, 2020). In addition, all the data is obtained through SAOCOM-1A. This data-set serves as an effective test case for the upcoming NISAR mission, considering that the available ALOS-2 data covers a broader time range with limited images and therefore larger temporal baselines.

However, the SAOCOM data still needs some processing steps, including coregistration and removal of the flat earth phase as well as the topographic phase. An example of an image recorded by SAOCOM-1A can be found in Figure 3.8.

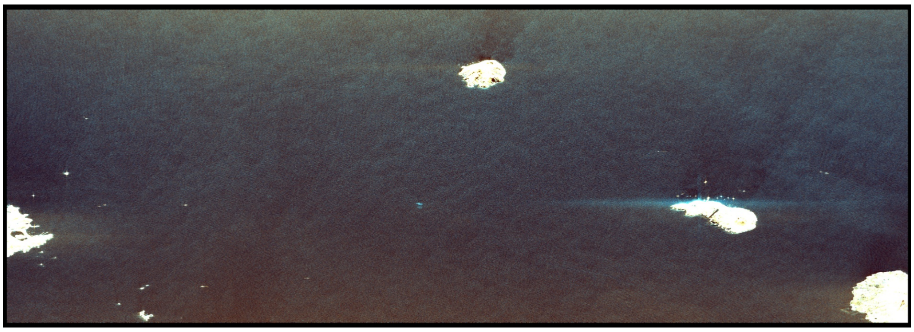

Figure 3.8: Image recorded by SAOCOM-1A encompassing both Saba and St. Eustatius.

3.2.5 GNSS

In addition to SAR data, GNSS data is considered. Comparison of the obtained results with ground truth data is of crucial importance for validation purposes. To this end, the GNSS stations, operated by KNMI and KNMI/kadaster, are utilized. Both islands accommodate four permanent and continuously recording GNSS sensors, as visualized in Figure 3.9a and Figure 3.9b, indicated by the green and blue triangles. The GNSS stations were set up at various points in time and therefore not all sites have been operational throughout the time frame considered for InSAR. The first installation occurred in early 2018 and the final in early to mid-2022, for both Saba and St. Eustatius.

The data can be accessed either through Earthscope (UNAVCO) or Nevada Geodetic Laboratory (NGL). The latter is considered and provides processed time series data in ascii text in a so-called tenv3 format. The processing has been performed and described by Blewitt et al. (2018). NGL extracts raw GPS data from over 17000 stations worldwide and produces numerous data products, including position coordinates (latitude, longitude and height) with different data intervals, reference frames and latencies. The latency refers to the lag time between data acquisition and data availability (Blewitt et al., 2018). The GPS data considered is the 24 Hour Final Solutions. The geodetic coordinate reference system used is IGS14, which is in units of meters. The variables of interest include the north, east and up components, given in m.

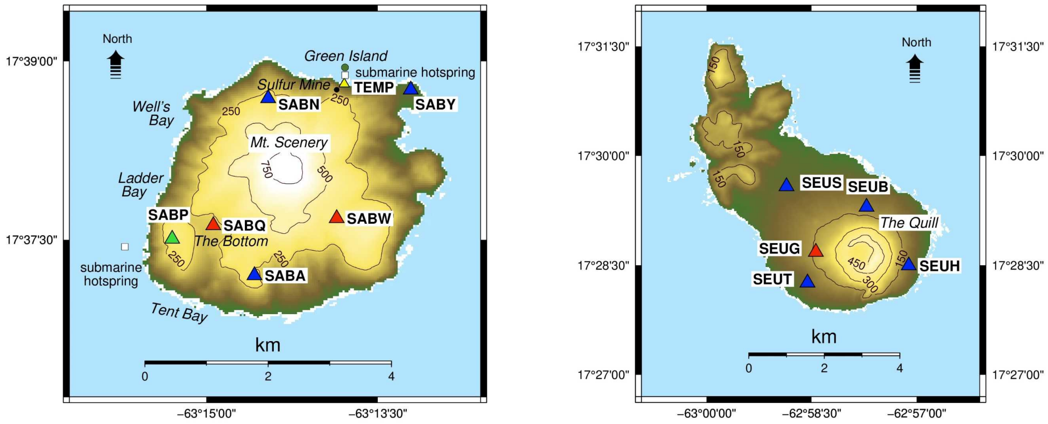

Figure 3.9: Ground-based Monitoring Network on Saba and St. Eustatius: GNSS station = green triangle, seismometer = red triangle, GNSS station + seismometer = blue triangle.

4 Methodology

In this chapter, an overview of the approaches for processing InSAR data is provided. Specifically, the steps required to answer the research question and sub-questions. The chapter is divided into two sections, the first section focuses on the development of SBAS software (Section 4.1), while the second section discusses the PSI method (Section 4.2). Software is available at TUD for the PSI method: the DePSI algorithm. In contrast, for the SBAS method software needs to be developed. The implementation is done using Python.

4.1 SBAS Software Development

In this section, the general workflow of the implemented SBAS method is described in terms of the processing chain, i.e., the technical considerations, as well as a step-by-step procedure of the theoretical considerations. Finally, some of the technical challenges faced during the development stage are highlighted.

4.1.1 Automatized processing chain

To realize an automatized volcanic monitoring system based on InSAR, several factors are of importance. First, to manage the extensive amount of data, efficient storage approaches are crucial. Packages in Python such as xarray, dask and zarr enable efficiency as well as the storage of (labeled) heterogeneous data in multi-dimensional Numpy arrays (Hoyer and Hamman, 2017). Another package which offers an extension of xarray / dask to obtain an (In)SAR datamodel is in development, the so-called SarXarray package (*sarxarray* 2023). More specifically, a coregistered SLC stack saved in binary format can be loaded into an xarray.Dataset object, after which basic operations can be applied similar to ordinary dataset objects. This package is considered at the base of this research. Second, the processing chain relies on efficient workflows. That is, rather than using iterative methods, where possible the required computations are performed simultaneously for all pixels and/or time dimensions. In addition, the use of dictionaries, i.e., key-value data structures, is exploited to keep track of e.g. selected data pair combinations in an efficient way.

The processing chain of the SBAS method is automatized in accordance with the DORIS output. The DORIS software (B. Kampes et al., 2003) is used to generate interferometric products including the radar-coded DEM, coherence maps and interferograms from SLC data. In addition, the products are georeferenced, i.e., the latitude, longitude and height coordinates are available for each pixel. The overall work flow of the InSAR processing done using DORIS is visualized in Figure 4.1.

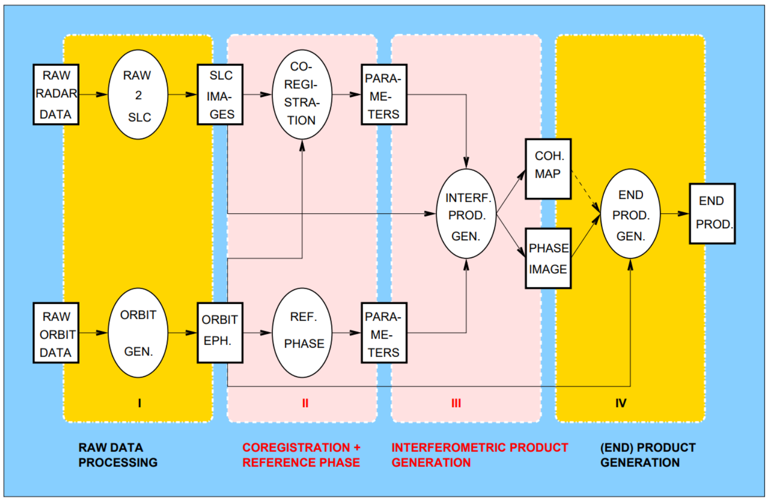

Figure 4.1: DORIS workflow of InSAR processing (B. Kampes et al., 2003).

From previous work (Korevaar, 2020), coregistered interferograms in the single-mother configuration are made available using DORIS, including flat-earth as well as topographic phase removal. The available Sentinel-1 data has been processed using DORIS version 5, whereas ALOS-2 is processed using DORIS version 4 and, therefore, require a somewhat different approach to load the data. These interferograms are the starting point for the SBAS processing chain. The required information to load in the data can be extracted from the DORIS metadata to obtain information regarding the output format (e.g. shape, data type) of the data-set as well as the perpendicular and temporal baselines. The processing flow can be defined by means of nine main functions, as outlined below.

1. Loading the input data into an xarray.Dataset
2. Interferometric Pair Selection
3. Interferogram + Coherence Generation
4. Multilooking
5. Masking
6. Phase Unwrapping
7. Linear Inversion
8. Correction Unwrapping Errors
9. Output Generation

These main functions rely on several sub-functions and allow for a variety of user-defined parameters that can be set, e.g. based on the satellite data considered. In addition, desired thresholds for the pair selection and masking procedures can be defined. The 'Masking' step entails both water masking and land masking, where land masking is divided into two different masking approaches. Similarly, in the 'Correction Unwrapping Errors' step two different approaches are available. Another crucial factor to consider is how to present the end results to the user in a useful and efficient way. To do so, the results can be exported as GeoTIFFs to allow for analysis in GIS software and comparison with other maps, such as topographic maps to clarify and be able to understand and assess differences in results from the different data and methods. A schematic of the implemented processing chain is visualized in Figure 4.2. The processing chain for ALOS-2 can be ran locally due to the limited amount of data available. Considering the significantly large amount of data from Sentinel-1, an HPC environment is used to run the full data-set. Specifically, a so-called Dask SLURMCluster is set up to enable parallel processing.

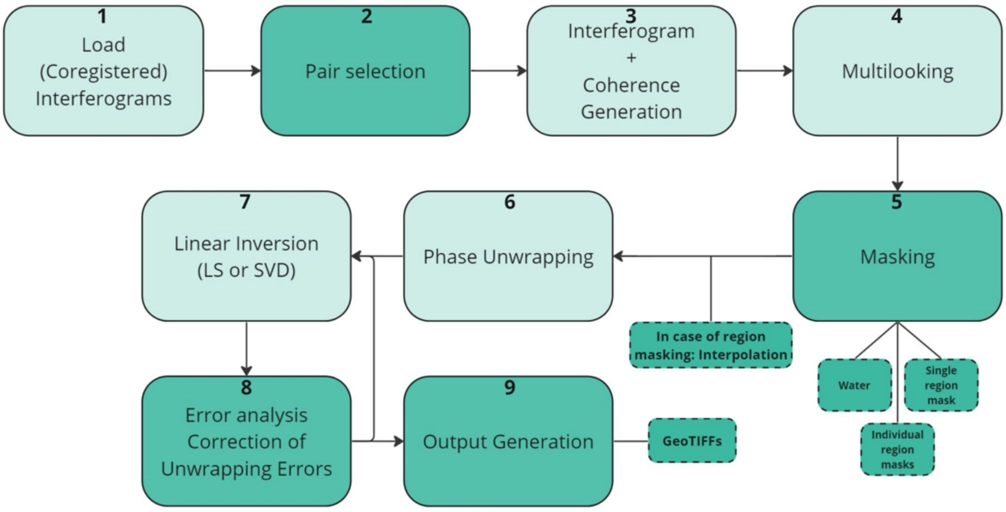

Figure 4.2: SBAS processing flowchart. The steps in which new approaches are explored to enhance the method, are emphasized using a darker shade.

4.1.2 Step-by-step procedure

Step 1: Loading the input into a xarray.Dataset

The algorithm is initialized according to the DORIS output files. Specifically, after setting the path to the 'cint.srd' files, which consist of the single-mother interferograms after the flat earth and topographic phase removal, a list of these respective paths is generated and sorted in ascending order based on the acquisition timestamps. To load the interferogram stack into a xarray.Dataset, using the SARXARRAY package, the metadata contained within the 'ifgs.res' is read to extract the appropriate shape corresponding to the specific data set. Furthermore, the data type should be specified. User-defined chunk sizes can be set to facilitate reading and processing the data in chunks, enhancing memory efficiency and processing time. Moreover, DORIS provides the corresponding latitude and longitude coordinates, i.e., 'lam.raw' and 'phi.raw' files, which are assigned to the resulting xarray.Dataset.

Step 2: Interferometric Pair Selection

An important step in the SBAS development involves the selection of interferometric data pairs to minimize the spatial and temporal decorrelation phenomena. Therefore, subsets with small spatio-temporal baselines are considered. The coherence serves as a measure of the quality of an interferogram. Specifically, any changes in the radar reflectivity of a scene, which is manifested as decorrelation in the phase difference of two images, will have an effect on the resulting coherence. Hence, a selection process based on the coherence is implemented. The selection can be carried out in numerous ways, three approaches are explored here (Table 4.1).

Approach 1	Average coherence over land
Approach 2	Average coherence over volcanic region
Approach 3	Modeled coherence

Table 4.1: Approaches considered for the pair selection.

The first approach involves a selection based on the average coherence over land. To do so, the coherence map is generated for either all (unique) interferogram combinations, for example in the case of ALOS-2, or for a subset, when dealing with a bigger stack like Sentinel-1. The selection of this subset could be done based on a certain criterion, e.g. the maximum spatio-temporal baselines. Furthermore, a mask is generated to separate the land from the water, as explained in detail in the 'Masking' step. Considering that the coherence differs across the islands, i.e., some parts are characterized by vegetation but also several by open field, the obtained coherence may not be representative of the region around the volcano. Therefore, in the second method, a region around the volcano is considered. Based on a user-defined threshold of the desired minimum coherence, data pairs can be selected. A drawback of both approaches is that they can be computationally expensive, since the coherence for a significant number of interferograms has to be determined, especially for Sentinel-1 data which has a revisit time of twelve days. This calls for an alternative approach.

The third and final approach considers a predicted coherence value, modeled using the temporal and perpendicular baselines. For this approach a tool is written based on the available metadata from the DORIS software, which holds information regarding the baselines. Considering that the particular output is according to the single-mother configuration, the perpendicular baselines need to be determined in accordance with the short-baseline configuration in a similar way to the interferogram generation of all unique combinations. This theoretical coherence is based on the fact that the coherence between two images is mainly affected by the temporal baseline as well as the perpendicular (spatial) baseline and can, therefore, be predicted using these parameters. A linear coherence behavior is assumed. It is also known as the integrated correlation coefficient γ^m (Van Leijen, 2014; B. M. Kampes, 2006; Tao et al., 2020) and is defined by:

$$\gamma^m = g\left(B_\perp^{\mathrm{md}}, B_{\perp_{\max}}\right) \cdot g\left(B_\mathrm{T}^{\mathrm{md}}, B_{\mathrm{T}_{\max}}\right), \tag{4.1.1}$$

where

$$g\left(B, B_{\max}\right) = \max(1 - |B|/B_{\max}, 0). \tag{4.1.2}$$

Then, similarly to the first and second approach, a selection can be made based on a set threshold for a desired minimum coherence. Fine tuning of the $B_{\perp_{\max}}$ and $B_{T_{\max}}$ parameters is performed by comparing with the pair selection result based on the actual coherence values. This calibration procedure of the third approach is performed once for the different satellites. The approaches are explored by considering ALOS-2 as well as a subset of the available Sentinel-1 SLC's, due to the significant difference in data availability. Specifically, a subset that comprises 10 SLC's and features a data gap is considered. The selected settings, threshold and the resulting number of data pairs selected are represented in Table 4.2. It should be noted that the total amount of unique combinations, for a subset consisting of 10 SLC's, equals 45.

	$B_{T\,\max}$ [days]	$B_{\perp\max}$ [m]	Threshold [-]	Selected pairs Approach 1 [-]	Selected pairs Approach 2 [-]	Selected pairs Approach 3 [-]
Sentinel-1	72	7100	0.3	17	9	20
ALOS-2	1152	14500	0.3	45	31	29

Table 4.2: Pair selection settings and result. The total number of pairs equals 45. Approach 3 is calibrated using Approach 1 for Sentinel-1 and Approach 2 for ALOS-2.

The resulting baseline plots for the different approaches are presented in Figure 4.3, Figure 4.4 and Figure 4.5 for both Sentinel-1 and ALOS-2. Considering Sentinel-1 first, it can be observed in Figure 4.3a, Figure 4.5a and Table 4.2 that the selected pairs resulting from the first and third approach merely differ by three pairs. Of the resulting 17 only one pair differs, the rest of the selection is identical. Due to the similar results, the parameters considered for the modeled coherence are deemed to be properly tuned and can, therefore, be used rather than the actual coherence. In addition, as the most recent image of the data stack is not part of a cluster when following the first approach (Figure 4.3a), the third approach might be more suitable. Finally, when considering the second approach, significant data gaps occur as shown in Figure 4.4a which is undesirable. It is important to highlight that even in the third approach, two distinct clusters are formed. As explained in Section 2.2.1, this is not uncommon for SBAS. The SVD method can be applied in this case, such that the independent subsets can be effectively combined in the linear inversion step. In contrast, the results following the different approaches vary significantly for ALOS-2. Following the first approach, all unique combinations are selected. This can be explained by the relatively high coherence achieved with L-band imaging. In the second approach 31 pairs are selected. Considering the revisit time of ALOS-2 (less images in total), the first and second approach may be feasible as computational expense is not a limiting factor. The second approach may, however, be more optimal considering that most interferograms are still considered based on the coherence around the volcano itself. Also considering the fact that L-band is expected to result in more reliable interferograms, on account of the coherence. However, in light of the anticipated increase in L-band data availability, the third approach may be the more favorable option. The fine tuning of the parameters is done based on the results following the second approach. This leads to 29 identical pairs in the third approach.

Depending on the revisit time of the satellite, one approach may thus be more feasible than another. The modeled coherence could be a suitable measure to base the selection algorithm on as it avoids having to calculate the coherence for all combinations. Since SAOCOM has a revisit time of 16 days and NISAR will have a revisit time twelve days, a modeled coherence will likely be more feasible in these cases.

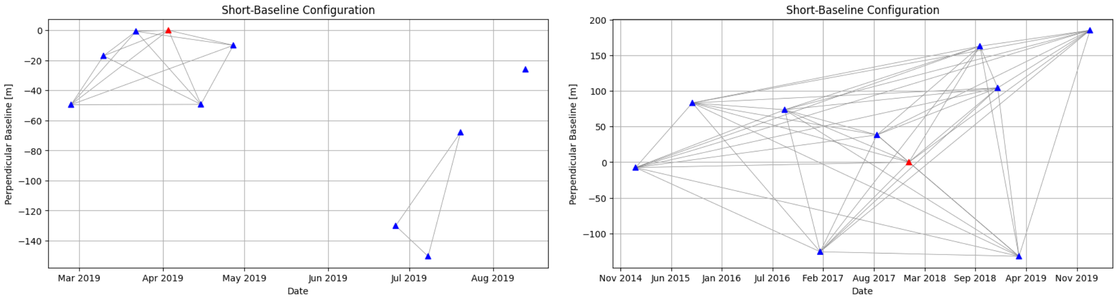

(a) Sentinel-1

(b) ALOS-2

Figure 4.3: Baseline plot for Approach 1. The red triangle represents the original mother SLC.

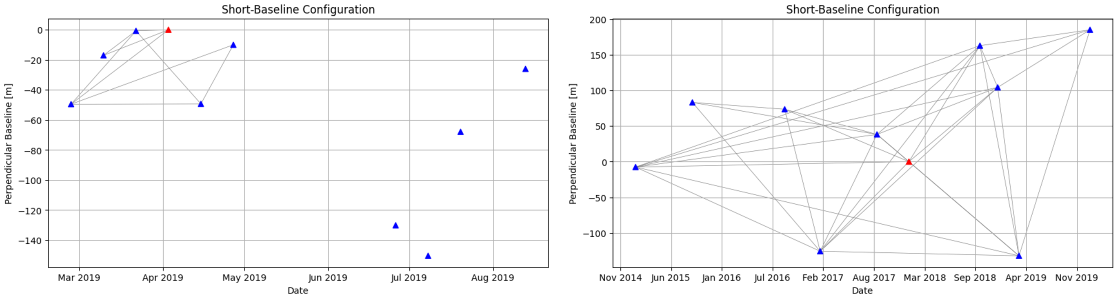

(a) Sentinel-1

(b) ALOS-2

Figure 4.4: Baseline plot for Approach 2. The red triangle represents the original mother SLC.

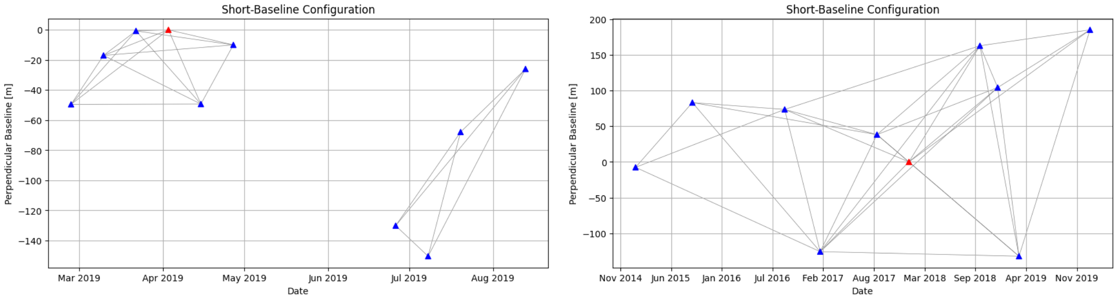

(a) Sentinel-1

(b) ALOS-2

Figure 4.5: Baseline plot for Approach 3. The red triangle represents the original mother SLC.

Step 3: Interferogram and coherence Generation

An important step towards implementation of SBAS involves considering the available coregistered interferograms, resulting from the DORIS software, to generate a new set of unique interferogram combinations. Specifically, by combining the single-mother interferograms in such a way that a short-baseline configuration is obtained. As illustrated in Figure 4.6, the PSI and SBAS baseline configurations differ significantly. The short-baseline configuration can be achieved by considering that an interferogram can be obtained by means of the complex conjugated multiplication of coregistered SLC images. In a similar way two interferograms can be combined to obtain a new one, however one needs to account for the original mother image. i.e., let P_{01} and P_{02} be the available complex phasors and P_{12} the desired combination, the following procedure is followed

$$\begin{aligned} P &= A\exp(i\psi), \\ P_{01} &= P_0 \cdot P_1^* = A_0 A_1 \exp(i(\psi_0 - \psi_1)), \\ P_{02} &= P_0 \cdot P_2^* = A_0 A_2 \exp(i(\psi_0 - \psi_2)), \\ P_{12} &= P_{01} \cdot P_{02}^* = A_0 A_1 A_0 A_2 \exp(i((\psi_0 - \psi_1) - (\psi_0 - \psi_2))). \end{aligned} \tag{4.1.3}$$

Since ψ_0 cancels in the last expression, the only thing left to do is account for the A_0^2 in the expression for P_{12}. This leads to

$$\begin{aligned} P_{12} = P_{01} \cdot P_{02}^* &= A_0 A_1 A_0 A_2 \exp(i(\psi_2 - \psi_1))/A_0^2. \\ &= A_1 A_2 \exp(i(\psi_2 - \psi_1)). \end{aligned} \tag{4.1.4}$$

Hence, apart from the single-mother stack, the amplitude of the mother image is needed. Accordingly, the coherence for each of these combinations needs to be determined. The pixels require some kind of multilooking to obtain an estimation of the expectation. Considering that the islands are relatively small, a moving average filter is deemed feasible. A moving average would be desirable as the original resolution of the interferogram is maintained. Because of the moving window, the estimates will be strongly correlated. Then, with the following equation the coherence can be determined:

$$|\hat{\gamma}| = \frac{\left|\sum_{n=1}^{N} P_1^{(n)} P_2^{*(n)}\right|}{\sqrt{\sum_{n=1}^{N} \left|P_1^{(n)}\right|^2 \sum_{n=1}^{N} \left|P_2^{(n)}\right|^2}}. \tag{4.1.5}$$

In this equation, the amplitude of the interferogram is divided by the square-root of the squared (original) amplitudes of the corresponding SLC's, after averaging over a window of N pixels. This procedure is repeated for the different time dimensions (interferometric data pairs) n.

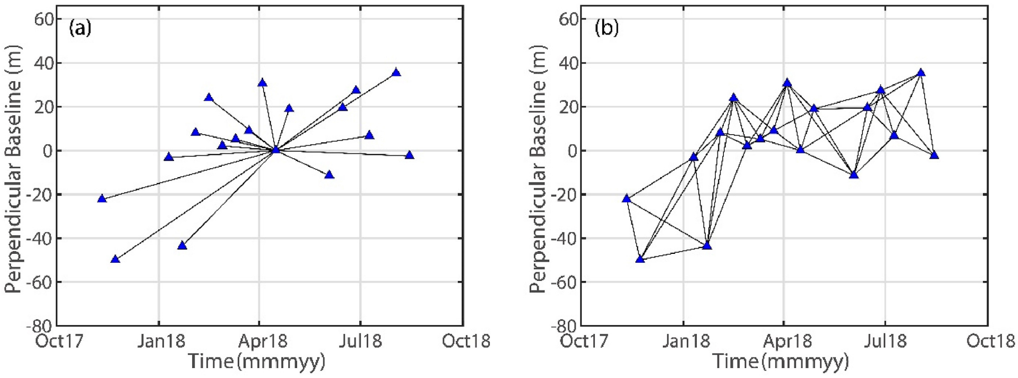

Figure 4.6: An example of a baseline plot for the a) PSI (single-mother) and b) SBAS (short-baseline) approach. Source: Li et al. (2022).

Step 4: Multilooking

Multilooking simply refers to the (complex) averaging of adjacent cells over some window, to improve phase statistics and limit the computation time, as described in more detail in 2.2.1. To achieve this, non-overlapping patches are generated and averaged. This is applied to both the interferograms and the corresponding coherence. It is worth emphasizing that the moving average approach, employed for the coherence estimation, is based on the same window size, i.e., the windows are correlated. It is expected that the multilooking procedure has a minimal impact on the correlation of the coherence estimates. In the case of the interferograms, the imaginary part and real part are averaged separately, after which both are combined again. The window size is chosen such that roughly a square window in the slant range and azimuth direction is achieved. This can be done by considering the azimuth and (ground) range spacing. Consequently, for Sentinel-1 a 3:11 window, based on a pixel spacing of 3.8 (range) x 13.9 m (azimuth), is considered and for ALOS-2 both a 12:7 window and 24:14 window are compared, based on a pixel spacing of 9.1 (range) x 5.3 m (azimuth) for the Stripmap FB mode.

Step 5: Masking

Before the phase unwrapping step it is important to mask incoherent regions, like the area covered by water, to limit the computation time but also to avoid unwrapping mistakes and with that facilitate data interpretation. A total of three different approaches are considered to do so, as summarized in Table 4.3 below.

Approach 1	Single Mask preserving all land pixels (water mask)
Approach 2	Single Mask based on mean coherence
Approach 3	Individual Masks for every data pair

Table 4.3: Masking approaches considered. The first is used to mask out the water, the second and third are different approaches to also mask land pixels.

The first approach involves masking out the water, while preserving the pixels that are part of the land. An initial idea was to generate the mask based on the DEM due to the sharp water-land transition. However, for St. Eustatius this transition is not distinguishable everywhere. The boundary is more distinctive for Saba, owing to the steeper slopes, however still does not provide complete coverage. A mask based on the mean reflection did seem to show complete coverage for Saba, but only for ALOS-2. Therefore, an alternative strategy is required for the other data sets. In the alternative procedure, an edge detection algorithm is implemented on an image with high coherence. Since the surface of water bodies changes instantly, complete decorrelation occurs. Hence, a mask based on the coherence shows promise. However, this leads to some isolated pixels and clusters in the water (first column in Figure 4.7a for St. Eustatius and Figure 4.7b for Saba). These are filtered out by setting a condition on the maximum number of neighbors for a pixel to be classified as isolated. In addition, the clusters are identified and removed based on a threshold of maximum connected components. The results of each of these steps are visualized in Figure 4.7a for St. Eustatius using Sentinel-1 data. Similarly, the results for Saba are visualized for Sentinel-1 in Figure 4.7b. However, with this approach all land pixels will be considered, even those with low coherence. Hence another mask for land pixels is desired, where the mask from the first approach, based on either a mean reflection or coherence-based mask, is used as a base to mask the water. Specifically, regions of low coherence are also unwrapped which could lead to unwrapping errors. This would affect the accuracy of the deformation estimates. Therefore, a mask based on a coherence threshold is desired to filter out these unreliable regions. In the second approach this is accomplished by generating a mask based on the mean coherence, taken over the different time dimensions. To do this, a threshold of minimum coherence is set to 0.3, which has shown to achieve a reasonable balance between removing noise and preserving useful information and spatial coverage (Reinosch et al., 2020). Furthermore, the study by Xue Chen et al. (2020) discusses a comparative analysis of landslides, highlighted in Section 1.2, in which a coherence threshold of 0.3 yielded useful and consistent results. A drawback of this approach is that as a single mask is used for all the time dimensions, some pixels will never be considered. That is, even if some pixels have a higher coherence but the mean value does not, these pixels will also be discarded. In addition, in the same way, pixels that might be unreliable, e.g. low coherence, for certain time dimensions will be included.

An alternative is to generate individual masks for each interferogram based on the same coherence threshold, as employed in Approach 3. This would be desirable as, in this case, only the observations that are deemed reliable, in terms of meeting the coherence threshold criteria, are taken into consideration for each of the different interferograms. In other words, this approach allows for the use of temporary scatterers. However, this also means that in some cases there will be a solution for a certain pixel, while in other cases not. Hence, for each pixel the observation vector will be different and as a result so will the design matrix used for the inversion. The linear inversion process will, therefore, be based on a different number of observations for each pixel, which could be a problem if the estimation is only based on a single observation for instance. This complicates the linear inversion process. By setting a threshold based on the minimum number of observations for each pixel, this can be done. Each of the described masking approaches are considered such that the results can be compared.

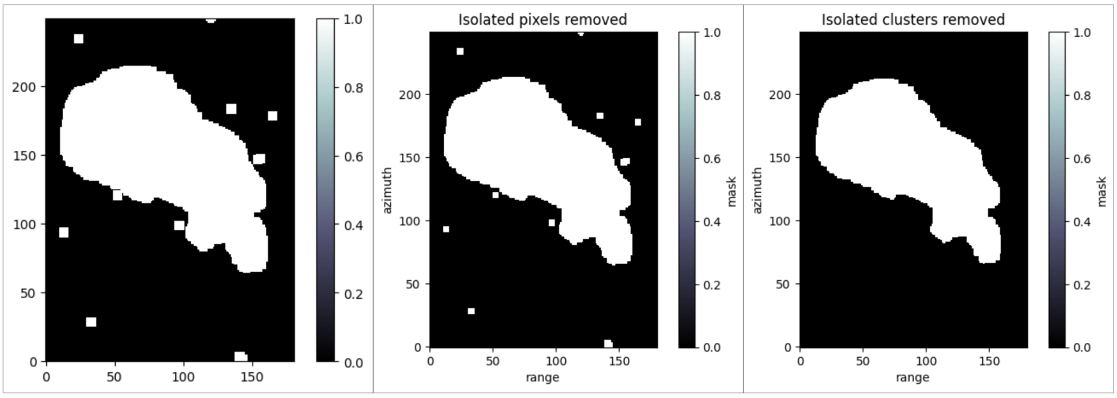

Edge Detection

Remove Isolated Pixels
< 3 neighbors

Remove Clusters
< 60 components

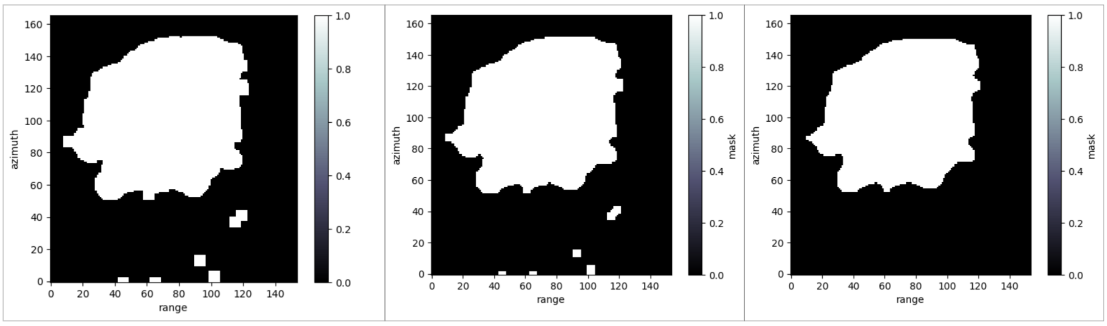

Edge Detection

Remove Isolated Pixels
< 7 neighbors

Remove Clusters
< 100 components

Figure 4.7: The coherence-based mask is generated with an edge detection algorithm (left). Resulting isolated pixels (middle) and clusters (right) can be removed based on maximum neighbor and connected components criteria, respectively.

In addition to a coherence-based mask, to account for unreliable regions based on decorrelation phenomena, there are still other potentially problematic regions that need to be identified before data interpretation. For example, a layover-shadow mask to account for the geometric distortion effects in elevated terrain is desired. To achieve such a mask, satellite orbit information, including the different incidence angles, and the DEM are required. In Van Natijne et al. (2022), a tool is developed in Google Earth Engine (GEE) for a world-wide InSAR sensitivity index. The sensitivity index is a geometric property and can be defined as a scale factor relating the downslope deformation to the change in the LOS range, observed through InSAR. Mathematically, it can be defined as the orthogonal projection of downslope deformation direction on the LOS of the radar. The shadow and layover effects are estimated using an algorithm based on the DEM and satellite orbits (Van Natijne et al., 2022). A low sensitivity index implies that the radar might have reduced effectiveness in detecting downslope deformation, potentially leading to unreliable deformation estimates. The tool relies on the exact Sentinel-1 orbital data, encompassing both the ascending (t164) and descending (t127) satellite tracks. Figure 4.8 illustrates the sensitivity index for variable terrain for the different Sentinel-1 tracks of Saba and St. Eustatius. It should be noted that flat terrain is denoted as no data. While this approach is directly applicable to the Sentinel-1 data, in the case of ALOS-2 data it offers insights into these effects. To improve the data interpretation of the results it is useful to consider these values.

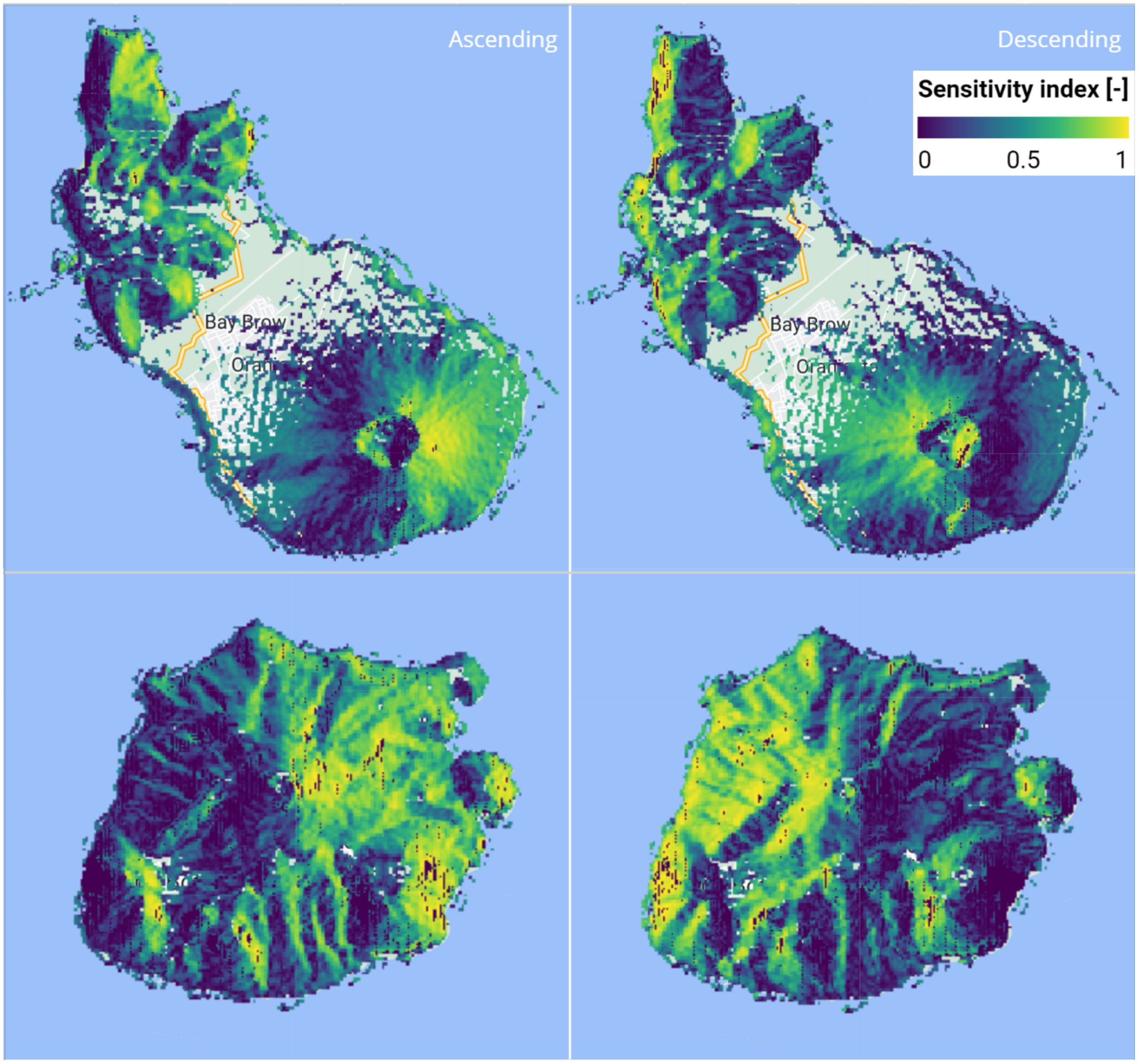

Figure 4.8: Sentinel-1 Sensitivity index for both the ascending (t164) and descending (t127) track. A low sensitivity index can indicate limited radar effectiveness in detecting downslope deformation. Flat terrain, e.g., the Kultuurvlake on St.Eustatius, is marked as no data. Source: Van Natijne et al. (2022).

Step 6: Phase Unwrapping

Thus far the phase information considered represents the wrapped phase. The interferometric phase is ambiguous and is constrained to the $[-\pi, +\pi)$ interval. However, to be able to translate phase values to topographic height values from an interferogram and produce deformation estimates, the unwrapped phase is required. Phase unwrapping is one of the most complicated steps in the data processing chain, yet a crucial part. The publicly available two-dimensional phase unwrapping algorithm SNAPHU will be used for this purpose. The SNAPHU technique as proposed by Chen and Zebker (2001), solves for phase unwrapping in a probabilistic framework, formulating it as a maximum a posteriori (MAP) problem. That is, the most likely unwrapped solution is found by maximizing the conditional probability of the phase-unwrapped solution using cost functions, given the observable input data. This input data refers to multiple data-sets, such as the wrapped interferometric phase, image intensity and the coherence.

Several user-defined settings exist within SNAPHU, allowing for improving the quality of the results. The minimum requirements include the wrapped phase input file as well as its line length. As SNAPHU unwraps everything, even when the coherence equals 0, a mask is required to avoid unwrapping errors as well as unnecessary computing. As described in the DORIS manual, the created masks can be used as weights to set the complex interferogram values to 0. These regions equal to 0 will still be unwrapped, however, the reliable areas will not be affected. As a result, aside from limiting the unwrapping issues, the process is also more efficient. Python is used as an interface to call SNAPHU, by running a command line through the os module.

Some of the user-defined parameters are set through the configuration file, including the path to input data: the coherence and wrapped phase. In addition, various statistical models exist relating the input data to the unwrapped phase solution, as this is dependent on the measured quantity. i.e., SNAPHU enables a selection of three built-in models for topography data, deformation data and, finally, smooth generic data. The model for deformation data can be set by enabling the 'DEFO' option in the configuration file.

The unwrapping procedure is repeated for all masking approaches described in the previous step. The quality of the unwrapped results can be validated by following and comparing the order of the changing colors across the different masking results. In addition, the occurrence of fringes in the wrapped phase can give an indication of the range of unwrapping values that can be expected. Overall the unwrapped phase results seemed to be consistent for the water masked and single masked results. In contrast, when using the individual masking approach some unwrapping issues are encountered. These issues are likely due to the location of the masked points. As a consequence, the connection between points is limited resulting in a badly resolved unwrapped phase. Therefore an alternative unwrapping approach is required for the individual masking. That is, after masking and before unwrapping the resulting gaps are filled using nearest-neighbor interpolation. This result is then unwrapped, after which the masks can be applied again, leading to consistent results.

To identify unwrapping issues, difference maps can be generated between the unwrapping results following the different masking approaches. In theory, if the unwrapping process was successful, the unwrapped results are expected to be around the same, thus resulting in 0, or at least a constant offset. If this is not the case unwrapping errors can be identified, for instance when only part of the island shows a constant offset. This can be useful to explain erroneous patterns in the unwrapping results. It is important to emphasize that this procedure is effective only if the error is not present in all the masking approaches.

Step 7: Linear Inversion

Now that the unwrapped phase values are estimated, the unknown SAR mother and daughter image phase values can be solved for, i.e. the cumulative deformation phase values. This can be done using a linear inversion technique, which involves generating a design matrix relating the interferometric phase values and solving a system of linear equations to estimate the unknown parameters. It should however be noted that the unwrapped phase values are a combination of contributions from different sources, such as atmospheric signal, while the goal is to identify the deformation signal. An approach similar to the one followed in (Tao et al., 2020) is considered. Ignoring possible atmospheric and topographic artifacts, the deformation phase, denoted $\delta\phi_i(r,x)$, for a pixel located at (r,x) for an unwrapped differential interferogram can be expressed as

$$\begin{aligned}\delta\phi_i(r,x) = \phi\left(t_B,r,x\right) - \phi\left(t_A,r,x\right) = -\frac{4\pi}{\lambda}\left[d\left(t_B,r,x\right) - d\left(t_A,r,x\right)\right], \\ i = 1,2,\ldots,M\end{aligned} \tag{4.1.6}$$

where $d(t_A,r,x)$ and $d(t_B,r,x)$ represent the LOS cumulative deformations at different times t_A and t_B with $(t_A < t_B)$ with respect to the t_0 epoch which is assumed as reference to avoid rank deficiency and to obtain absolute values rather than differences. For now, the difference in phase is considered, after the inversion the phase is converted to the displacement. Then the unknowns are a vector of size Nx1 of the LOS cumulative phase values $\phi^T = [\phi(t_1),...,\phi(t_N)]$, which in simple terms are the SAR image phases, with respect to t_0. For each of these images the sum of a total of three phase terms is estimated (Monserrat et al., 2009), represented as

$$\phi_i = \phi_{\text{defo}} + \phi_{\text{atmo}} + \phi_{\text{orb}}. \tag{4.1.7}$$

The observation vector of size Mx1 composes of the phase values $\delta\phi^T = [\delta\phi_0,...,\delta\phi_M]$ resulting from the unwrapped interferograms. The design matrix is of size MxN, missing one column with respect to t_0, and relates the different phase combinations. Hence, it consists of 0,1 and -1.

In accordance, a linear system of M equations in N unknowns for each pixel at location (r, x) can be derived and reorganized in matrix form

$$\delta\phi = A\phi. \tag{4.1.8}$$

The design matrix A is dependent on the set of M differential (unwrapped) interferograms and is generated based on the resulting pair selection. For example, if the first row represents the case where $\delta\phi_0 = \phi(t_1) - \phi(t_0)$ and the second row the case where $\delta\phi_2 = \phi(t_2) - \phi(t_1)$, this results in

$$\underset{M,N}{A} = \begin{bmatrix} 1 & 0 & 0 & 0 & \dots \\ -1 & 1 & 0 & 0 & \dots \\ \dots & \dots & \dots & \dots & \dots \\ \dots & \dots & \dots & \dots & \dots \end{bmatrix}. \tag{4.1.9}$$

Given the fact that InSAR is a relative technique, to measure relative displacement a spatial reference point, in addition to a reference epoch in time (t_0), is required. This reference point is typically arbitrary, but to improve data interpretation this point should ideally be a stable, i.e. non-deforming, location, as the displacement of a point is dependent on its value. However, in practice, this is often uncertain, making the selection of a reference pixel a challenging task. If any noise is present in the reference pixel, this will translate to all other pixels. Phase stability can be related to a high coherence as this indicates low phase variance. Therefore pixels with high coherence are considered to be good options. However, this does not give any indication regarding the height or deformation. Since the region around the airport, both for Saba and St. Eustatius, is assumed to experience no deformation based on the GNSS station, a coherent reference pixel is chosen near this location.

The system of equations can then be solved using least squares

$$\hat{\phi} = (A^T A)^{-1} A^T \delta\phi. \tag{4.1.10}$$

Depending on the small-baseline subset resulting from the pair selection, the system of equations can either be rank-full, when a single connected network exists, or rank deficient when multiple clusters of networks exist. In the latter case, $(A^T A)$ is a singular matrix, in other words the inverse does not exist. To still obtain an estimate for the unknown cumulative phase deformation, the singular value decomposition method (SVD) can be applied. Specifically, SVD is a matrix decomposition technique that allows to determine the so-called pseudo-inverse such that the linear system of equations can still be solved. The general idea is that a matrix is broken down into a product of three other matrices that are easier to work with

$$A = USV^T, \tag{4.1.11}$$

where U has a size of MxM and is referred to as the left-singular matrix of A, and V is of size NxN and is the so-called right-singular matrix of A. Furthermore, S is defined as

$$\underset{M,N}{S} = \begin{bmatrix} \Sigma & 0 \\ 0 & 0 \end{bmatrix}, \tag{4.1.12}$$

with

$$\Sigma = \operatorname{diag}(\sigma_1, \dots, \sigma_{N-L+1}), \tag{4.1.13}$$

in which $\sigma_1, \ldots, \sigma_{N-L+1}$ are the non-zero singular values of A and L represents the number of different SBAS subsets. Given that the pseudo-inverse of A is $A^+ = VS^+U^T$, then $\hat{\phi}$ can be estimated by

$$\hat{\phi} = A^+\delta\phi = VS^+U^T\delta\phi, \tag{4.1.14}$$

with

$$\mathbf{S}^+_{M,N} = \begin{bmatrix} \Sigma^{-1} & 0 \\ 0 & 0 \end{bmatrix}. \tag{4.1.15}$$

The result is affected by atmospheric noise, possible closure phase as well as other sources such as unwrapping errors, as explained in Section 2.2.1. To validate the deformation phase values it is crucial to identify these sources and account for them where possible. Therefore the residuals are considered. To do so, the adjusted observations ($\delta\hat{\phi}$) are determined by solving

$$\delta\hat{\phi} = A\hat{\phi}. \tag{4.1.16}$$

This result is then compared to the observations ($\delta\phi$) to obtain the residuals

$$\hat{e} = \delta\phi - \delta\hat{\phi}. \tag{4.1.17}$$

In theory, the residuals should equate to zero, i.e. since the network of interferograms are derived from SLC's, the unwrapped phase should form a closed loop. However, in practice, this is often not the case due to unwrapping errors or as a result of phase closures due to multilook averaging (Ansari et al., 2021). These different sources of error can be identified due to the significant difference in magnitude. The unwrapping error will be a multiple of 2π ($a * 2\pi$), however the error resulting from multilooking will likely be less than $\frac{1}{2}\pi$. This distinctive difference allows for the identification of the source of error. By plotting the residuals, spatial analysis can be performed. Nonetheless, the unwrapping error will be averaged out over the connected data pairs and therefore will not be exactly $a * 2\pi$ in the residuals.

To obtain a linear estimation for each pixel a line is fitted to the obtained deformation phase time series. To do so, least-squares is implemented again. In this case the unknowns consist of the offset (b) and the slope (m) for each pixel. Considering that the slope intercept formula is defined as

$$y = mx + b, \tag{4.1.18}$$

the design matrix consists of two columns and N rows, where the first column consists of 1's due to the constant offset and the second column of time, expressed in the number of days relative to the very first data set which will be set to 0. This leads to the following system of equations

$$\begin{bmatrix} y_1 \\ y_2 \\ \vdots \\ y_N \end{bmatrix} = \begin{bmatrix} 1 & t_1 \\ 1 & t_2 \\ \vdots & \vdots \\ 1 & t_N \end{bmatrix} \begin{bmatrix} b \\ m \end{bmatrix} + \begin{bmatrix} e_1 \\ e_2 \\ \vdots \\ e_N \end{bmatrix}. \tag{4.1.19}$$

This is then repeated for each pixel. In Figure 4.9 an example for one pixel of a fitted line to a time-series consisting of ten SAR images.

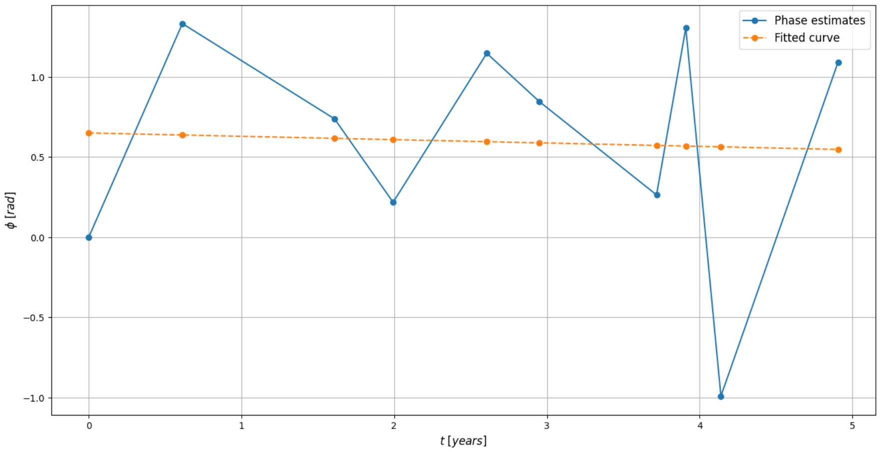

Figure 4.9: Example of a line fitting result for the estimated time-series of one pixel.

Step 8: Correction unwrapping errors

The correct estimation of phase ambiguities (phase unwrapping) is crucial for ensuring the reliability of the deformation time series. Given the magnitude of the unwrapping error, i.e., a multiple of 2π, the impact on the quality of the results is significant. Therefore, it is important to correct for the errors where possible. To achieve this, a deeper understanding of how an unwrapping error influences the least-squares results and translates in the residuals is necessary. In other words, such that the source of the error can be identified, i.e. the data pair containing the error as well as the extent of the affected region. Once the affected region is identified, necessary corrections can be applied.

To do so, a test case is considered using the Sentinel-1 SBAS network from track 127 where different SLC images from 2019 are selected and, based on their respective spatio-temporal baselines, combined into interferograms. An unwrapping error of 2π is simulated in one of the interferograms to analyze the impact on the residuals. First, a different number of interferometric data pairs have been examined to see whether the source can be identified in the residuals. It was found that the source could be successfully identified when considering at least four interferograms. When considering three interferograms the error was divided equally over these different data pairs and, therefore, undetectable. In the final test case considered, four different SLC images from 2019 are selected and combined into a total of six interferograms. The selected data pairs are illustrated in a baseline plot in Figure 4.10. The same processing steps, as described in this section, are followed. However, an unwrapping error of 2π is simulated and incorporated into a rectangular region within one of the (unwrapped) interferograms, as can be observed in Figure 4.11.

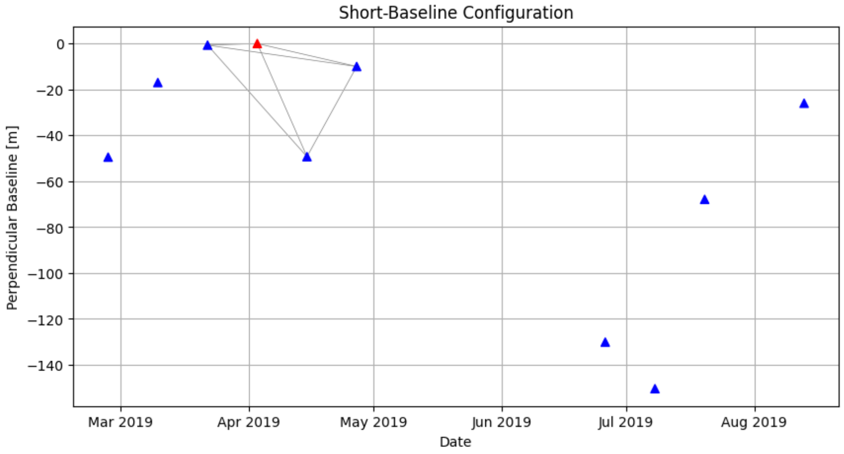

Figure 4.10: Simulation Unwrapping Error using six data pairs from the Sentinel-1 SBAS network.

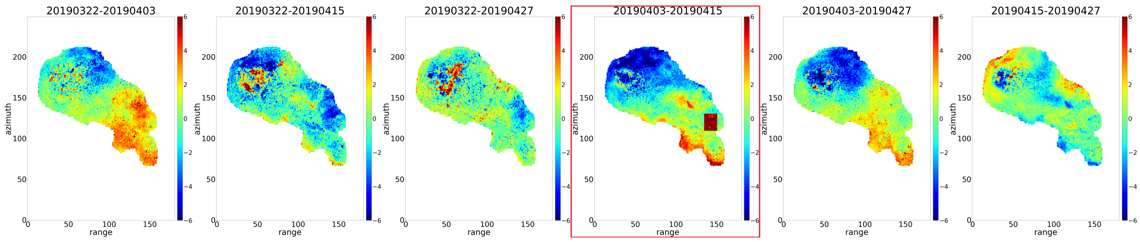

Figure 4.11: Simulation unwrapping error of 2π incorporated in rectangular region of the data pair indicated with the red bounding box.

In Monserrat et al. (2009) a phase unwrapping correction procedure is proposed in which a residual testing method is applied to correct for unwrapping mistakes. The method described involves an iterative procedure in which outlier candidates are selected based on a fixed residual threshold, starting with the maximum residual. The selected outlier candidate is then temporarily removed from the network, after which a new least squares estimation is performed. The new residuals are compared with the old residuals. If the residuals is within a given threshold, it is either re-sustained or rejected. This procedure is repeated until all outlier candidates are considered.

A drawback of using this approach is that when an observation is temporarily removed, the residual of that particular observation can also not be evaluated. As a result, only the residuals from the remaining time-dimensions of the same pixel can be compared to the old residuals. While these residuals are affected as well, the impact is not as significant. In addition, the rejection or re-sustainment of the outlier candidates is dependent on a user-defined threshold, which is undesirable due to its subjective nature. Theoretically, the residuals should eventually converge to zero without the presence of unwrapping errors. However, this will not be the case due to phase closures, which complicates the selection of a threshold. Therefore an alternative approach is considered where instead of temporarily removing the outlier candidates, the outlier candidates are corrected by either adding or subtracting 2π, depending on the sign of the residual. Then, the overall model test (OMT) is used to stop the correction for a certain outlier candidate.

Moreover, it is desirable to make the process as efficient as possible. Therefore an alternative approach is considered that aims to correct for all outlier candidates in a single step, rather than using an iterative approach like proposed by Monserrat et al. (2009). However, to do so the unwrapping error pattern needs to be identified. Notably, unwrapping errors manifest as isolated 'islands' within the data. In addition, the knowledge obtained regarding the detection of the error source using a test case can be used to identify the data-pair containing the unwrapping error. The complete procedure is tested and verified using the test case as described in the beginning of this step. The procedure contains three steps: identification of the data-pair containing the unwrapping error, identification of the error region and the residual testing. In addition, a similar method to Monserrat et al. (2009), in which the outlier candidates are temporarily removed, is applied for comparison. The user-defined threshold is based on the sum of the old residuals, excluding the residual of the epoch containing the error, in comparison to the new residuals where the observation is removed. The outlier candidates and the epoch containing the unwrapping error are identified by the procedure outlined below.

The testing approach follows the structure of the so-called Detection, Identification and Adaptation (DIA) procedure (Teunissen, 1990). As the name suggests, the first step involves detecting the presence of an error, followed by identifying/locating the erroneous pixels and, ultimately, the final step revolves around adapting the error. The procedure is as follows. The overall model test (OMT) statistic is used to detect the presence of an error and is evaluated for the original residual values ($\hat{e}_0^T$), by

$$T_{q=m-n} = \hat{e}_0^T Q_{yy}^{-1} \hat{e}_0. \tag{4.1.20}$$

Currently, the identity matrix I is used as the covariance matrix Q_yy, hence, indicating a variance of 1 rad^2. However, ideally the covariance matrix would be based on the data precision, e.g., using the coherence. This aspect should be a focus for future work. The null hypothesis (the nominal model, providing the estimation) is sustained if

$$T_{q=m-n} < K_{\alpha}, \tag{4.1.21}$$

where K_{α} is the critical value and is extracted from the Chi-square distribution table for a given level of significance α and the degrees of freedom $q = m - n$. m represents the number of observations, while n represents the number of unknowns.

Then, 2π is added or subtracted to each pixel (adaption), depending on the sign of the phase value, and least-squares is applied again. The new residuals are determined and compared and the OMT can be calculated again to update the condition. The procedure is repeated until the OMT is sustained for each outlier candidate and all errors are corrected for or until a maximum number of iterations is reached. Once the condition is met for a specific pixel, the final result for this pixel will not be updated anymore. In addition, if the null hypothesis already was sustained before adding/subtracting 2π, the pixel is also not corrected. For the identification, residual testing is considered i.e., the new residuals compared to the old. Another option is to use the w-test rather than the residuals. Since it is assumed that the observations are uncorrelated ($Q_{yy} = I$), the equation for the w-test is simplified to

$$w = \frac{\hat{e}_{i0}}{\sigma_{\hat{e}_{i0}}}, \tag{4.1.22}$$

where $\hat{e}_{i0}$ is the residual value and $\sigma_{\hat{e}i0}$ represents the diagonal of the Q_{ee} matrix, which follows from

$$\begin{aligned} Q_{\hat{x}\hat{x}} &= (A^T\, Q_{yy}\, A)^{-1}, \\ Q_{\hat{y}\hat{y}} &= A\, Q_{\hat{x}\hat{x}}\, A^T, \\ Q_{\hat{e}\hat{e}} &= Q_{yy} - Q_{\hat{y}\hat{y}}. \end{aligned} \tag{4.1.23}$$

Hence, as neither the design matrix A nor Q_{yy} change and as a consequence neither does $\sigma_{\hat{e}_{i0}}$, the only difference is that the residuals are scaled. Therefore, from a computational point of view, it is more efficient to directly consider the residuals.

The resulting effects of this approach as well as the one similar to Monserrat et al. (2009), are visualized by plotting the estimated deformation phase values for one epoch using the two different approaches. The original result, still containing the simulated (rectangular) error, next to the corrected results can be seen in Figure 4.12. The results reveal that for the approach similar to Monserrat et al. (2009) (middle figure), the erroneous pattern can still be recognized. However, the phase values are significantly lower compared to the original results (left figure). The error does not appear in the other residual testing approach anymore (right figure).

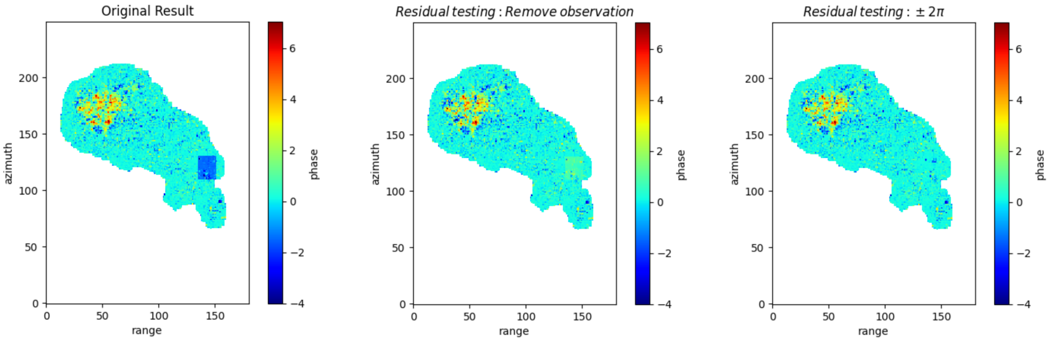

Figure 4.12: Simulation Unwrapping Error - Original result (left), approach comparable to Montserrat, 2009 (middle), residual testing approach (right).

To avoid iterating through each pixel in the dataset, a two-step pre-selection approach is implemented in which the data-pair containing the (potential) error is detected and the (potential) outlier candidates are identified. The outline of this identification and detection procedure is depicted in Figure 4.13. Details regarding these steps are provided below.

- **Detect the data-pair containing the (potential) unwrapping error**

  To identify the source of the unwrapping error i.e., the interferogram containing the maximum error, the phase residuals are analyzed locally. The residual data, which should be zero without unwrapping errors and phase closures due to multilooking, for each of the data-pairs is divided into regular patches, according to a user-defined window size. The aim is to find the patch for which all the corresponding pixels have an unwrapping error. To do so, the mean is computed over the residuals within each of the spatial patches for every data-pair. For each data-pair the patch with the maximum mean value is determined, after which these mean values are compared across all data-pairs (epochs). The epoch with the maximum mean patch is selected.

- **Identify the (potential) error region**

  In this step the potential outlier candidates (error pattern), within the detected epoch, are identified. Initially, the error pattern was detected by setting the closest integer of the mean of the maximum patch, found in the previous step, as a threshold. The residuals above this threshold are then selected as outlier candidates. It was found, when doing so, that the simulated rectangular error was detected for the most part. To get the complete rectangle however, the standard deviation of the residuals of the detected epoch (previous step) is considered and subtracted from the original threshold. This leads to the detection of the full rectangle, as can be observed in Figure 4.14. The remaining detected pixels are mainly concentrated around the crater, which can be expected as this is where most of the decorrelation occurs. As a result, the sparse number of remaining pixels after coherence-based region masking are likely not properly resolved in the phase unwrapping step.

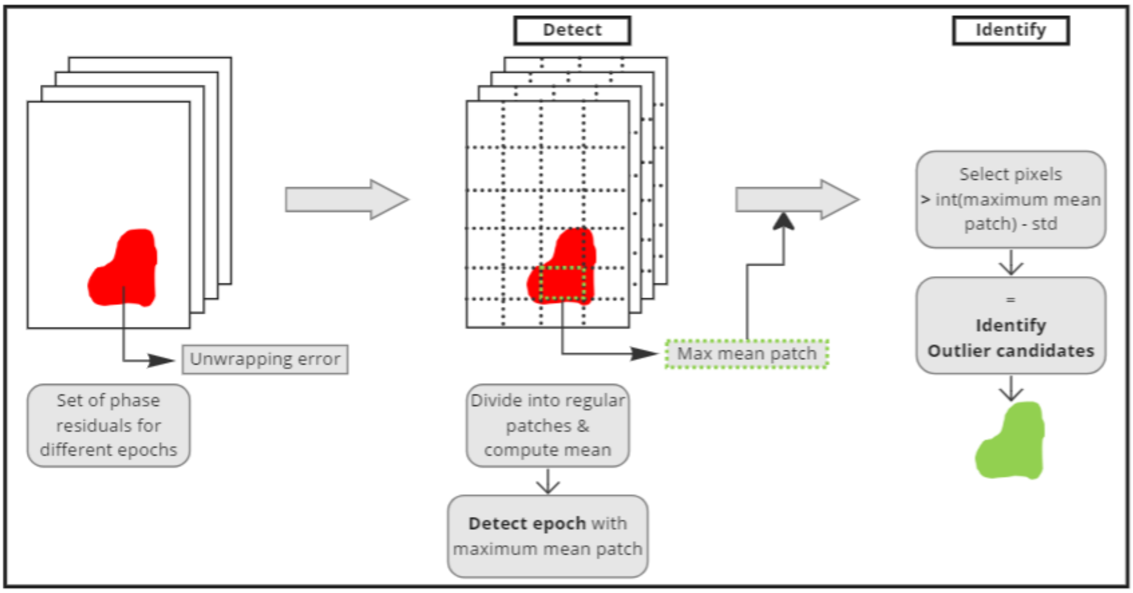

Figure 4.13: Illustration of the automated detection and identification procedure. In this sketch, an unwrapping error occurs in the first interferogram of the stack. The spatial patches are user-defined and the standard deviation (denoted 'std' in the figure) refers to the residuals of the detected epoch.

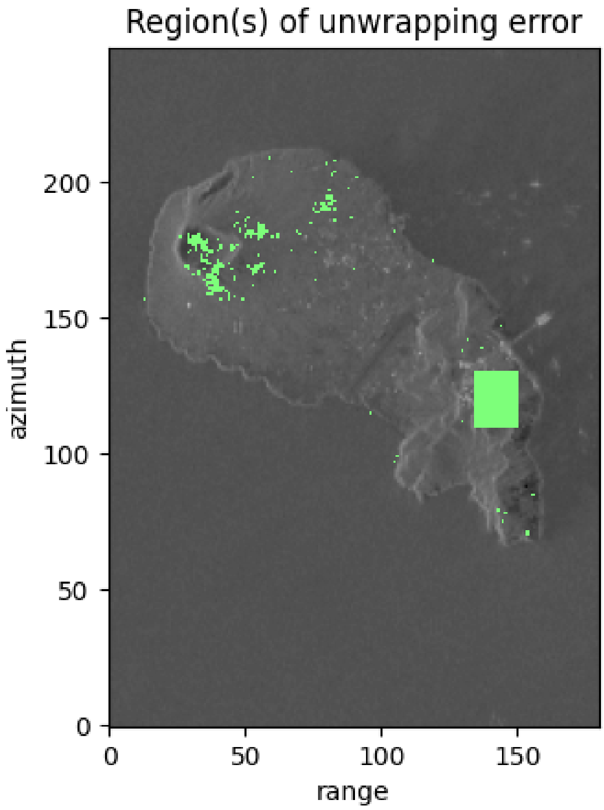

Figure 4.14: Automated identification of the (simulated) error region, indicated by the green pixels. The erroneous rectangle is successfully detected. Additionally, several pixels are detected in close proximity to the crater, which are expected to be strongly affected by decorrelation.

Alternatively, rather than an approach based on a spatial pattern, the data-pair containing the unwrapping error could potentially be identified by simply looking at the residual values, i.e., by summing the residual values along the columns of each of the time dimensions. Then, the histogram of the residuals can be plotted and peaks can be identified. Specifically, the presence of one prominent peak located around zero (see step 7), with minor deviations due to multilooking errors, is expected for the properly resolved unwrapped phase. In case of an unwrapping error, another smaller peak is expected. If these peaks are indeed distinctive, a threshold can be set to detect the error region. This approach could be more robust i.e., it is not sensitive to the choice of the user-defined window size for the generated patches. However, the success of this approach is highly dependent on the presence of distinct peaks and is explored in the results in Section 5.2.

Step 9: Output generation

The main output entails the estimated deformation time-series and velocities. In addition, other outputs, including the residuals, spatial and temporal coherence, are essential to assess the quality of the estimates. To geocode the results, the latitude and longitude binary output files from DORIS are used. Due to the multilooking step, the latitude and longitude results need to be averaged accordingly. In addition, a grid in radar coordinates is used to store the latitude and longitude values. Therefore, it is necessary to perform interpolation and resampling to a regular grid in latitude and longitude coordinates. Considering the data size, to limit computation time a nearest-neighbor (NN) interpolation method is opted for. This choice has reduced the computation time compared to, e.g., inverse distance weighting (IDW). For each regular grid cell, the indices of the irregular grid points that fall within this cell are used. If multiple data points are present within the same regular grid cell, the average is taken. To limit the computation time a K-D tree, a space-partitioning data structure, is used to enable fast NN queries. To present the outputs in a convenient manner, the results are exported as GeoTIFFs.

4.1.3 Challenges

Throughout the development stage a variety of technical challenges were encountered. Initially, a common issue was related to memory allocation as a result of the large data structures used or simply insufficient available memory. These could largely be solved by considering an HPC environment and parallel computing. However, some of these memory errors arose when using the SarXarray package and were not necessarily related to the available memory, but rather to incorrect loading of the data. This could be attributed to a variety of different issues, such as the data type specified, the set path to the input data and the data shape. The error was not raised when loading the stack but only after printing or plotting the values.

Overall, it could be challenging to find efficient approaches to execute different steps in the algorithm. The usage of dictionaries was found to be an efficient and effective approach, e.g. to keep track of the selected pairs in terms of their respective index such that the interferograms, corresponding coherence and the design matrices could be generated accordingly. Another example which illustrates the efficacy of using dictionaries, is related to the individual masking approach. In this case, an alternative approach is required for the linear inversion step. Specifically, for each pixel different time dimensions are included and, therefore, both the observation vector as well as the design matrices are different. Hence, in contrast to the water mask and single mask approach, this computation cannot be performed in a single step for all pixels. To still limit the computation time, the unique matrices are determined and clustered. For each unique matrix, the corresponding indices of the original complete set of matrices (and thus of the observation vector) is stored in a dictionary, such that the correct design matrix is assigned to the corresponding observation vector. In the most significant case, this reduced the number of computations by a factor of ~ 10 (35625 to 3483). This translates to a reduction in computation time of 18.82 to 0.23 s, while maintaining consistent conditions. Given that this particular code is repeated following the correction of the unwrapping errors, the cumulative impact becomes more substantial. In terms of the masking approach in general, due to the absence of a sharp boundary between land and water in the DEM, especially in the case of St. Eustatius, different approaches were considered. For example, using amplitude information, i.e. the mean reflection map, or phase information. Ultimately, the application of an edge detection algorithm to the coherence values yielded promising results. However, this approach also raised difficulties, notably, the presence of isolated pixels as well as clusters of pixels in the water. Additional measures were required to remove these.

In addition, due to phase closures as a result of multilooking, the selection of a threshold to detect the unwrapping error is challenging. That is, without multilooking the residuals should be zero and the identification of unwrapping errors would be more straightforward. Therefore, it is difficult to automatize the selection of a threshold.

4.2 DePSI

The DePSI algorithm composes a main script for the processing steps, called 'depsi.m', and a routine for implementing additional filtering procedures, called $'depsi\_post.m'$. The main script executes the nine processing steps, outlined in Section 2.2.2, while the $'depsi\_post.m'$ script allows for locally filtering the results. In previous work, the main script has already been applied to the available data and, therefore, the $'depsi\_post.m'$ routine is of interest to set user-defined thresholds. Thresholds can be set for the temporal coherence, the local temporal coherence and the spatio-temporal consistency. Depending on the selected thresholds, the PS density can differ significantly. Consequently, the aim is to maximize the PS density, while filtering out unreliable PS.

The output is dependent on the selected options within $'depsi\_post.m'$ and can include spatial plots and histograms of the amplitude dispersion, ensemble coherence and spatio-temporal consistency. Furthermore, plots are generated of the removed points, enabling visual assessment of the selected thresholds. The final results are saved using both a binary format and comma-seperated values (csv) to facilitate analysis within GIS software and with other (geodetic) measurements. In addition, an interactive environment is available in which points can be manually removed, if desired, or to visualize the time series of the final PS.

5 Results

This chapter begins with an examination of the expected deformation on Saba and St. Eustatius using GNSS data in Section 5.1. The results obtained through the SBAS approach are then presented in Section 4.1 and for the PSI approach in Section 5.3. The algorithm is applied to the available Sentinel-1 tracks as well as the ALOS-2 paths (described in Section 3.2). In addition, for SBAS, the different masking approaches are compared.

5.1 Validation: GNSS

To gain insight into the current expected deformation in the area of investigation, ground truth data obtained from the GNSS stations on the islands (location indicated in Figure 3.9a and Figure 3.9b) are considered. GNSS is an absolute positioning technique within a geodetic reference system. In order to compare the results with InSAR, some additional processing steps are required beyond what was performed by NGL. Specifically, considering that InSAR is a relative technique, the horizontal displacement as a result of plate tectonics is not visible in InSAR measurements since the whole island is affected. Consequently, a stable reference point is missing. Therefore, GNSS is made relative, to allow for comparison with InSAR. One of the GNSS stations is used as a reference station for each island such that the horizontal displacement cancels out. For both islands, the station nearest to the airport is selected. For Saba, this is the station denoted by 'SABY', while for St. Eustatius the station is denoted by 'SEUS'. As a result of this, the seasonal effect is subtracted as well. Furthermore, outliers are removed, the measurements are taken relative to the median, which was set to zero, and a rolling mean is evaluated to be able to follow the overall trend over the years. Finally, given that the GNSS stations were deployed at different time instances, some stations have longer recorded time periods than others. Therefore only those time instances that exhibit overlap across all four stations are taken into account.

The three resulting components, North-South, East-West and the vertical, are visualized in Figure 5.1 and Figure 5.2 for Saba and St. Eustatius respectively. It can be observed that the current deformation is stable overall with about a cm noise level in the vertical direction, as can be seen in the first row of both figures, and approximately 5 mm horizontal noise, as shown in the middle/bottom panels.

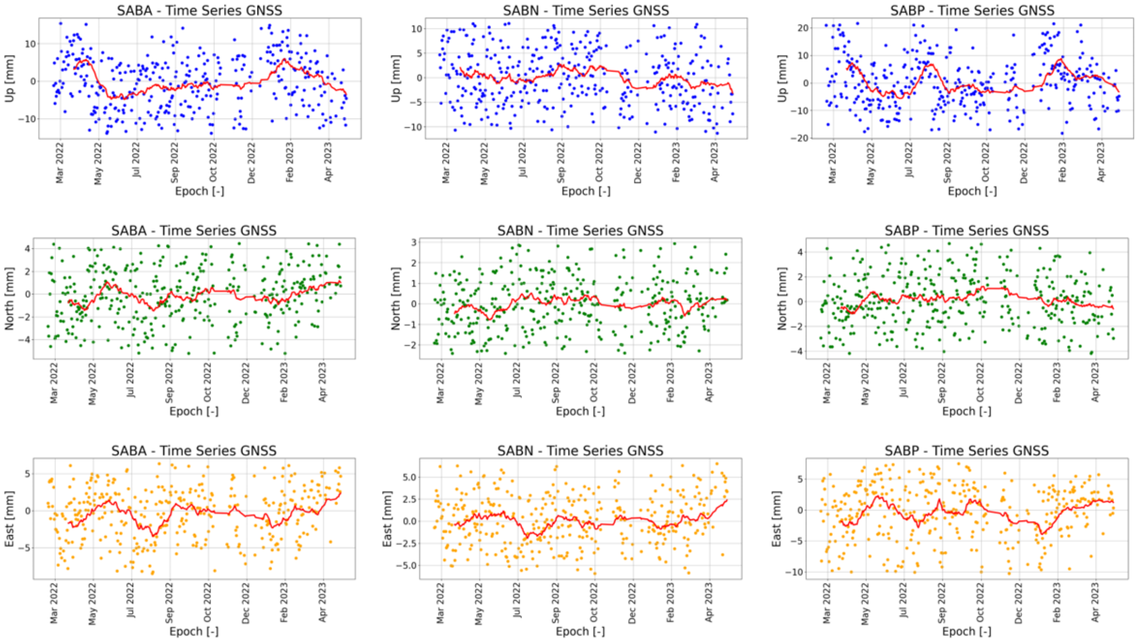

Figure 5.1: Saba GNSS data using Station 'SABY' as reference station. Top row shows "Up" component, middle row the "North" component and bottom row the "East" component.

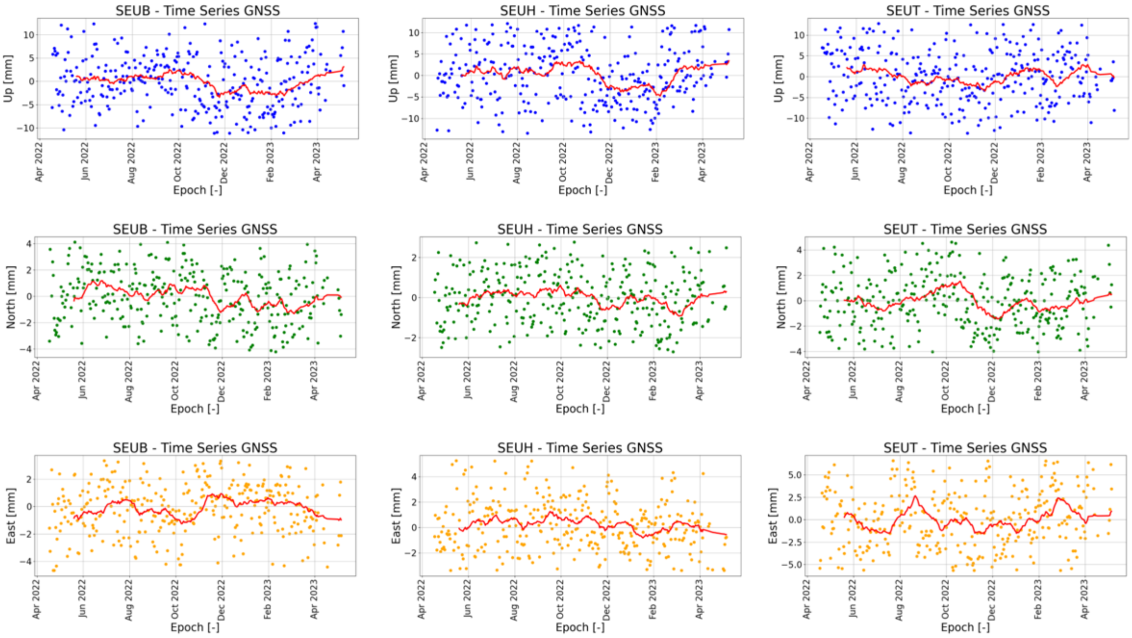

Figure 5.2: St. Eustatius GNSS data using Station 'SEUS' as reference station. Top row shows "Up" component, middle row the "North" component and bottom row the "East" component.

5.2 SBAS

In this section, the results from the SBAS approach are presented. Subsection 5.2.2 discusses the ALOS-2 results, while Subsection 5.2.1 focuses on the Sentinel-1 results. The intermediate results, following from the processing steps, are first considered. This is followed by the final results, i.e., the estimated deformation time-series and velocities.

5.2.1 ALOS-2

Intermediate Results

After loading the data sets into a xarray.dataset in Python, the first step is the selection of data pairs based on the modeled coherence approach, as described in Section 4.1. Due to the limited availability of ALOS-2 data, the number of data pairs combined according to the short-baseline configuration result in over 40 unique pairs. This is significantly less compared to Sentinel-1. After the selection procedure, in which the parameters are fine-tuned using actual coherence values, over half of the data pairs remain, as illustrated in Table 5.1. The proportion of data pairs that remain for ALOS-2 relatively high, which is a promising outcome. In addition, it is noteworthy that none of the data sets exhibit any data gaps, as can be observed from the baseline plots in Figure 5.3.

	St. Eustatius		**Saba**
ALOS-2	**Path 37**	**Path 36**	**Path 37**
Original Pairs	45	55	45
Selected Pairs	29	32	29

Table 5.1: ALOS-2 - The unique number of data pairs versus the selected pairs following the selection procedure using the third approach. Both paths are ascending.

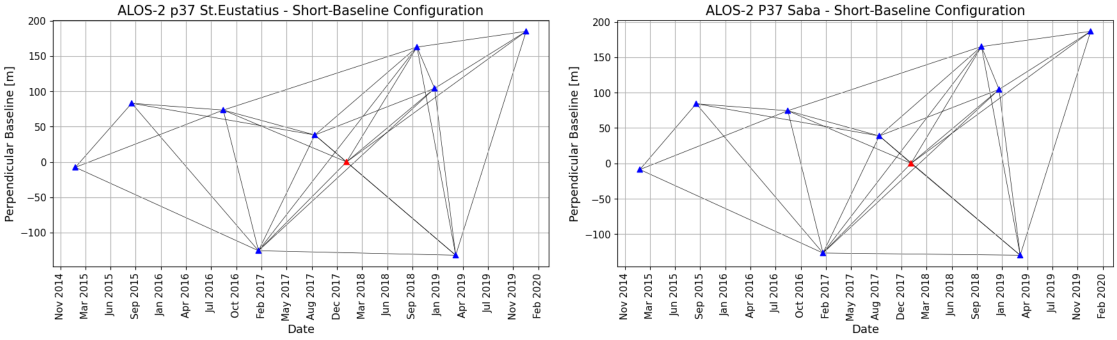

(a) ALOS-2 Path 37 St. Eustatius.

(b) ALOS-2 Path 37 Saba.

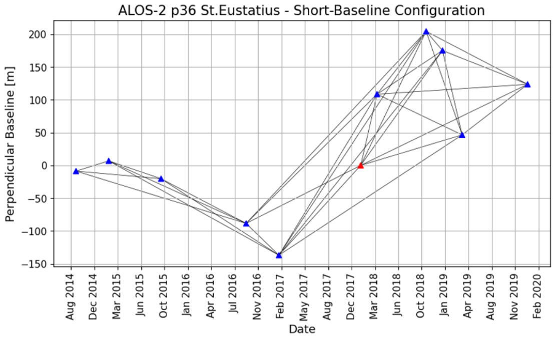

(c) ALOS-2 Path 36 St. Eustatius.

Figure 5.3: Short-baseline configuration plots. The red triangle represents the original mother SLC in the single-mother configuration.

The interferograms and corresponding coherence are obtained accordingly. The coherence has been analyzed in a so-called 'coherence matrix', to assess the change in coherence depending on the temporal baselines. In other words, the interferograms are ordered in time per SLC for each row and column. The diagonal is left empty, since an interferogram between the same SLC does not exist. Considering the fact that a larger temporal baseline typically leads to increased decorrelation, it is expected that the coherence is higher along the diagonal as the columns next to each other are closer in time. The resulting coherence matrix for Path 37 for St. Eustatius is visualized in Figure 5.4. As expected, the coherence increases with decreasing temporal baselines and the data pairs with higher coherence are located closer to the diagonal. The discarded data pairs are indicated with red rectangles in Figure 5.4 and are situated along the outer boundaries of the matrix.

Figure 5.4: ALOS-2 St. Eustatius Path 37 coherence matrix. The discarded data pairs are highlighted with red rectangles.

Multilooking is performed using a window size of 24:14 for the data of Path 37 for both St. Eustatius and Saba, to reduce noise and to limit computation time on account of the size of the acquired scene. For Path 36 St. Eustatius a window size of 12:7 is considered, as a window size of 24:14 did not appear to show reliable results on account of the unrealistic high variability of the estimated deformation velocities. To achieve the latter the Path 36 data set is also run using an HPC environment, as is done for Sentinel-1. This is because, with a window size of 12:7, the unique matrices calculated in the individual masking result in over 28,000 iterations, which is too computationally heavy to run locally. As a result of multilooking, the stochastic noise decreases and phase estimation improves. However, the spatial resolution is affected. The effect of reduced noise and decreasing spatial resolution is illustrated using Figure 5.5 for a subset of Path 36, such that the different window sizes can be compared. An increasing window size leads to a decreased spatial resolution, resulting in a noticeable loss of detail in the interferograms in the bottom row. This complicates the detection of small-scale deformations and could potentially lead to signal loss.

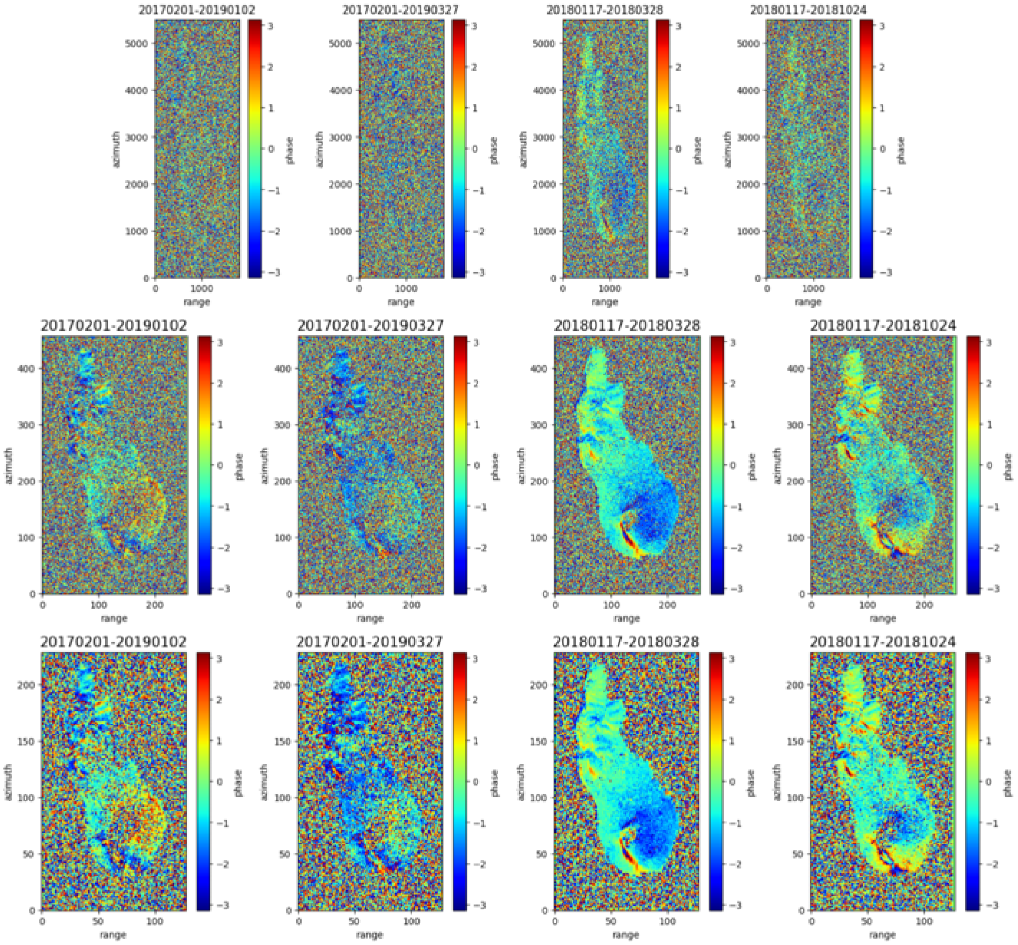

Figure 5.5: ALOS-2 Path 36 St. Eustatius - The effect of multilooking on the original interferograms (top row), using a window size of 12:7 (middle row) and 24:14 (bottom row).

The coherence-based masks are generated for the different paths and are visualized in Figure 5.6a and Figure 5.6b, for Saba and St. Eustatius Path 37, and in Figure 5.6c for St. Eustatius Path 36. For the individual masks, only the masks for the data pairs with the smallest and largest temporal baselines are displayed. The complete set of masks can be found in the appendix. A coherence threshold of 0.3 is applied to both the single and individual masks. The results reveal that the single mask approach (left column) includes considerably fewer pixels compared to the individual mask with the smallest temporal baseline (right column). The individual mask corresponding to the largest temporal baseline (middle column) shows the opposite, suggesting that not all pixels encompassed by the single mask may be reliable across all epochs. This shows promise for the individual masking approach. However, to avoid an under-determined system in the linear inversion step, an additional threshold will be set to only consider those pixels in the individual masks with at least the same number of observations as unknowns. In addition, for both islands it appears that the region surrounding the volcano exhibit lower coherence. This could be expected due to the steep slopes and dense vegetation cover. Consequently, with the exception of few isolated pixels, for Saba the area around the summit of Mt. Scenery on Saba is masked. For St. Eustatius, a comparable pattern can be observed with the single masking approaches, however, to a lesser degree. Since SBAS considers the spatial relationship between pixels in the phase unwrapping step, the unwrapped phase values of isolated pixels on the summit are unreliable. In the case of Saba, merely the outer flanks of the volcano remain for both masking approaches. Regarding St. Eustatius, the single mask approach also excludes substantial portions of the volcano flanks. The specific side of the flank being masked likely follows from the side-looking geometry. Specifically, both paths are ascending and the eastern part of the flanks in Figure 5.6b and Figure 5.6c (left) is masked. In contrast, the spatial coverage achieved with the individual masking approach for small temporal baselines is significant and extends to nearly the entire island. Finally, when considering the shape of the mask for Saba, sharp edges can be observed at the eastern side of the island. This is particularly apparent for the individual mask with smallest temporal baselines (right most image in Figure 5.6a). Around these edges gullies exist, which are deep channels resulting from streams. These features could possibly explain the occurrence of the edges. However, the edges seem too sharp to be a result of natural phenomena and might be a processing artifact, also considering the fact that for Sentinel-1 these edges are not visible.

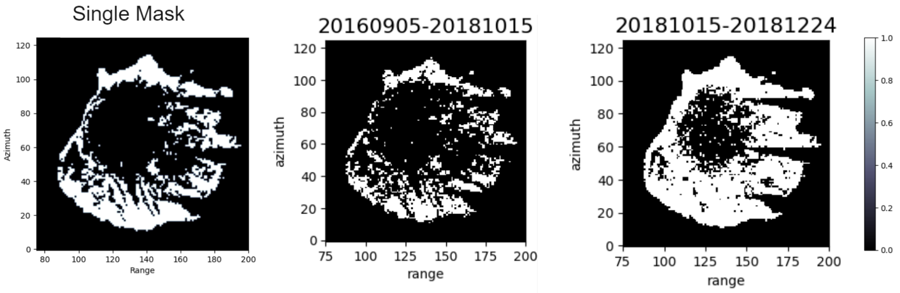

(a) ALOS-2 Path 37 Saba.

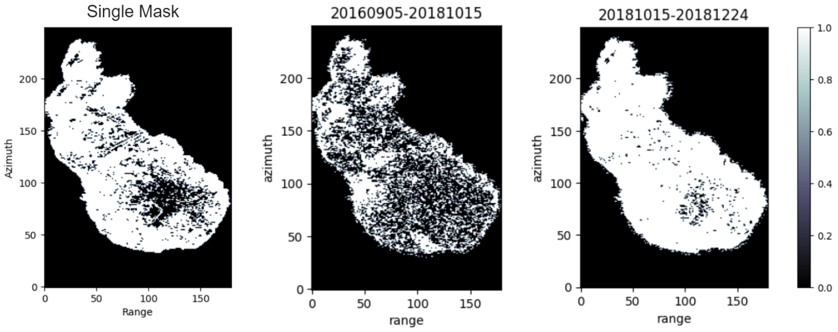

(b) ALOS-2 Path 37 St. Eustatius.

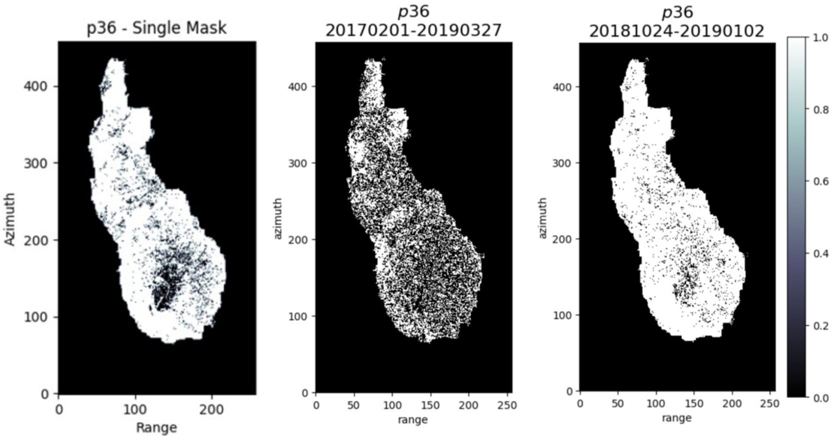

(c) ALOS-2 Path 36 St. Eustatius.

Figure 5.6: Single mask approach (left) compared to the individual masks for the largest temporal baseline (middle) and smallest temporal baseline (right). The masks are binary, selected pixels are assigned a value of 1.

In Figure 5.7, the original wrapped phase is followed by the unwrapped results for each of the masking approaches for an example data pair of ALOS-2. Considering that currently no deformation is expected, fringes are absent in the wrapped result and values near zero are expected for the unwrapped results. During the phase unwrapping procedure some difficulties arose in the individual masking approach, as described in Section 4.1. For the individual masking approach, the original approach is shown along side the improved solution, following the nearest-neighbor interpolation approach.

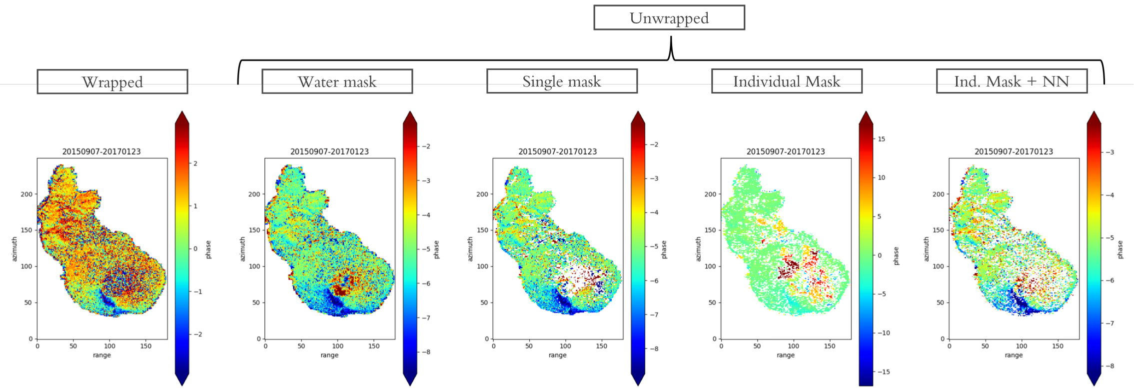

Figure 5.7: ALOS-2 - Wrapped phase result followed by the unwrapped phase results for the masking approaches. The individual masking approach leads to inconsistent results on account of areas with limited pixel connection. This is solved by applying a (nearest-neighbor) interpolation before unwrapping (right).

On account of the relative nature of InSAR measurements, the selection of a spatial reference is crucial, as explained in Section 4.1. i.e., any noise in the reference pixel translates to all pixels. The airport is focused on, as this location is assumed to be relatively stable for both islands. Using the mean coherence, averaged along the different time dimensions, a high coherence pixel can be selected. An example of this approach is presented in Figure 5.8a.

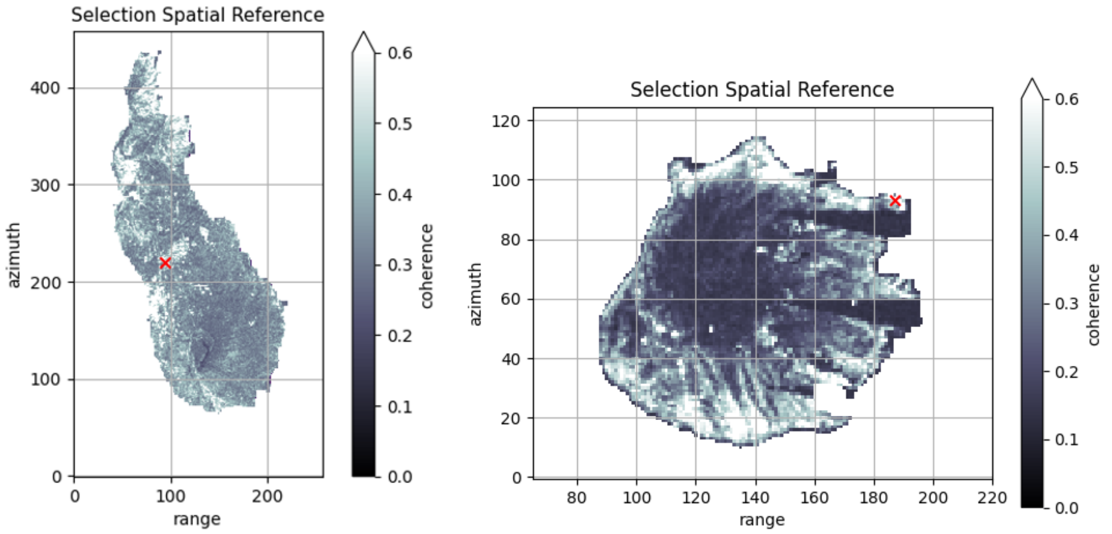

(a) ALOS-2 p36 St. Eustatius.

(b) ALOS-2 p37 Saba.

Figure 5.8: The selection of a spatial reference point, indicated by the red cross. The reference pixel is selected near the airport, as this location is assumed to be stable (non-deforming), at a high coherence pixel using the mean coherence map.

Final Results

After acquiring the unwrapped phase, the linear inversion step can be applied and deformation estimates can be derived. The linear deformation estimates are expressed in mm/year and, as concluded from the GNSS results in Section 5.1, current deformation at the islands is expected to be minimal. Hence, deformation values near zero are expected. Assuming that there is no deformation currently, the standard deviation gives the spread of the signal around zero and can be used for the precision. It is important to emphasize that the results are relative to the selected spatial reference pixel and, as such, cannot be interpreted in absolute terms. In addition, when interpreting the results, it is important to consider that the DEM error is not estimated and that an atmospheric correction has not been applied. The atmospheric effect can lead to inaccuracies in the deformation estimates, demanding careful consideration when interpreting the data. Therefore, the primary focus is on the consistency (see Subsection 1.3) of the results, e.g., the identification of specific areas experiencing significant changes over time, rather than relying on the numerical values of the deformation estimates. Histograms are used to visualize and understand the statistical distribution of the estimates and for the identification of outliers. Under the assumed conditions of no deformation, the histogram should reflect this with a central peak around zero and minimal variability. The degree of variability can be assessed through the standard deviation. Geometric distortion effects must also be recognized to assess the reliability of certain displacement estimates. Finally, negative LOS displacement indicates movement towards the satellite and thus uplift.

The linear deformation estimates for Saba, specifically Path 37, are depicted for the different masking approaches in Figure 5.9, i.e., the water mask (top row) as well as the single (middle row) and individual (bottom row) masking approaches respectively. The masking approaches instantly prove to be crucial in the calculation of deformation estimates. Namely, when comparing the different approaches, the one without mask shows significant changes at multiple locations as well as sudden jumps. The histogram in Figure 5.9b is somewhat skewed and the highest peak is not centered near zero, but rather is located between 5-10 mm/year. Furthermore, some outliers are observed reaching magnitudes up to 40 mm/year. This is not realistic and this result appears to mainly show noise. These findings align with the description in Section 4.1, that is to avoid unwrapping mistakes, incoherent regions should be excluded.

When comparing the other masking approaches, it can be observed that most values are centered at or around zero. Generally, it seems that a consistent pattern occurs for both approaches, as can be seen in Figure 5.9c, Figure 5.9e and the respective difference map in Figure 5.10. Specifically, a trend can be observed across the island. The values with somewhat higher magnitudes are primarily located near locations with a low sensitivity index in Figure 4.8 and may be a result of the layover effect. Although this figure is for the Sentinel-1 tracks, the affected locations are assumed to be comparable for ALOS-2. However, a difference that immediately stands out, is the extent of the outliers. The histogram in Figure 5.9f, shows outliers exceeding a magnitude of 125 mm/year. This could possibly be explained by the isolated pixels found around the summit of the volcano. These pixels are deemed unreliable as they are not connected to any of the other points in the SBAS network and hence the phase unwrapping procedure fails to unwrap these properly. However, these isolated pixels also cause high magnitude values in the single masking approach and therefore this does not explain why the values are considerably larger for the individual masking approach. It could be that these outliers stem from pixels that are selected in only a few epochs, resulting in using a relatively low number of observations for velocity estimation, thereby exposing them to the full effect of the atmosphere component and DEM errors. However, given that only pixels with an equal number of observations and unknowns are taken into account, this effect is not expected to be this significant. Another reason could be the fact that the singular value decomposition (SVD) method is considered for some pixels in the individual masking approach. This because of the variable structure of the design matrix, which may lead to singular matrices. As explained in Section 2.2.1 the SVD method could introduce large discontinuities, which could explain the susceptibility of the individual masking approach to outliers. When examining the histogram in greater detail in Figure 5.9g and by considering the standard deviation of the estimates as presented in Table 5.2, it can be seen that the distribution is similar to Figure 5.9d, both closely resembling a Gaussian distribution, and that overall mm order precision is acquired using both approaches. Considering the limited data availability and the notably larger revisit time compared to Sentinel-1, these are promising results.

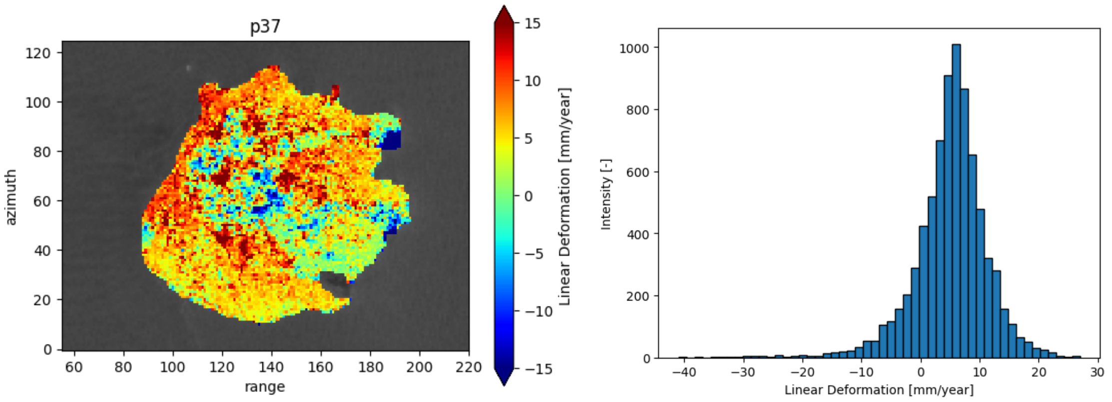

(a) Water mask.

(b) Water mask histogram.

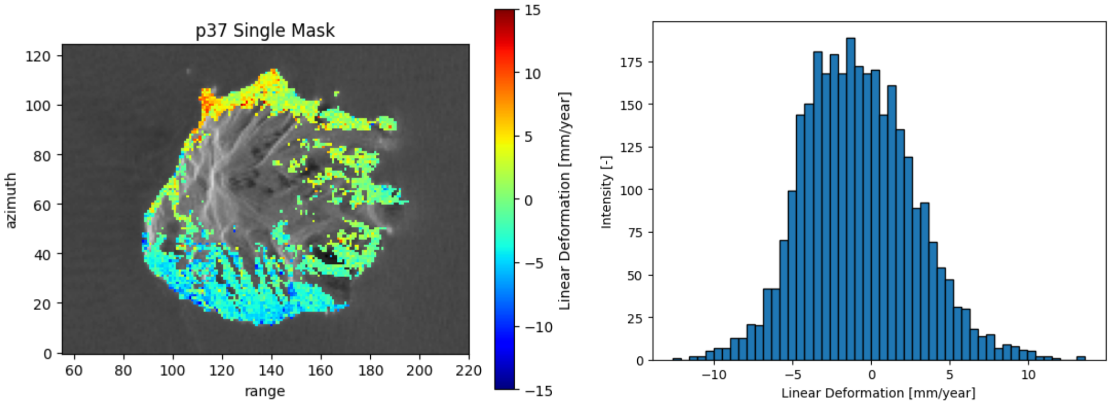

(c) Single mask.

(d) Single mask histogram.

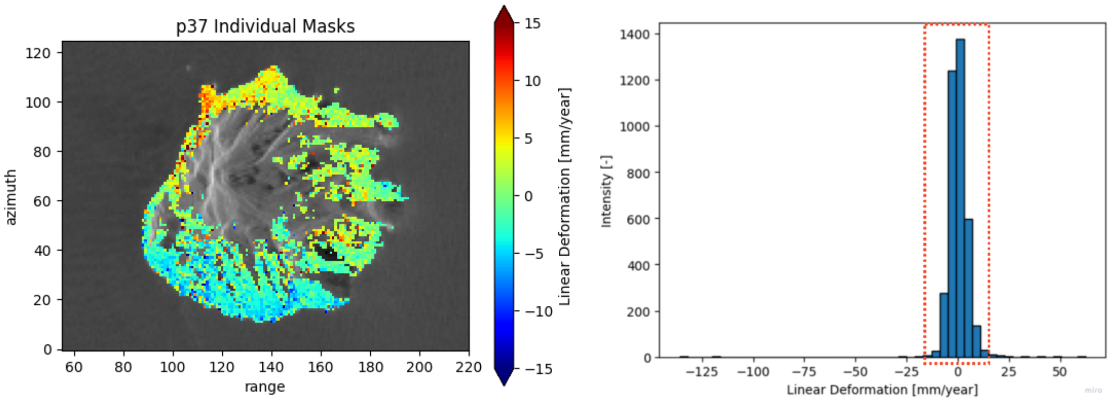

(e) Individual masks.

(f) Individual masks histogram.

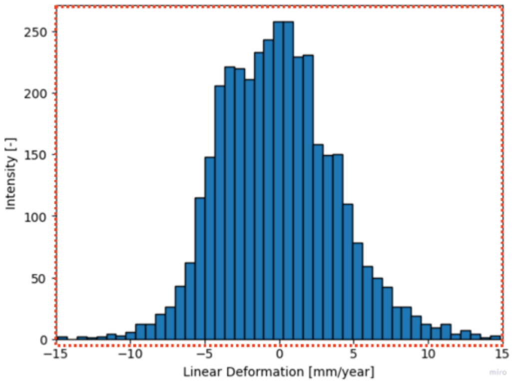

(g) Individual masks histogram zoomed-in version.

Figure 5.9: ALOS-2 Path 37 Saba - Linear deformation estimates, (Continued . . .)

Figure 5.9: (Continuation . . .) for the different masking approaches and corresponding histograms.

		Water mask	Single mask	Individual masks
St. Eustatius	**Path 37**	5.14	4.52	5.84
	Path 36	6.86	5.52	6.54
Saba	**Path 37**	6.30	3.50	5.78

Table 5.2: ALOS-2 - Standard deviation of the linear deformation estimates in [mm/year].

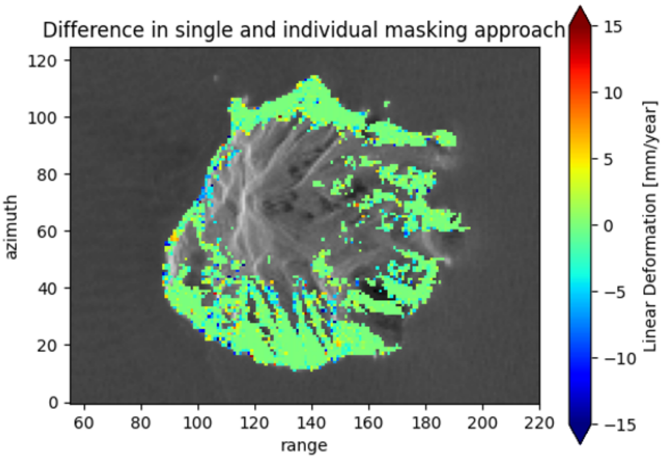

Figure 5.10: ALOS-2 Path 37 Saba - Difference map of the linear deformation estimates following from the single and individual masking approaches. Overall, values near zero can be observed.

Further analysis is performed by considering the residual values. The residuals are used as a collective term for different components, including the atmospheric effect, unwrapping errors, noise as a result of decorrelation and, in the case of SBAS, phase closures from multilooking. For visualization purposes as well as for data interpretation, the residuals are divided by 2π to show the error as the integer number of full cycles. The residuals are shown in Figure 5.11a, Figure 5.11b and Figure 5.11c for the three approaches. It is evident that without a land mask, the residuals are notably higher than for the other approaches and show varying patterns of different magnitudes. These patterns are further analyzed by means of difference maps of the unwrapped phase values. In theory, if the unwrapping procedure was successful, the difference in the unwrapped phase should be around zero. In Figure 5.12a, the difference map between the unwrapped water mask phase values and the single mask phase values is visualized. The outcomes suggest the presence of an unwrapping error in one of the approaches, owing to the constant offset of a magnitude of 2π. The unwrapped phase values of both approaches imply that these unwrapping errors stem from the water mask approach, as depicted in Figure 5.12b. This finding strengthens the outcomes drawn from the linear deformation estimates, highlighting that the absence of a mask results in inclusion of unreliable pixels, making this approach more prone to unwrapping mistakes. In addition, it can be observed that for a smaller temporal baseline, the residuals are overall lower due to the minimized decorrelation phenomena.

Between the single (Figure 5.11b) and individual (Figure 5.11c) masking approaches small differences can be observed. All in all, the residuals are close to zero with some exceptions. When looking closely, the pixels showing somewhat higher residual values in the single masking approach seem to not be covered by the individual masks. In addition, the south part of the island seems have higher residual values in some cases for both approaches. It is unsure whether these are unwrapping errors, as the difference maps do not indicate this. In addition, an unwrapping error will likely be visible as an isolated 'island' with a constant value, which does not seem to be the case here. Considering that one of these have a temporal baseline of almost two years (20180108-20190318) this could also be attributed to other error sources.

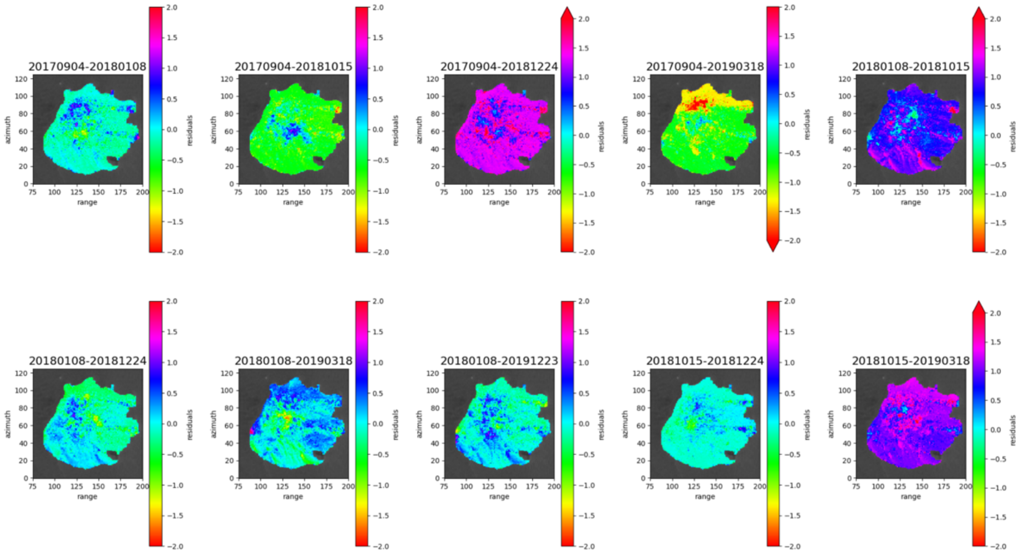

(a) Water mask.

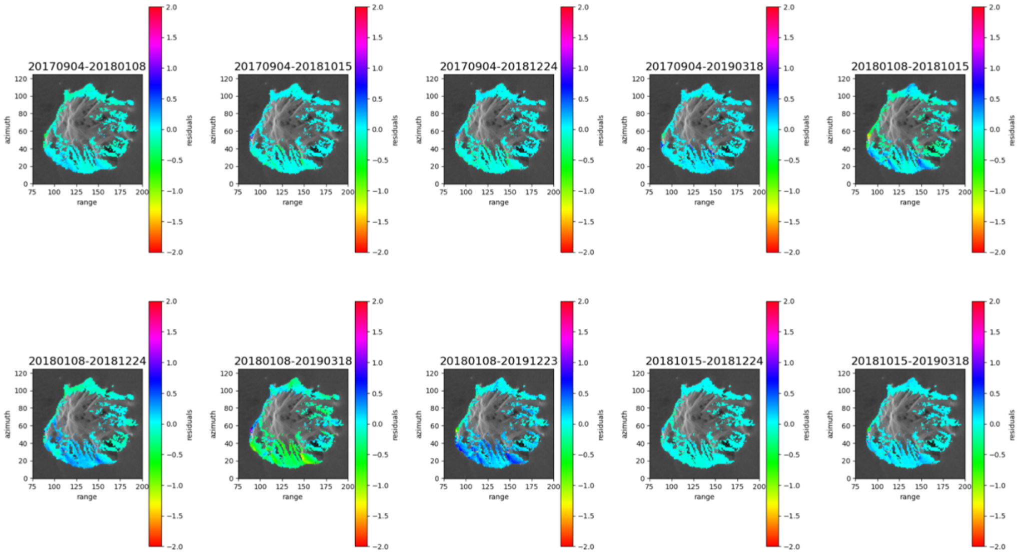

(b) Single mask.

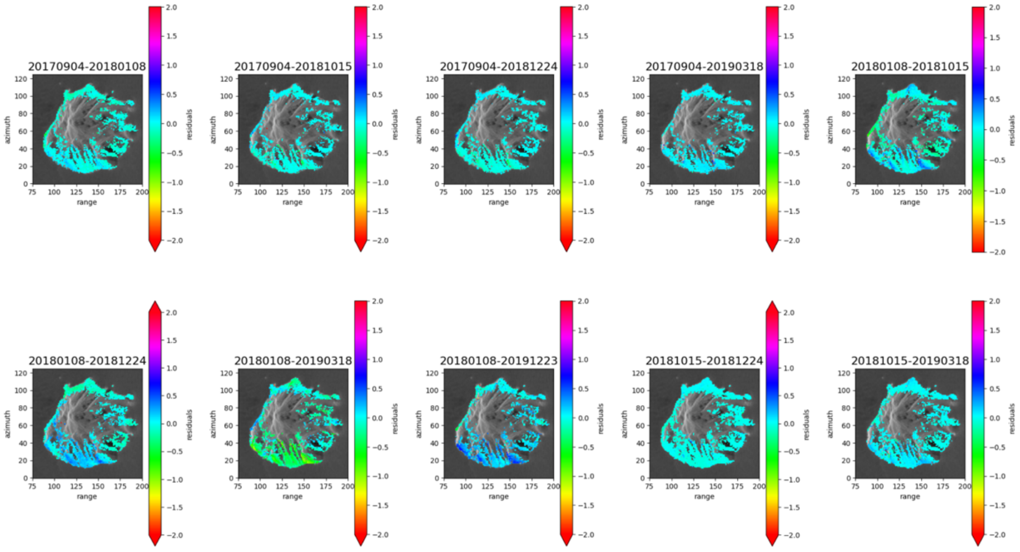

(c) Individual Masks.

Figure 5.11: ALOS-2 Path 37 Saba - Residuals of the different masking approaches. For visualization purposes, the residuals [rad] are divided by 2π to show the error as (Continued . . .)

Figure 5.11: (Continuation . . .) the integer number of full cycles. The residuals are considerably higher for the water mask (top rows). Overall, the single mask (middle rows) and, in particular, individual masks (bottom rows) show residual values near zero with some exceptions.

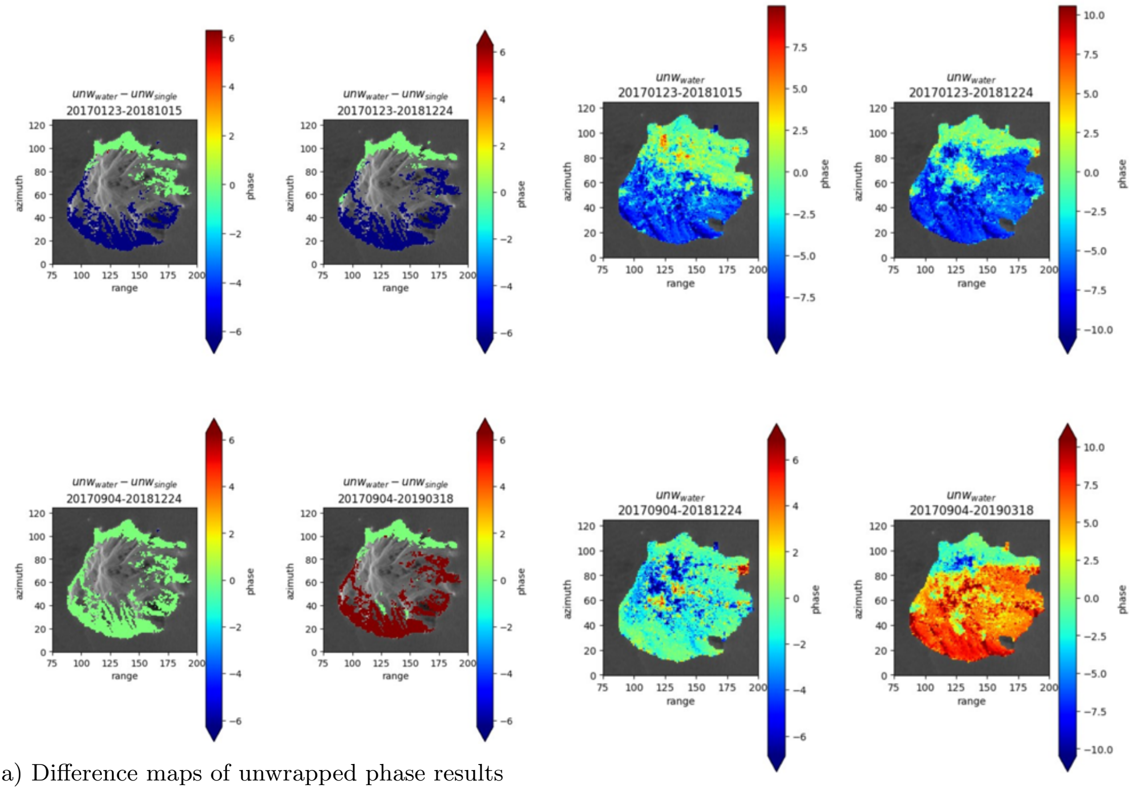

(a) Difference maps of unwrapped phase results of the water mask and the single masks.

(b) Unwrapped phase results for water mask results.

Figure 5.12: ALOS-2 Path 37 Saba - Identify unwrapping errors in water mask results.

The data sets containing St. Eustatius are also considered. When evaluating the deformation estimates and looking at the residuals, the outcomes of both data sets suggested the presence of an unwrapping error in the single mask approach, specifically for Path 36 with a window size of 12:7 and for Path 37 with a window size of 24:14. In Figure 5.13 a subset of the residuals of Path 37 is visualized. In this subset an erroneous pattern appears in the northern part of St. Eustatius affecting multiple data pairs, as indicated in the figure. By plotting difference maps, the unwrapping error source is identified, as shown in Figure 5.17b. Similarly, an unwrapping error for Path 36 is identified. Looking at a subset of the residuals of Path 36 for both the water mask as well as the single mask approach, in Figure 5.14, another erroneous pattern seems to be present in both approaches, this time in the southern part of the island around the volcano. Considering that the error occurs in both approaches, the difference maps of the individual masking approach, with respect to the single masking approach, is used to identify the source, as can be seen in Figure 5.16. For both paths, the unwrapping error occurred within a data pair with a temporal baseline of over two years. In comparison to Sentinel-1, for ALOS-2 larger baselines are included due to the higher coherence. The decreased coherence associated with the larger baselines, possibly only slightly exceeding the coherence threshold of 0.3, may explain the unwrapping errors found. These unwrapping errors will be addressed in the subsection on unwrapping error correction. The final deformation estimates will be discussed after this correction has been applied.

In addition, in both paths a strong signal can be observed on the flank of the volcano, as indicated by the red circles in the residual figures (Figure 5.13 and Figure 5.14). This seems to be located around the Sugar Loaf-White Wall complex. As described in Section 3.1, this formation is characterized by nearly vertical cliffs and composed of significantly different rock types compared to the rest of the island. A possible explanation for the occurrence of this signal is that the topographic phase is not properly deducted in the pre-processing steps performed in DORIS. Specifically, due to the steepness of the bedrock, the DEM might not have been accurate, resulting in an inadequate subtraction of topography.

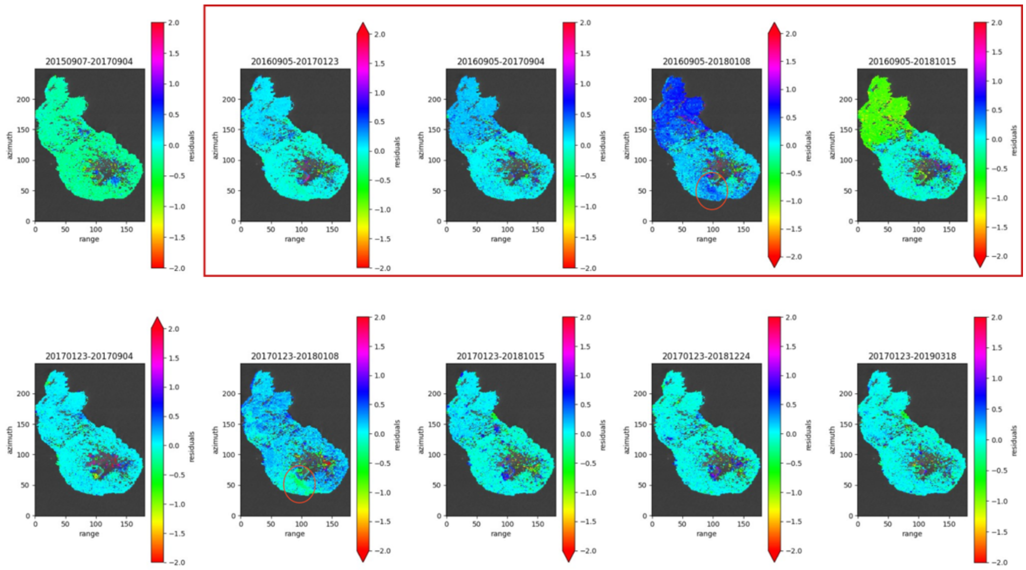

Figure 5.13: ALOS-2 Path 37 St. Eustatius - Residuals of the single mask approach. For visualization purposes, the residuals [rad] are divided by 2π to show the error as the integer number of full cycles. An erroneous pattern arises and is visible among different data pairs (enclosed by red bounding box), indicating that one of these likely has an unwrapping error.

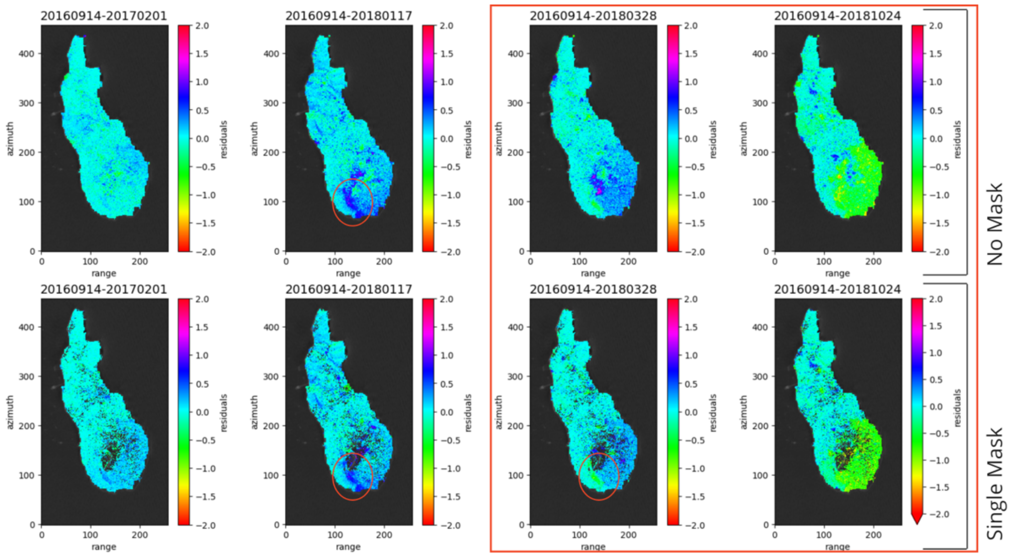

Figure 5.14: ALOS-2 Path 36 St. Eustatius - Residuals of the single mask approach. For visualization purposes, the residuals [rad] are divided by 2π to show the error as the integer number of full cycles. An erroneous pattern arises and is visible among different data pairs (enclosed by red bounding box), indicating that one of these likely has an unwrapping error.

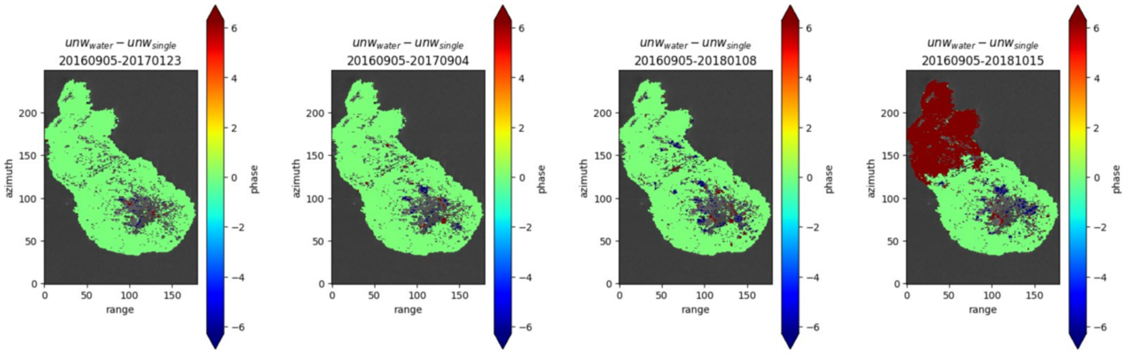

Figure 5.15: ALOS-2 Path 37 St. Eustatius - Difference maps between the unwrapped phase following from the water masking (no inland masking) and single masking approach. A constant offset can be observed in one of the data pairs (right figure), corresponding to an unwrapping error.

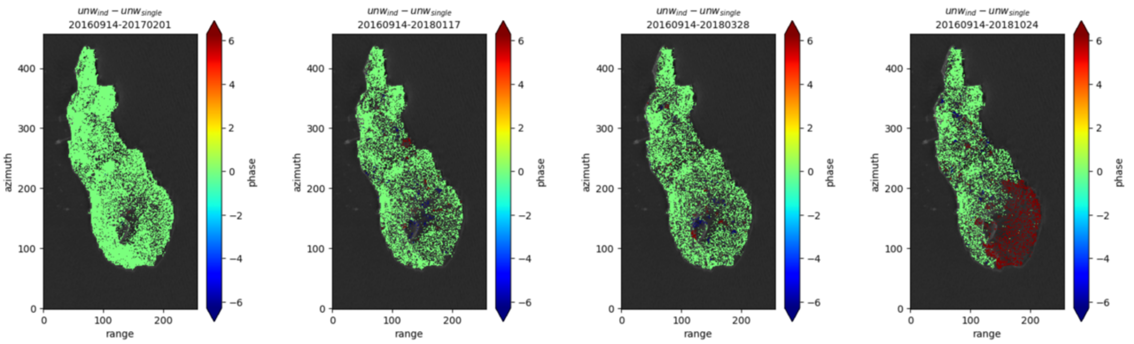

Figure 5.16: ALOS-2 Path 36 St. Eustatius - Difference maps between the unwrapped phase following from the individual masking and single masking approach. A constant offset can be observed in one of the data pairs (right figure), corresponding to an unwrapping error.

Correction Unwrapping Error

The procedure followed for the unwrapping error correction is described in detail in Section 4.1. The results from ALOS-2 are used to demonstrate the effectiveness of the residual testing approaches. The first step is the automated identification of the data pair containing the unwrapping error. This step has proven successfully for both Path 36 and Path 37 using a patch size of 20x20 pixels. The second step involves identifying the affected region, the so-called outlier candidates, using the threshold based on the maximum (absolute) mean patch value and the standard deviation of the selected data pair from the previous step. The detected outlier candidates are visualized in Figure 5.17a for Path 37 and Figure 5.18a for Path 36. For reference, difference maps, which can be used to compare and validate the detected erroneous region, are also plotted in Figure 5.17b (water and single mask) and Figure 5.18b (individual and single mask). The results reveal the detection of most of the erroneous pattern, with the exception of a few pixels. In addition, some other outlier candidates are selected near the volcano in Figure 5.17a, which could be expected and also show an offset in the difference map in Figure 5.17b. Path 36 shows some other pixels with constant offset distributed over different parts of the island, as visible in Figure 5.18b. These smaller regions are also picked up in Figure 5.18a. In the northernmost part of the island, some outlier candidates are selected that are not visible in the difference map. This is because the difference map only shows those pixels that are present in both masking approaches. Therefore this could very well be erroneous pixels, however it cannot be checked. It should be noted, that should some of the selected outlier candidates not be erroneous, this will be identified following the residual threshold or OMT test, depending on the approach used, in the residual testing procedure. As a result, the value of these pixels will be left unchanged.

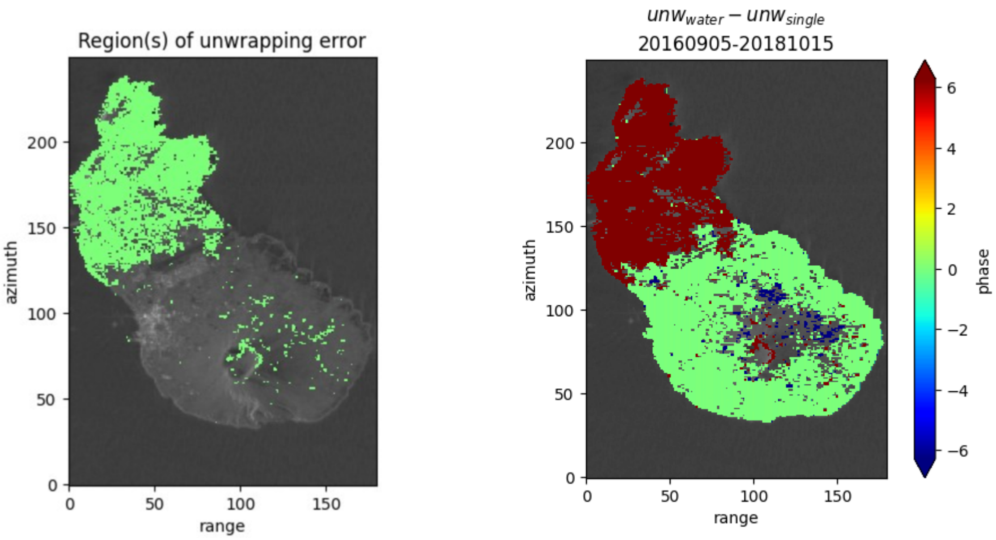

(a) Detected unwrapping error region Path 37.
(b) Difference map Path 37.

Figure 5.17: ALOS-2 Path 37 St. Eustatius - Automatized detection of the unwrapping error (left) compared to the actual erroneous region using the difference maps between the water and single masks (right). The majority of the erroneous pattern has been detected by the algorithm.

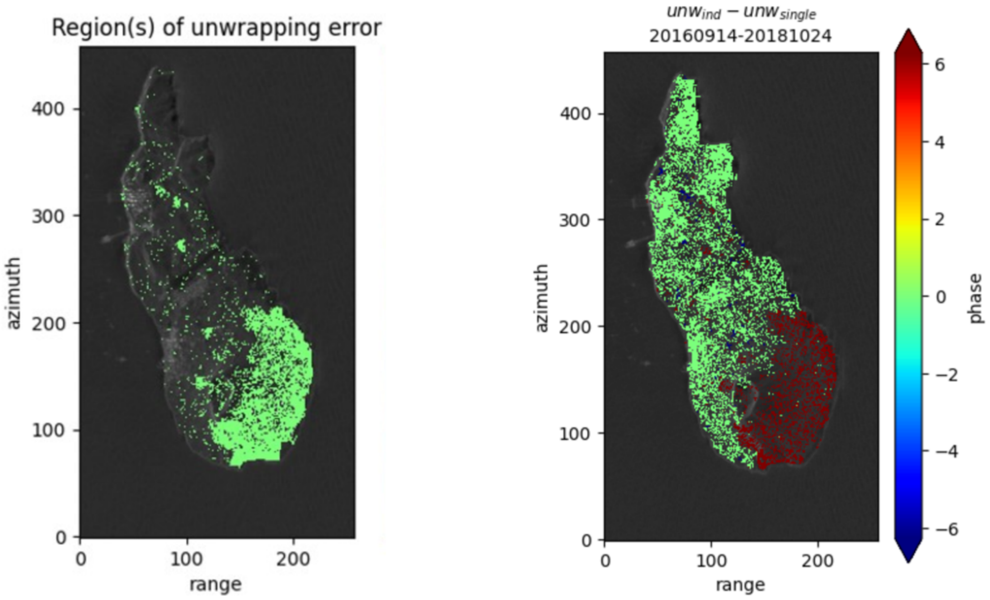

(a) Detected unwrapping error region Path 36.
(b) Difference map Path 36.

Figure 5.18: ALOS-2 Path 36 St. Eustatius - Automatized detection of the unwrapping error (left) compared to the actual erroneous region visible from the (water-single mask) difference maps (right). The majority of the erroneous pattern has been detected by the algorithm.

Then the residual testing step is applied. Both the interferogram removal and interferogram correction approaches are implemented and compared. The first is based on a residual threshold and temporarily removes the so-called outlier candidate pixels, which were identified in the previous step. For each separate pixel the new residuals are compared. However, since the updated residuals of the outlier candidates for the actual data pair cannot be obtained through this approach, the residuals of the other time dimensions are compared to the post-removal residuals. Therefore, a threshold is set based on the sum of the (absolute) original residuals, not including the erroneous data pair, compared to the updated residuals. The second, newly developed approach entails a threshold based on the OMT test and temporarily corrects the outlier candidates. If the correction results in the acceptance of the OMT test result, the value is adjusted accordingly and will not be updated anymore. The exact settings used for the adaptive approach are shown in Table 5.3.

The approaches are compared by visual interpretation of the results as well as the standard deviations of the estimated velocities. But first, the original residuals are compared to the updated residuals after the correction process. This can only be done for the second approach. Figure 5.19 and Figure 5.20 represent the original and updated residuals following the correction procedure. It can be observed, from the spatial plots as well as the histograms, that after the correction most of the residuals are approaching zero in both cases. The distinct peaks in the histograms, in particular apparent for Path 37 likely owing to the size of the affected region, are significantly reduced. However, especially for Path 37, there are still some pixels within the error region that have not been updated. This could suggest that the threshold should be lowered by means of changing the significance level, denoted α, but the value of 0.0001 is already relatively low.

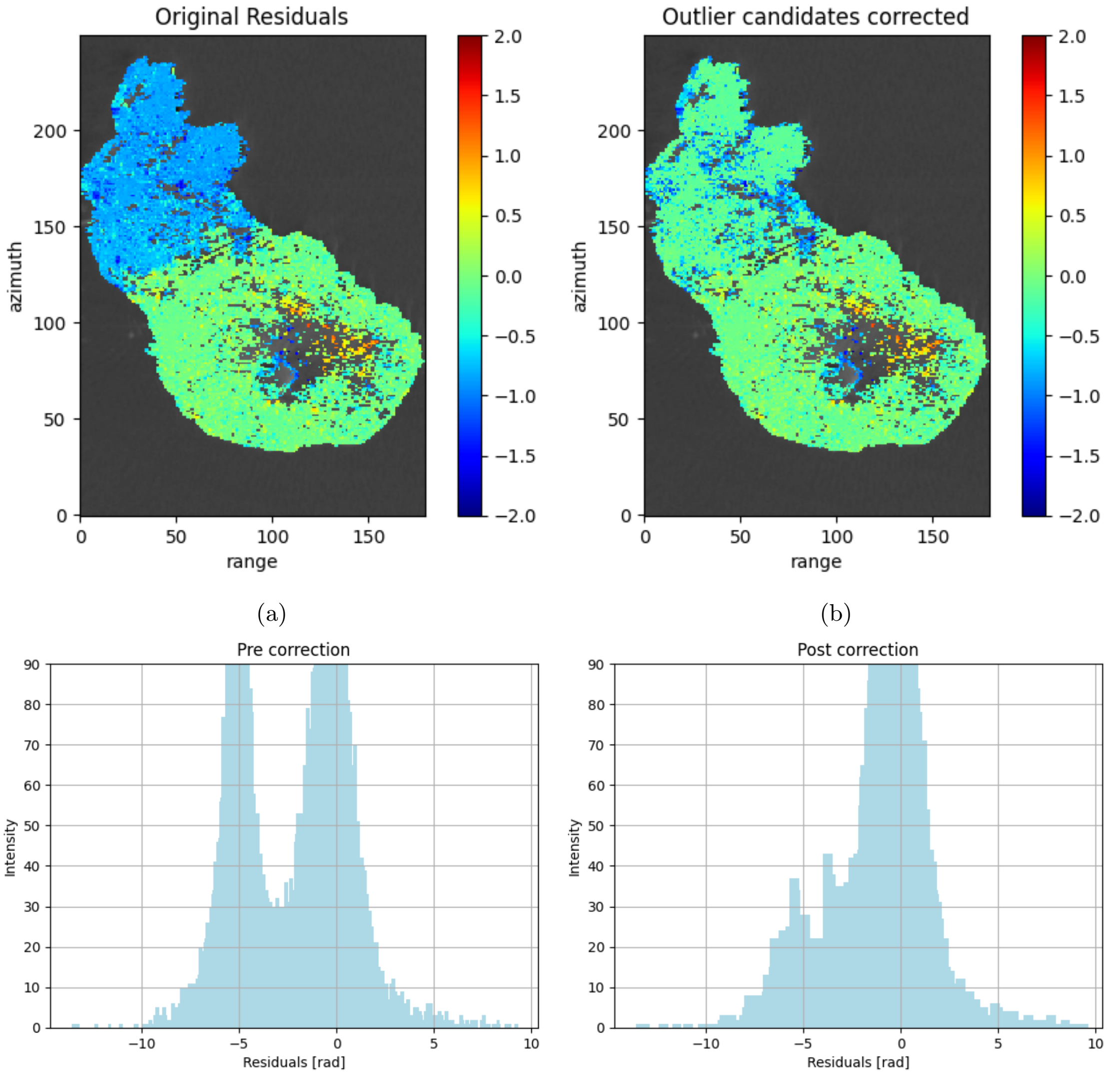

(a) (b)

(c) (d)

Figure 5.19: ALOS-2 Path 37 St. Eustatius - Residuals pre- (left column) and post- (right column) correction for the interferogram adaptive approach. In a) and b), the residuals [rad] are divided by 2π to show the error as the integer number of full cycles.

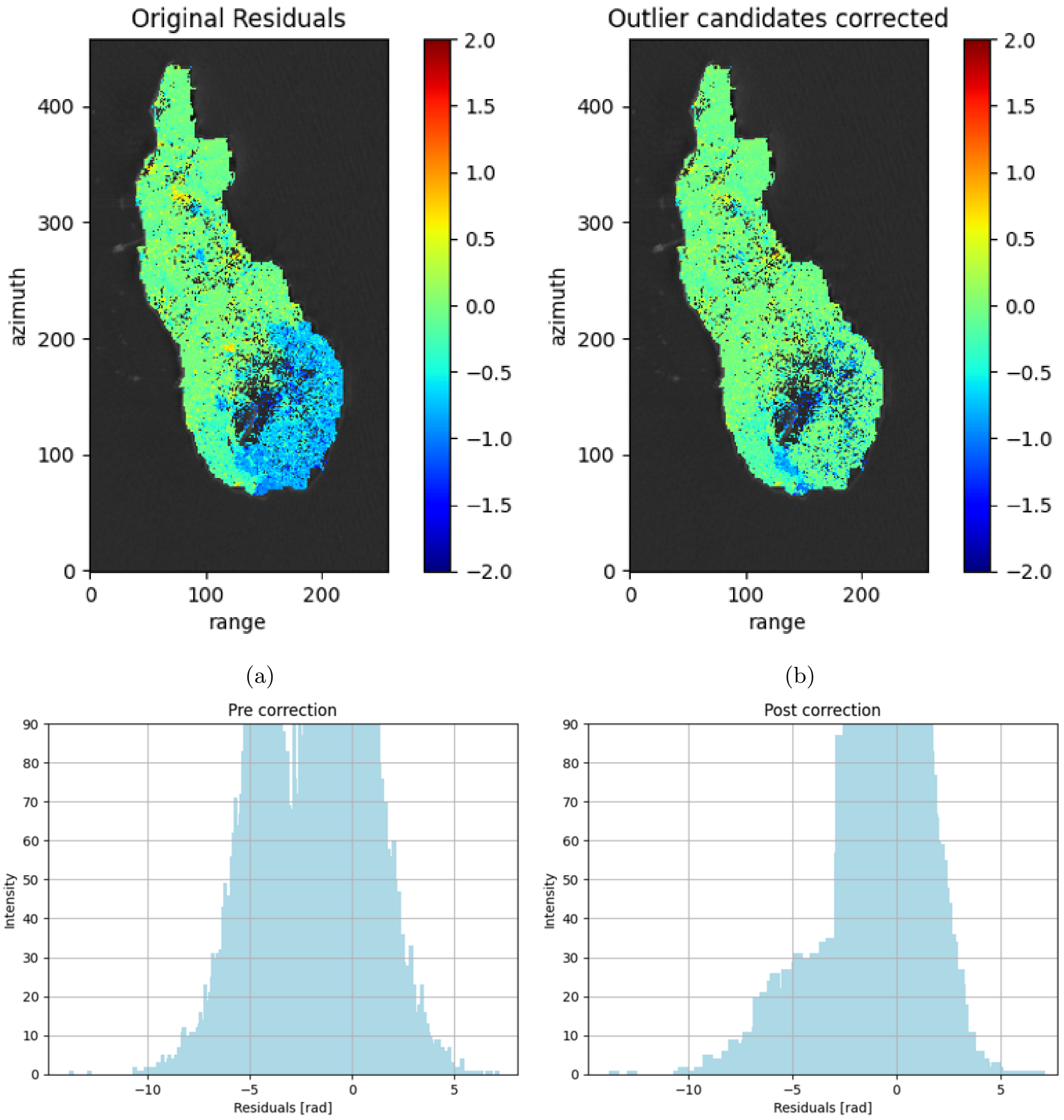

(a) (b)

(c) (d)

Figure 5.20: ALOS-2 Path 36 St. Eustatius - Residuals pre- (left column) and post- (right column) correction for the interferogram adaptive approach. In a) and b), the residuals [rad] are divided by 2π to show the error as the integer number of full cycles.

The original results, i.e., before the removal or correction of the outlier candidates, are presented in Figure 5.21. For Path 36, the error occurs both in the water masking approach and the single masking approach. The unwrapping errors appear to have a significant effect on the results, showing high magnitude values at the location of the error. Due to the limited data pairs this effect is more pronounced than would be the case for Sentinel-1 for instance. Furthermore, the central peaks in the histograms of Path 36 for both approaches are not centered at 0 and show some outliers. However, it should be noted that this is also dependent on the chosen reference pixel. Path 37 does not show any alarming values near the unwrapping error region. This can be explained when looking at the results obtained through the Water mask and individual masking approaches, which show a constant offset in the northern part of the island. The single mask approach solution, although overall closer to zero, does not align with these results. In Path 37 a strong red anomaly can be observed in the northern region. This location corresponds to a steep cliff and could give rise to layover effects. This suggestion is strengthened by the fact that the same anomaly can be identified in the results of Path 36, which is also an ascending path and should therefore also experience layover effects on the same side of the cliff.

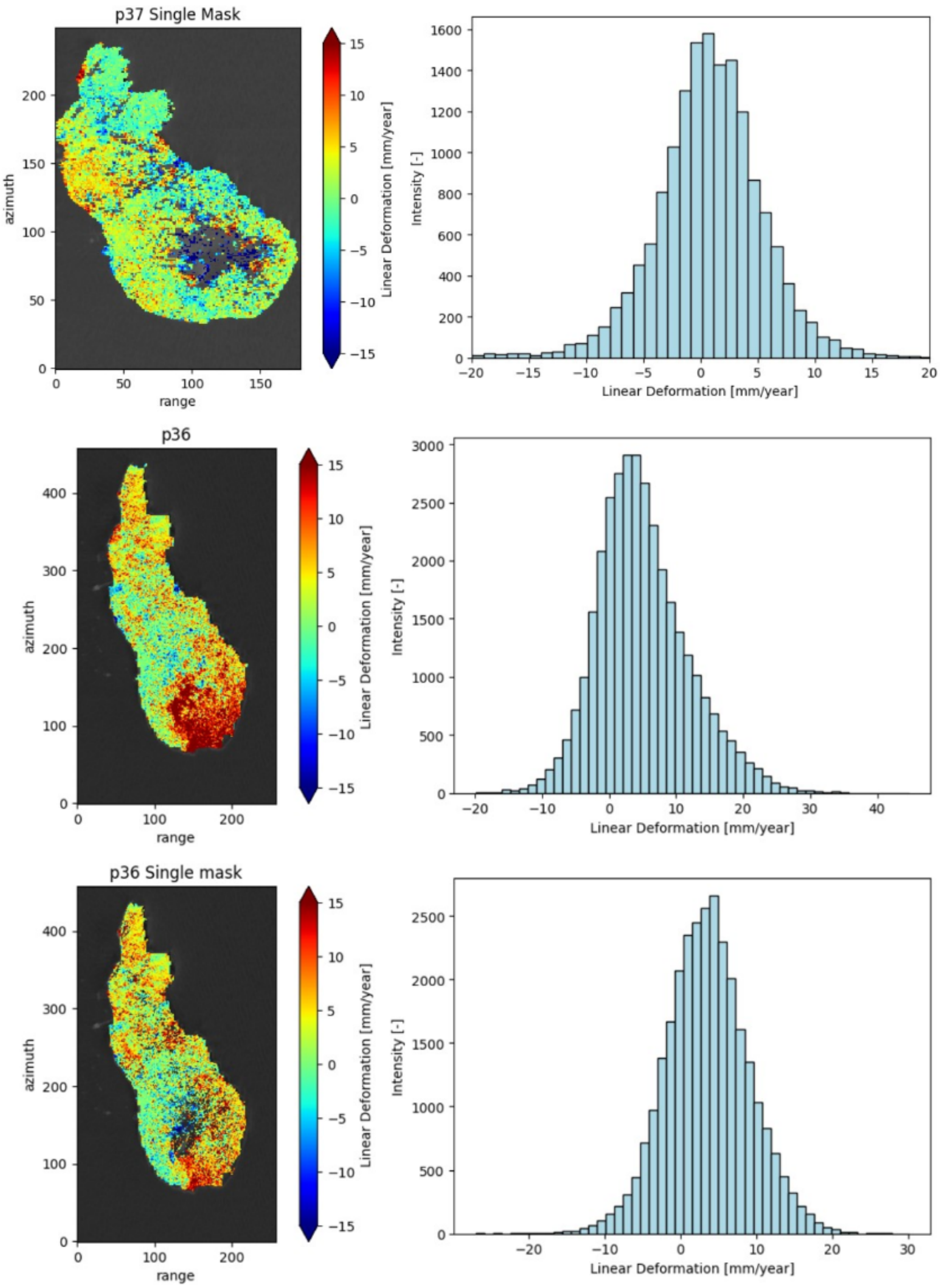

Figure 5.21: Original linear deformation estimates for Path 37 single masking approach and Path 36 water masking approach and single masking approach.

	Settings			
	alpha	**Ka**	**Outlier candidates**	**Corrected candidates**
Path 37	0.0001	52.39	5810	4356
Path 36	0.0001	55.52	7988	5484

Table 5.3: Settings and results for the adaptive testing approach demonstrated using ALOS-2 results for St. Eustatius.

The results obtained after the removal and correction of the outlier candidates are depicted in Figure 5.22 and Figure 5.23. For both paths, the figures reveal consistency in the outcomes of the different masking approaches. In comparison to the original results, the histograms of Path 36 are now centered around zero. An average deformation behaviour of zero is observed overall, with mm order deviations. In contrast, Path 37 shows a more skewed histogram following the correction/removal of the outlier candidates. This change is primarily attributed to the northern part of the island, as discussed above. However, it is worth noting that the distribution of the individual masking approach exhibits a distinct pattern, in which its central peak around zero significantly diverges from the other values. A possible explanation for this prominent peak in the individual masking approach is that exclusively pixels with high coherence (> 0.3) are selected for each epoch separately. However, it is important to highlight that for Path 36 the individual masking approach exhibits a more Gaussian distribution. This difference might be influenced by variations in noise levels, i.e., Path 36 has been multilooked using a smaller window size. In terms of the different testing approaches, the distributions appear similar. However, due to the different thresholds used, the first approach (removal) accepts more of the outlier candidates as erroneous. The standard deviations of the original results are presented in Table 5.2 and the updated standard deviations are shown in Table 5.4. Both approaches show improvements for Path 36. The updated standard deviations for Path 37 result in an increased value, on account of the increased magnitude in the northern part. For both paths, the standard deviation is smaller for the adaptive approach. Yet the difference is relatively small, especially for Path 36. Considering that the adaptive method allows for retaining all observations and for comparison of the updated residuals with the original data, it is the preferred approach.

Finally, a distinct changing pattern can be observed in the southern part of the island for Path 36 in Figure 5.22, even after the unwrapping error correction. The pattern is consistent in all three approaches and is near the Sugar Loaf-White Wall complex, which previously also showed a strong signal in the residuals of both paths. This pattern is also, to a lesser extent, apparent for Path 37 in Figure 5.23. Earlier in this section, this was attributed to the potentially incorrect topographic phase removal. For Path 36, the affected area is slightly larger than for Path 37. It should also be taken into account that, when comparing its location to the sensitivity index in Figure 4.8, part of this location also corresponds to a low sensitivity index for the ascending track of Sentinel-1, which likely is comparable for the ascending paths of ALOS-2. This pattern could therefore be amplified due to a mix of reflections, following from layover effects.

Single Masks		**Original**	**Outlier candidates removed**	**Outlier candidates corrected**
St. Eustatius	**Path 36**	5.52	5.49	5.44
	Path 37	4.52	5.22	4.94

Table 5.4: ALOS-2 - Standard deviation of the improved single mask linear deformation estimates in [mm/year].

Alternatively, as mentioned in Section 4.1, an approach based on the detection of peaks in the histogram of the residuals could aid in the automatic identification of the unwrapping error. Using such an approach could allow for a more robust threshold selection for the detection of outlier candidates. However, this requires the presence of distinct peaks, such that a threshold can be set. As can be observed from the histogram of the original residuals for Path 36 in Figure 5.20c, two relatively large peaks can be identified. In contrast, the residuals histogram for Path 37 in Figure 5.19c does not show distinct peaks. These outcomes suggest that this approach may not be optimal in all cases. However, further investigation may be required after the estimation and removal of the atmospheric component and the DEM errors.

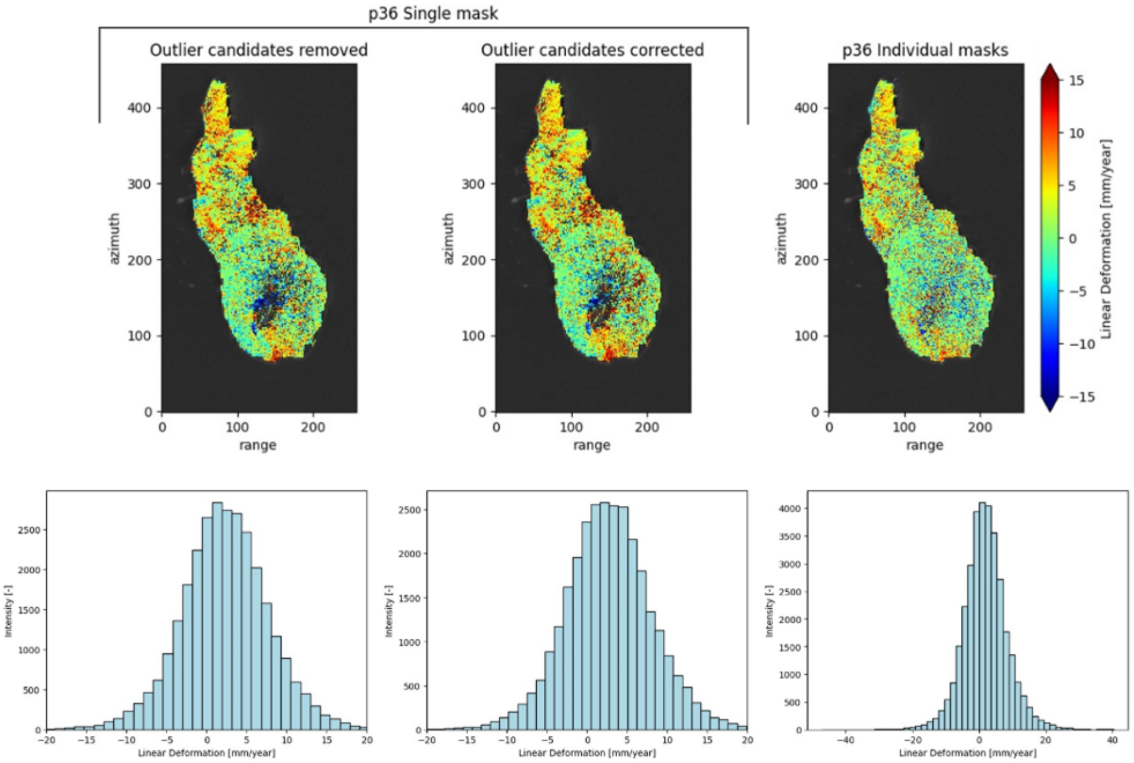

Figure 5.22: Linear deformation estimates for ALOS-2 Path 36, including corrected linear deformation estimates for the single masking approach using both testing approaches. The individual mask (right) is compared to the updated single masking results (left and middle) using the interferogram removal and adaptive approach, respectively.

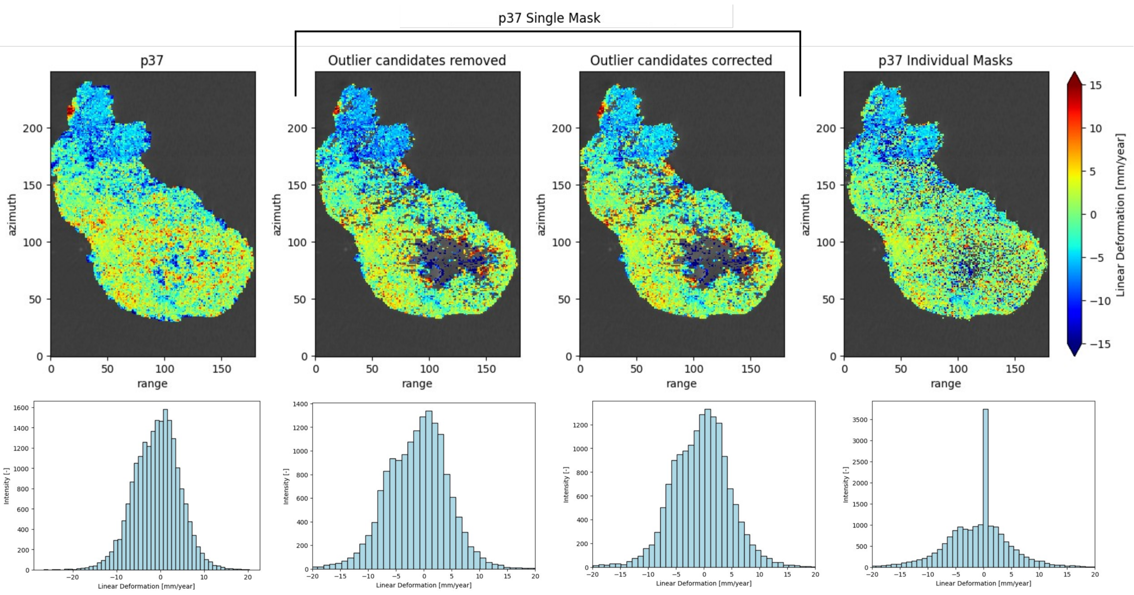

Figure 5.23: Linear deformation estimates for ALOS-2 Path 37, including corrected linear deformation estimates for the single masking approach using both testing approaches. The water mask (left) and individual masks (right) are compared to the updated single masking results (middle) using the interferogram removal and adaptive approach, respectively.

To perform a consistent comparison, the results for Path 37 using the same multilooking window as for Path 36 are also considered. The linear deformation estimates of St. Eustatius Path 37, using this same multilooking window of 12:7, are visualized in Figure 5.24. The corresponding standard deviations of the estimates, following from different masking approaches, are presented in Table 5.5. First of all, the results again reveal consistency among the different masking approaches. Secondly, in this case, the different datasets also indicate a relatively high level of consistency, when comparing Figure 5.24 to Figure 5.22. Specifically, in both paths generally higher values can be observed in the northern part of St. Eustatius, while other regions are overall relatively close to zero. However, with the exception of the isolated pixels near the crater of the Quill as well as the distinct pattern in Path 36 around the Sugar Loaf-White Wall complex, which is not as apparent for Path 37. Given the distinct locations of the selected pixels in both paths, to enable a comparison the linear deformation estimates of both Paths are geocoded. Then, the values of Path 36 are interpolated, using nearest neighbor interpolation, to the nearest (latitude and longitude) coordinates of Path 37. Consequently, a (geocoded) difference map between the individual masking results of Path 36 and Path 37 can be generated and is visualized in Figure 5.25. The majority of the pixels appear to be around zero, indicating consistency between the paths, with some exceptions in particular near the crater of the Quill. Moreover, as opposed to what can be observed using a window size of 24:14 in Figure 5.23, the distributions in Figure 5.24, in particular the distribution for the individual masking approach, approach a more Gaussian distribution similar to Path 36 in Figure 5.22.

Finally, the use of this particular window for Path 37 did not lead to any unwrapping errors in the single mask, in contrast to the results using a window size of 24:14 as illustrated previously in this section. Typically, using a larger window size can reduce the (stochastic) noise, as described in Section 2.2. However, it could be that when using a larger window over regions where decorrelation strongly varies, pixels of varying phase quality are averaged. This can introduce unwrapping challenges as regions of low coherence are more prone to unwrapping errors (see Section 4.1).

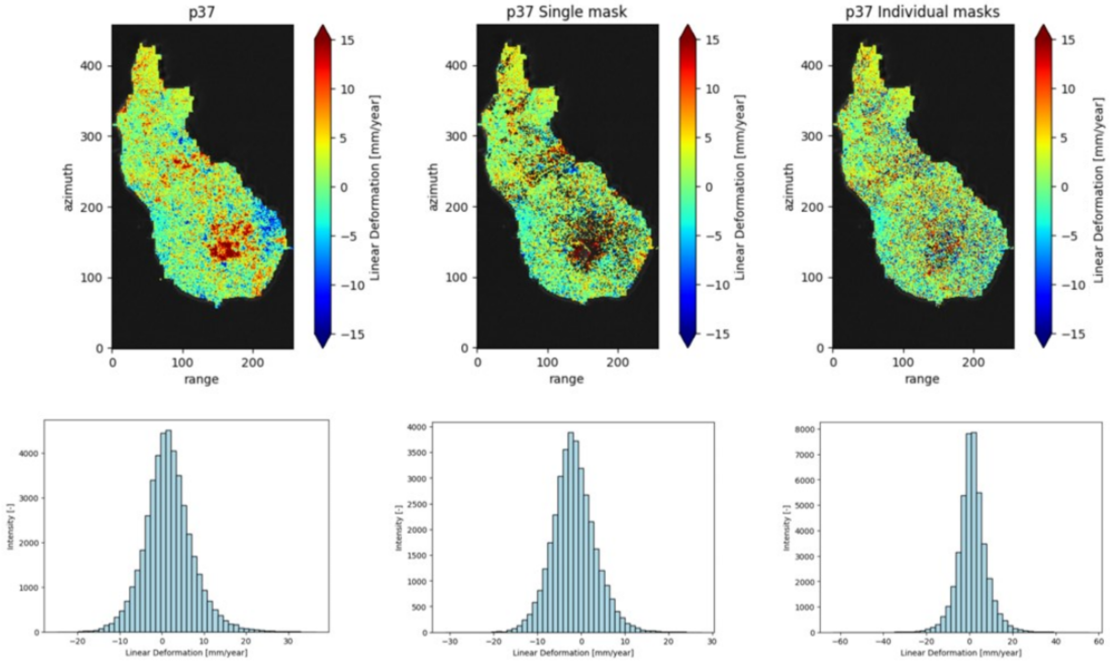

Figure 5.24: Linear deformation estimates for ALOS-2 Path 37 with window size 12:7, including the water (left), the single (middle) and the individual masking approaches (right). The results reveal a relatively high level of consistency both between the masking approaches and with the results for Path 36 using the same multilooking window.

	Water mask	**Single mask**	**Individual masks**
St. Eustatius Path 37	5.72	4.91	6.66

Table 5.5: ALOS-2 St. Eustatius - Standard deviation of the linear deformation estimates in [mm/year] following from Path 37 with a window size of 12:7.

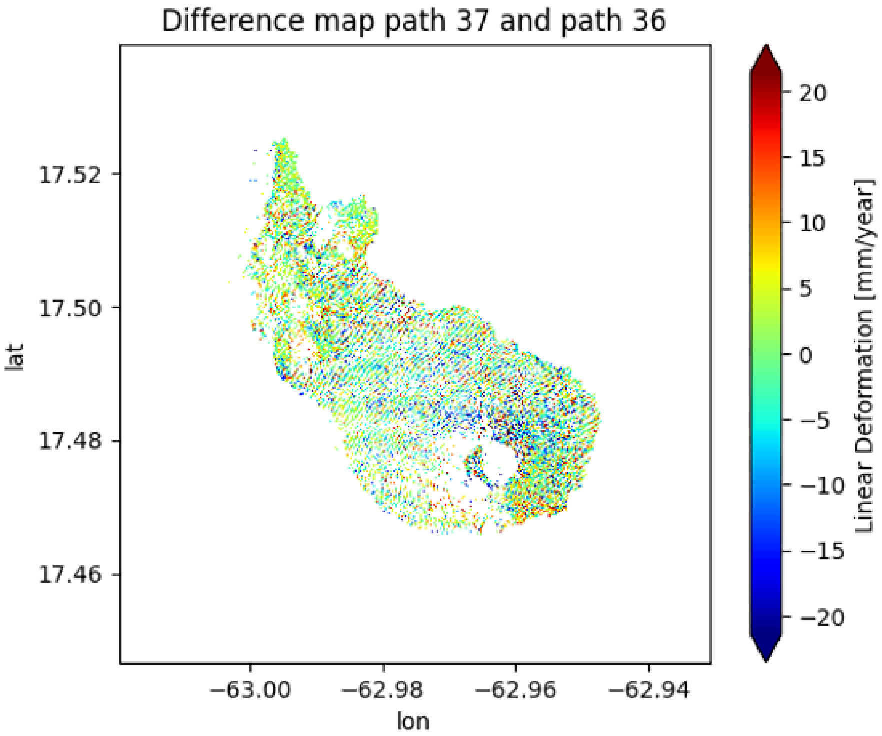

Figure 5.25: ALOS-2 St. Eustatius - Difference map between the linear deformation estimates of Path 37 and Path 36, following from the individual masking approach. The geocoded results are used to enable the comparison. Furthermore, since the selected pixels from both paths occur at distinct locations, nearest neighbor interpolation of the values of path 36 to the nearest coordinates of path 37 is performed. The majority of the pixels appear to have values near zero.

5.2.2 Sentinel-1

Comparable steps to those carried out for ALOS-2 are executed and presented for Sentinel-1. If applicable, any findings similar to those previously elaborated upon for ALOS-2 are not extensively detailed for Sentinel-1.

Intermediate Results

The data pairs are combined according to the short-baseline configuration, resulting in over 6000 unique pairs for each of the Sentinel-1 data sets. The model-based selection procedure considerably decreases the number of data pairs deemed useful to about 400, as can be observed from Table 5.6. This could be expected considering the time frame from 2014 to 2020, where large temporal baselines are not selected. Yet, on account of the rich Sentinel-1 data archive characterized by a relatively short revisit time, a significant number of data pairs is left. The short-baseline configuration plots are visualized in Figure 5.26, for both the different tracks and islands. It can be observed that for all cases data gaps occur. This means that for Sentinel-1 the implemented SVD approach is considered, such that all available data pairs can be used in the estimation. For track 127, all the SLC's are included but two data gaps occur for St. Eustatius, see Figure 5.26a, and one for Saba, see Figure 5.26b. The difference in the selected data pairs for track 127 can be explained by the issues encountered due to the variations in swath coverage for the St. Eustatius data set, as described in Section 3.2.1. Regarding track 164, in addition to the data gap, one of the SLC's is excluded from the network. Based on these resulting baseline plots, the determining factor in the selection process appears to primarily be the temporal baseline.

	St. Eustatius		Saba	
Sentinel-1	**t127 (des)**	**t164 (asc)**	**t127 (des)**	**t164 (asc)**
Original Pairs	6670	7503	7140	7503
Selected Pairs	354	424	376	424

Table 5.6: Sentinel-1 - The unique number of data pairs and the number of selected pairs.

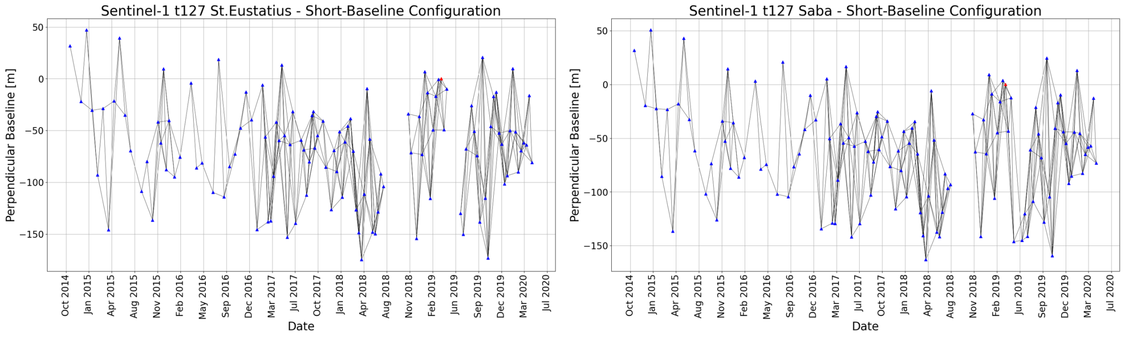

(a) Sentinel-1 track 127 St. Eustatius.

(b) Sentinel-1 track 127 Saba.

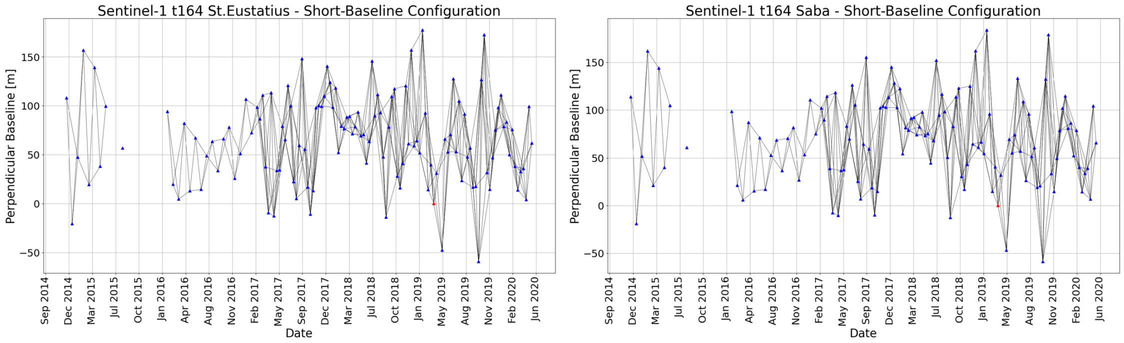

(c) Sentinel-1 track 164 St. Eustatius.

(d) Sentinel-1 track 164 Saba.

Figure 5.26: Short-baseline configuration plots. The red triangle represents the original mother SLC in the single-mother configuration. In all cases data gaps occur.

Similar to the procedure taken for ALOS-2, a coherence matrix for a subset of Sentinel-1 track 127 data, spanning nearly six months in 2019, has been generated. The selected subset has not been submitted to the selection procedure and intentionally contains a data gap, to allow for comparison with increasing temporal baselines. As depicted in Figure 5.27, the outcomes indicate that while the coherence remains relatively high for baselines shorter than a month, signal decorrelation occurs even when the data pairs are relatively close to the diagonal. Namely, the effect is significant even when the baseline extends to as much as two months, which corresponds to the minimum temporal baseline for ALOS-2. Therefore, as could be expected from the difference in wavelength, Sentinel-1 seems to be more sensitive to the temporal baseline. These findings provide insight into the proportion of data pairs that remain following the selection procedure. Similar conclusions can be drawn from Figure 5.28. In this figure, four interferogram are displayed with varying temporal baselines, from twelve days up to approximately two months. Accordingly, these interferograms exhibit varying noise levels. Both the original pixels and the multilooked results, with a window of (3,11), are presented. After multilooking, the phase noise is notably decreased.

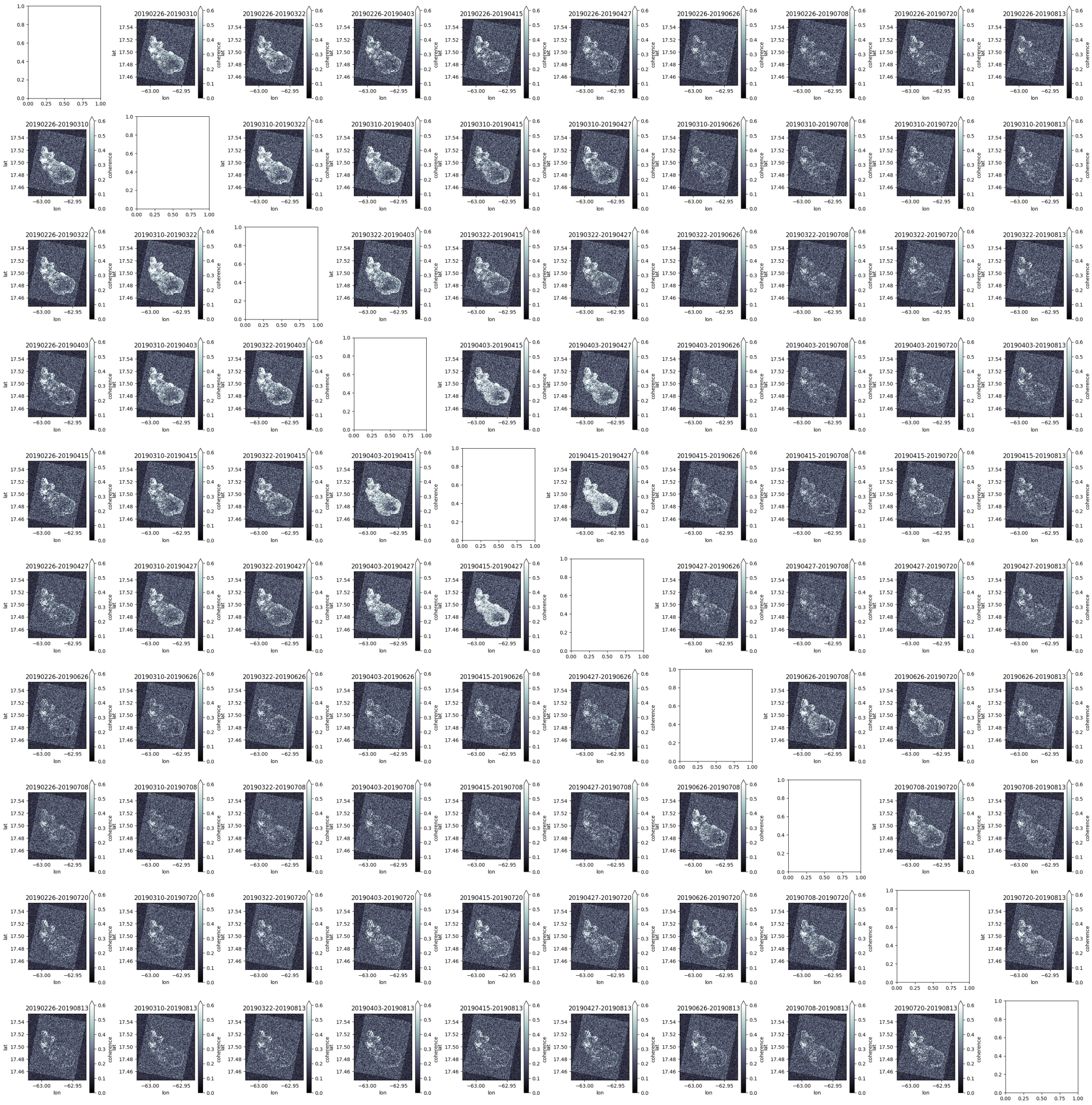

Figure 5.27: Sentinel-1 t127 - (Geocoded) coherence matrix for a subset of 10 SLC's in 2019.

Given this susceptibility of Sentinel-1 to decorrelation, as observed from the coherence maps, the selection process yields a maximum baseline of approximately two months for track 127 as well as for Saba track 164, and even less for St. Eustatius track 164. Owing to the abundant data availability and revisit frequency, the application of Sentinel-1 remains promising.

The coherence masks are generated using the same settings as for ALOS-2 and are displayed in Figure 5.29 and Figure 5.30, for Saba and St. Eustatius respectively. In comparison to ALOS-2, the substantial difference in coverage immediately stands out. While the flanks of Saba are overall covered relatively well for Sentinel-1, the coverage for St. Eustatius is notably lower compared to what was observed with ALOS-2.

Furthermore, while the difference in baseline is not particularly significant, the distinct variations in coverage among the individual masks is notable. Additionally, a considerable number of isolated pixels exist. Higher pixel density occurs around the outer flanks of Saba as well as certain regions in St. Eustatius away from the volcanic region. In contrast, the number of isolated pixels in the single mask approach are less pronounced. The single mask approach shows relatively good coverage of the outer flanks on Saba. For St. Eustatius most of the selected pixels are located away from the volcanic region, around urban area and low vegetation. However, the limited number of selected pixels in the individual masks with larger baselines, indicate how many potentially unreliable points might be included in the single mask approach.

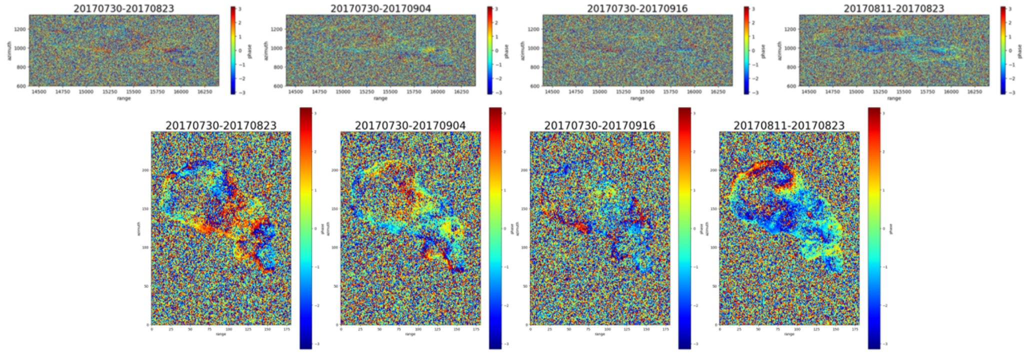

Figure 5.28: Sentinel-1 t127 St. Eustatius - Original pixels compared to multilooked results.

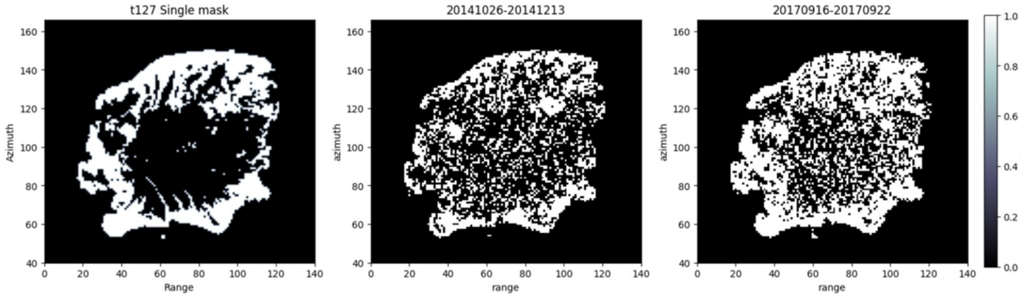

(a) Sentinel-1 t127 Saba

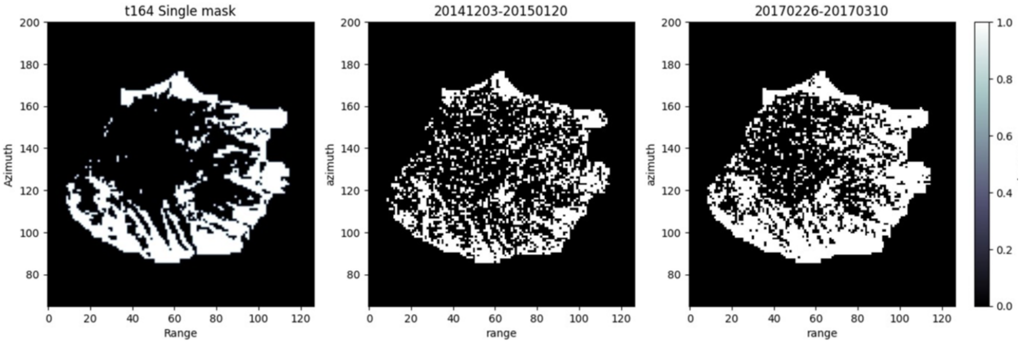

(b) Sentinel-1 t164 Saba

Figure 5.29: Single mask approach (left) compared to the individual masks for the largest temporal baseline (middle) and smallest temporal baseline (right).

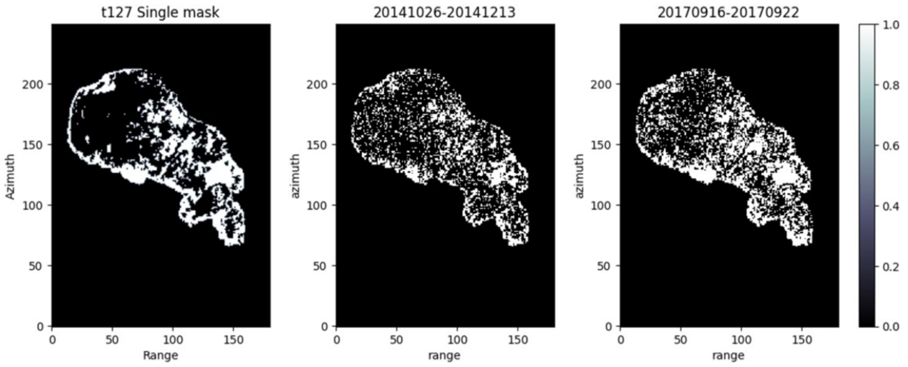

(a) Sentinel-1 t127 St. Eustatius

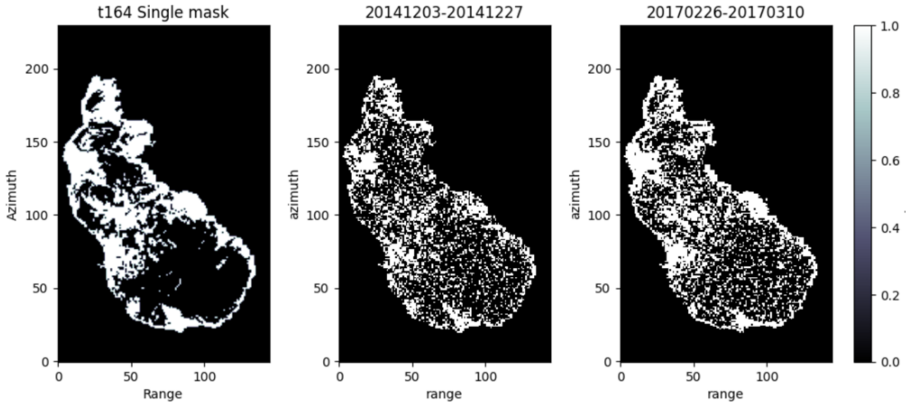

(b) Sentinel-1 t164 St. Eustatius

Figure 5.30: Single mask approach (left) compared to the individual masks for the largest temporal baseline (middle) and smallest temporal baseline (right).

Throughout the unwrapping process it was found that unwrapping errors did not only occur using the individual masking approach without interpolation, but, in particular cases for Sentinel-1, also with the single masking approach. This can be explained on account of the minimal coverage, resulting in some limited connected components. Therefore a similar approach, i.e., nearest-neighbor interpolation, is applied to the single masked phase and coherence before the phase unwrapping procedure. An example for such an unwrapping error in the individual masking procedure, is visualized in Figure 5.31.

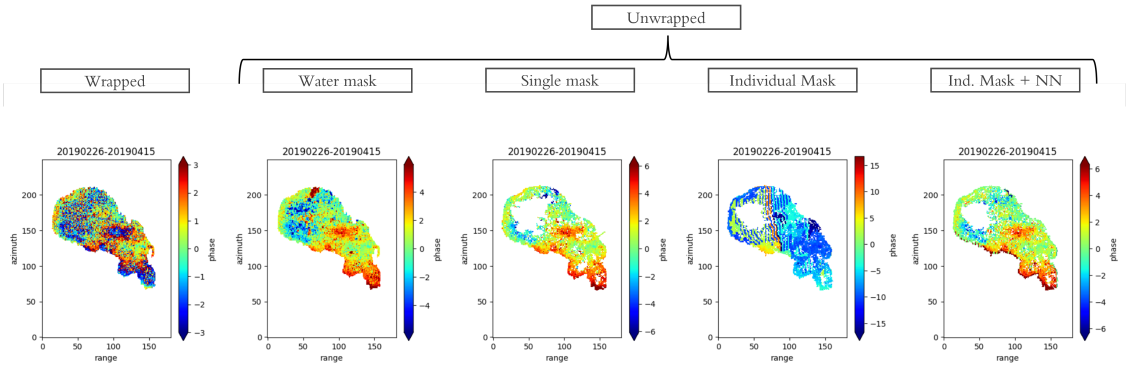

Figure 5.31: Sentinel-1 - Wrapped phase result followed by the unwrapped phase results for the masking approaches. The individual masking approach leads to inconsistent results on account of areas with limited pixel connection. This is solved by applying a (nearest-neighbor) interpolation before unwrapping (right).

Final Results

The linear deformation estimates obtained for Sentinel-1 are presented in Figure 5.32 for Saba and in Figure 5.33 for St. Eustatius, for both tracks. The same procedure and considerations as described in the final results of ALOS-2 are taken into account. However, the results for Sentinel-1 do not include an unwrapping error correction, as the current procedure is confined to the epoch with the highest error and more unwrapping errors are expected to occur. Given the assumption that no deformation occurs, values near zero are expected with the spread in the results serving as an indicator of precision. Nonetheless, it is important to highlight that the atmospheric component and DEM errors influence the results.

The results reveal once again the importance of the masking approaches, showing unrealistic jumps in the values. The same conclusions can be drawn when considering the residuals of the different masking approaches in Figure 5.34. Specifically, as was found for ALOS-2, the residuals are considerably higher for the approach without a mask, compared to the other approaches. Hence the focus is on the two remaining masking approaches.

Generally an increased number of observations, assuming good data quality, can result in more precise estimates. On account of the amount of data available for Sentinel-1, one of the prominent differences is the lower variability in the linear deformation estimates overall. The variability is described in terms of the standard deviation and is presented in Table 5.7, showing relatively low variability in the mm scale per year. On average, the single masking approach seems to have the lowest variability among the different approaches considered. However, when considering the histograms and the deformation estimate maps, the individual masking approach seems to have values closer to zero, showing a distinct central peak at zero in the histograms. In addition, overall the individual masking results seem to exhibit a more homogeneous distribution of the values, also indicated with the difference map in Figure 5.35b, while the single mask results show different regions with changing patterns that are inconsistent among the masking approaches, as depicted in the difference map in Figure 5.35a. More specifically, the histograms of the single masking approaches are more skewed and, all in all, the central peaks in the histograms of the single masking approaches are not centered at zero. This is especially apparent for Saba track 164 and St. Eustatius path 127. This difference in the standard deviations can be explained on account of the presence of outliers in the individual masking approach, similar to what was observed with ALOS-2. In the worst case, observed for St. Eustatius track 164 in Figure 5.33b, these outliers reach values exceeding a magnitude of 300 mm/year. These values seem to primarily occur at isolated pixels near high slopes in the north of the island, showing high magnitude values as well as near the summit of the volcano and are especially high for track 164. Looking at the standard deviations of the individual masking approach for track 164, the values are considerably larger than those for track 127.

The more heterogeneous patterns observed for the single masking approach may be partially deemed unreliable based on the layover and shadowing effects. The sensitivity index is used to interpret these patterns and is illustrated in Figure 4.8. i.e., for the ascending track 164, the most northern part of the island is characterized by a steep slope. The slope facing the sensor shows a change in values, compared to the other side, corresponding to a low sensitivity index in Figure 4.8. This can be due to the fact that layover effects occur which can lead to the summation of the reflections and thus unreliable results. The same occurs on the other side of the slope for the descending track 127. Also, for track 127 a strong signal toward the northern flank behind the volcano, shows similar high values and accordingly a low sensitivity index. Again, for track 164 the values on the west-south flank also correspond to a low sensitivity index. A similar, yet less defined pattern can be observed for the individual masks. If these patterns are not taking into account, the single masking and individual masking approaches appear to become more consistent.

One of these changing patterns in the single masking approaches, and to a lesser extent also in the individual masking approach, are however visible in both tracks for Saba. The pattern is especially evident for descending track 127, corresponding to a high sensitivity index at this location, and is consistent with the results for ALOS-2. That is, a strong signal showing uplift appears at one of the steep cliff located at the western part of the island. On June 9 2014 a landslide occurred at this exact location. Although the available data does not start until later 2014 for both ALOS-2 and Sentinel-1, the evolution in the years that followed is substantial. It should be noted that, on account of the steepness, the layover effect can cause a combination of different reflections causing this pattern for ALOS-2 p37 and Sentinel-1 track 164. However, the values have a significant magnitude and the cliff is characterized by barren rocks and hence relatively high coherence. Therefore, the values could possibly be influenced by this event.

Other patterns are likely on account of unwrapping errors. As mentioned earlier, the single masks generated for Sentinel-1 exhibit considerably lower coverage than for ALOS-2. Despite this larger coverage with ALOS-2, unwrapping errors were detected for the single mask approach. Therefore, the same can be expected for Sentinel-1 with even less coverage, limiting the connectivity between pixels in the spatial network. By considering the residuals of the single masking approach, for a subset of St. Eustatius track 127 and Saba track 164 in Figure 5.34b and Figure 5.34e, it can be observed that some erroneous patterns arise. Conversely, the residuals from the individual masking approach in Figure 5.34c and Figure 5.34f, show values closer to zero with merely some constant offset near the volcanic region for St. Eustatius in the first two examples. The generation of difference maps between unwrapped data results, as done for ALOS-2, validate this hypothesis. However, considering the number of data pairs for Sentinel-1 and that the residual testing approaches are based on the data pair with the highest error, the correction of a single unwrapping error in over 300 data pairs, will not be as effective as for the approximately 30 data pairs for ALOS-2. This highlights the importance of the correction of unwrapping errors and indicates the need for the expansion of the approaches to more than one data pair. Finally, some of the diverse patterns may also result from geometric distortions depending on the track considered.

Overall, the different masking approaches give different outcomes for Sentinel-1. This indicates a low level of robustness as well as low reliability. More consistent results are however expected after expanding the unwrapping error correction procedure to all the erroneous epochs. More research is needed to confirm this.

		Water mask	**Single mask**	**Individual masks**
St. Eustatius	**t127**	4.84	3.38	2.65
	t164	4.42	3.89	5.46
Saba	**t127**	5.81	3.85	4.71
	t164	4.79	3.11	5.50

Table 5.7: Sentinel-1 - Standard deviation of the linear deformation estimates in [mm/year].

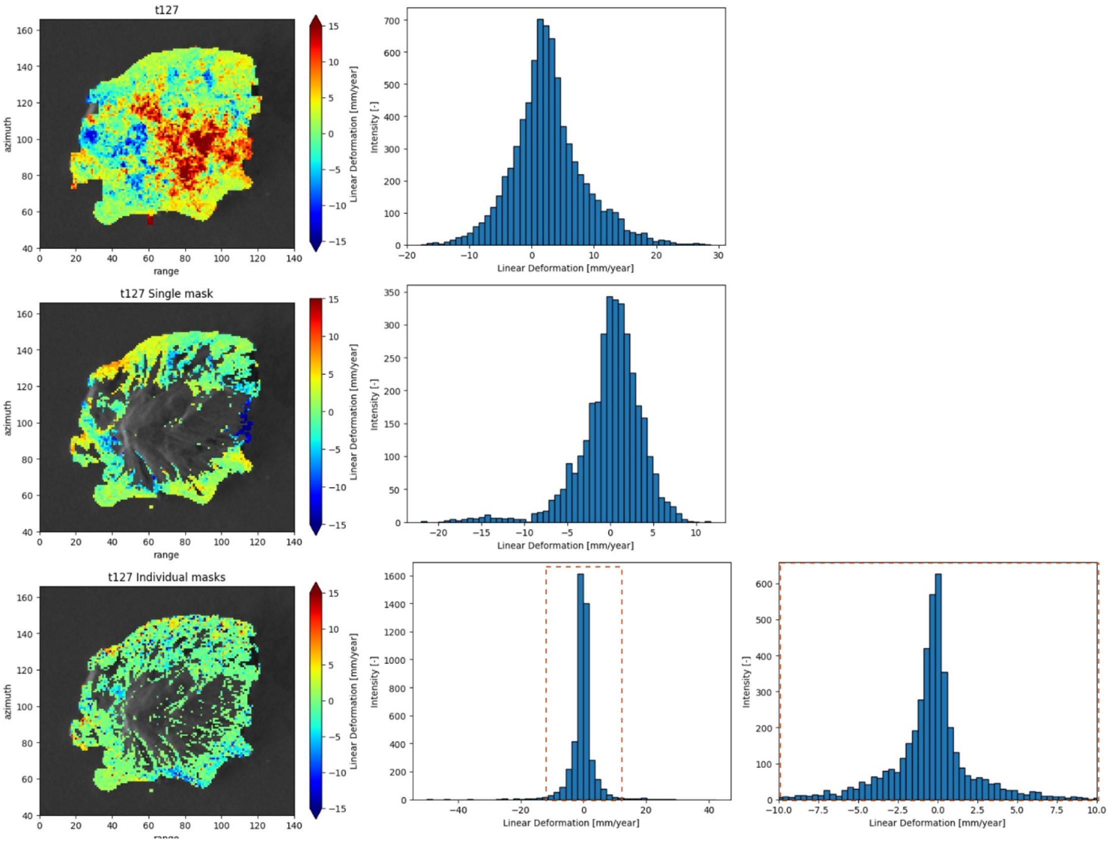

(a) t127

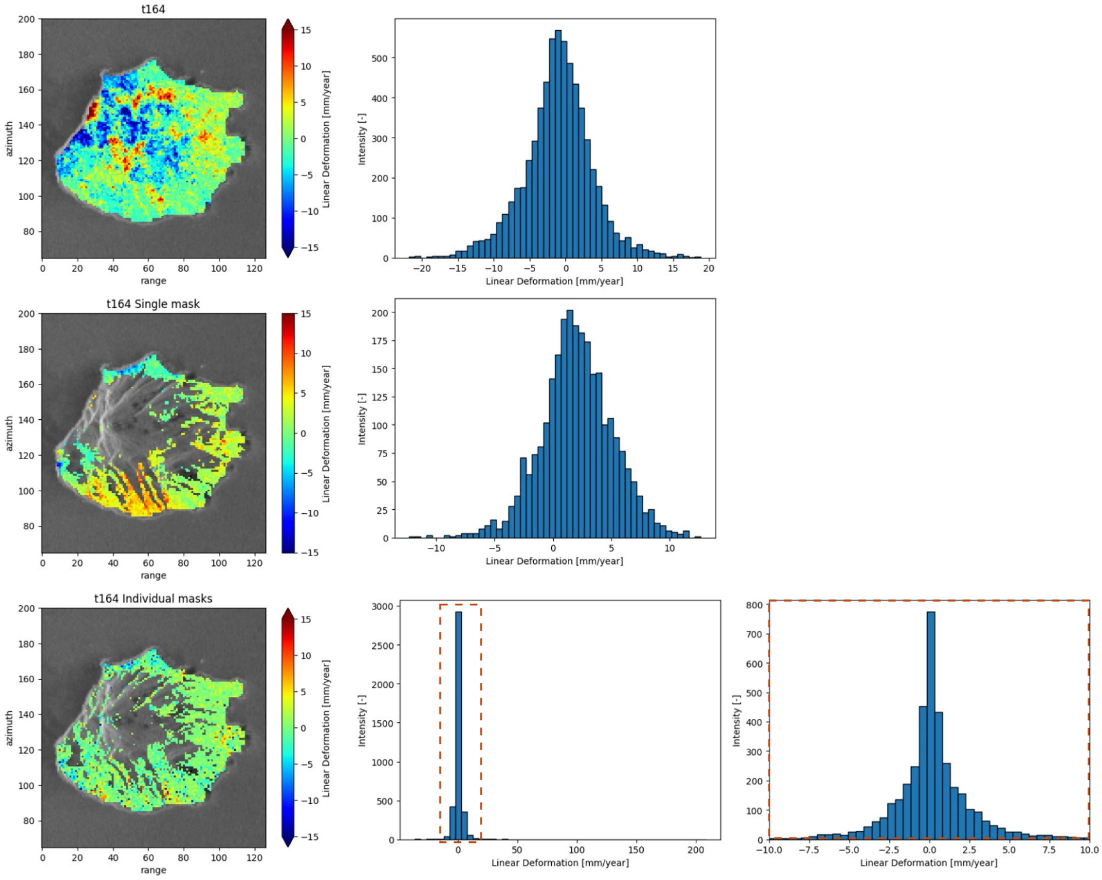

(b) t164

Figure 5.32: Sentinel-1 Saba- Linear deformation estimates for all masking approaches.

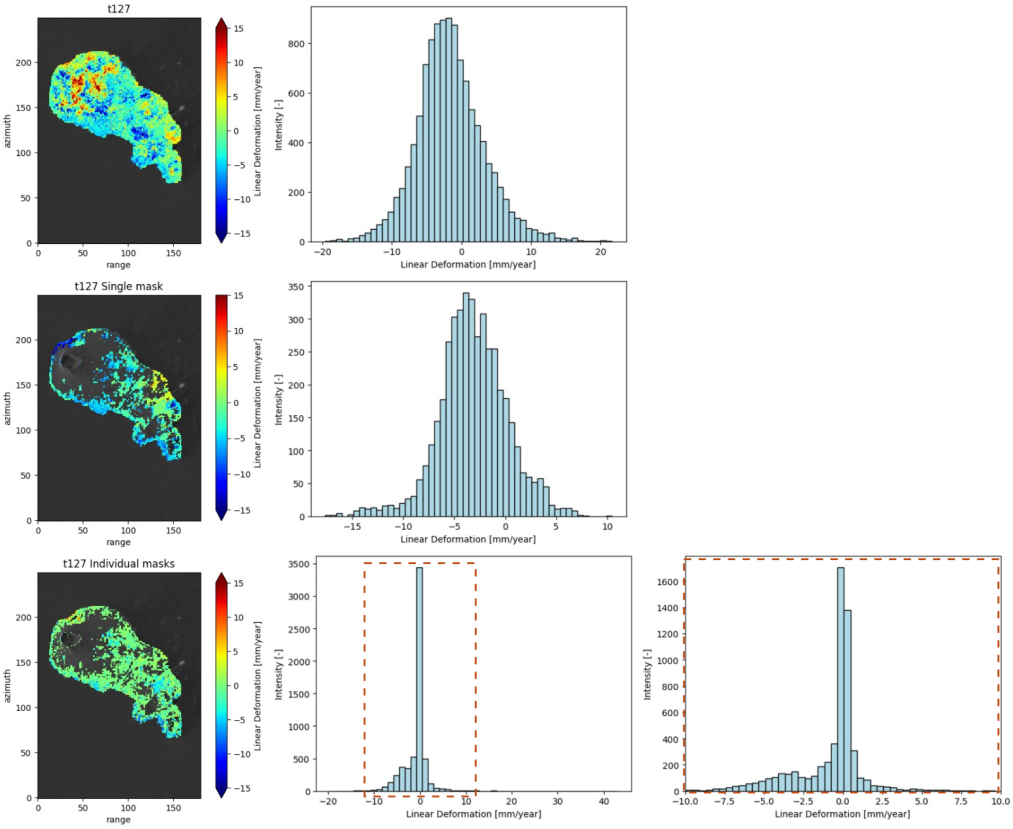

(a) t127

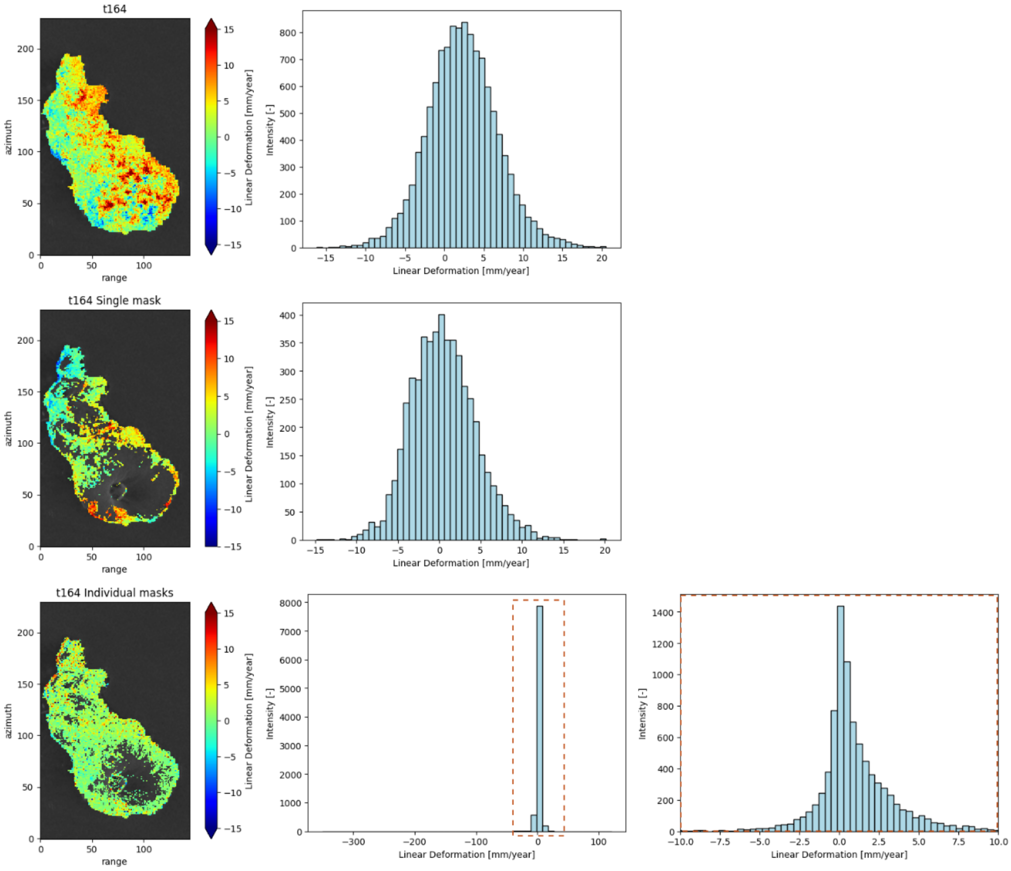

(b) t164

Figure 5.33: Sentinel-1 St. Eustatius - Linear deformation estimates for all masking approaches.

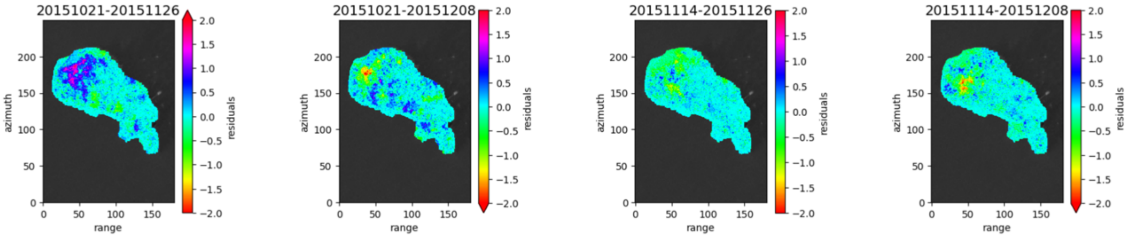

(a) Water mask.

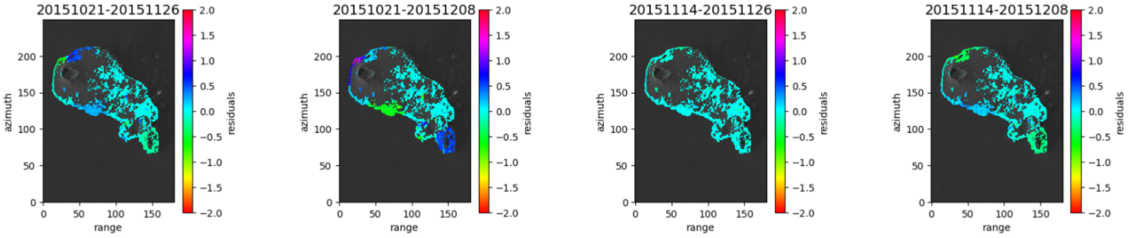

(b) Single mask.

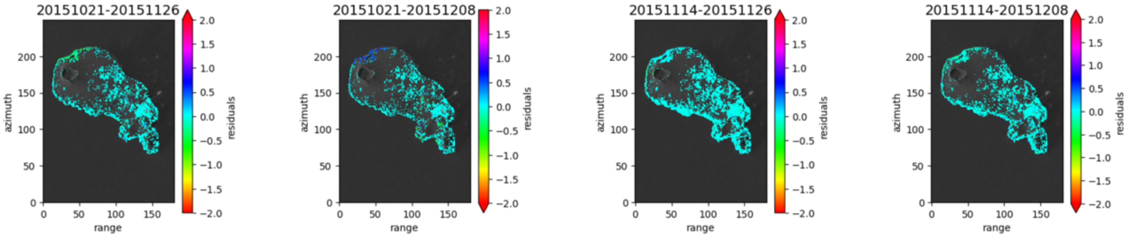

(c) Individual Masks.

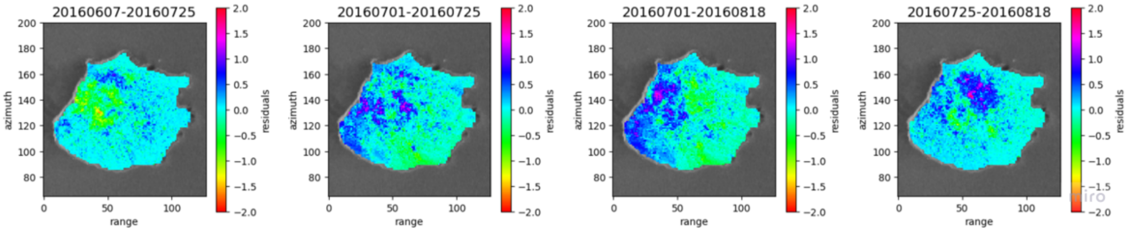

(d) Water mask.

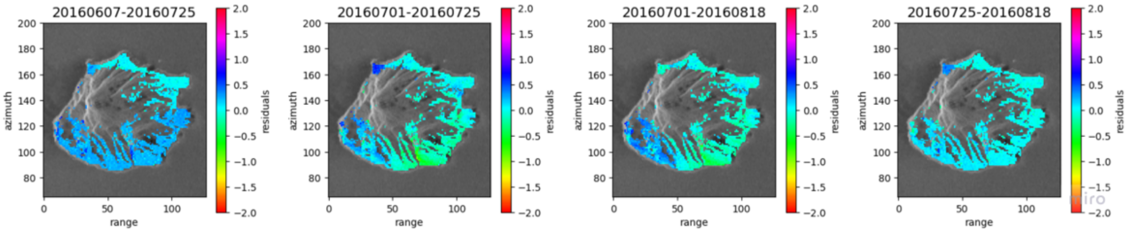

(e) Single mask.

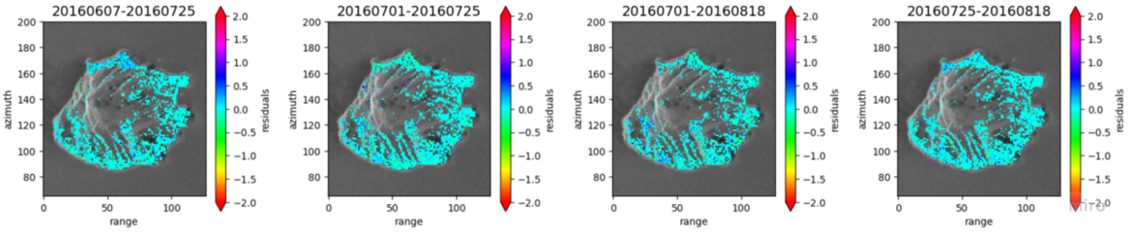

(f) Individual Masks.

Figure 5.34: Sentinel-1 t127 St. Eustatius and t164 Saba - Residuals. For visualization purposes, the residuals [rad] are divided by 2π to show the error as the integer number of full cycles. For both islands, the water mask approach mainly shows noise. The single masking approach appears to be more prone to unwrapping errors compared to the individual masking approach, which overall shows residual values near zero.

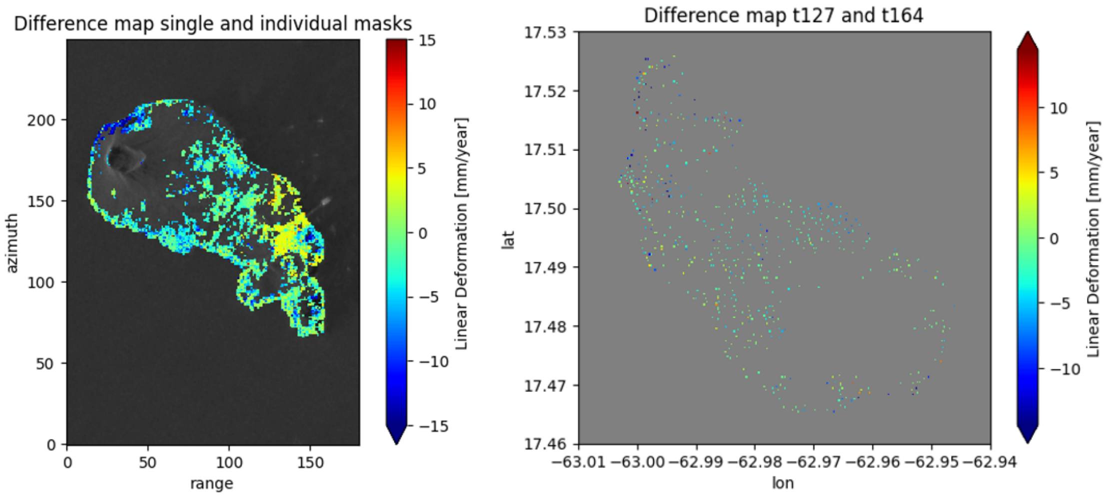

(a) Sentinel-1 St. Eustatius t127.

(b) Sentinel-1 St. Eustatius t127 and t164.

Figure 5.35: Difference maps of the linear velocity estimates between a) the single and individual masking approaches of St. Eustatius t127 and b) the individual masking approaches for t127 and t164. To enable the comparison for b), the geocoded results are used. Furthermore, since the selected pixels from both paths occur at distinct locations, nearest neighbor interpolation of the values of t164 to the nearest coordinates of t127 is performed. Figure a) reveals inconsistency between the masking approaches, while for figure b) the majority of the pixels appear to have values near zero indicating a higher level of consistency.

5.2.3 Data analysis

The geocoded results can be exported as GeoTIFFs and loaded into QGIS. This allows to investigate where certain pixels are selected depending on the wavelength used, particularly for which land types, and to further inspect the occurrence of artifacts.

A frequently encountered problem involves the presence of pixels within the water. In several cases, denoted by orange bounding boxes in Figure 5.36a and Figure 5.36b, this can be linked to the presence of rock boulders in the water. However for St. Eustatius Path 37, depicted by red bounding boxes in Figure 5.36a, pixels occur in the water along the entire western coastline. This could partially be attributed to the occurrence of side lobes. The oil terminals in the northern region of the island are very strong reflectors, as also shown on the mean reflection map (Figure 3.6a), leading to high coherence. The side lobes will therefore also result in a high coherence and are thus incorporated into the coherence-based water mask. However, this does not explain that this pattern is observable along the entire western coastline. The red bounding box, depicted in Figure 5.36b, presents another scenario where pixels are selected in the water along the western coast of Saba. In this case the extent is confined to a steep cliff, marked in red. This cliff corresponds to the location of the previously mentioned landslide in Section 5.2. Both this track, encompassing Saba, and St. Eustatius Path 37 are ascending, thus the sensor is facing the slope, introducing layover effects. It is possible that the layover effect may not be accurately handled within DORIS. There is no specific functionality for layover, foreshortening and shadow in DORIS. Specifically, the DEM used for the georeferencing may be misaligned, affecting the heights assigned to the steep slope. Alternatively, the relatively simple bilinear interpolation used in DORIS may not account for the layover effect properly. In addition, the northern part of St. Eustatius represents the oldest geological unit and is primarily characterized by barren rocks, which are subject to erosion. There is a possibility that the DEM is outdated and does not accurately reflect the significant changes caused by erosion.

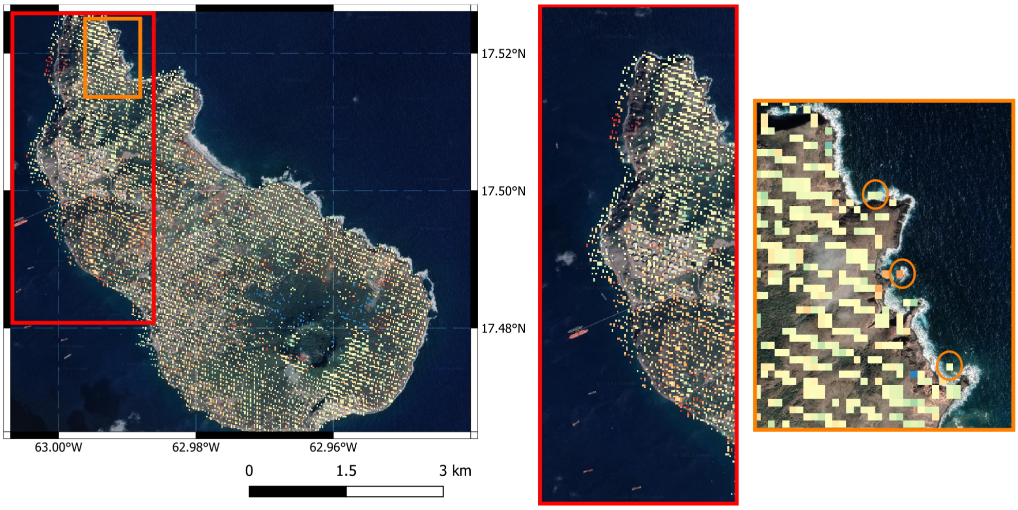

(a) ALOS-2 St. Eustatius Path 37.

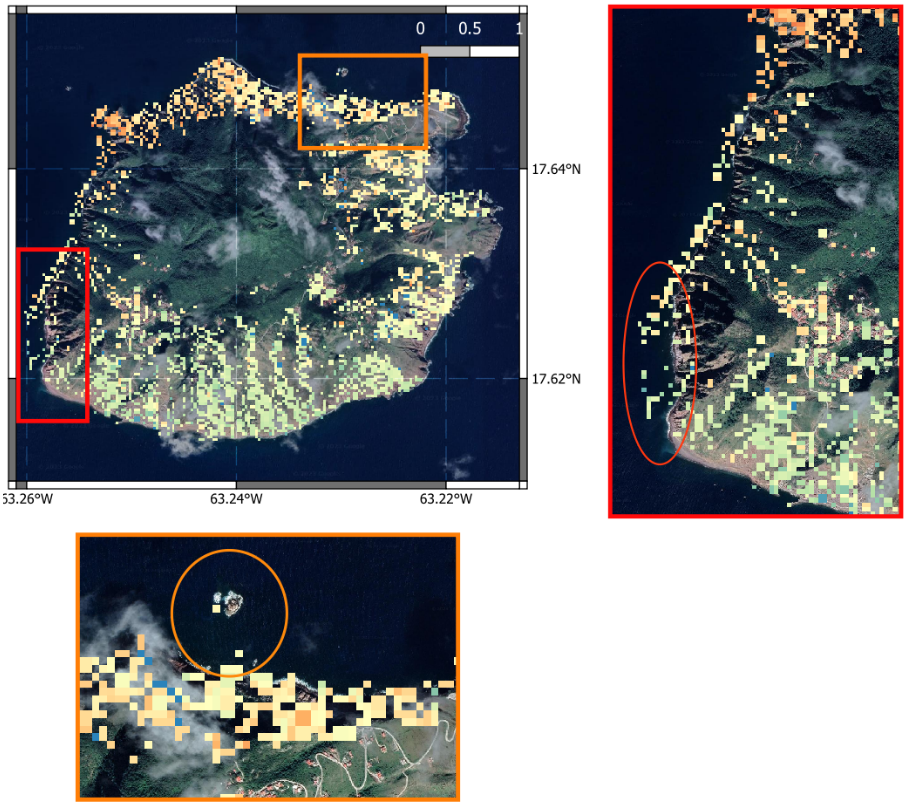

(b) ALOS-2 Saba Path 37.

Figure 5.36: Pixels occur in the water. In some cases, as indicated by the orange bounding box, these can be explained by rocks in the water. In other cases, indicated with the red bounding box, these pixels may be on account of the misaligned DEM used for the georeferencing in DORIS.

A striking difference in spatial pixel coverage can be observed between the ALOS-2 Path 37 result in Figure 5.38a and the Sentinel-1 track 127 result in Figure 5.38b. ALOS-2 provides relatively homogeneous coverage across the island of St. Eustatius, with the exception of the north-east part of the flanks. The limited selection of pixels on this part of the flank, as indicated by the orange bounding box in Figure 5.38a, is likely a result of radar shadow, following from the ascending track. Conversely, the opposite side of the flank, depicted using a red bounding box in the same figure, shows a lot more points. In contrast, for Sentinel-1 most pixels are selected around the harbor, urban areas, denoted using an orange bounding box, and bare rock, denoted using a yellow bounding box in Figure 5.38b. The orange bounding box encompasses an urban area located at the Kultuurvlakte. It can be observed that for Sentinel-1 the pixels are concentrated around houses and open fields, e.g. the airport, but not in more vegetated terrain. When comparing this to the yellow bounding box for ALOS-2 in Figure 5.38a, these vegetated areas are covered. Regarding the flanks of the Quill, few pixels are selected for Sentinel-1, as shown by the red bounding box. With the exception of the Sugar Loaf-White Wall complex as well as some urban areas and bare fields.

When considering a smaller window for ALOS-2, as is done for Path 36 in Figure 5.37 using a window size of 12:7, the coverage significantly increases. Radar shadow appears to occur in the northern part of the island, as indicated with a red circle, but most of the island is covered. However, not all estimates are likely reliable on account of, e.g., geometric distortions. The southeast flank of the Quill exhibits a low sensitivity index in Figure 4.8, thus raising concerns in regard to its reliability. Furthermore, it should be noted that an increased number of isolated pixels are present around the summit of the Quill, which should be corrected for. In addition, several outliers appear to occur across the island.

Similarly, the results for Saba, specifically ALOS-2 Path 37 and Sentinel-1 track 164 are displayed in Figure 5.39a and Figure 5.39b, respectively. Once again, concerning the coverage, the difference between Sentinel-1 and ALOS-2 is significant. Additionally, as indicated by the red bounding box in both figures, Sentinel-1 primarily captures bare rocks and urban areas, while ALOS-2 also includes more vegetated areas. This pattern is also notable in the area enclosed by the orange box. However, in contrast to what is observed for St. Eustatius, merely the outer flanks of Mt. Scenery are covered for Saba, even in the case of ALOS-2. Some pixels are still present in ALOS-2 closer to the summit of Mt.Scenery, however these are sparse and hence unreliable. Finally, the potential processing artifact characterized by sharp edges in the mask, as previously mentioned, is illustrated using the yellow bounding box. It can be observed that this area is situated at the airport and contains land types such as urban and low vegetation, which are expected to exhibit high coherence. Moreover, for Sentinel-1, this sharp edge is not visible. Therefore, this indeed appears to be a processing artifact.

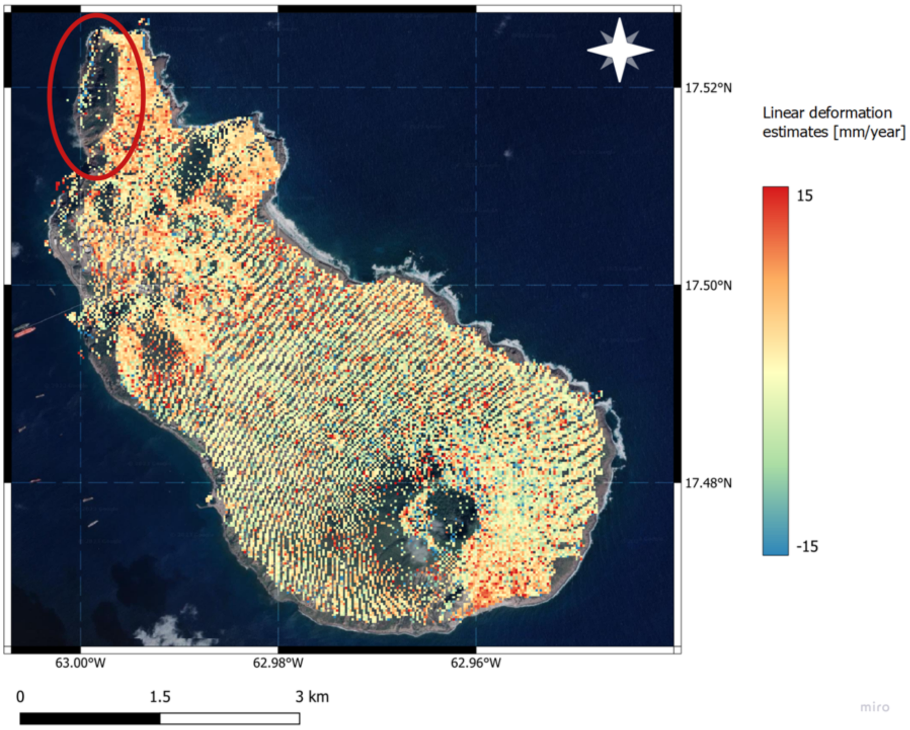

Figure 5.37: ALOS-2 St. Eustatius Path 36 - An artifact, likely due to radar shadow, is highlighted in red. Most of the island is covered, however these may not all be reliable due to e.g., geometric distortions.

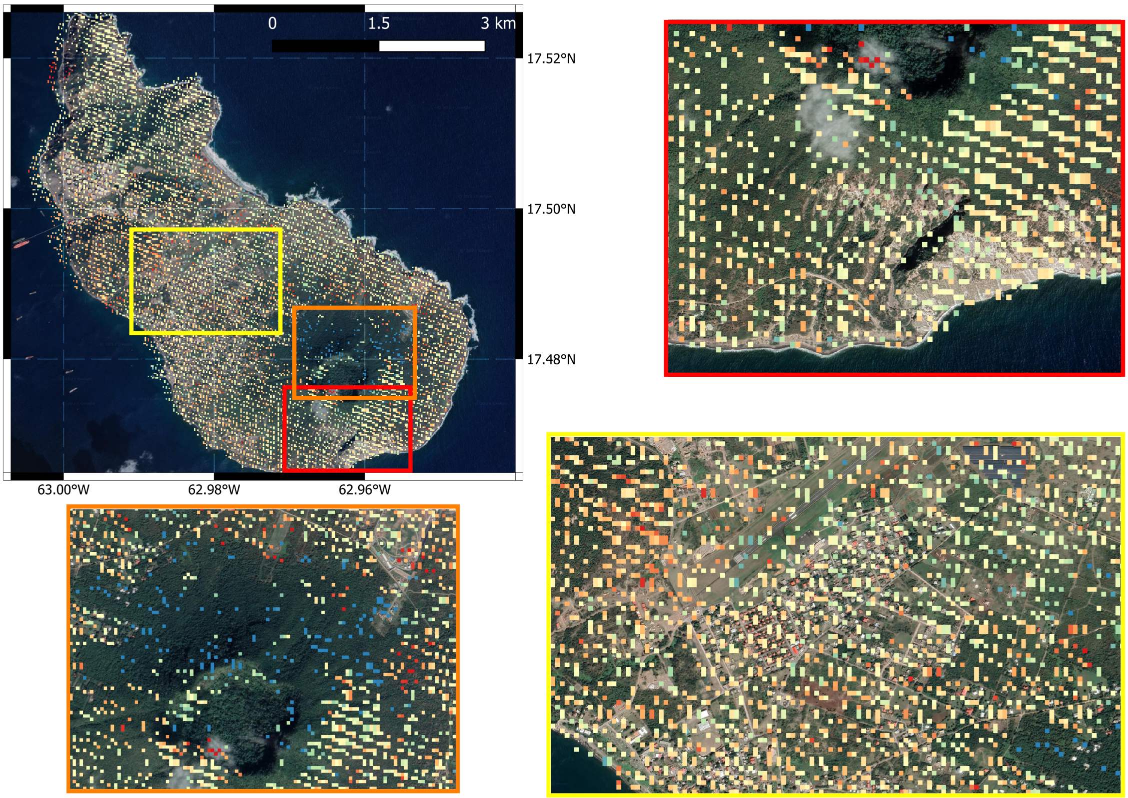

(a) ALOS-2 St. Eustatius Path 37.

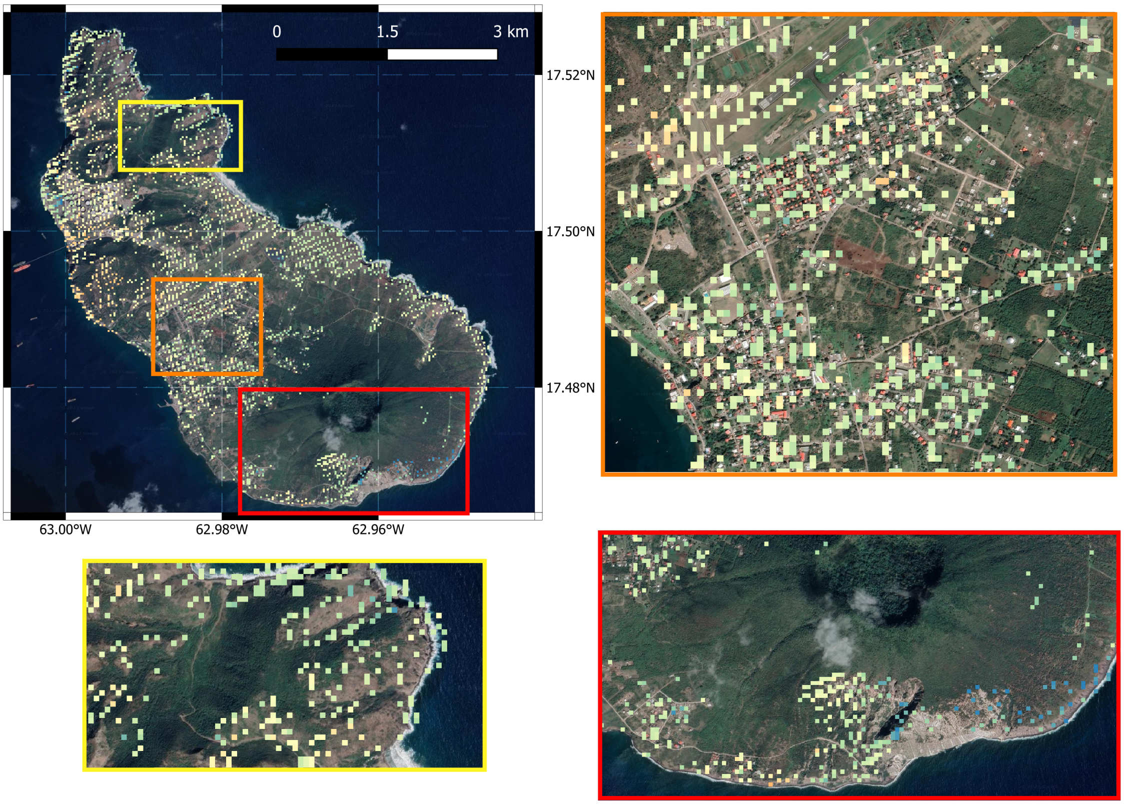

(b) Sentinel-1 St. Eustatius track 127.

Figure 5.38: Bounding boxes are used to highlight interesting features. In general, for ALOS-2 (top figure), nearly homogeneous coverage of St. Eustatius is achieved, except for the north-eastern part of the flanks (orange box). For Sentinel-1 (bottom figure) the coverage is considerably less. Most pixels are selected around the harbor, urban areas (orange box) and bare rock (yellow box).

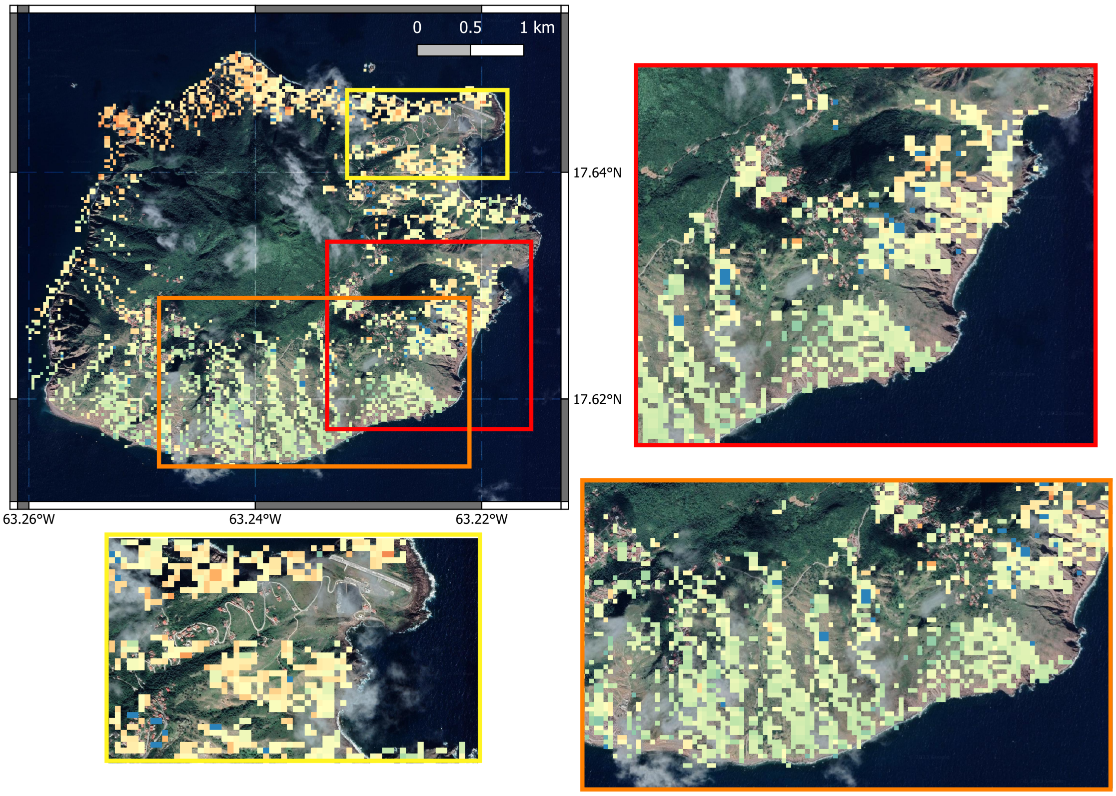

(a) ALOS-2 Saba Path 37.

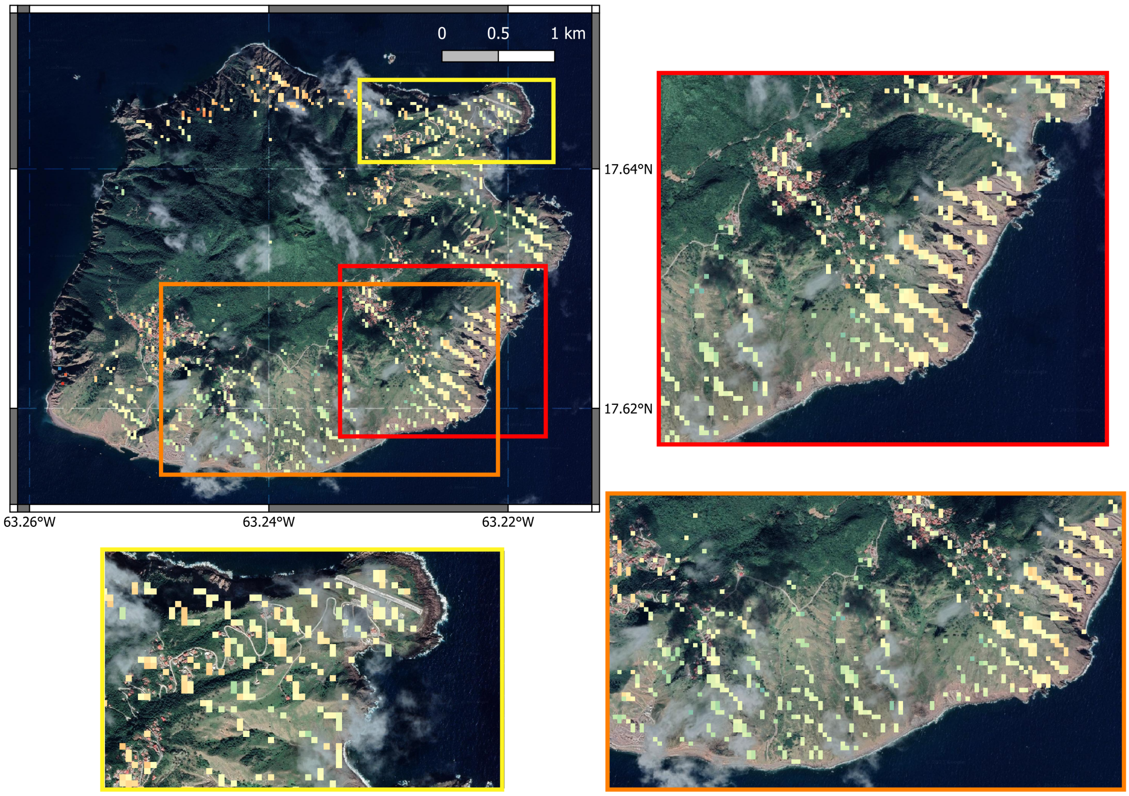

(b) Sentinel-1 Saba track 164.

Figure 5.39: Bounding boxes are used to highlight interesting features. ALOS-2 (top figure) includes densely vegetated areas, while Sentinel-1 (bottom figure) mainly captures bare rocks and urban areas (red and orange boxes). Furthermore, a processing artifact is visible for ALOS-2 (yellow box). In contrast to St. Eustatius, only the outer flanks of the volcano are covered.

5.2.4 Quality Metric: Minimal Detectable Deformation

The minimal detectable deformation (MDD) serves as a quality metric for the detectability of a specific deformation signal. It can be defined as the minimum (estimated) deformation signal that can be detected and distinguished from noise for a pre-defined detectability power (γ) and significance level (α) (Chang et al., 2018). A rough approximation for the MDD ($|\nabla_i|$), assuming an average redundancy (Teunissen, 1989), can be obtained by solving for

$$|\nabla_i| \approx \sigma_{y_i} \left(\frac{\lambda_0}{(m-n)/m} \right)^{1/2}, \tag{5.2.1}$$

where σ_{y_i} is the standard deviation, λ_0 the non centrality parameter, m the number of observations and n the number of unknowns. The MDD is determined for the linear velocity estimates, such that σ_{y_i} can be approximated using the standard deviation following from the single and individual masking approaches as presented in Table 5.2, Table 5.4 and Table 5.7. The average standard deviations of the different tracks and single and individual masking approaches for Sentinel-1 and ALOS-2 are considered for both islands. Furthermore, considering that the number of observations m equals each of the pixels on the islands, the redundancy $m-n$ is also significant, thus $(m-n)/m \approx 1$, and the equation can be simplified to

$$|\nabla_i| \approx \sigma_{y_i} (\lambda_0)^{1/2}. \tag{5.2.2}$$

Finally, standard values for λ_0 for different values of α, γ and the degrees of freedom q, are provided by Teunissen (1989). For $q = 1$, $\alpha = 0.05$ and $\gamma = 0.8$, the value of λ_0 equals about 8. Using a MATLAB function to obtain a more accurate estimation, yields a value of 7.8489. The resulting values of the MDD are presented in Table 5.8. It can be observed that for the worst-case scenario, the MDD equals about 1.5 cm/year.

	Sentinel-1		**ALOS-2**	
	Saba	**St. Eustatius**	**Saba**	**St. Eustatius**
Standard deviation [mm/year]	3.48	3.64	3.50	5.19
MDD [mm/year]	9.75	10.20	9.81	14.54

Table 5.8: The (average) standard deviations for the linear velocity estimates and corresponding MDD for Sentinel-1 and ALOS-2 and both islands.

5.2.5 Concluding Remarks

The results reveal that for both Sentinel-1 and ALOS-2 mm order precision is achieved. Hence, as outlined in Section 1.2, given that in the case of volcanic activity cm up to even dm-scale displacements are expected, such changes should be visible in the deformation estimates. Sentinel-1 stands out on account of its extensive data availability, resulting in over 300 selected data pairs that can be used in the estimation of the deformation values. On the other hand, ALOS-2 compensates for the sparse data availability through its wavelength, limiting decorrelation phenomena as a result of the dynamic vegetation. This means that, even in densely vegetated areas, L-band can effectively capture and monitor changes. The outcomes of ALOS-2 show promise for the implementation of L-band monitoring, even with limited data availability and large temporal baselines. The spatial coverage achieved using ALOS-2 is extensive, providing nearly homogeneous coverage of St. Eustatius, even on the flanks of the Quill, and on the outer flanks Mt. Scenery on Saba. However, due to the low temporal resolution, the detection of fast surface deformation is challenging. The upcoming NISAR mission will complement the current missions with a revisit time of twelve days, providing continuous L-band imaging.

In regard to the masking approaches, it was found that without any land masking the results seem more prone to unwrapping mistakes and the residuals are significantly higher. Furthermore, the central peak in the histograms did not seem centered around zero. Given the assumption of no deformation, values near zero are expected and the spread in values serves as a measure of precision. The single masking approach appeared to be more robust than the individual masking approach, in particular on account of the lower variability as well as the susceptibility of the individual masking approach to outliers. However, generally the deformation estimates for the individual masking approach were closer to zero and the approach appeared to be less prone to unwrapping errors. This was particularly evident for the Sentinel-1 results, in which the histogram of the estimates following from the individual masking approach were centered closer to zero and the residuals did not indicate any erroneous patterns. Overall, the findings reveal a relatively high level of consistency (see Subsection 1.3) among the different masking approaches for ALOS-2. For St. Eustatius, this was apparent after the correction of the unwrapping errors. In contrast, for Sentinel-1 the level of consistency is considerably lower, which is likely mainly on account of the unwrapping errors in the single masking approach.

Still, some challenges arise. The masks show some pixels in the water, which in most cases could be explained by rock boulders in the water or on account of an outdated DEM considered in DORIS. Furthermore, the results for Sentinel-1 indicate the presence of multiple unwrapping errors, suggesting the need for the expansion of the adaptive method to more than one data pair. In addition, an atmospheric correction and estimation of the DEM errors is desired to be able to draw more definitive conclusions regarding the obtained values and, thus, improve data interpretation. Moreover, a layover-shadow mask would be desirable to improve data interpretation.

5.3 PSI

In previous work (Korevaar, 2020) the DePSI software was already applied to the available data sets. For Sentinel-1, not all data sets yielded a closed network, which is essential since the values are relative to a specific spatial reference point. In other words, separate networks do not lead to consistent results, resulting in the rejection of the data stacks from Saba track 164 and St. Eustatius track 127 in this analysis. Hence, these will not be considered here. The key findings derived from the PSI results are highlighted in this Section. For a more detailed analysis of the PSI results, the reader is directed to the study by Korevaar (2020).

The DePSI post software is rerun to explore different filtering parameters. However, to indeed minimize the number of PS in the water while maximizing the number of PS, the thresholds as set by Korevaar (2020) have been considered here as well and are presented in Table 5.9. In addition, considering that InSAR is a relative method, to allow for better comparison with the results from SBAS, outlined in Section 5.2, the spatial reference point is adjusted in *depsi_post.m* to correspond with the same location selected for SBAS. That is, near the airport at a location of high (temporal) coherence, as can be observed in Figure 5.40. It should be noted that as the selected pixels for PSI likely not correspond to those in SBAS, that this is approximate. The spatial reference pixel does not only impact the deformation estimates, but also affects the temporal coherence estimates and is therefore crucial to consider.

The results for Sentinel-1, i.e. the temporal coherence and the linear deformation estimates, are displayed in Figure 5.41 and Figure 5.43 for Saba track 127 and St. Eustatius track 164. The findings indicate a limited spread in the linear deformation estimates, especially for Saba (Figure 5.41). The linear deformation values for Saba appear to be relatively constant and, following from the histogram, are approximately between -12 and 6 mm/year with a central peak around 0 mm/year. Generally, the majority of PS seem to occur in areas with limited vegetation such as in the capital, the Bottom, and the northern region characterized by bare rocks. These regions are also characterized by higher temporal coherence. The entire western coastline is not covered by PS, possibly owing to vegetation and steep slopes. Furthermore, limited PS are detected around the summit of Mt. Scenery. In regard to St. Eustatius, a similar pattern can be observed where the PS mainly occur around the northern region of the island, characterized by bare rocks and limited vegetation, as well as the Kultuurvlakte. The PS density is minimal on the flanks of the Quill and are confined to the coast lines and the villages located on the northwestern part of the flanks. In contrast, compared to Saba, the linear deformation indicates a larger variation across the entire island. The higher magnitude values generally correspond to lower temporal coherence.

The histogram indicates values between -40 and 20 mm/year, but the central peak is still centered around 0 mm/year.

The results for ALOS-2 are visualized in Figure 5.42 and Figure 5.44 for Saba Path 37 and St. Eustatius Path 36 and 37. The results reveal a more uniform spread of selected PS across St. Eustatius for both paths. Overall, the number of selected PS is signficantly larger compared to Sentinel-1 for both islands. However, a significant fraction of the selected PS are detected in the water. For Saba, Mt. Scenery still shows limited PS on the summit. In regard to St. Eustatius, the PS density is particularly limited on the eastern flank of the Quill for both paths. The temporal coherence of Saba and St. Eustatius exhibits notably higher values than for Sentinel-1. This is particularly evident near the coastlines of Saba and in the northern region of St. Eustatius, which could be expected on account of the different wavelengths. The deformation estimates for Saba are centered around 0 mm/year, as visible from the histogram in Figure 5.42, however indicate a relatively high variability with values ranging between -80 to 60 mm/year. For St. Eustatius the spread in values even ranges between -80 and 100 mm/year, as can be observed from the histograms in Figure 5.44. These magnitudes are unrealistic. The high magnitude values are not constrained to specific locations but rather occur across the islands, showing inconsistencies between e.g. the St. Eustatius results from both paths. These values do show some correlation to the temporal coherence, e.g. the northernmost region of Path 36 St. Eustatius (bottom panel in Figure 5.44) shows an increase in linear deformation values corresponding to a decrease in temporal coherence. However, this is not the case for all PS.

	Temporal coherence [-]	**Local temporal coherence [-]**	**STC [mm]**
ALOS-2	0.6	0.6	10
Sentinel-1	0.4	0.4	10

Table 5.9: Filtering parameters considered in the DePSI post software.

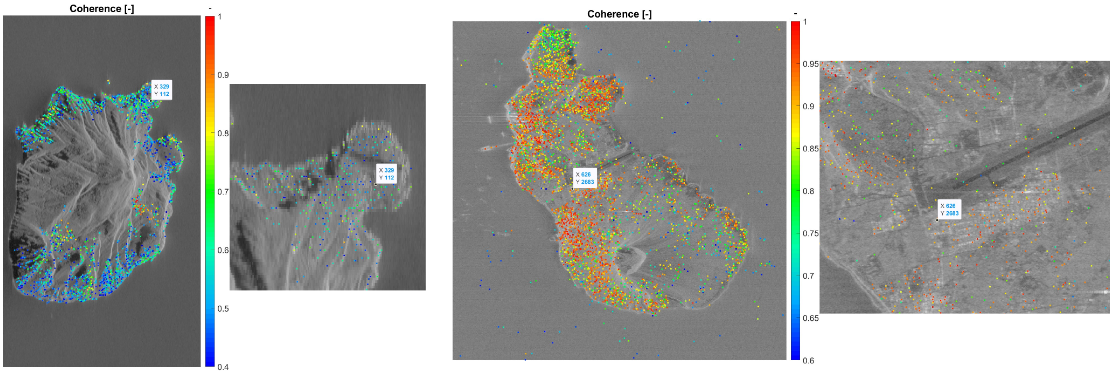

Figure 5.40: Selection of a spatial reference point around the designated SBAS location, denoted in radar coordinates and located at the bottom-left corner of the white box.

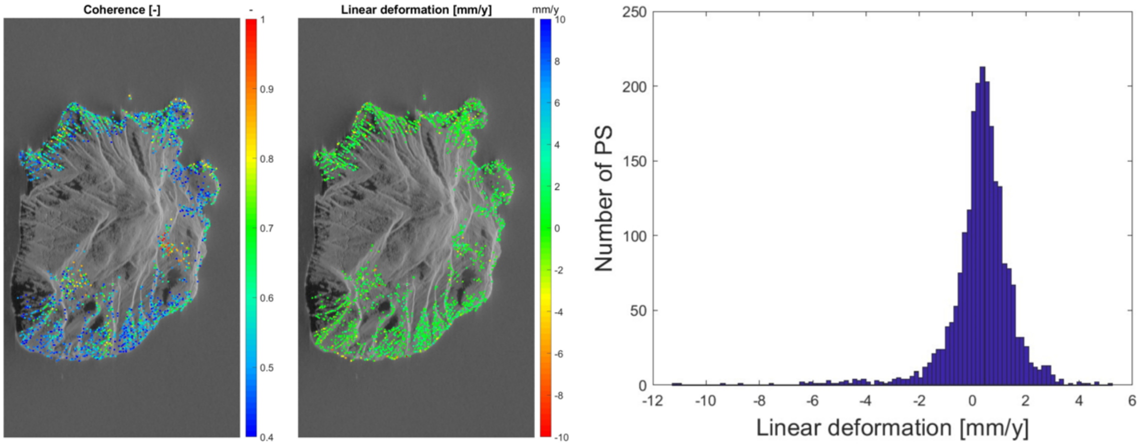

Figure 5.41: Sentinel-1 track 127 Saba - PSI results temporal coherence (left) and linear deformation estimates (middle) with corresponding histogram (right).

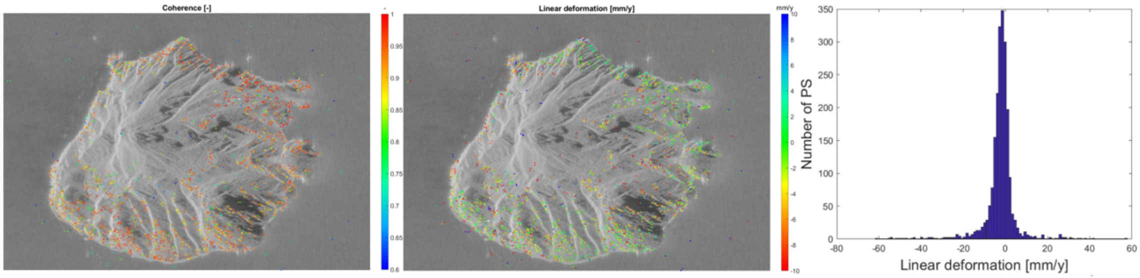

Figure 5.42: ALOS-2 Path 37 Saba - PSI results temporal coherence (left) and linear deformation estimates (middle) with corresponding histogram (right).

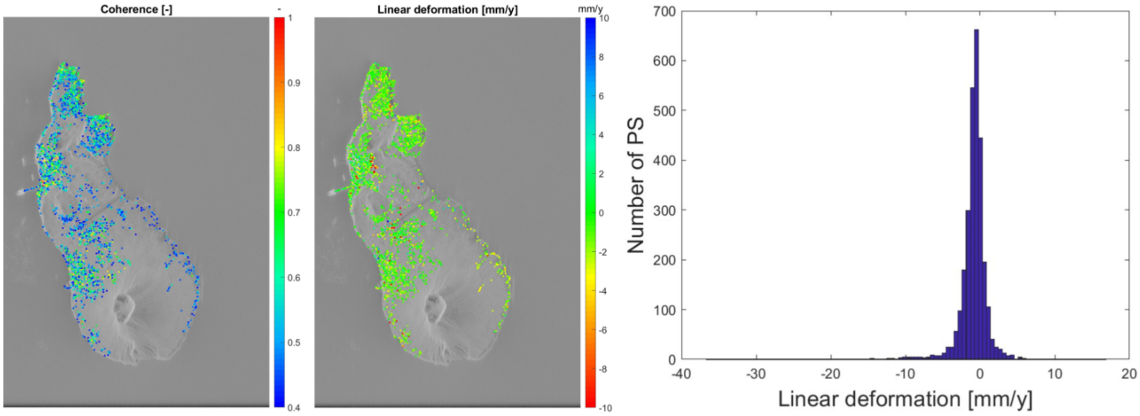

Figure 5.43: Sentinel-1 track 164 St. Eustatius - PSI results temporal coherence (left) and linear deformation estimates (middle) with corresponding histogram (right).

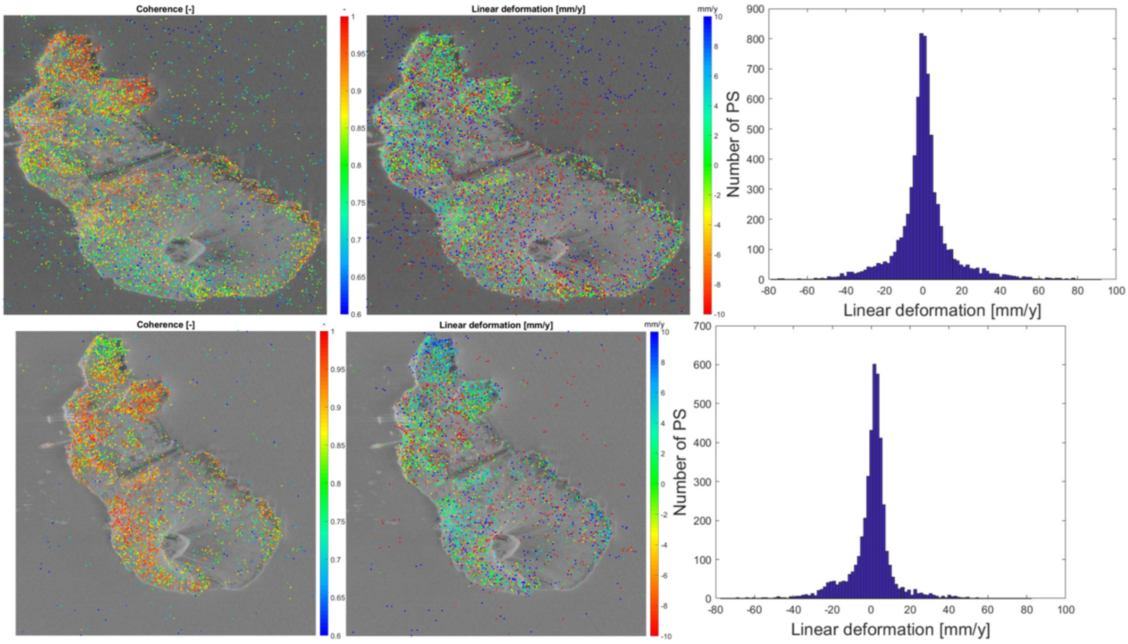

Figure 5.44: ALOS-2 Path 36 (bottom) and 37 (top) St. Eustatius - PSI results temporal coherence (left) and linear deformation estimates (middle) with corresponding histogram (right).

6 Discussion

6.1 SBAS results

In this section, some of the findings from the results presented in Section 5.2, are selected for closer examination. Insights are offered regarding their significance as well as potential implications and solutions.

The results obtained from SBAS demonstrate precision at the mm scale for both Sentinel-1 and ALOS-2. This implies that in the event of volcanic activity, which is expected to induce surface displacements ranging from cm up to even dm's (Section 1.2), these changes will be visible in the deformation estimates. However, it should be noted that early signs of volcanic activity may not be as pronounced at the onset of the event. Consequently, these signal may not appear strongly in the deformation estimates. Since early detection is crucial for providing timely warning to the local authorities, the implementation of an atmospheric correction of the InSAR estimates is necessary. Furthermore, if an anomaly is detected within the linear deformation estimates, it is essential to consider the instantaneous velocities of the most recent epochs in the time-series.

Noteworthy findings emerge from the various masking approaches considered. The results from ALOS-2 exhibit a relatively high level of consistency among the different masking approaches. In regard to the St. Eustatius paths, this consistent pattern is acquired after implementation of the unwrapping error correction. Therefore, it appears that the ALOS-2 results are independent of the selected mask. In contrast, overall, the Sentinel-1 results give different outcomes. This indicates a low level of robustness and low reliability. This is surprising considering the substantial data availability of Sentinel-1. The individual masking approaches, aside from few larger outliers, show a relatively small spread in values. In addition, the residuals are closer to zero than for the single masking approach. The single masking approach results indicated the presence of several unwrapping errors and therefore the individual masking results may be more reliable. Further investigation is required however to draw more solid conclusions.

The different testing approaches showed significant improvements, for both the interferogram removal and adaptive approaches, leading to a relatively high level of consistency in the ALOS-2 results. Due to the presence of numerous unwrapping errors that appeared in Sentinel-1, an expansion of the testing approach to correct multiple erroneous epochs rather than one is desired. Hence, the approach should be extended with an iterative loop. The corrective method is preferred on account of the direct comparison between the old and new residuals and because of the preservation of the observations. However, the thresholds used to reject or re-sustain outlier candidates differ among the approaches and resulted in the sustainment of more outlier candidates for the approach based on the (temporary) removal of these outlier candidates. This could also mean that the threshold for this approach is too low, compared to the corrective method. More research regarding the appropriate thresholds is required, however due to the (overall) similar results, the corrective method is preferable. In addition, the selection of a threshold for the identification of the erroneous pattern is challenging. The implemented approach, explained in Section 4.1, does show promising results. The majority of the erroneous patterns in both ALOS-2 paths for the St. Eustatius have been successfully detected and corrected. Alternative approaches to set a more optimal threshold, should however be explored to find a more robust approach. In addition, an approach in which epochs with even a single outlier candidate are corrected.

6.2 Comparative analysis PSI and SBAS

An assessment of the most suitable method for InSAR-based volcanic monitoring on Saba and St. Eustatius is performed, based on both a theoretical as well as a semi-quantifiable approach. In the theoretical assessment, literature review is key. The limitations and strengths of both methods are explored to be able to understand correspondence and declare differences in the results, in terms of estimated deformation time series, obtained by the two methods. However, ultimately, the suitability will depend on the specific characteristics and conditions of the study area. Ideally, ground truth data, from the GNSS stations for instance, could be used to evaluate the accuracy of the deformation measurements. However, this is limited to four measurement locations per island. Also, GNSS data shows that currently no ground-deformation occurs, which further complicates the comparison due to the absence of a strongly variable signal. Alternatively, decorrelation phenomena can be used as a measure of the quality of the InSAR measurements. Both methods are susceptible to decorrelation, however the extent to which the methods are affected can differ depending on the conditions of the area. The coherence characterizes the extent of decorrelation phenomena. The quantifiable comparison of the results will therefore be based on the precision of the displacement time series, in terms of the temporal coherence. It should be noted that the results from both approaches cannot be compared 1:1, since the atmospheric and height corrections have not been applied to SBAS. This complicates the comparison process based on quantitative measures. A more qualitative comparison is based on 1) the spatial distribution as well as density, 2) difficulties encountered in the processing steps and 3) computational requirements. Concluding remarks are then made regarding the (expected) ability to detect volcanic signals.

Literature review

The respective advantages and limitations of both methods, as found from literature, are summarized. First of all, SBAS is characterized by its extensive spatial coverage, offering a distinct advantage over PSI. While PSI typically provides high PS density in urban areas and bare rocks, its coverage might be limited in more rural regions and on steep slopes where ground deformation can also occur. Therefore, SBAS could be more useful for studying deformation over large regions and for spatially correlated deformation signals i.e., part of an interconnected pattern. On the other hand, following the multilooking step in SBAS, the spatial resolution is reduced and high-quality signals may be lost. Given that PSI relies on individual pixels, rather than spatially correlated pixels as in SBAS, it maximizes spatial resolution and minimizes signal loss (Xue Chen et al., 2020; Yao et al., 2022). Hence, SBAS may be less suitable for detecting local deformations (Crosetto et al., 2016), e.g., of a civil structure.

On account of the selection of single coherent pixels in PSI, the complete available interferometric stack is exploited (Ferretti et al., 2000). In other words, a so-called full network approach is considered. This allows for extensive phase information and improved error estimation, such as the atmospheric signal delay (Van Leijen, 2014). In contrast, the SBAS method is restricted by the spatio-temporal baseline and could therefore result in less accurate estimation of atmospheric errors (Li et al., 2022). Nonetheless, the combination of the baseline restriction and coherence-based pixel selection procedure as well as the multilooking operation of the SBAS method, allow for significantly limiting the decorrelation phenomena (Berardino et al., 2002). Therefore, compared to the full network approach of PSI, SBAS is considered to perform well in the case of fast decorrelated pixels (Izumi et al., 2022). PSI is more prone to the limitations in the ability to measure fast deformation phenomena, on account of the ambiguous nature of the phase observations. In addition, the ability of PSI to detect a non-linear trend is highly dependent on the number of SAR images in a stack (Xue Chen et al., 2020). However, typically multiple baseline subsets are formed following the SBAS approach. As a result, rank deficiency problems arise during the least-squares inversion procedure. To address this problem the SVD method can be used, although its application can introduce large discontinuities (Berardino et al., 2002).

In terms of some of the processing steps, PSI generally demands a predefined deformation model as input for resolving the phase ambiguities. If the deformation history is known, this can allow for the identification of unreliable data. In addition, the PS density can be improved. If this is not the case, a deformation model is assumed, which could contribute to model imperfections (unmodeled deformation) if the deformation model is not representative of the true deformation in the specific study area (Van Leijen, 2014). The selected model can dominate the time series patterns, which is crucial to take into account during data interpretation (Crosetto et al., 2016). Conversely, there is no need to assume a deformation model in SBAS. Furthermore, establishing a network in PSI with adequate coverage over the study area is crucial to obtain consistent deformation estimates. Regarding the multilooking procedure in SBAS, aside from the reduced spatial resolution and less accurate position following from averaging the latitude and longitude over the same windows as done for the multilooking procedure, a phase bias correlated with the temporal baseline is introduced. On the contrary, PSI enables the identification of relatively stable scattering points without the use of multilook processing.

Spatial Coverage

SBAS is known for its extensive spatial coverage, however the extent of the coverage of both methods is dependent on the study area as well as the coherence threshold used. Specifically, as the coherence threshold increases, noise decreases, but this leads to a decrease in spatial coverage and, potentially, the loss of valuable data, and is thus a trade-off. To compare this extent the results of both methods are imported into QGIS. SBAS results are available in GeoTIFF format, while PSI results are available in .csv format. The Sentinel-1 results are compared: track 164 for St. Eustatius Figure 6.1a, and track 127 for Saba Figure 6.1b. Since the individual masking approach generally resulted in values closer to zero and less variability, with the exception of some large outliers, the individual mask results are considered here. It is worth noting that for ALOS-2 the coverage is notably more extensive, as described in Section 5.2 but a constant shift in the geocoded results obtained from DePSI for ALOS-2 data, make a comparison currently not feasible. However, the number of selected pixels for all data sets, following from the different methods and masking approaches, are included in Table 6.1.

In Figure 6.1a, a substantial contrast appears in the coverage achieved by SBAS in comparison to PSI. It can be observed that on average the coverage acquired by SBAS is distributed among a significant portion of the island. Nonetheless, the heavily vegetated areas have limited coverage, as previously noted in the data analysis in Section 5.2, in comparison to ALOS-2. In contrast, PSI primarily detects PS in urban areas and bare fields, resulting in concentrated PS clusters. This pattern is especially prominent in the northern region of the island, characterized by erosion, sparse vegetation and the oil terminal, evident on the complete map of St. Eustatius. A close examination of the urban areas around the Kultuurvlakte, depicted by the yellow bounding box, reveal a similar pattern. That is, PS density is significant near stationary structures such as houses, while the fields surrounding such structures have limited PS coverage. Additionally, smooth surfaces characterized by low reflectivity, like the airport runway included in the yellow bounding box, show low PS density. Conversely, the SBAS pixels show relatively high and consistent coverage over the fields, except for densely vegetated patches, as well as along the entirety of the airport runway. Similarly, in the volcanic region marked by the orange bounding box, there is notable PS density in the urban areas on the north-west and south-west flanks. However, the steeper slopes, like the Sugar Loaf-White Wall complex as well as the progressively vegetated areas up the slope of the Quill, primarily rely on SBAS for coverage. Depending on the type of volcanic activity, various deformation patterns can emerge. Small-scale deformation at the summit or flank of the volcano could occur prior to the onset of eruptive activity, therefore it is essential to have coverage over these areas. However, when magma is accumulating, broader deformation could extend from the flanks of the volcano up to the entire island. Another interesting finding arises in the region designated by the green bounding box, i.e., a considerable number of PS appear in the water. These could possibly be explained on account of a height estimation error, resulting in a geolocation error.

For Saba, it is more challenging to acquire any coverage of the summit of Mt. Scenery, even with SBAS, as evident from Figure 6.1b. Few isolated SBAS pixels are distributed around the summit, but owing to the number of pixels, they seem unreliable. The coverage primarily occurs on the outer flanks for both methods. As was observed for St. Eustatius, PSI predominantly exhibits high PS density around urban area, as depicted with the yellow bounding box. From this region it can be observed that even in the case of limited to no vegetation, the PS density is relatively low on steeper slopes. Within the region bounded by the green box, it can be observed that although the PS density is relatively high on specific parts of the weathered slopes, this is not the case everywhere. i.e., inside the steep sided valleys ('guts') running down the slopes of Mt.Scenery, the density decreases. This could partially be on account of radar shadow, however in that case the exact same pattern should be visible for SBAS, which is not the case everywhere. Furthermore, at higher elevations on the slopes of Mt. Scenery, there is a significant drop in PS density in comparison to the SBAS pixels. The distribution of both SBAS pixels and PS is denser and more homogeneous towards the northern region of Saba, likely due to the bare cliffs. Another interesting pattern is observed around the western coastline of Saba, indicated with an orange bounding box. The entire coastline is covered by SBAS, while for a substantial portion of the cliff not a single PS is detected.

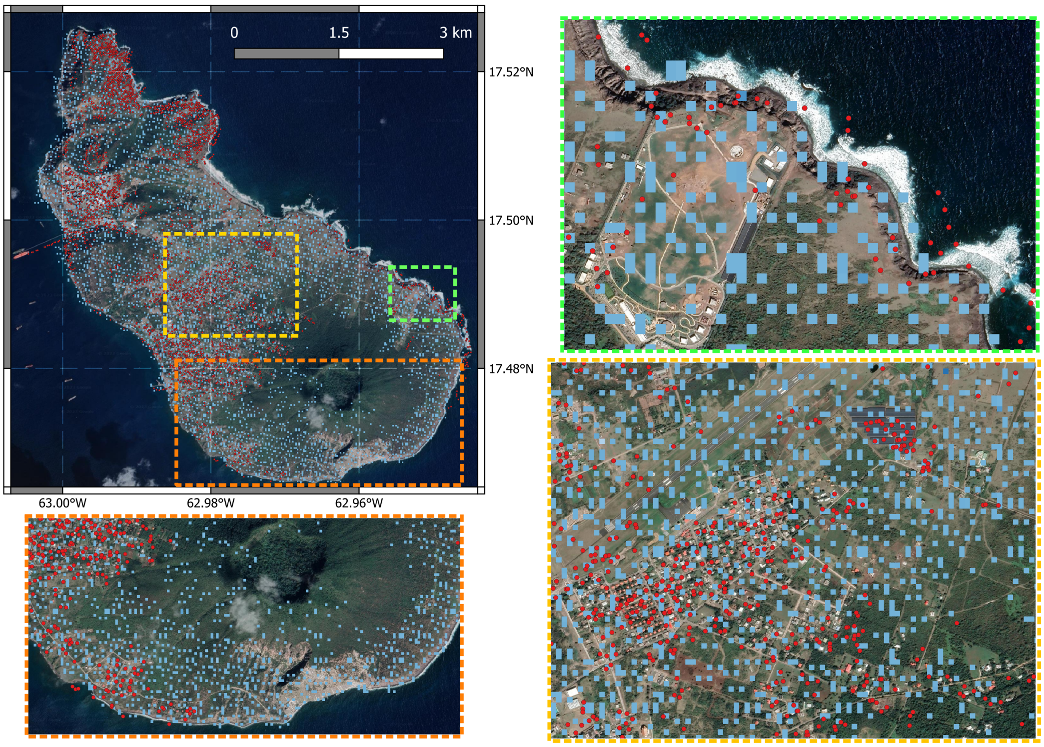

(a) Sentinel-1 track 164 St. Eustatius.

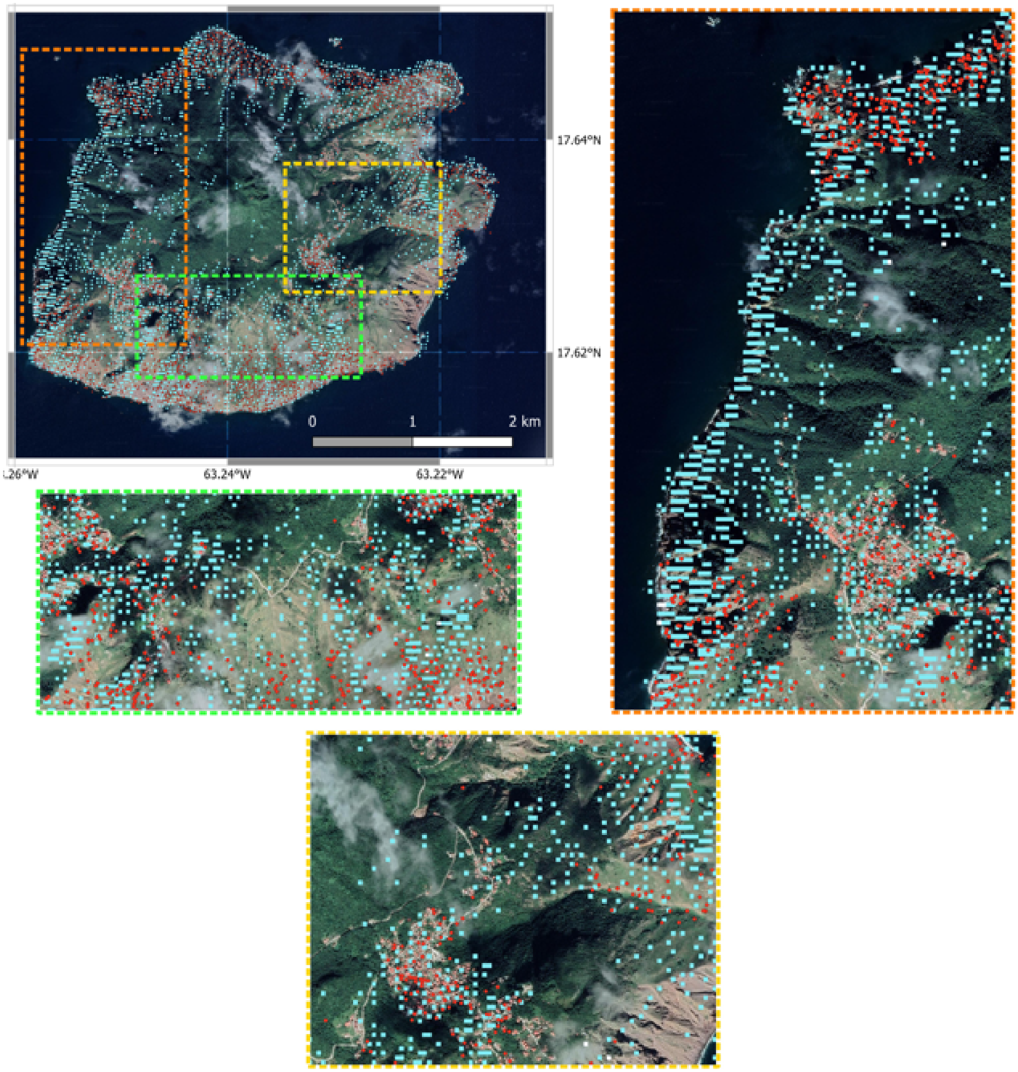

(b) Sentinel-1 track 127 Saba.

Figure 6.1: Geocoded PSI and SBAS results in QGIS. Bounding boxes are used to highlight interesting features. The red pixels indicate the detected PS from the PSI method, the blue pixels follow from the SBAS approach.

Hence, SBAS gives measurements where PSI does not, including large portions of the flanks of the Quill, along the cliffs on Saba and the outer flanks of Mt. Scenery. For monitoring purposes as much coverage as possible is desired, especially on the flanks of the volcano, such that no volcanic deformation signal goes unnoticed in areas of low PS density. Given the especially challenging conditions on these islands, deformation rates of steeper rural areas could hold important information in times of volcanic unrest.

	St. Eustatius			**Saba**	
	Sentinel-1	**ALOS-2**		**Sentinel-1**	**ALOS-2**
	track 164 ascending	**path 36 ascending**	**path 37 ascending**	**track 127 descending**	**path 37 ascending**
PSI	2842	4262	7222	2249	2275
SBAS single mask	5226	29373	35377	3451	3093
SBAS individual masks	8728	33218	42663	4532	3720

Table 6.1: The number of selected PS and SBAS pixels (single and individual masks).

Processing steps

The processing steps for the SBAS and PSI approaches present a range of difficulties that vary depending on the particular study area. The challenges encountered for Saba and St. Eustatius are highlighted here.

One of the challenges faced for PSI involves the construction of a spatial network to connect individual PS. This network is created using arcs, as described in Section 2.2.2, to establish a spatial relationship among these PS. If a single network cannot be constructed, i.e. on account of large distances between PS, this has implications for the deformation estimates. Specifically, in the scenario of separate networks, each of these are relative to a distinct spatial reference, resulting in inconsistencies that prevent meaningful comparisons. This issue was encountered in the analysis of two Sentinel-1 data sets, yielding three separate networks, as presented in Figure 6.2: St. Eustatius track 127 (top figure) and Saba track 164 (middle figure), leading to the rejection of the respective data stacks. Furthermore, even when a single network can be established, the density of the network is an essential factor to obtain a more redundant network and thereby increasing the reliability of the estimates as well as improving the detection of unwrapping errors. In addition, the coverage across the study area is important for the atmosphere estimate. The bottom figure in Figure 6.2 illustrates the network for St. Eustatius track 164. While a single network was acquired, the density and coverage are not optimal. The arcs are primarily concentrated in specific regions, with sparse distribution in other parts of the island, i.e. the isolated PS on the south-eastern part of the island. In addition, the urban area on the western flank of the Quill lacks arc connections. Consequently, this could lead to difficulties in the phase unwrapping procedure, which will impact the deformation estimates in those regions. In comparison, the SBAS approach relies on the spatial relationship between the pixels, rather than looking at individual point scatterers, and hence does not require such an approach. However, a comparable issue arises in the masking step. Due to large distances between certain selected pixels in the masking procedure, similar to PSI, some pixels are not connected within the spatial network. As a result, the phase values of these individual pixels are not resolved correctly during the unwrapping procedure and thus yield unreliable deformation estimates. This phenomenon typically occurs around incoherent regions which still contain some coherent pixels, such as the summit of the volcanoes as shown in Figure 6.3 for St. Eustatius path 37. These isolated pixels are characterized by unrealistically high magnitude values and should be removed. However, for SBAS, this problem does not complicate the construction of a network, nor does it impact the reliability of an entire stack, as is the case with PSI. In addition, a relatively quick fix can be applied to solve for this problem, e.g. by using a moving filter based on the number of neighbors in each window.

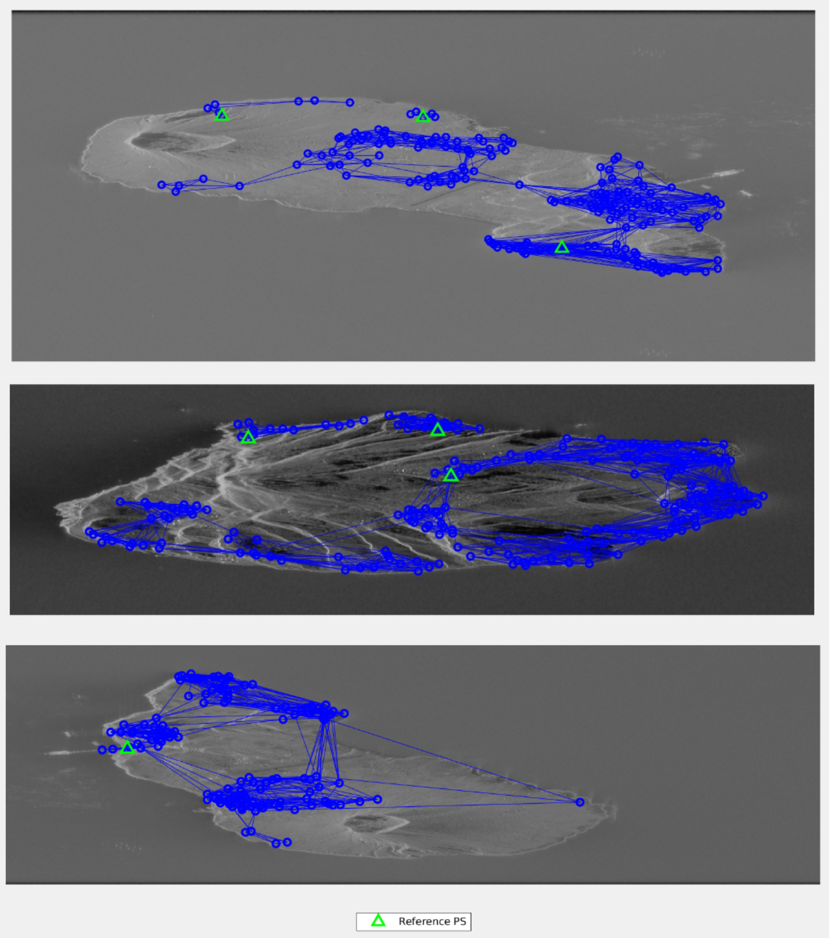

Figure 6.2: Problems arise during the construction of a spatial network in PSI. In some cases separate networks are obtained, leading to the rejection of these stacks (top and middle), or e.g. the network coverage is sub-optimal (bottom), potentially leading to unwrapping errors.

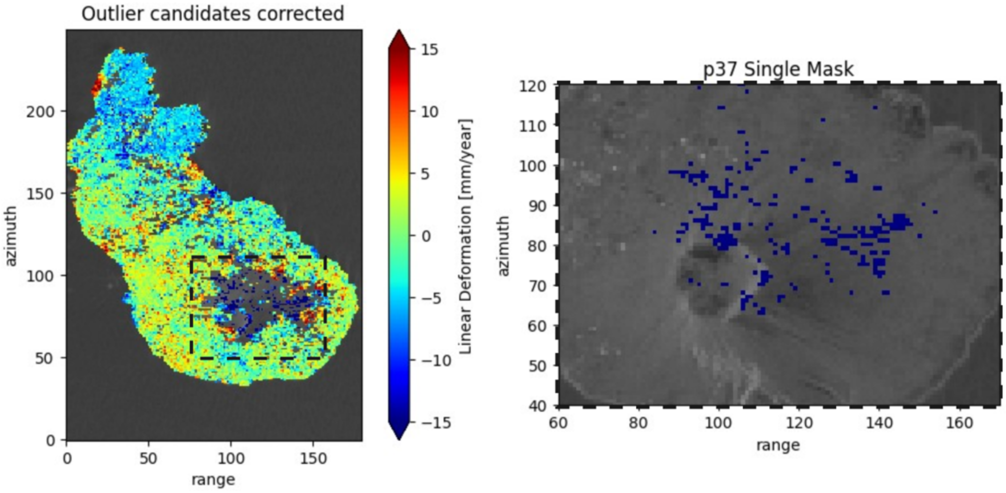

Figure 6.3: ALOS-2 St. Eustatius path 37 - Isolated pixels are typically found in incoherent regions, e.g., the summit of the Quill. These are not properly linked in the unwrapping process and are therefore unreliable.

The multilooking step in the SBAS approach involves averaging the latitude and longitude coordinates, corresponding to the radar coordinates, over the same window. This procedure affects the accuracy of the geocoded location and the suitability of SBAS for detecting local deformations, e.g., at the scale of individual buildings. However, in the context of volcanic monitoring, it is also possible that deformation will extend across a significant area, rather than being confined to a localized region. On the other hand, the multilooking procedure introduces a noise term that is correlated with the temporal baseline. Since SBAS relies on selecting coherent interferograms, typically characterized by minimal temporal and perpendicular baselines, the impact of this phase bias should be taken into consideration. The effect of using different window sizes for multilooking is demonstrated for the ALOS-2 path 37 data set for Saba in Figure 6.4. The results generally show consistency, in terms of the observed patterns. Greater detail is captured with the smaller window size due to the increased number of selected pixels. However, accordingly an increased number of the previously mentioned isolated pixels occur around the summit of Mt. Scenery. While the PSI method may not require the use of multilook processing given that individual pixels are considered, the spatial coverage obtained is limited, as discussed in the preceding step. In other words, to facilitate the study of large-scale deformations, i.e., those occurring over a wide area, the use of multilooking becomes necessary.

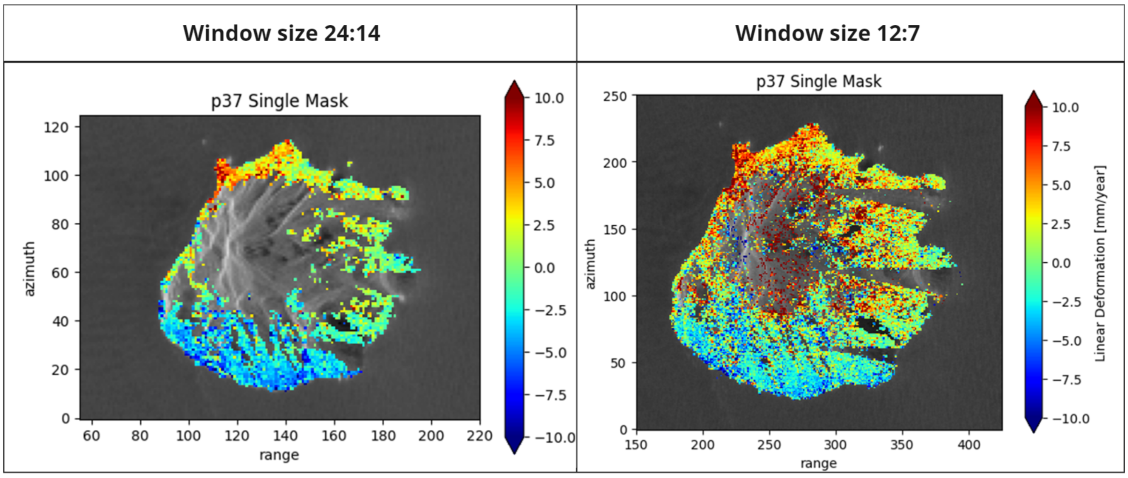

Figure 6.4: ALOS-2 path 37 Saba - Linear deformation estimates using different window sizes for multilooking: a larger one (24:14) resulting in less isolated pixels (left) and a smaller one (12:7) showing greater detail but more isolated pixels (right).

Finally, PSI requires a predefined deformation model of the expected deformation. Due to the uncertainty around the eruption history of both Saba and St. Eustatius, given that the last recorded volcanic eruptions likely occurred around 1640 A.D. and 1755-1625 years B.P., it might be difficult to model the deformation in case of unrest. i.e., a linear model is likely suitable for dormant behavior, but it may fail to detect sudden uplift or subsidence during volcanic unrest. Incorrect deformation modeling can affect volcanic risk assessment. That is, overestimation or underestimation of the deformation could lead to incorrect conclusions. Particularly in the case of underestimation, this can compromise the effectiveness of early warning systems and delay evacuation. Additionally, during the spatial ambiguity resolution step, arcs are deemed unreliable based on their temporal coherence. This can occur due to model imperfections, e.g. due to unmodeled deformation, rather than noise levels, resulting in excluding these arcs (Van Leijen, 2014). One of the advantages of SBAS is that it does not require a deformation model as input.

Computational requirements

To facilitate automated InSAR volcano monitoring, it is essential to carefully assess the computational requirements. To ensure timely warning of local authorities in the event of volcanic activity, the software must provide data within a reasonable time frame.

In general, PSI typically demands more storage considering that all available data is utilized.

Although storage demands significantly decrease after the selection of PS, the analysis of individual pixel time series can be quite time consuming as it involves more complex computations. In contrast, SBAS requires fewer data selection steps compared to PSI and relies on multilooked pixels, reducing computational complexity.

To improve the processing times involved, efforts to enhance the efficiency of both approaches are necessary. Specifically, to increase the efficiency for SBAS, if feasible, the computations for SBAS have been implemented for all pixels and/or time-dimensions in one go. Conversely, PSI involves iterative procedures that cannot be circumvented as done for SBAS. Furthermore, in the context of volcano monitoring, it may be critical to explore alternative ways for incorporating new images, without a complete rerun. This is a trade-off between limiting processing time and improving estimations. For instance, the atmospheric approximation differs when adding a new image, which would make it desirable to rerun everything such that the atmospheric approximation can be improved. Owing to the complexity of the analysis of individual pixels, it may be more feasible to implement something like this for SBAS than for PSI.

Precision

The precision is assessed based on the temporal coherence, but to enable comparisons, additional steps are required. PSI relies on individual point scatterers and, therefore, the quality description cannot be done based on spatial coherence like in SBAS. Instead, the temporal coherence is considered. The temporal coherence could give an indication of how well the methods perform in capturing the temporal variability of the scattering properties of pixels. To still be able to compare between the two methods based on coherence, the same metric can be determined for SBAS. For each pixel, with respect to the spatial reference pixel, a line is fitted through the deformation time series to obtain the model phase. Using Equation 2.2.9, the temporal coherence can be obtained for SBAS. It is important to highlight once again that exact one-to-one comparisons of the results are not possible This is because in the case of SBAS, e.g. the atmospheric signal delay and height corrections have not been accounted for. This also has an effect on the temporal coherence, introducing a distance dependency with respect to the reference PS. Furthermore, the temporal coherence is not sensitive to unwrapping errors. To address this, additional metrics should be considered, such as the standard deviation or the root mean square error. However, due to the absence of an atmospheric correction in SBAS, these metrics are not suitable for comparing the results for the different methods. Therefore, the primary focus lies on assessing the consistency of the results.

The temporal coherence for the different data sets are presented in Figure 6.5 and Figure 6.6, for St. Eustatius and Saba, respectively. Notably, the Sentinel-1 SBAS results exhibit remarkably low temporal coherence, as can be observed from the lower right-most figures. Overall, Sentinel-1 is expected to have a lower temporal coherence than ALOS-2 on account of the difference in wavelengths. This is also apparent for the PSI Sentinel-1 results in the right most figure for both islands in comparison to ALOS-2 results (first two columns). However, for SBAS these values are exceptionally low, with most values below 0.4. This can likely be explained by the absence of an atmospheric correction for SBAS, which is especially challenging for shorter wavelength, like C-band, due to signal attenuation. Consequently, definitive conclusions in regard to the precision should be drawn after applying an atmospheric correction. However, the distance dependency with respect to the reference PS is evident in the Sentinel-1 results for both islands, with higher values near the spatial reference pixel (lower right columns).

For ALOS-2, a generally consistent pattern emerges across the islands in both PSI and SBAS, as well as in the different masking approaches. This is particularly evident for St. Eustatius, where higher temporal coherence can predominantly be observed in the central region of the island, near the Kultuurvlakte. This observation aligns with the expectations, on account of the low terrain variability and limited vegetation of this area. In addition, the northern region of the island, extending up to the harbor area, is characterized by high temporal coherence and shows homogeneity, especially in the individual masking results obtained from SBAS. This can be attributed to factors such as the the bare bedrock in the north as well as the presence of oil terminals near the harbor. Notably, especially path 36 yields high coherence values for both methods. In contrast, the southern part of the island, near the Quill, reveals more variability in coherence values. This variability could be linked to the dynamic vegetation covering the Quill, which alters the scattering properties. Depending on the specific path, certain sections of the flanks have lower values for PSI as well SBAS, likely due to geometric distortions. The temporal coherence patterns observed for SBAS seem to be consistent with PSI overall, with the exception of the area corresponding to the Sugar Loaf-White Wall complex. As has been discussed in Section 5.2, this location displayed a strong signal which may result from incorrect topographic phase removal in the pre-processing steps.

Furthermore, the temporal coherence among the different methods and masks for Saba also shows consistency (Figure 6.6). The temporal coherence is relatively high on the flanks of Mt. Scenery, but decreases toward the summit in all cases. The cliff on the western coastline, exhibits somewhat lower temporal coherence, potentially on account of the 2014 landslide, which has caused significant terrain changes over the years. In addition, the steep gullies in the southern part of Saba also display lower coherence values, in particular for SBAS. Conversely, the northern part of the island is characterized by relatively high temporal coherence in all cases.

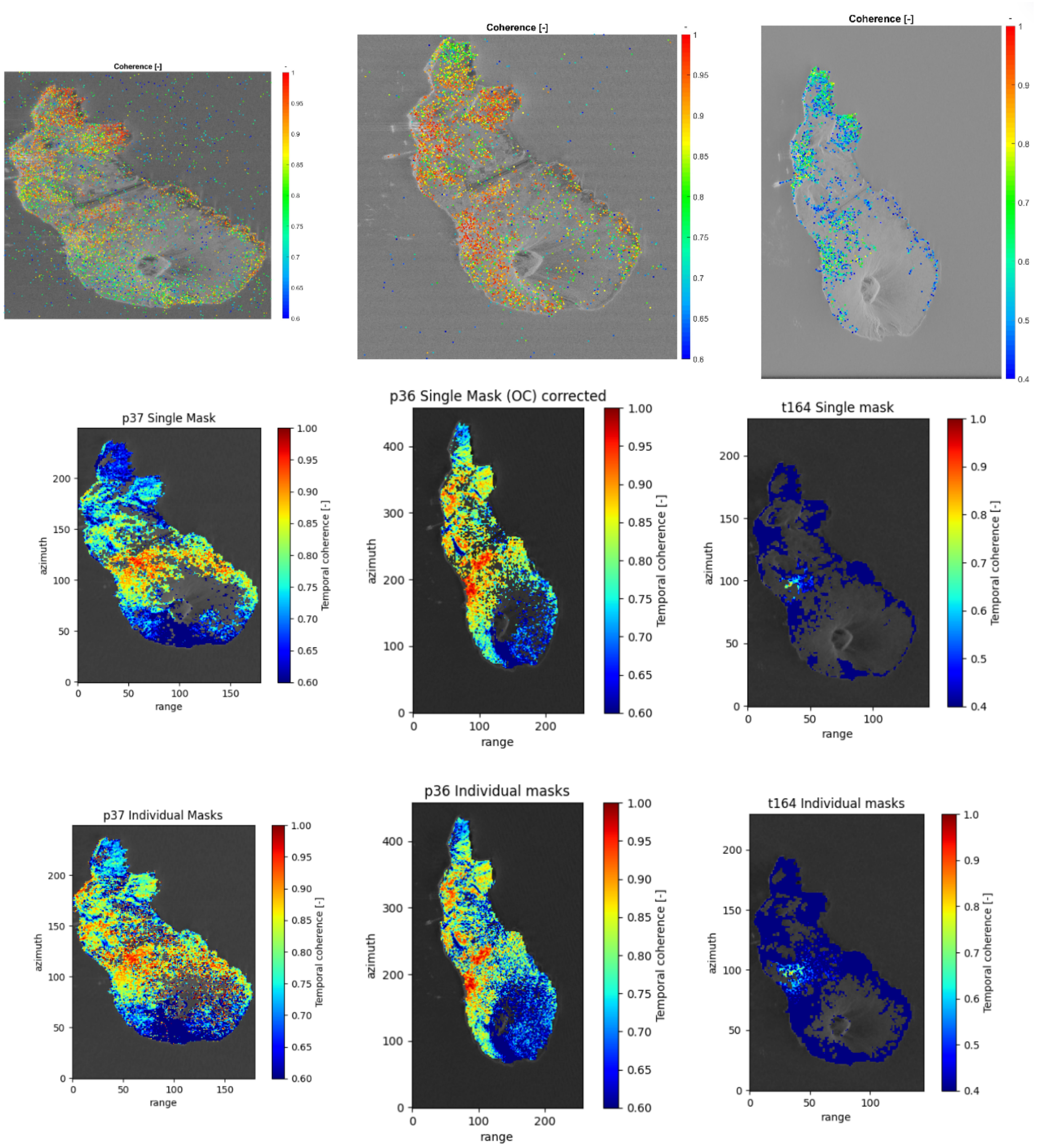

Figure 6.5: Temporal coherence of St. Eustatius for the ALOS-2 (first two columns) and Sentinel-1 (last column) results of PSI (top panel) and SBAS for the single masking approach (middle panel) and the individual masking approach (bottom panel).

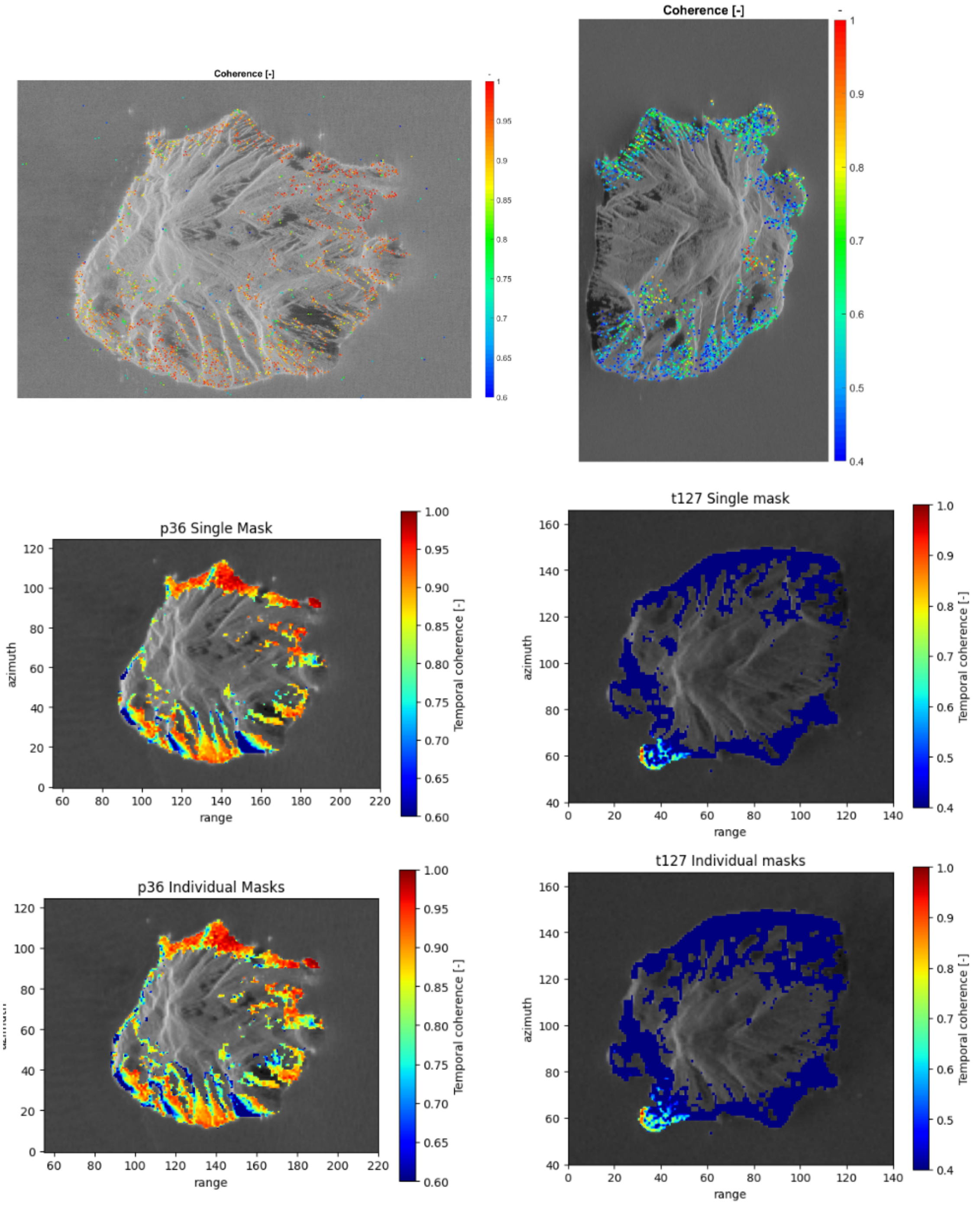

Figure 6.6: Temporal coherence of Saba for the ALOS-2 (first column) and Sentinel-1 (second column) results of PSI (top panel) and SBAS for the single masking approach (middle panel) and the individual masking approach (bottom panel).

Concluding remarks: final assessment

Assessing which method is better suited for capturing specific deformation patterns in the event of volcanic activity for Saba and St. Eustatius remains complicated. From literature it is evident that SBAS typically excels in capturing large-scale deformations and is particularly suitable for spatially correlated deformation signals. Furthermore, the baseline restriction as well as the coherence-based pixel selection approaches in SBAS allow for measuring fast deforming pixels. This is important as rapid and substantial changes can occur close to the eruption event, making it essential to capture these changes. In contrast, PSI enables the detection of small-scale (local) deformation because of the 1D+2D unwrapping approach. This enables the identification of subtle, yet significant, surface changes that might be indicative of volcanic activity. In addition, the full network approach of PSI leads to improved error estimation, i.e. the atmospheric correction estimation. The presence of an atmospheric phase component may significantly reduce the accuracy of a detected deformation signal or, in the worst case scenario, mask the signal.

The results indicate promise for the SBAS method. The findings highlight a significant difference in terms of the spatial coverage achieved by both methods. For monitoring purposes, coverage of the summit and the flanks of the volcano is desired. In terms of St. Eustatius, the steeper slopes of the Quill as well as the progressively vegetated areas up the slopes, primarily rely on SBAS for coverage. The majority of PS are located around the northern region of St. Eustatius. However, the Kultuurvlakte and smaller urban areas on the outer flanks of the Quill also show some PS coverage. For Saba, it was challenging to acquire coverage near the summit of Mt. Scenery following both methods. Any coverage is limited to the outer flanks of the volcano. However, SBAS pixels are found at higher elevations on the slopes compared to the selected PS. The PS are mainly selected along the coastlines, aside from the entire western coastline of Saba. Owing to the single volcanic complex on Saba, even pixels along the coastline could experience volcanic deformation prior to eruptive activity.

The different processing steps reveal some difficulties for both methods. For PSI, these are primarily related to network problems. This caused the rejection of two complete Sentinel-1 stacks, while these stacks have been successfully processed using SBAS. Furthermore, in some cases sub-optimal coverage, i.e. due to large distances between selected PS, of the network occurred. This can lead to unwrapping errors. Similar problems arise for SBAS on account of isolated pixels, particularly around the summit of the volcanoes. These pixels are unreliable and should not be interpreted as deformation. Another difficulty for SBAS is related to the multilooking step, introducing a phase bias and affecting the detail captured by the method. However, to facilitate large-scale deformation studies and still enable an efficient monitoring system, multilooking is a necessary step. In regard to PSI, the need for a pre-defined deformation model of the expected deformation is challenging. Incorrect deformation modeling can affect volcanic risk conclusions and is therefore crucial to consider.

Finally, for the precision it is not possible to draw definitive conclusions due to presence of the DEM error and atmospheric component for SBAS. For Sentinel-1, this resulted in very low temporal coherence values. The temporal coherence for ALOS-2, showed a relatively high level of consistency among the different methods and masking approaches. An atmospheric correction is required to compare the methods based on the precision, and possibly accuracy.

Following from the literature as well as from the results, both methods have distinct advantages and limitations. SBAS shows great promise, providing coverage where PSI does not. Furthermore, the method can be made relatively efficient compared to PSI, which is an important factor to be able to provide near-real time monitoring. However, PSI offers capabilities for detecting small-scale deformations. Given the uncertainty around the expected deformation pattern, a hybrid approach may be beneficial to exploit the strengths of both methods, such that the limitations of one can be compensated by the other. In this way signal loss, e.g., either from limited spatial coverage or from limited spatial resolution (due to multilooking), can be minimized.

7 Conclusions & Recommendations

In this study, the primary aim is to address the following fundamental question:

Is the SBAS approach a viable technique
for an InSAR-based volcanic monitoring system
on the tropical islands of Saba and St. Eustatius?

The results reveal that, yes, there is capability to develop SBAS into a volcanic monitoring tool on these islands, but more development is needed to achieve that goal. It excels in terms of the extensive spatial coverage as well as computational efficiency and, generally, shows consistency among different masking approaches based on the observed patterns, trends and difference maps. Both Sentinel-1 and ALOS-2 can effectively be used for monitoring purposes, overall demonstrating precision at the mm scale. This implies that in the event of volcanic activity, which is expected to induce surface displacements ranging from cm up to even dm's, these changes will be visible in the deformation estimates, with the minimal detectable deformation (MDD) signal estimated at about 1.5 cm/year in the worst-case scenario. L-band imagery proves to be particularly suitable for the tropical conditions of the study area i.e., dense rainforests, on account of its longer wavelength providing higher coherence in comparison to C-band even for larger temporal baselines. C-band remains promising owing to the abundant data availability and revisit frequency. However, as early signs of volcanic activity may be subtle, these signals might be below the detection limit. Early detection is essential to guarantee timely warning of the local authorities, therefore it is crucial to apply corrections for both atmospheric and DEM components to effectively lower the detection limit. Additionally, depending on the smoothness of the deformation signal, a certain spatial sampling may be necessary. For a spatially smooth signal, coarse spatial sampling may suffice to detect the signal, while fine spatial sampling is necessary for more abrupt signals.

To offer additional insight into the main findings, the sub-questions are addressed accordingly:

What is the procedure involved in the implementation of the SBAS time series software and which steps can be improved to enhance the efficiency and robustness of SBAS with respect to the standard approach?

The SBAS approach is developed in accordance with the DORIS output, based on state-of-the-art Python packages such as XARRAY, DASK and ZARR. Furthermore, the SARXARRAY package extends the functionality of these tools for (In)SAR processing. In addition, efficient workflow strategies e.g., minimizing the use of iterative approaches, are explored to reduce computational costs. The processing chain consists of nine main steps. In steps 2) interferometric pair selection, 5) masking and 8) correction unwrapping errors, new approaches are explored to enhance the SBAS method in terms of the efficiency and/or robustness.

Specifically, to improve the computational efficiency a model-based pair selection approach, calibrated using average coherence values, is implemented in step 2). Furthermore, in step 5), three different masking approaches are generated using the coherence to improve the robustness. These approaches include a i) water mask, ii) single mask based on mean coherence and iii) individual masks based on the coherence for every interferometric pair. Approach iii) enables the use of temporary scatterers, but, in turn, demands an iterative and hence more time-consuming approach for the linear inversion step. To improve the efficiency, an efficient inversion scheme that involves clustering unique design matrices is implemented, which reduced the computation time from 18.82 to 0.23 s. Findings suggest that results using approach i) seem more prone to unwrapping mistakes, possibly due to the inclusion of regions of low coherence, and, particularly in the case of the typically lower coherence achieved with Sentinel-1, primarily represent noise.

To investigate the results, an assumption is made based on the GNSS data, i.e., that currently no deformation occurs. Thus, estimated velocity values near zero are expected and therefore the standard deviation serves as a measure of the variability around zero and gives an indication of the precision. It is emphasized that the results are relative to the selected reference pixel and, as such, cannot be interpreted in absolute terms. In addition, phase contributions from the DEM error and atmospheric component are still included and demand careful consideration when interpreting the data. All in all, the findings demonstrate a relatively high level of consistency among the different masking approaches for ALOS-2, based on the observed patterns and difference maps. In the case of St. Eustatius, this consistency became evident following the correction of the unwrapping errors in step 8) through two distinct testing procedures: an interferogram removal approach, similar to Monserrat et al. (2009), and an adaptive approach based on the Delft Detection, Identification, Adaptation (DIA) procedure (Teunissen, 1990). This step not only improves the robustness, but also the overall reliability of the results. Both approaches show improvements in terms of the consistency between velocity estimates from the different masking approaches and the differences are minimal. Therefore the adaptive approach is preferred as it retains all observations and allows for comparison between the updated and original residuals. Conversely, for Sentinel-1 the level of consistency is lower. It is suspected that this inconsistency arises primarily on account of the numerous unwrapping errors found for the single masking approach. Hence, Sentinel-1 is still expected to be suitable for monitoring. This stresses the importance of the correction of unwrapping errors and indicates the need for the expansion of the approaches to more than one epoch. Approach ii) appeared to be more robust when compared to approach iii), in particular due to its lower variability as well as its reduced susceptibility to outliers. Nonetheless, the individual masking approach typically yields velocity estimates closer to zero and appears to be less prone to unwrapping errors. Further investigation, following the correction of the atmospheric component and DEM errors, may offer insights into the preferred masking approach.

How can the obtained results from the SBAS and PSI method be compared?

A preliminary comparison is performed based on a theoretical approach and a semi-quantitative approach, addressing 1) spatial coverage, 2) difficulties encountered in the processing steps, 3) computational requirements and 4) precision. In the theoretical approach, literature review plays a central role to evaluate the limitations and strengths of both methods. However, ultimately, the suitability depends on the specific application, i.e. the conditions of the study area. Ideally, ground truth data from the GNSS stations could be used to evaluate the accuracy of the deformation estimates. However, this is limited to four measurement locations per island, and the GNSS data indicates that currently no deformation occurs, adding complexity to the comparison based on quantitative measures. In addition, as the SBAS results still include the atmospheric and DEM component, the methods cannot be compared 1:1.

What are the advantages, limitations and sources of error associated with the PSI and SBAS approaches in the area of interest?

SBAS excels in applications that require extensive spatial coverage and is typically suitable for capturing spatially correlated deformation signals. PSI excels in applications where high spatial resolution is required and enables the detection of small-scale displacement e.g., up to a single building, owing to the 1D+2D unwrapping. In addition, the full-network approach in PSI allows for extensive phase information and improved error estimation, while the baseline restrictions in SBAS allows for measuring fast deforming pixels.

How do PSI and SBAS compare in their ability to detect potential volcanic deformation signals on the islands of Saba and St. Eustatius?

In regard to the semi-quantifiable approach, SBAS offers superior spatial coverage, especially on the crater and flanks of the Quill on St. Eustatius and the outer flanks and western coastline of Saba. Furthermore, both methods face processing challenges. The multilooking step in SBAS introduces a phase bias but is necessary for large-scale deformation studies. PSI demands a pre-defined deformation model, where incorrect deformation modeling can affect volcanic risk assessment, especially in the case of underestimation of the deformation. In both methods network problems can occur. In the case of PSI this even led to rejection of two Sentinel-1 stacks, for SBAS the impact is less significant.

Assessing the suitability of the methods for detecting volcanic deformation signals in the event of volcanic activity on Saba and St. Eustatius remains complicated. Given the uncertainty around the expected deformation pattern, a hybrid approach may prove advantageous to minimize signal loss. In this way the strengths of both methods can be used, such that the limitations of one method are compensated by the other method. It should be noted however that, regardless of the chosen mask, wavelength or method, acquiring coverage around the summit of Mt. Scenery on Saba remains challenging. In addition, the presence of the DEM and atmospheric component in the final results complicates the comparison based on the precision for Sentinel-1. Overall, the temporal coherence for ALOS-2 showed a similar pattern for both methods as well as the masking approaches. However, to provide a 1:1 comparison of the precision and possibly accuracy, more research is required after the correction.

What is the added value of the SAR L-band imaging in the volcanic monitoring system?

The use of L-band imagery has proven to show promise in capturing and monitoring changes, even with the limited ALOS-2 data availability and significant time intervals between acquisitions. L-band offers coverage in areas where C-band cannot, including densely vegetated regions and on relatively steep slopes. It achieves nearly homogeneous coverage of St. Eustatius, encompassing significant portions of the Quill's flanks, and the outer flanks of Mt. Scenery on Saba. However, the limited temporal resolution of ALOS-2 reduces its ability to detect fast surface deformation. Nevertheless, the upcoming NISAR mission will enhance current capabilities by providing continuous L-band imaging with a revisit time of twelve days.

In summary, the results obtained through SBAS demonstrate promise, particularly for L-band. A comparison with the PSI approach suggests that a hybrid method could be beneficial to enhance understanding of volcanic deformation, also taking into account the unknown future deformation pattern caused by potential volcanic activity on Saba and St. Eustatius. However, there is room for improvement. Future work should focus on incorporating atmospheric and DEM corrections into the SBAS approach, to further compare the different masking approaches, investigate the precision and improve the detection of early signs of volcanic activity. Furthermore, the unwrapping errors for Sentinel-1 need to be accounted for. Finally, while the preliminary comparative analysis indicates distinct advantages and limitations for both methods, additional research is required to draw definitive conclusions i.e., regarding the precision.

7.1 Contributions

This research led to the following contributions:

- The implementation of an SBAS approach using state-of-the-art Python libraries (e.g., (SAR)XARRAY, DASK, ZARR) and efficient workflows for big data analysis.
- The evaluation of three different interferometric pair selection approaches, with considerations for computational efficiency and satellite revisit times.
- The implementation and evaluation of three different coherence-based masking approaches.
- The implementation of an efficient inversion scheme in the case of the individual masking approach, allowing for the use of temporary scatterers.
- The design and implementation of a phase unwrapping error detection approach for SBAS based on the Delft Detection, Identification, Adaptation (DIA) methodology.
- A preliminary comparative analysis between the SBAS and PSI methodologies for volcanic monitoring on Saba and St. Eustatius, based on a theoretical and semi-quantifiable approach.

7.2 Recommendations

Recommendations are given based on the remaining key challenges addressed throughout this study:

- It can be challenging to distinguish the atmospheric effect and DEM errors from the deformation signal. To allow for timely warning of the local authorities in case of volcanic activity, it is crucial to effectively pick up on more subtle surface deformations that may precede a volcanic eruption. Therefore, it is essential to incorporate atmospheric and DEM corrections into the SBAS approach.

- In study areas characterized by terrain variability, layover and shadowing effects are introduced. Consequently, geometric distortion effects occur. To improve data interpretation, a layover-shadow mask would be desirable, such that unreliable regions can be masked.
- There is no specific functionality for layover, foreshortening and radar shadow in DORIS. This could lead to misalignment of the DEM. When dealing with conditions similar to those on Saba and St. Eustatius, this effect can be significant e.g., as indicated by the presence of pixels in the water near steep cliffs for both islands. Therefore, it is recommended to implement this functionality in DORIS.
- The implemented adaptive method for unwrapping errors in SBAS should be expanded to multiple epochs to account for the numerous unwrapping errors in e.g., Sentinel-1. Furthermore, to improve the robustness of the detection of unwrapping errors in SBAS, alternative approaches should be explored, i.e. based on residual peak detection. However, this is challenging due to the multilooking effect.
- Regarding the pair selection approach based on a modeled coherence, a more complex relation can be considered. Specifically, a linear behaviour may not be representative everywhere on the island, e.g., where vegetation cover is dense. Therefore, depending on the location, a different relation can be considered. For example, a quadratic relation could be considered where vegetation cover is high, while linear behaviour might be more representative of bare rocks.
- Isolated pixels remain after the masking approaches in SBAS. These pixels are often located around regions characterized by low coherence, such as the summit of the volcano. They are not included in the spatial network, leading to unwrapping errors. and are therefore deemed unreliable and should be removed. This could for instance be done by a filter based on the number of neighbours of each pixel.
- Study the SAOCOM data as an additional source of L-band data. Temporal coverage is critical to consider for monitoring purposes. Currently, with the available ALOS-2, it is not possible to detect fast surface deformation. However, the upcoming NISAR mission will provide continuous L-band data, with a revisit time of twelve days, and could be used to extend the monitoring network.
- To realize an automatized multi-technique InSAR-based volcanic monitoring system, aside from the processing steps, improvements in terms of the automatizing of the system and the integration with the current volcanic monitoring system on the islands are required. Additional features e.g., to be able to select a desired subset from the larger swaths through drawing a polygon in Google Earth, would improve the automation. In terms of integration, the InSAR-based volcanic monitoring system is an addition to the existing ground monitoring system, comprising of broadband seismometers, continuous GNSS stations and, on Saba, a temperature sensor. Integration with GNSS could be useful, in the case a deformation signal spatially exceeds the size of the island. In addition, an indispensable part of a (volcanic) monitoring system comprises a dashboard to present the results to the end user in an understandable manner. The design of such a dashboard requires consideration regarding the tools needed, target audience, desired technical aspects and combination of different techniques.

8 Appendix

In this section, the complete sets of individual masks for ALOS-2 Path 37 are presented. Due to the sizes of the figures, they are displayed on the following pages. The results for Path 37 of both St. Eustatius and Saba are visualized in Figure 8.1 and Figure 8.2. The interferogram pair selection procedure resulted in 29 interferograms.

Figure 8.1: ALOS-2 Path 37 St. Eustatius - The complete set of individual masks. The masks are binary and either has a value of 0 or 1.

Figure 8.2: ALOS-2 Saba Path 37 - The complete set of individual masks. The masks are binary and either has a value of 0 or 1.

References

[1] Joanna Slawinska and Alan Robock (2018). “Impact of volcanic eruptions on decadal to centennial fluctuations of Arctic sea ice extent during the last millennium and on initiation of the Little Ice Age”. In: *Journal of Climate* 31.6, pp. 2145–2167. DOI: https://doi.org/10.1175/JCLI-D-16-0498.1.

[2] Alan Robock (May 2000). “Volcanic eruptions and climate”. en. In: *Reviews of Geophysics* 38.2, pp. 191–219. ISSN: 87551209. DOI: 10.1029/1998RG000054. URL: http://doi.wiley.com/10.1029/1998RG000054 (visited on Aug. 31, 2023).

[3] USGS (2023). *Volcanic gases can be harmful to health, vegetation and infrastructure — U.S. Geological Survey.* URL: https://www.usgs.gov/programs/VHP/volcanic-gases-can-be-harmful-health-vegetation-and-infrastructure#:~:text=Breathing%5C%20air%5C%20with%5C%20more%5C%20than,is%5C%20a%5C%20hazard%5C%20in%5C%20Hawaii. (visited on Mar. 3, 2023).

[4] Xinyuan Bai, Shaojing Xie, and Yanjun Zhu (Apr. 2022). “Evolution, Causes and Influence Factors of Taal Volcanic Activities”. In: *IOP Conference Series: Earth and Environmental Science* 1011.1, p. 012041. ISSN: 1755-1307, 1755-1315. DOI: 10.1088/1755-1315/1011/1/012041. URL: https://iopscience.iop.org/article/10.1088/1755-1315/1011/1/012041 (visited on Mar. 3, 2023).

[5] S. K. Ebmeier, J. Biggs, et al. (Jan. 2013). “Applicability of InSAR to tropical volcanoes: insights from Central America”. en. In: *Geological Society, London, Special Publications* 380.1, pp. 15–37. ISSN: 0305-8719, 2041-4927. DOI: 10.1144/SP380.2. URL: https://www.lyellcollection.org/doi/10.1144/SP380.2 (visited on Mar. 3, 2023).

[6] Elske De Zeeuw - van Dalfsen and Reinoud Sleeman (Aug. 2018). “A Permanent, Real-Time Monitoring Network for the Volcanoes Mount Scenery and The Quill in the Caribbean Netherlands”. en. In: *Geosciences* 8.9, p. 320. ISSN: 2076-3263. DOI: 10.3390/geosciences8090320. URL: http://www.mdpi.com/2076-3263/8/9/320 (visited on Mar. 3, 2023).

[7] Tereza Pultarova (Jan. 2022). *How satellites have revolutionized the study of volcanoes.* en-US. URL: https://www.space.com/how-satellites-revolutionized-study-of-volcanoes (visited on Mar. 20, 2023).

[8] J. Aswathi et al. (Apr. 2022). “InSAR as a tool for monitoring hydropower projects: A review”. en. In: *Energy Geoscience* 3.2, pp. 160–171. ISSN: 26667592. DOI: 10.1016/j.engeos.2021.12.007. URL: https://linkinghub.elsevier.com/retrieve/pii/S2666759221000809 (visited on Mar. 3, 2023).

[9] F.J. Van Leijen (2014). “Persistent Scatterer Interferometry based on geodetic estimation theory”. PhD thesis. Delft University of Technology. DOI: 10.4233/UUID:5DBA48D7-EE26-4449-B674-CAA8DF93E71E. URL: http://resolver.tudelft.nl/uuid:5dba48d7-ee26-4449-b674-caa8df93e71e (visited on Feb. 13, 2023).

[10] F. Albino et al. (2020). “Automated methods for detecting volcanic deformation using Sentinel-1 Insar Time Series illustrated by the 2017–2018 unrest at Agung, Indonesia”. In: *Journal of Geophysical Research: Solid Earth* 125.2. DOI: 10.1029/2019jb017908.

[11] Yu Morishita et al. (Jan. 2020). “LiCSBAS: An Open-Source InSAR Time Series Analysis Package Integrated with the LiCSAR Automated Sentinel-1 InSAR Processor”. en. In: *Remote Sensing* 12.3, p. 424. ISSN: 2072-4292. DOI: 10.3390/rs12030424. URL: https://www.mdpi.com/2072-4292/12/3/424 (visited on Mar. 7, 2023).

[12] Kateřina Fárová et al. (2019). “Comparing DInSAR and PSI techniques employed to sentinel-1 data to monitor highway stability: A case study of a massive Dobkovičky landslide, Czech Republic”. In: *Remote Sensing* 11.22, p. 2670. DOI: 10.3390/rs11222670.

[13] Fausto Guzzetti, ed. (2021). *Understanding and reducing landslide disaster risk. Volume 2, From mapping to hazard and risk zonation.* eng. OCLC: 1237439721. Cham: Springer. ISBN: 9783030602277.

[14] Shaowei Li, Wenbin Xu, and Zhiwei Li (Mar. 2022). “Review of the SBAS InSAR Time-series algorithms, applications, and challenges”. en. In: *Geodesy and Geodynamics* 13.2, pp. 114–126. ISSN: 16749847. DOI: 10.1016/j.geog.2021.09.007. URL: https://linkinghub.elsevier.com/retrieve/pii/S1674984721000860 (visited on Mar. 8, 2023).

[15] Casey D. Allen, ed. (2017). *Landscapes and Landforms of the Lesser Antilles.* en. World Geomorphological Landscapes. Cham: Springer International Publishing. ISBN: 9783319557854

9783319557878. DOI: 10.1007/978-3-319-55787-8. URL: http://link.springer.com/10.1007/978-3-319-55787-8 (visited on Mar. 8, 2023).

[16] A. Korevaar (2020). “InSAR as a volcanic monitoring tool for Saba and St. Eustatius: A comparison of ALOS-2, Sentinel-1 and PAZ data”. en. In: URL: https://repository.tudelft.nl/islandora/object/uuid%5C%3A744e94b2-ebf9-4e05-8c31-f4a1dc439313 (visited on Feb. 14, 2023).

[17] A. G. Konings et al. (Sept. 2017). “L-band vegetation optical depth and effective scattering albedo estimation from SMAP”. en. In: *Remote Sensing of Environment* 198, pp. 460–470. ISSN: 00344257. DOI: 10.1016/j.rse.2017.06.037. URL: https://linkinghub.elsevier.com/retrieve/pii/S0034425717302961 (visited on Feb. 17, 2023).

[18] Matthew C. Garthwaite et al. (2019). “A Simplified Approach to Operational InSAR Monitoring of Volcano Deformation in Low- and Middle-Income Countries: Case Study of Rabaul Caldera, Papua New Guinea”. In: *Frontiers in Earth Science* 6. ISSN: 2296-6463. (Visited on Feb. 20, 2023).

[19] Andrew Hooper et al. (Dec. 2004). “A new method for measuring deformation on volcanoes and other natural terrains using InSAR persistent scatterers: A NEW PERSISTENT SCATTERERS METHOD”. en. In: *Geophysical Research Letters* 31.23. ISSN: 00948276. DOI: 10.1029/2004GL021737. URL: http://doi.wiley.com/10.1029/2004GL021737 (visited on Mar. 8, 2023).

[20] E.P. Joseph et al. (2022). “Responding to eruptive transitions during the 2020–2021 eruption of La Soufrière volcano, St. Vincent”. In: *Nature Communications* 13.1. ISSN: 2041-1723. DOI: 10.1038/s41467-022-31901-4. URL: https://doi.org/10.1038/s41467-022-31901-4 (visited on Aug. 11, 2023).

[21] S. K. Ebmeier, B. J. Andrews, et al. (Dec. 2018). “Synthesis of global satellite observations of magmatic and volcanic deformation: implications for volcano monitoring & the lateral extent of magmatic domains”. en. In: *Journal of Applied Volcanology* 7.1, p. 2. ISSN: 2191-5040. DOI: 10.1186/s13617-018-0071-3. URL: https://appliedvolc.biomedcentral.com/articles/10.1186/s13617-018-0071-3 (visited on Aug. 14, 2023).

[22] Geoffrey Wadge et al. (Jan. 2000). “Operational Use of InSAR for Volcano Observatories: Experience from Montserrat”. In: *European Space Agency, (Special Publication) ESA SP*.

[23] Piyush Shanker et al. (July 2011). “Comparison of Persistent Scatterers and Small Baseline Time-Series InSAR Results: A Case Study of the San Francisco Bay Area”. In: *IEEE Geoscience and Remote Sensing Letters* 8.4, pp. 592–596. ISSN: 1545-598X, 1558-0571. DOI: 10.1109/LGRS.2010.2095829. URL: http://ieeexplore.ieee.org/document/5692806/ (visited on Aug. 15, 2023).

[24] Xue Chen et al. (2020). “Comparison between PS and SBAS Insar techniques in monitoring shallow landslides”. In: *Understanding and Reducing Landslide Disaster Risk*, pp. 155–161. DOI: 10.1007/978-3-030-60311-3_17.

[25] Jiaming Yao, Xin Yao, and Xinghong Liu (Sept. 2022). “Landslide Detection and Mapping Based on SBAS-InSAR and PS-InSAR: A Case Study in Gongjue County, Tibet, China”. en. In: *Remote Sensing* 14.19, p. 4728. ISSN: 2072-4292. DOI: 10.3390/rs14194728. URL: https://www.mdpi.com/2072-4292/14/19/4728 (visited on Aug. 15, 2023).

[26] Michal Camejo-Harry et al. (Apr. 2023). “Monitoring volcano deformation at La Soufrière, St Vincent during the 2020–21 eruption with insights into its magma plumbing system architecture”. en. In: *Geological Society, London, Special Publications* 539.1, SP539–2022–270. ISSN: 0305-8719, 2041-4927. DOI: 10.1144/SP539-2022-270. URL: https://www.lyellcollection.org/doi/10.1144/SP539-2022-270 (visited on Aug. 10, 2023).

[27] M. John Roobol and Alan L. Smith (2004). *Volcanology of Saba and St. Eustatius, Northern Lesser Antilles*. eng. Wetenschappen: Koninklijke Nederlandse Akademie. ISBN: 9789069843841.

[28] M Shinozuka and B Mansouri (2009). “Synthetic aperture radar and remote sensing technologies for structural health monitoring of civil infrastructure systems”. en. In: *Structural Health Monitoring of Civil Infrastructure Systems*. Elsevier, pp. 113–151. ISBN: 9781845693923. DOI: 10.1533/9781845696825.1.114. URL: https://linkinghub.elsevier.com/retrieve/pii/B9781845693923500049 (visited on Feb. 21, 2023).

[29] Antonio Pepe and Fabiana Calò (Dec. 2017). “A Review of Interferometric Synthetic Aperture RADAR (InSAR) Multi-Track Approaches for the Retrieval of Earth’s Surface Displacements”. en. In: *Applied Sciences* 7.12, p. 1264. ISSN: 2076-3417. DOI: 10.3390/app7121264. URL: https://www.mdpi.com/2076-3417/7/12/1264 (visited on Feb. 21, 2023).

[30] R. F. Hanssen (2001). “Radar interferometry: Data interpretation and error analysis”. en. In: URL: https://repository.tudelft.nl/islandora/object/uuid%5C%3Aa83859d5-c034-427e-b6a9-114c4b008d19 (visited on Feb. 21, 2023).

[31] Luca Dell’Amore, Michelangelo Villano, and Gerhard Krieger (June 2019). “Assessment of Image Quality of Waveform-Encoded Synthetic Aperture Radar Using Real Satellite Data”. In: *2019 20th International Radar Symposium (IRS)*. Ulm, Germany: IEEE, pp. 1–10. ISBN: 9783736998605. DOI: 10.23919/IRS.2019.8768185. URL: https://ieeexplore.ieee.org/document/8768185/ (visited on Feb. 21, 2023).

[32] NASA (2020). *What is Synthetic Aperture Radar?* URL: https://www.earthdata.nasa.gov/learn/backgrounders/what-is-sar.

[33] Sentinel Online (2023). *User Guides - Sentinel-1 SAR - Interferometry - Sentinel Online - Sentinel Online*. URL: https://sentinels.copernicus.eu/web/sentinel/user-guides/sentinel-1-sar/product-overview/interferometry (visited on Feb. 21, 2023).

[34] P.W. Webley et al. (Jan. 2002). “Atmospheric water vapour correction to InSAR surface motion measurements on mountains: results from a dense GPS network on Mount Etna”. en. In: *Physics and Chemistry of the Earth, Parts A/B/C* 27.4-5, pp. 363–370. ISSN: 14747065. DOI: 10.1016/S1474-7065(02)00013-X. URL: https://linkinghub.elsevier.com/retrieve/pii/S147470650200013X (visited on Aug. 25, 2023).

[35] Xiaohong Chen, Qian Sun, and Jun Hu (Nov. 2018). “Generation of Complete SAR Geometric Distortion Maps Based on DEM and Neighbor Gradient Algorithm”. en. In: *Applied Sciences* 8.11, p. 2206. ISSN: 2076-3417. DOI: 10.3390/app8112206. URL: http://www.mdpi.com/2076-3417/8/11/2206 (visited on Aug. 25, 2023).

[36] Lin Wu et al. (Dec. 2021). “A Novel Method for Layover Detection in Mountainous Areas with SAR Images”. en. In: *Remote Sensing* 13.23, p. 4882. ISSN: 2072-4292. DOI: 10.3390/rs13234882. URL: https://www.mdpi.com/2072-4292/13/23/4882 (visited on Oct. 11, 2023).

[37] Andreas Vollrath, Adugna Mullissa, and Johannes Reiche (Jan. 2020). “Angular-Based Radiometric Slope Correction for Sentinel-1 on Google Earth Engine”. en. In: *Remote Sensing* 12.11, p. 1867. ISSN: 2072-4292. DOI: 10.3390/rs12111867. URL: https://www.mdpi.com/2072-4292/12/11/1867 (visited on June 30, 2023).

[38] P. Berardino et al. (Nov. 2002). “A new algorithm for surface deformation monitoring based on small baseline differential SAR interferograms”. en. In: *IEEE Transactions on Geoscience and Remote Sensing* 40.11, pp. 2375–2383. ISSN: 0196-2892. DOI: 10.1109/TGRS.2002.803792. URL: http://ieeexplore.ieee.org/document/1166596/ (visited on July 26, 2023).

[39] Riccardo Lanari et al. (Apr. 2007). “An Overview of the Small BAseline Subset Algorithm: a DInSAR Technique for Surface Deformation Analysis”. en. In: *Pure and Applied Geophysics* 164.4, pp. 637–661. ISSN: 0033-4553, 1420-9136. DOI: 10.1007/s00024-007-0192-9. URL: http://link.springer.com/10.1007/s00024-007-0192-9 (visited on Mar. 20, 2023).

[40] Homa Ansari, Francesco De Zan, and Alessandro Parizzi (2021). “Study of Systematic Bias in Measuring Surface Deformation With SAR Interferometry”. In: *IEEE Transactions on Geoscience and Remote Sensing* 59. DOI: 10.36227/techrxiv.11672532. URL: https://ieeexplore.ieee.org/stamp/stamp.jsp?tp=&arnumber=9130052 (visited on Aug. 18, 2023).

[41] Yujie Zheng et al. (2022). “On Closure Phase and Systematic Bias in Multilooked SAR Interferometry”. In: *IEEE Transactions on Geoscience and Remote Sensing* 60, pp. 1–11. ISSN: 0196-2892, 1558-0644. DOI: 10.1109/TGRS.2022.3167648. URL: https://ieeexplore.ieee.org/document/9758802/ (visited on Aug. 18, 2023).

[42] Michele Crosetto et al. (May 2016). “Persistent Scatterer Interferometry: A review”. en. In: *ISPRS Journal of Photogrammetry and Remote Sensing* 115, pp. 78–89. ISSN: 09242716. DOI: 10.1016/j.isprsjprs.2015.10.011. URL: https://linkinghub.elsevier.com/retrieve/pii/S0924271615002415 (visited on Aug. 28, 2023).

[43] Hanwen Yu et al. (Mar. 2019). “Phase Unwrapping in InSAR : A Review”. In: *IEEE Geoscience and Remote Sensing Magazine* 7.1, pp. 40–58. ISSN: 2168-6831, 2473-2397, 2373-7468. DOI: 10.1109/MGRS.2018.2873644. URL: https://ieeexplore.ieee.org/document/8672140/ (visited on Aug. 22, 2023).

[44] A. Ferretti, C. Prati, and F. Rocca (Sept. 2000). “Nonlinear subsidence rate estimation using permanent scatterers in differential SAR interferometry”. In: *IEEE Transactions on Geoscience and Remote Sensing* 38.5, pp. 2202–2212. ISSN: 01962892. DOI: 10.1109/36.868878. URL: http://ieeexplore.ieee.org/document/868878/ (visited on Aug. 28, 2023).

[45] B. Kampes, R. Hanssen, and Z. Perski (2003). “Radar Interferometry With Public Domain Tools”. en. In: *Proceedings of FRINGE* 3.

[46] Bert M. Kampes (2006). *Radar interferometry: persistent scatterer technique.* Remote sensing and digital image processing v. 12. OCLC: ocm71238108. Dordrecht, the Netherlands: Springer. ISBN: 9781402045769 9781402047237.

[47] Cristian Rossi and Michael Eineder (Dec. 2015). “High-Resolution InSAR Building Layovers Detection and Exploitation”. In: *IEEE Transactions on Geoscience and Remote Sensing* 53.12, pp. 6457–6468. ISSN: 0196-2892, 1558-0644. DOI: 10.1109/TGRS.2015.2440913. URL: http://ieeexplore.ieee.org/document/7128381/ (visited on Sept. 1, 2023).

[48] M.J. Roobol A.L. Smith (n.d.[a]). *Saba.* en-US. URL: https://uwiseismic.com/ (visited on May 3, 2023).

[49] B.S.J. Nijhof & A.O. Debrot J.A. de Freitas A.C. Rojer (2016). *A landscape ecological vegetation map of Saba (Lesser Antilles).* eng. Den Helder: IMARES.

[50] M.J Defant et al. (June 2001). “The geology, petrology, and petrogenesis of Saba Island, Lesser Antilles”. en. In: *Journal of Volcanology and Geothermal Research* 107.1-3, pp. 87–111. ISSN: 03770273. DOI: 10.1016/S0377-0273(00)00268-7. URL: https://linkinghub.elsevier.com/retrieve/pii/S0377027300002687 (visited on May 2, 2023).

[51] M.J. Roobol A.L. Smith (n.d.[b]). *St. Eustatius.* en-US. URL: https://uwiseismic.com/ (visited on May 3, 2023).

[52] B.S.J. Nijhof & A.O. Debrot J.A. de Freitas A.C. Rojer (2014). *A landscape ecological vegetation map of Sint Eustatius (Lesser Antilles).* eng. Den Helder: IMARES. ISBN: 9789069846798.

[53] ESA (n.d.[a]). *Sentinel-1 Overview.* URL: https://sentinels.copernicus.eu/web/sentinel/missions/sentinel-1/overview (visited on Aug. 10, 2023).

[54] — (n.d.[b]). *Mission Summary.* URL: https://sentinels.copernicus.eu/web/sentinel/missions/sentinel-1/overview/mission-summary (visited on Aug. 10, 2023).

[55] — (n.d.[c]). *Mission ends for Copernicus Sentinel-1B satellite.* URL: https://www.esa.int/Applications/Observing_the_Earth/Copernicus/Sentinel-1/Mission_ends_for_Copernicus_Sentinel-1B_satellite (visited on Aug. 10, 2023).

[56] — (2012). *ALOS-2 (Advanced Land Observing Satellite-2) / Daichi-2.* URL: https://www.eoportal.org/satellite-missions/alos-2#performance-specifications.

[57] Takeshi Motohka, Yukihiro Kankaku, and Shinichi Suzuki (May 2017). “Advanced Land Observing Satellite-2 (ALOS-2) and its follow-on L-band SAR mission”. In: *2017 IEEE Radar Conference (RadarConf).* Seattle, WA, USA: IEEE, pp. 0953–0956. ISBN: 9781467388238. DOI: 10.1109/RADAR.2017.7944341. URL: http://ieeexplore.ieee.org/document/7944341/ (visited on Sept. 11, 2023).

[58] NASA (Dec. 2022). *Quick Facts.* URL: https://nisar.jpl.nasa.gov/mission/quick-facts/.

[59] Kent Kellogg et al. (Mar. 2020). “NASA-ISRO Synthetic Aperture Radar (NISAR) Mission”. In: *2020 IEEE Aerospace Conference.* ISSN: 1095-323X, pp. 1–21. DOI: 10.1109/AERO47225.2020.9172638.

[60] ESA (n.d.[d]). *About SAOCOM.* URL: https://earth.esa.int/eogateway/missions/saocom.

[61] SAOCOM project (2020). *SAOCOM-1 LEVEL 1 PRODUCTS FORMAT.* Tech. rep. Ministerio de Ciencia Tecnología e Innovación. URL: %7Bhttps://saocom.veng.com.ar/L1-product-format-EN.pdf%7D.

[62] G. Blewitt, W.C. Hammond, and C. Kreemer (Sept. 2018). “Harnessing the GPS Data Explosion for Interdisciplinary Science”. In: *Eos* 99. ISSN: 2324-9250. DOI: 10.1029/2018EO104623. URL: https://eos.org/project-updates/harnessing-the-gps-data-explosion-for-interdisciplinary-science (visited on Aug. 11, 2023).

[63] Stephan Hoyer and Joe Hamman (Apr. 2017). “xarray: N-D labeled Arrays and Datasets in Python”. In: *Journal of Open Research Software* 5.1, p. 10. ISSN: 2049-9647. DOI: 10.5334/jors.148. URL: https://openresearchsoftware.metajnl.com/article/10.5334/jors.148/ (visited on Nov. 7, 2023).

[64] *sarxarray* (Oct. 2023). DOI: 10.5281/ZENODO.10044256. URL: https://zenodo.org/doi/10.5281/zenodo.10044256 (visited on Aug. 6, 2023).

[65] Qiuxiang Tao et al. (Nov. 2020). “The performance of LS and SVD methods for SBAS InSAR deformation model solutions”. In: *International Journal of Remote Sensing* 41.22, pp. 8547–8572. ISSN: 0143-1161. DOI: 10.1080/01431161.2020.1782504. URL: https://doi.org/10.1080/01431161.2020.1782504 (visited on Apr. 10, 2023).

[66] Eike Reinosch et al. (May 2020). “InSAR time series analysis of seasonal surface displacement dynamics on the Tibetan Plateau”. en. In: *The Cryosphere* 14.5, pp. 1633–1650. ISSN: 1994-0424. DOI: 10.5194/tc-14-1633-2020. URL: https://tc.copernicus.org/articles/14/1633/2020/ (visited on Sept. 29, 2023).

[67] A.L. Van Natijne et al. (July 2022). “World-wide InSAR sensitivity index for landslide deformation tracking”. en. In: *International Journal of Applied Earth Observation and Geoinformation* 111, p. 102829. ISSN: 15698432. DOI: 10.1016/j.jag.2022.102829. URL: https://linkinghub.elsevier.com/retrieve/pii/S1569843222000310 (visited on Aug. 29, 2023).

[68] Chen and Zebker (Feb. 2001). “Two-dimensional phase unwrapping with use of statistical models for cost functions in nonlinear optimization”. en. In: *Journal of the Optical Society of America A* 18.2, p. 338. ISSN: 1084-7529, 1520-8532. DOI: 10.1364/JOSAA.18.000338. URL: https://opg.optica.org/abstract.cfm?URI=josaa-18-2-338 (visited on Aug. 21, 2023).

[69] O. Monserrat et al. (Nov. 2009). “A tool for 2+ 1D phase unwrapping: application examples”. In.

[70] P. J. G. Teunissen (Sept. 1990). “An Integrity and Quality Control Procedure for Use in Multi Sensor Integration”. In: *Proceedings of the 3rd International Technical Meeting of the Satellite Division of the Institute of Navigation*, pp. 513–522.

[71] Ling Chang, Rolf P. B. J. Dollevoet, and Ramon F. Hanssen (May 2018). “Monitoring Line-Infrastructure With Multisensor SAR Interferometry: Products and Performance Assessment Metrics”. In: *IEEE Journal of Selected Topics in Applied Earth Observations and Remote Sensing* 11.5, pp. 1593–1605. ISSN: 1939-1404, 2151-1535. DOI: 10.1109/JSTARS.2018.2803074. URL: https://ieeexplore.ieee.org/document/8306273/ (visited on Nov. 16, 2023).

[72] P. J. G. Teunissen (1989). *Mathematische Geodesie II, Inleiding toetsingstheorie.* Lecture notes. Faculty of Geodetic Engineering, Delft University of Technology, Delft.

[73] Yuta Izumi et al. (Nov. 2022). “Temporal Subset SBAS InSAR Approach for Tropical Peatland Surface Deformation Monitoring Using Sentinel-1 Data”. en. In: *Remote Sensing* 14.22, p. 5825. ISSN: 2072-4292. DOI: 10.3390/rs14225825. URL: https://www.mdpi.com/2072-4292/14/22/5825 (visited on Sept. 12, 2023).